



Faculteit Wetenschappen
Departement Fysica

Excitonic complexes in transition metal dichalcogenides and related materials

Excitonische complexen in transitiemetaal dichalcogeniden en gerelateerde materialen

Proefschrift voorgelegd tot het behalen van de graad van
doctor in de wetenschappen: fysica
aan de Universiteit Antwerpen te verdedigen door

Matthias Van der Donck

Promotor
Prof. Dr. François Peeters

Antwerpen, September 2019

Members of the jury:**Chair**

Prof. Dr. Sara Bals, Universiteit Antwerpen, Belgium

Supervisor

Prof. Dr. François Peeters, Universiteit Antwerpen, Belgium

Members

Prof. Dr. Michiel Wouters, Universiteit Antwerpen, Belgium,

Prof. Dr. David Neilson, Universiteit Antwerpen, Belgium,

Prof. Dr. Dirk Lamoen, Universiteit Antwerpen, Belgium,

Prof. Dr. Vincent Meunier, Rensselaer Polytechnic Institute, USA,

Dr. Artem Mishchenko, University of Manchester, UK

Contact Information

Matthias Van der Donck

G.U. 205

Groenenborgerlaan 171

2020 Antwerpen

Belgium

matthias.vanderdonck@uantwerpen.be

*This work was supported by the Flemish Science Foundation (FWO-VI)
through an aspirant fellowship.*

Acknowledgements

It is impossible to complete a doctoral education all by oneself and that is why it is now due time to give credit to all those who helped me along the way.

First of all I would like to thank my promotor Prof. Dr. François Peeters for making sure I always had a clear objective in mind but still allowing me the freedom to explore my own ideas as well. I am also very grateful for the additional guidance of Dr. Mohammad Zarenia (during the first part of my PhD) and Prof. Dr. David Neilson (during the second part of my PhD) with whom I had a lot of instructive and enjoyable discussions.

I would also like to thank everyone in the CMT group for the pleasant atmosphere which they created and for our weekly entertaining games of football. Special thanks go out to Ben, Nikolas, and Robbe for the countless and often intense lunchtime discussions covering more or less every topic imaginable and for always being available for a much-needed break.

Finally, a big thank you to my family and friends who, through the many great moments which we shared during the last four years, kept me aware of the fact that there is a life outside of the university as well. Last, but not most, I want to thank my girlfriend Charlotte for her truly unconditional love and support and for always being there for me.

Matthias Van der Donck
Antwerp, September 2019

Abstract

In this thesis the properties of excitons, which are bound states of an electron and a hole, and higher order excitonic complexes such as trions and biexcitons are studied in monolayer transition metal dichalcogenides (TMDs) and related materials such as monolayer black phosphorus and TMD heterostructures.

For excitons a comparison is made between the finite element solutions of the multi- and single-band model, showing that the former lowers the binding energy and leads to a reordering of and breaking of degeneracies between different angular momentum intervalley excitons. For trions and biexcitons the stochastic variational method is employed to numerically solve the single-band model. For all three excitonic complexes it is found that the binding energies, which are calculated for different combinations of TMDs and substrates and which are compared with theoretical and experimental results from the literature, are extremely large.

Next, the presence of a perpendicular magnetic field is considered and shown to increase the binding energy of excitons, trions, and biexcitons in monolayer TMDs. The diamagnetic shifts of these excitonic complexes are found to increase with increasing substrate dielectric constant and by calculating the exciton Landau levels it is demonstrated how the magnetic field alters the degeneracies of the excited states. Furthermore, it is shown that so-called dark excitons exhibit an exceptionally strong valley Zeeman effect in the presence of a tilted magnetic field.

Monolayer materials with anisotropic band masses are considered next and it is shown that in black phosphorus this anisotropy persists in the excitonic complexes while in TiS_3 it does not. It is found that applying uniaxial tensile strain increases the exciton binding energy in black phosphorus.

Interlayer excitons in TMD heterostructures are also studied and it is shown that additional polarization effects in these systems can significantly decrease their binding energy, which is calculated for all possible combinations of TMDs. The experimental signature of these interlayer excitons is found to be tunable by means of a perpendicular electric field.

Finally, the possibility of interlayer excitonic superfluidity, which is currently intensively sought after in experiments, in a superlattice of TMD heterostructures is investigated and very high critical temperatures of up to 270 K are obtained.

This thesis contributes new insights to the topic of strongly bound excitonic complexes in two-dimensional materials, including the tunability of their properties and their importance in exotic phenomena such as high-temperature superfluidity.

Abstract - Nederlands

In deze thesis worden de eigenschappen van excitonen, welke gebonden toestanden zijn van een elektron en een holte, en hogere orde excitonische complexen zoals trionen en biexcitonen bestudeerd in monolaag transitiemetaal dichalcogeniden (TMDs) en gerelateerde materialen zoals monolaag zwarte fosfor en TMD heterostructuren.

Voor excitonen wordt een vergelijking gemaakt tussen de eindige elementen oplossingen van het multi- en eenbandmodel, wat aantoont dat het multibandmodel de bindingsenergie verlaagt en leidt tot een herschikking van en een breking van ontarding tussen intervallen excitonen met verschillende draaimomenta. Voor trionen en biexcitonen wordt de stochastisch variationele methode gebruikt om het eenbandmodel numeriek op te lossen. Voor alle drie de excitonische complexen wordt gevonden dat de bindingsenergieën, welke berekend worden voor verschillende combinaties van TMDs en substraten en welke vergeleken worden met theoretische en experimentele resultaten uit de literatuur, extreem groot zijn.

Vervolgens wordt de aanwezigheid van een loodrecht magneetveld beschouwd en er wordt aangetoond dat dit de bindingsenergie van excitonen, trionen en biexcitonen in monolaag TMDs verhoogt. Er wordt gevonden dat de diamagnetische shift van deze excitonische complexen toeneemt met toenemende diëlektrische constante van het substraat en aan de hand van de berekende exciton Landau-niveaus wordt getoond hoe het magneetveld de ontarding van de geëxciteerde toestanden verandert. Voorts wordt aangetoond dat zogenoemde donkere excitonen een uitzonderlijk sterk vallei Zeeman-effect vertonen in de aanwezigheid van een schuin magneetveld.

Monolaag materialen met anisotrope bandmassa's worden vervolgens onderzocht en er wordt gevonden dat in zwarte fosfor deze anisotropie zich doorzet in de excitonische complexen terwijl dit in TiS_3 niet het geval is. Het blijkt dat het uniaxiaal uitrekken van zwarte fosfor leidt tot een verhoging van de exciton bindingsenergie.

Verder worden interlaag excitonen in TMD heterostructuren bestudeerd en er wordt aangetoond dat additionele polarizatie-effecten in deze systemen hun bindingsenergie, welke wordt berekend voor alle mogelijke combinaties van TMDs, aanzienlijk kunnen verlagen. De experimentele aanwijzing voor deze interlaag excitonen blijkt controleerbaar te zijn met een loodrecht elektrisch veld.

Ten slotte wordt de mogelijkheid tot interlaag excitonische superfluiditeit, waar momenteel intensief naar wordt gezocht in experimenten, in een superrooster van TMD heterostructuren onderzocht en zeer hoge kritische temperaturen tot 270 K worden gevonden.

Deze thesis draagt nieuwe inzichten bij aan het domein van sterk gebonden tweedimensionale excitonische complexen in monolaag materialen, waaronder hoe hun eigenschappen kunnen worden gecontroleerd en hun belang in exotische fenomenen zoals hoge-temperatuur superfluiditeit.

List of publications

Publications related to this thesis

1. **M. Van der Donck**, M. Zarenia, and F. M. Peeters, *Excitons and trions in monolayer transition metal dichalcogenides: A comparative study between the multiband and the quadratic single-band model*, Physical Review B **96**, 035131 (2017). (chapters 3 and 4)
2. **M. Van der Donck**, M. Zarenia, and F. M. Peeters, *Strong valley Zeeman effect of dark excitons in monolayer transition metal dichalcogenides in a tilted magnetic field*, Physical Review B **97**, 081109(R) (2018). (chapter 5)
3. **M. Van der Donck**, M. Zarenia, and F. M. Peeters, *Excitons, trions, and biexcitons in transition-metal dichalcogenides: Magnetic-field dependence*, Physical Review B **97**, 195408 (2018). (chapters 4 and 5)
4. **M. Van der Donck** and F. M. Peeters, *Interlayer excitons in transition metal dichalcogenide heterostructures*, Physical Review B **98**, 115104 (2018). (chapter 7)
5. **M. Van der Donck** and F. M. Peeters, *Rich many-body phase diagram of electrons and holes in doped monolayer transition metal dichalcogenides*, Physical Review B **98**, 115432 (2018). (chapter 2)

6. **M. Van der Donck** and F. M. Peeters, *Excitonic complexes in anisotropic atomically thin two-dimensional materials: Black phosphorus and TiS_3* , Physical Review B **98**, 235401 (2018). (chapter 6)
7. **M. Van der Donck** and F. M. Peeters, *Spectrum of exciton states in monolayer transition metal dichalcogenides: Angular momentum and Landau levels*, Physical Review B **99**, 115439 (2019). (chapters 3 and 5)
8. **M. Van der Donck**, S. Conti, A. Perali, A. R. Hamilton, B. Partoens, F. M. Peeters, and D. Neilson, *High temperature 3D electron-hole superfluidity in a superlattice*, Nature Physics (submitted). (chapter 8)
9. S. Conti, **M. Van der Donck**, A. Perali, F. M. Peeters, and D. Neilson, *Exploiting multicomponent effects in bilayer transition metal dichalcogenides for enhanced electron-hole superfluidity*, Physical Review Letters (submitted). (chapter 8)
10. L. L. Li, **M. Van der Donck**, and F. M. Peeters, *Strain tunable plasmons and excitons in monolayer and bilayer phosphorene*, (manuscript in preparation). (chapter 6)

Other publications

11. **M. Van der Donck**, F. M. Peeters, and B. Van Duppen, *Transport properties of bilayer graphene in a strong in-plane magnetic field*, Physical Review B **93**, 115423 (2016).
12. **M. Van der Donck**, F. M. Peeters, and B. Van Duppen, *Comment on “Creating in-plane pseudomagnetic fields in excess of 1000 T by misoriented stacking in a graphene bilayer”*, Physical Review B **93**, 247401 (2016).
13. **M. Van der Donck**, C. De Beule, B. Partoens, F. M. Peeters, and B. Van Duppen, *Piezoelectricity in asymmetrically strained bilayer graphene*, 2D Materials **3**, 035015 (2016).
14. W. Wang, B. Van Duppen, **M. Van der Donck**, and F. M. Peeters, *Magneto-polaron effect on shallow-impurity states in the presence of magnetic and intense terahertz laser fields in the Faraday configuration*, Physical Review B **97**, 064108 (2018).

15. H. M. Abdullah, **M. Van der Donck**, H. Bahlouli, F. M. Peeters, and B. Van Duppen, *Graphene quantum blisters: A tunable system to confine charge carriers*, Applied Physics Letters **112**, 213101 (2018).
16. J. Merckx, **M. Van der Donck**, B. Van Duppen, and F. M. Peeters, *Inhomogeneous magnetic field effects in kinked, rippled, and wrinkled graphene*, (manuscript in preparation)
17. T. Rey, R. Van Pottelberge, **M. Van der Donck**, F. M. Peeters, and B. Van Duppen, *Hydrogen-like confinement in anisotropic TMTs: Breaking of angular degeneracy*, (manuscript in preparation)

Contents

List of Abbreviations	xix
1 Introduction	1
1.1 A short history of excitons	1
1.2 Entering the flatlands	5
1.3 Potential applications of monolayer TMDs	7
1.3.1 Exciton-based applications	8
1.4 Goal and organization of the thesis	10
2 Electrons and holes in monolayer TMDs	13
2.1 From bulk to monolayer	13
2.1.1 Crystal structure and symmetry	13
2.1.2 Electronic structure	14
2.1.3 Spin-orbit coupling	17
2.2 Life in the valleys	19
2.2.1 Effective Hamiltonian	19
2.2.2 Circular dichroism	23
2.2.3 Berry curvature	25
2.2.4 Magnetic field effects	26
2.3 A hole in the band	29
2.4 Interparticle interaction potential	30
2.5 Many-body phases in monolayer TMDs	33
2.5.1 Many-body Hamiltonian	34

2.5.2	Variational solution	36
2.5.3	Numerical results	38
2.5.4	Conclusion	43
3	Excitons in monolayer TMDs	45
3.1	Exciton Hamiltonian eigenvalue equation(s)	45
3.1.1	Exact solution for $\mathbf{K} = \mathbf{0}$ excitons	48
3.1.2	Approximate solution for $\mathbf{K} \neq \mathbf{0}$ excitons	49
3.1.3	Single-band model	51
3.2	Numerical results	52
3.2.1	Ground state binding energy	52
3.2.2	Exciton energy spectrum	56
3.2.3	Wave function and interparticle distance	61
3.2.4	Absorbance spectrum	65
3.3	Experimental measurement of the exciton binding energy	67
3.4	Conclusion	69
4	Trions and biexcitons in monolayer TMDs	71
4.1	A short history of trions and biexcitons	71
4.2	Trions in monolayer TMDs: a first attempt	72
4.3	Stochastic variational method	75
4.4	Numerical results	79
4.4.1	Binding energy	79
4.4.2	Wave function	83
4.5	Experimental measurement of the trion and biexciton binding energy	85
4.6	Conclusion	88
5	Magnetic field effects on excitonic complexes in monolayer TMDs	91
5.1	Exciton Landau levels	91
5.2	Strong valley Zeeman effect of dark excitons in a tilted magnetic field	95
5.2.1	Influence of the different Zeeman effects on the exciton energies	95
5.2.2	PL spectrum in a tilted magnetic field	98
5.3	Magnetic field dependence of the ground state properties of excitonic complexes	101
5.3.1	Binding energy	103
5.3.2	Wave function and interparticle distance	107
5.3.3	Diamagnetic shift	109

5.4	Conclusion	113
6	Excitonic complexes in anisotropic 2D materials	115
6.1	Anisotropic 2D materials	115
6.2	Binding energy	117
6.3	Correlation function and interparticle distance	121
6.4	Excitons in strained bP	124
6.5	Conclusion	127
7	Interlayer excitons in TMD heterostructures	129
7.1	TMD heterostructures: band alignment and interlayer coupling	129
7.2	Interlayer interaction potential	132
7.3	Numerical results	136
7.4	Conclusion	145
8	Excitonic superfluidity in TMD heterostructures	147
8.1	A short history of (conventional) superfluidity	147
8.2	Excitonic superfluidity	149
8.3	Berezinskii-Kosterlitz-Thouless transition	150
8.4	Superlattice of TMD heterostructures	152
8.4.1	Energy spectrum and eigenstates	152
8.4.2	Coulomb matrix elements between superlattice eigenstates	156
8.4.3	Superfluid properties	159
8.4.4	Numerical results	160
8.5	Conclusion	166
9	Conclusion and outlook	167
9.1	Summary	167
9.2	Situating the novelty of this thesis	171
9.3	Outlook	173
A	Three-band tight-binding Hamiltonian for monolayer TMDs	175
B	Derivation of the spin-orbit coupling	179
B.1	Relativistic quantum mechanical approach	179
B.2	Classical approach	180
C	Matrix elements between correlated Gaussian basis functions	183

D Kinetic energy of single vortices and vortex-antivortex pairs	187
E Derivation of the superfluid gap equation	189
Bibliography	195
Curriculum Vitae	221

List of Abbreviations

1D	One-dimensional
2D	Two-dimensional
3D	Three-dimensional
BCS	Bardeen-Cooper-Schrieffer
BEC	Bose-Einstein condensate
BKT	Berezinskiĭ-Kosterlitz-Thouless
bP	Black phosphorus
FEM	Finite element method
hBN	Hexagonal boron nitride
LED	Light-emitting diode
PL	Photoluminescence
RPA	Random phase approximation
SVM	Stochastic variational method
TMD	Transition metal dichalcogenide

CHAPTER 1

Introduction

1.1 A short history of excitons

The concept *exciton* was first proposed by Yakov Frenkel in 1931 [1], although he referred to it as *excitation wave*, in an attempt to explain the discrete lines in the emission spectra of iodine and related materials. His idea was based on a simple one-dimensional (1D) monatomic lattice in which all atoms are in the ground state, except for one atom in which an electron is optically excited to a higher energy level. This is schematically illustrated in Fig. 1.1. Furthermore, he neglected electron-electron interactions and assumed the electron positions to be fixed at their respective atomic nuclei. His main realization was that, even though the electrons are fixed, the electron excitation is not confined to a particular atom, but rather can hop between different atoms. Through either radiative or vibrational processes the highest-energy electron of atom i loses an amount of energy while the highest-energy electron of atom $i+1$ gains that same amount. In other words: the excitation is a quasiparticle which transfers energy but does not transfer charge. This quasiparticle is called an exciton. Because he assumed the electrons to be fixed, the exciton is always located around a single atomic nucleus and, as a consequence, a very tightly bound exciton whose size is of the order of the unit cell of the surrounding crystal is still referred to today as a *Frenkel exciton* and is mostly found in alkali halides such as kitchen salt.

Even though Frenkel's work was groundbreaking, his theory failed to explain

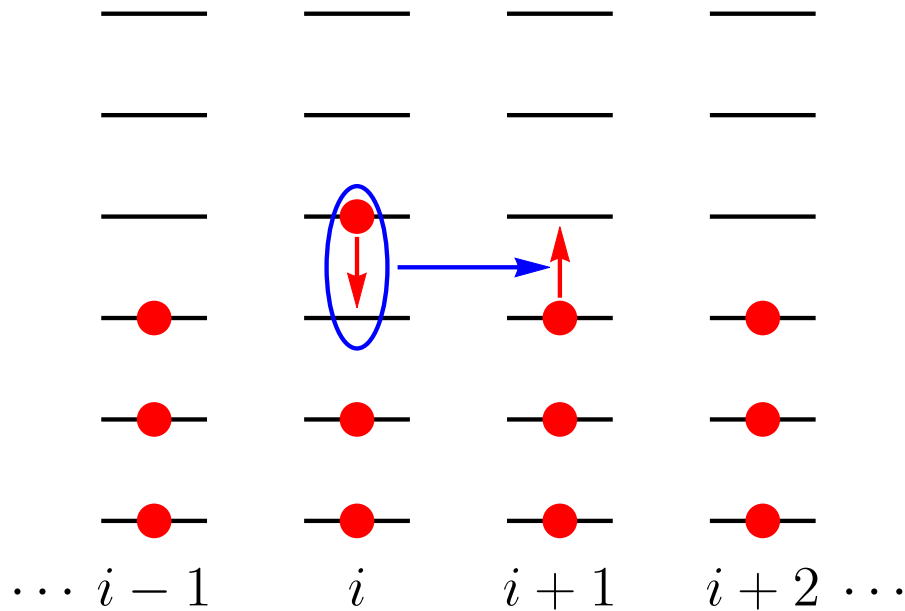


Figure 1.1: Schematic illustration of the Frenkel exciton in a 1D monatomic lattice. Electrons are indicated by the red dots, whereas the exciton is denoted by the blue ellipse. Exciton transport through energy exchange of electrons is shown by the colored arrows.

the discrete lines found in the emission spectra of semiconductors. This is because he neglected electron-electron interactions, which play an important role in understanding excited electron states in semiconductors as these can propagate quasi-freely through the lattice. Looking back now at the simple picture in Fig. 1.1, imagine that the excited electron can travel freely between the atomic sites. At each atomic site there are N electrons (in this case 3) repelling the excited electron, except at atomic site i where it is repelled by $N - 1$ electrons, i.e. it is less repelled by site i . This will cause the electron to be pushed towards site i , meaning that there is an effective attraction. The same result can be obtained by neglecting the bound electrons and introducing a positively charged quasiparticle: the *hole*, which was first introduced by Dirac in 1930, i.e. simultaneously with Frenkel's first description of the exciton. The attractive interaction between the electron and the hole causes the exciton to have a hydrogen atom-like internal structure, i.e. the presence of discrete energy levels, which leads to the observed lines in the emission spectra. For the three-dimensional (3D) hydrogen atom these energy levels are

	Ge	Si	CdS	ZnO	GaAs
E_b	5 [4]	10 [5]	28 [6]	59 [7]	3.4 [8]

Table 1.1: Experimentally obtained exciton binding energy (meV) for different 3D semiconductors.

given by

$$E_n = -\frac{1}{2} \left(\frac{e^2}{4\pi\epsilon_0} \right)^2 \frac{\mu}{\hbar^2 n^2}, \quad (1.1)$$

with n a strictly positive integer and with $\mu = m_0 m_P / (m_0 + m_P) \approx m_0$ the reduced mass with m_0 (m_P) the electron (proton) mass. For excitons the substitutions $m_0 \rightarrow m_e$, $m_P \rightarrow m_h$, and $\epsilon_0 \rightarrow \epsilon_r \epsilon_0$ have to be made in the above expressions with m_e (m_h) and ϵ_r the electron (hole) effective band mass and the relative dielectric constant of the material, respectively. The internal exciton structure was first mathematically described by Gregory Wannier [2] and, as a consequence, excitons which are spread out over multiple unit cells of the surrounding crystal are referred to as *Wannier excitons* and are mostly found in semiconductors. The excitons discussed in this thesis are all Wannier type excitons.

Over the years excitons have been studied, both theoretically [3] and experimentally, in numerous 3D semiconductors and insulators such as germanium [4], silicon [5], cadmium sulfide [6], zinc oxide [7], gallium arsenide [8, 9], titanium dioxide [10, 11], and lithium fluoride [9]. A number of experimentally obtained exciton binding energies for different 3D semiconductors are listed in Table 1.1, which shows that these values do not exceed 60 meV.

In the late 1960s molecular-beam epitaxy was developed, in which atoms from different elements are sublimed in ultra-high vacuum and subsequently condensed on a substrate with a controlled deposition rate, allowing for the creation of heterostructures of different semiconductors. When the stacking of certain semiconductors leads to a type-I band alignment, a quantum well is formed which can be made as thin as a few nanometers. This is shown in Fig. 1.2 for the most famous example, i.e. that of a GaAs/ $\text{Al}_x\text{Ga}_{1-x}\text{As}$ heterostructure. The x in $\text{Al}_x\text{Ga}_{1-x}\text{As}$ indicates the fraction of AlAs (as opposed to GaAs) in the alloy, which from now on will be abbreviated to AlGaAs. Charge carriers in these quantum wells are quasi-two-dimensional (quasi-2D) and therefore these systems immediately gained a lot of attention because of their novel physics and promising potential for applications such as transistors. Another consequence of the quasi-2D nature of the charge carriers is the relative increase in strength of the Coulomb interactions between them,

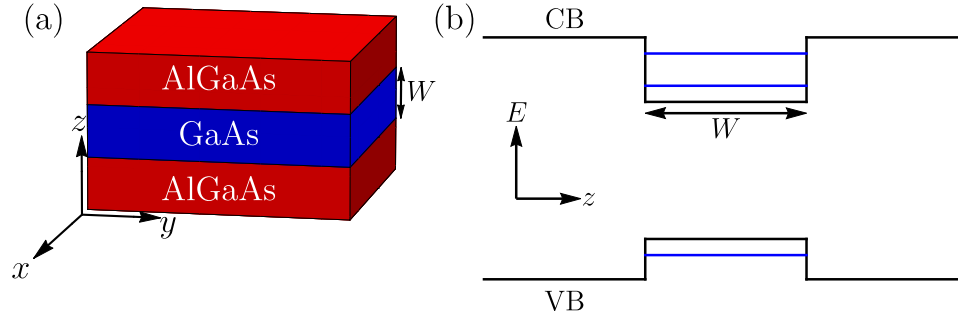


Figure 1.2: (a) Schematic illustration of a GaAs/AlGaAs heterostructure. GaAs acts as a quantum well of width W . (b) Energy diagram showing the lowest conduction band (CB) and highest valence band (VB) as a function of the perpendicular coordinate z . Two electron levels and one hole level which are localized in the quantum well are indicated.

which can for example be seen by considering the energy levels of the 2D hydrogen atom which are given by

$$E_n = -\frac{1}{2} \left(\frac{e^2}{4\pi\epsilon_0} \right)^2 \frac{\mu}{\hbar^2} \frac{1}{\left(n - \frac{1}{2}\right)^2}, \quad (1.2)$$

with n again a strictly positive integer [12]. This result shows that the ionization energy of a 2D ground state hydrogen atom is four times higher than that of a 3D ground state hydrogen atom. It is important to note that here “2D” only refers to the motion of the electron around the nucleus which is confined to a plane. The interaction potential between the two particles and its associated electromagnetic field is still 3D and therefore the increased ionization energy is the result of the vanishing kinetic energy in the direction perpendicular to the 2D plane. In theory the exciton binding energy should follow the same pattern, i.e. the 2D exciton energy levels are found by making the substitutions mentioned below Eq. (1.1) in the above expression. Indeed, experiments showed a continuous increase in exciton binding energy with decreasing quantum well width [13, 14], with reported exciton binding energies of up to 17 meV in a GaAs/AlGaAs heterostructure with a quantum well width of 5 nm [14]. Note that this value is larger than four times the exciton binding energy in 3D GaAs listed in Table 1.1, which can be attributed to three different effects [15]: the non-parabolicity of the conduction band which leads to an increasing effective mass with decreasing well width, the dielectric mismatch, i.e. the dielectric constant of the barrier material AlGaAs is smaller than that of the

well material GaAs, and the coupling of the exciton states with the filled valence band states. However, the exciton binding energy in a quantum well never reaches its theoretical maximum value for a vanishing well width because of the finite quantum well depth, e.g. 0.22 (0.16) eV for electrons (holes) in GaAs/AlGaAs. This causes the electrons and holes in GaAs to spill over into the neighboring AlGaAs and, as this effect increases with decreasing well width, the excitons tend to adopt a 3D behavior and their binding energy starts to decrease in the limit of very thin quantum wells. It was shown that, at some intermediate quantum well width, the exciton binding energy can reach almost three quarters of its theoretical maximum value [16].

There are two other factors limiting the exciton binding energy in these heterostructure quantum wells, apart from the spillover effect. The first one is that of the single-particle effective masses, which for GaAs are $0.0667m_0$ ($0.34m_0$) for electrons (holes), yielding a reduced exciton mass of $\mu = 0.0558m_0$. A smaller reduced mass leads to a larger kinetic energy which in turn leads to a smaller binding energy. The second one is that of the dielectric constants, which are given by $\varepsilon_r = 12.53$ and $\varepsilon_r = 10.06$ for GaAs and AlGaAs, respectively. These weaken the interaction potential and as such lower the binding energy. Therefore, in order to have very strong excitonic effects one would ideally need to have a perfectly 2D system for which the electron and hole effective masses are larger, preferably of the order of the free electron mass, and for which there is less dielectric screening.

1.2 Entering the flatlands

For a very long time, perfectly 2D crystals were thought to be thermally unstable. Peierls [17] and Landau [18] had shown that thermal fluctuations in 2D crystals would lead to atomic displacements of the order of the lattice constant and that therefore, due to the Lindemann criterion, the lattice would melt. Later, Mermin and Wagner [19] and Hohenberg [20] provided a more rigorous proof for this theory by showing that a spontaneous breaking of a continuous symmetry is not possible in 2D (or lower dimensions) at non-zero temperature. This general theorem, which precludes the existence of long-range order in 2D systems, also applies to crystals [21]. It was indeed confirmed experimentally that the melting temperature of thin films strongly decreases with decreasing number of layers and that these films become unstable when they are about 12 layers thick [22].

In 2004, however, Geim and his co-workers took the condensed matter world by surprise by reporting the experimental realization and characterization of atom-

ically thin films, i.e. films of single-layer thickness, of carbon atoms, also known as *graphene* [23–25]. To this end they used micromechanical cleavage, also known as the scotch tape method, in which layers are repeatedly peeled off graphite. This earned them the Nobel Prize in Physics in 2010. It should be noted that there were earlier experimental observations of graphene, however they all failed to experimentally establish its electronic properties [26]. Over the years, graphene has also been successfully synthesized using numerous other methods such as chemical cleavage, thermal decomposition of SiC, chemical vapor deposition, molecular beam epitaxy, cutting open carbon nanotubes, . . . The stability of a graphene sheet, which seems to violate the Mermin-Wagner theorem, is attributed to the fact that it is actually not a perfect 2D crystal because it forms a rippled structure. This increases the elastic energy but on the other hand reduces thermal fluctuations and as such reduces the total free energy [27]. These ripples were indeed detected and their height h was shown to scale with the width L of the graphene flake as $h \propto L^{0.6}$ [28].

In the years following its discovery, both theoretical and experimental research on graphene-related topics has exploded. This is mostly due to the extraordinary properties which this new material was soon found to exhibit, making it a very interesting material both from a theoretical as well as an application point of view. These properties include: an exceptionally high electron mobility [29], a very large thermal conductivity [30, 31], the ability to sustain extremely high electric current densities [32], and a very large intrinsic strength [33].

One of the most remarkable properties of graphene is its conical energy dispersion relation, which provides an experimentally accessible platform for studying quantum electrodynamics and gives rise to novel condensed matter physics. However, the lack of a band gap means that at any non-zero temperature, even when there is no external charge carrier doping, there will always be a minimal conductivity due to spontaneous electron-hole fluctuations. This effect is referred to as the formation of electron-hole puddles [25] and it is a big disadvantage with respect to potential applications in logical devices such as transistors, which require the device to be efficiently turned on and off. This inspired the quest for other 2D materials which have similar properties as graphene but which have a significant band gap in their energy spectrum. Using some of the synthesis methods listed above, this led to the discovery of numerous 2D materials such as single layers (monolayers) of transition metal dichalcogenides (TMDs, the most famous example being MoS₂ [34]), hexagonal boron nitride (hBN) [35], silicene (which has, as opposed to the other materials listed here, a small band gap of only a few meV) [36], black phosphorus (also known as phosphorene) [37, 38], . . . All these materials exhibit

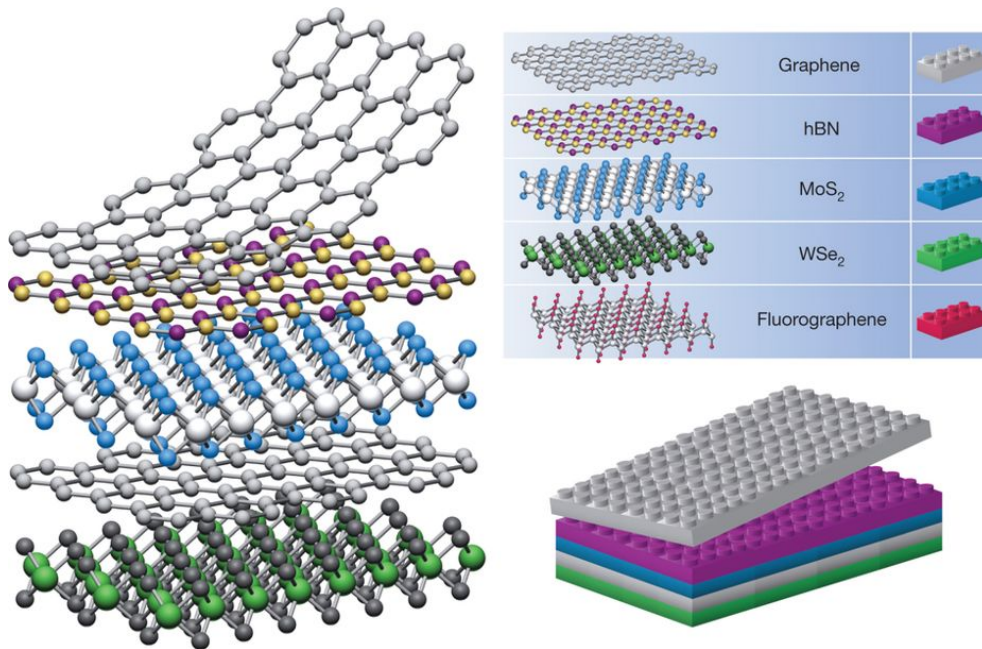


Figure 1.3: Constructing van der Waals heterostructures by using different 2D materials as building (Lego) blocks. Figure taken from Ref. [39].

interesting properties and show great potential for use in applications, however in this thesis the main focus will lie on monolayer TMDs. Furthermore, it is also possible to stack multiple layers of these different materials on top of each other in order to create so-called *van der Waals heterostructures* [39], as shown in Fig. 1.3.

1.3 Potential applications of monolayer TMDs

Monolayer TMDs share some of the remarkable properties of graphene. For example, monolayer MoS₂ was shown to be 30 times as strong as steel and to allow deformation up to 11% before breaking [40] (which compares to 20% for graphene). Similar mechanical properties were predicted for other monolayer TMDs [41], making them some of the strongest semiconducting materials and promising for applications in flexible electronics used in for example displays and wearable electronics. These examples also require conducting and insulating components, for which graphene and hBN can be used, respectively, and integrated with monolayer TMDs to form hybrid 2D electronics.

Carrier mobilities in monolayer TMDs are much lower than in graphene. At first sight this would make them less interesting as candidate materials for use in transistors, for which 2D materials in general are desirable because of the reduced power dissipation. However, the large band gap of monolayer TMDs results in high on/off current ratios, which allows for effective switching, largely because of the very low off-state conductance which leads to a very low power consumption during operation. In 2011 the first implementation of a transistor based on monolayer MoS₂ was reported which showed a room temperature mobility similar to that of graphene nanoribbons and thin silicon films and an on/off current ratio of 10⁸ with ultralow standby power dissipation [42]. This led to increased interest in monolayer TMD-based transistors as alternatives for low power applications [43].

The relatively high mobility of charge carriers in monolayer TMDs combined with the fact that the band gap is direct means that they are promising for use in photodetectors. The first monolayer MoS₂ photodetector showed a photoresponsivity comparable to that of graphene-based devices and lower than that of silicon-based devices [44]. However, two years later a monolayer MoS₂-based photodetector exhibiting a 10⁵-fold higher photoresponsivity than that of the first MoS₂ photodetector was fabricated [45]. This drastic improvement was explained to be the consequence of higher mobility, better contact quality, and a better positioning technique. These monolayer MoS₂ photodetectors operate in the visible light spectrum but are most effective for detecting green and yellow light. However, as will be seen in the next chapter, TMDs also exhibit an indirect band gap which decreases with increasing number of layers and thus allows the operating range of the photodetector to be tuned through the layer number. As such, a trilayer MoS₂ device has been shown to be ideal for detecting red light [46], which corresponds to a phonon-assisted transition across the indirect band gap. Therefore, a wide spectrum of light can be efficiently detected by combining photodetectors based on different TMDs and with different number of layers.

1.3.1 Exciton-based applications

There are also a number of potential applications of monolayer TMDs in which excitons play a crucial role. The first example is the use of monolayer TMDs in light-emitting diodes (LEDs), which would allow flexible, ultra-thin LEDs which are more energy-efficient and more easily tunable than LEDs based on 3D semiconductors to be made. Electrons and holes are injected in different parts of the monolayer TMD by means of back gates to form an in-plane *p-n* junction and are driven towards each other under the influence of a source-drain voltage, as is

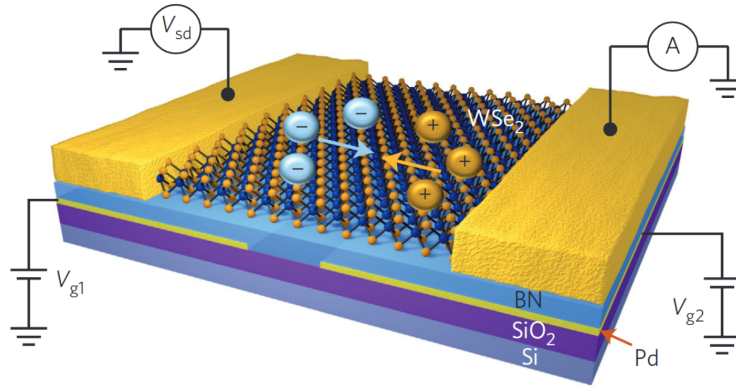


Figure 1.4: Schematic illustration of a monolayer WSe_2 p - n junction device with palladium (Pd) back gates (V_{g1} and V_{g2}) and a source-drain voltage (V_{sd}) applied to the source contact leading to a current (I) which is read out at the drain contact. The back gates are separated from the WSe_2 by hBN and the entire device sits on a layer of SiO_2 on a Si substrate. Figure taken from Ref. [47].

shown in Fig. 1.4. They then form excitons and subsequently recombine radiatively and as such generate light with a narrow spectrum. The frequency of the light is determined by the energy difference between the exciton energy and the electron-hole vacuum and therefore knowledge of exciton formation in monolayer TMDs and how to tune the exciton (binding) energy is crucial in order to fabricate optimal LEDs. These kind of devices were first realized in 2014 using monolayer WSe_2 [47–49].

Monolayer TMDs exhibit saturable absorption, i.e. the effect in which the light absorption of a material decreases with increasing light intensity above a certain saturation intensity. This effect occurs because the low-energy part of the valence band becomes depleted before the excited electrons can decay back to the valence band. Therefore, a crucial element determining the saturable absorption properties of a material is the rate at which electrons and holes recombine. In monolayer TMDs this rate is determined by the exciton lifetime, meaning that knowledge of exciton dynamics is vital for ideal use of monolayer TMDs in ultra-fast photonics. It was shown that the saturable absorption response of MoS_2 is faster than that of graphene [50]. Placing a material which exhibits saturable absorption in a laser cavity will cause it to repeatedly filter out low-intensity light and as such a pulsed laser beam can be created. Indeed it was shown that with the use of MoS_2 laser pulses in the near-infrared with pulse durations of 800 ps can be generated [51].

It is also possible to use monolayer TMDs as the gain medium in lasers. This is

mostly motivated by the fact that the excitons in these materials allow for a long-lived population inversion which is required to achieve stimulated emission and as such generate the laser gain. Furthermore, monolayer TMDs have a relatively large refractive index (6-7 in the visible wavelength range [52]) which leads to an increased optical confinement in the laser gain medium. Monolayer TMD-based lasers were first reported in 2015 using WSe₂ [53] and WS₂ [54].

1.4 Goal and organization of the thesis

The goal of this thesis is to study the properties of excitonic complexes, i.e. excitons and higher order complexes, in monolayer TMDs and in related materials such as monolayer black phosphorus and TMD heterostructures. The influence of a magnetic field on these excitonic complexes is investigated and the possibility of excitonic superfluidity in TMD heterostructures is examined.

The thesis is organized as follows.

In chapter 2 the physics of electrons and holes in monolayer TMDs is reviewed. An effective Hamiltonian is constructed which describes the low-energy electronic band structure of monolayer TMDs and it is shown how this Hamiltonian naturally gives rise to some of the interesting properties of these materials, such as circular dichroism, non-zero Berry curvature, and peculiar magnetic field effects. The interaction potential between charge carriers is derived and used to study different many-body phases in monolayer TMDs.

In chapter 3 excitons in monolayer TMDs are investigated. The two-body Dirac framework, which will be used throughout the thesis, is introduced and used to calculate several fundamental properties of different types of excitons. The chapter ends with a short discussion of the possible experimental verification of some of these properties.

In chapter 4 higher order excitonic complexes, i.e. consisting of 3 (*trions*) or 4 (*biexcitons*) particles, are studied. The stochastic variational method is introduced which allows to obtain accurate solutions for these mathematically complex systems. The possible experimental detection of these excitonic complexes is briefly explained at the end of the chapter.

In chapter 5 the presence of a uniform magnetic field is considered. The effect of a perpendicular magnetic field on the exciton energy levels is calculated and it is shown how a tilted magnetic field leads to an unusually strong *valley Zeeman effect* of so-called *dark excitons*. The influence of a perpendicular magnetic field on trions and biexcitons is also investigated.

In chapter 6 the focus is shifted to other 2D materials, i.e. monolayer black phosphorus and monolayer TiS_3 . These materials exhibit anisotropic electronic band structures and the effect of this anisotropy on the fundamental properties of excitons, trions, and biexcitons is studied.

In chapter 7 the attention is turned towards TMD van der Waals heterostructures in which one TMD is doped with electrons and the other with holes. This kind of system naturally gives rise to the formation of *interlayer excitons*. An appropriate interaction potential is derived and the effect of the dielectric environment above, below, and in between the two TMDs on the interlayer excitons is investigated.

In chapter 8 starts with a short history of (excitonic) superfluidity and a discussion of the fundamental difficulty with superfluidity in 2D. Next, the possibility of the formation of a high-temperature interlayer exciton condensate, i.e. the appearance of high-temperature excitonic superfluidity, in a superlattice of TMD van der Waals heterostructures is examined.

CHAPTER 2

Electrons and holes in monolayer TMDs

In this chapter the single-particle properties of electrons and holes in monolayer TMDs are first reviewed. An effective 2D Dirac Hamiltonian is constructed which describes the low-energy electronic band structure. The eigenstates are calculated and used to demonstrate a few specific properties of monolayer TMDs, i.e. circular dichroism and non-zero Berry curvature. Next, the presence of a uniform perpendicular magnetic field is considered and it is shown how this affects the energy spectrum and the eigenstates of the system. Finally, the interaction potential between charge carriers is derived and used to study different many-body phases in the absence and presence of a perpendicular magnetic field.

2.1 From bulk to monolayer

2.1.1 Crystal structure and symmetry

Transition metal dichalcogenides are semiconductors of the type MX_2 with M a transition metal atom (Mo, W, ...) and X a chalcogen atom (S, Se, ...). In this thesis four different monolayer TMDs will be studied: MoS_2 , MoSe_2 , WS_2 , and WSe_2 . These materials are, out of all the members of the TMD family, by far the most commonly found in the literature. It should be noted that, even though sometimes results will be shown for a specific material, the properties of these four TMDs are generally very similar and therefore the same qualitative results could be

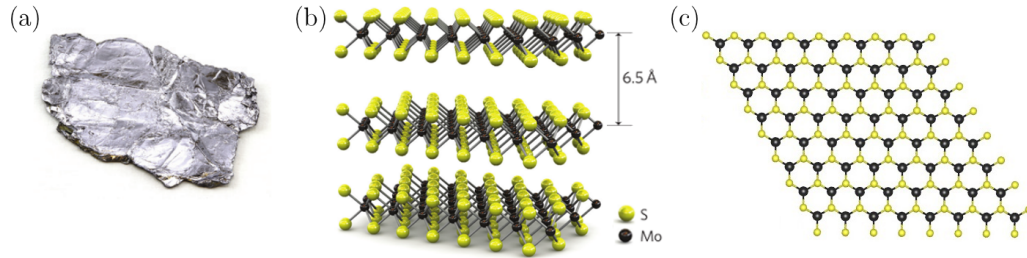


Figure 2.1: (a) Photograph of a bulk MoS₂ crystal which is approximately 1 cm wide. Figure taken from Ref. [57]. (b) Lattice structure of bulk MoS₂. Figure taken from Ref. [42]. (c) Top view of the lattice structure of monolayer MoS₂. The color of the atoms corresponds to the colors in (b).

obtained for a different choice of material. On the few occasions where there is an important difference between the TMDs an extensive discussion will be presented.

A photograph of a MoS₂ crystal is shown in Fig. 2.1(a). The lattice consists of a stack of elementary layers which are bound by weak van der Waals forces, as is shown in Fig. 2.1(b). Each layer is actually composed of three atomic sublayers, i.e. a sublayer of transition metal atoms in between two sublayers of chalcogen atoms. Both the interlayer distance, defined as the distance between the transition metal atom sublayers of adjacent layers, and the thickness of a layer, defined as the distance between the chalcogen sublayers of the same layer, are approximately 6.5 Å [55]. In their bulk form TMDs show so-called AB stacking, with the transition metal atoms of the odd layers and the chalcogen atoms of the even layers (and vice versa) sharing the same in-plane coordinates, and their symmetry space group is D_{6h}^4 , i.e. they show hexagonal symmetry and are inversion symmetric [56]. The monolayer TMD lattice is hexagonal in which the transition metal and chalcogen atoms each form a trigonal sublattice, as is shown in Fig. 2.1(c). As a result, the symmetry space group of monolayer TMDs is D_{3h}^1 , i.e. they show trigonal symmetry and are not inversion symmetric. They do, however, show reflection symmetry with respect to the x - y mirror plane, i.e. the plane in which the transition metal atoms are located. The unit cell contains one transition metal atom and two chalcogen atoms (one in each sublayer).

2.1.2 Electronic structure

The electronic band structure of bulk MoS₂, as calculated from density functional theory, is shown in the left panel of Fig. 2.2(a) and exhibits an indirect band gap

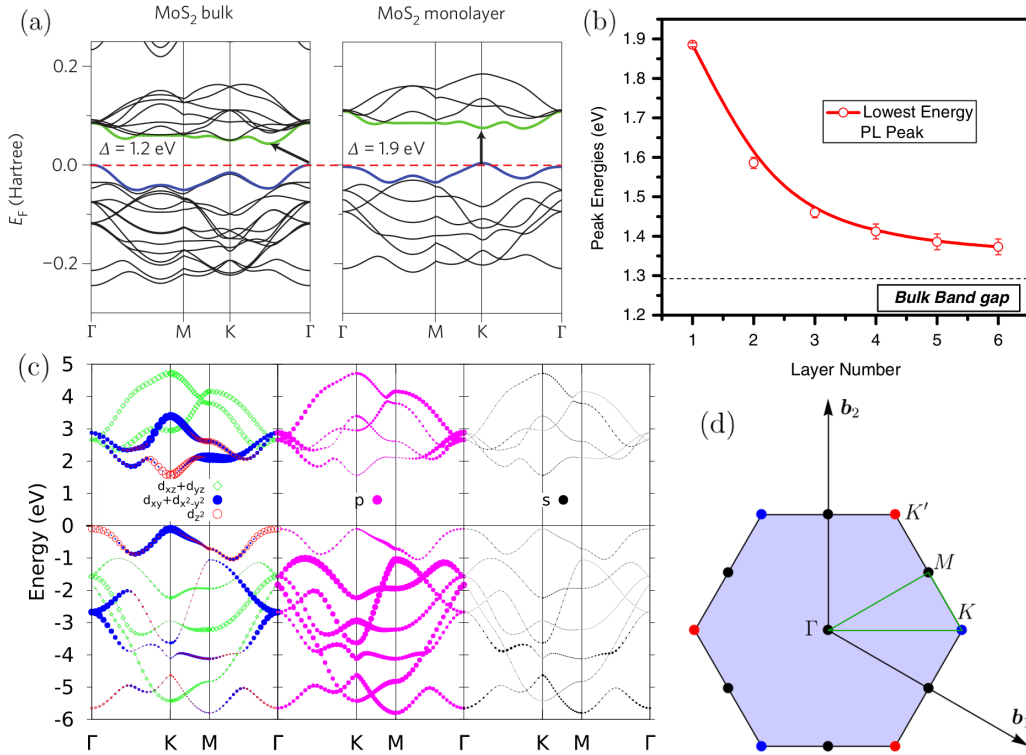


Figure 2.2: (a) Band structure calculated from density functional theory for bulk and monolayer MoS₂. The dashed line indicates the Fermi level and the arrows indicate the smallest band gap. The highest valence band (lowest conduction band) is shown in blue (green). Figure taken from Ref. [57]. (b) Experimentally determined band gap of few-layer MoS₂ as a function of the number of layers. The symbol for monolayer MoS₂ indicates a direct gap, the symbol for the other layer numbers indicates an indirect gap. The dashed line represents the (indirect) band gap of bulk MoS₂. Figure taken from Ref. [34]. (c) Orbital projected band structures for monolayer MoS₂ calculated from density functional theory. The size of the symbols is proportional to the contribution from the corresponding orbital. Figure taken from Ref. [60]. (d) First Brillouin zone of monolayer TMDs. The reciprocal lattice vectors b_1 and b_2 and the high symmetry points are indicated on the figure. The K (K') points are indicated in blue (red) and the path along which the band structures in (a) and (c) are calculated is shown in green.

around the Γ point. There is also a direct gap in the energy spectrum at the K point but it is considerably larger than the indirect one. It is also relevant to look at the orbital composition of the different states in the energy spectrum. The electron configuration of molybdenum is given by $[\text{Kr}]4d^55s^1$ and that of sulfur is given by $[\text{Ne}]3s^23p^4$. As a result, the relevant electronic states will be composed of the five molybdenum d orbitals ($\{d_{-2}, d_{-1}, d_0, d_1, d_2\}$ or equivalently the physically more relevant set of $\{d_{z^2}, d_{x^2-y^2}, d_{xy}, d_{xz}, d_{yz}\}$), the three sulfur p orbitals ($\{p_{-1}, p_0, p_1\}$ or $\{p_x, p_y, p_z\}$) as well as s orbitals stemming from both types of atoms. Density functional theory calculations show that there is an important difference between the conduction band states at the K point and those around the Γ point [58]. The former consist mostly of molybdenum d orbitals, which are located in the middle sublayer of each layer and are therefore relatively unaffected by interlayer coupling. The latter correspond to linear combinations of molybdenum d orbitals and antibonding sulfur p_z orbitals. As a result these states show a strong dependence on the interlayer coupling. When the number of layers in the system is reduced the direct band gap at the K point is almost unchanged while the indirect band gap around the Γ point is significantly increased. This was also confirmed experimentally as is shown in Fig. 2.2(b). In the monolayer limit the indirect band gap is larger than the direct gap and this transition occurs in all major TMDs (the electron configuration of tungsten (selenium) is $[\text{Xe}]4f^{14}5d^46s^2$ ($[\text{Ar}]3d^{10}4s^24p^4$) and therefore the above discussion holds for all four combinations of transition metal atoms and chalcogen atoms). The electronic band structure of monolayer MoS_2 is shown in the right panel of Fig. 2.2(a).

A useful first step towards an analytical model is the construction of a tight-binding model. Due to the periodicity of the lattice, the electron wave function needs to satisfy Bloch's theorem

$$T_{\mathbf{a}_i} \Psi = e^{i\mathbf{k} \cdot \mathbf{a}_i} \Psi, \quad (i = 1, 2), \quad (2.1)$$

with $T_{\mathbf{a}_i}$ the translation operator along the lattice vector \mathbf{a}_i and with \mathbf{k} the wave vector. As a consequence, the electron wave function can be written as a Bloch function $\Psi(\mathbf{r}) = e^{i\mathbf{k} \cdot \mathbf{r}} u(\mathbf{r})$ with $u(\mathbf{r})$ a function which has the periodicity of the lattice. Therefore, in the tight-binding model the basis functions are based on atomic orbital functions and are written as

$$\Phi_j(\mathbf{k}, \mathbf{r}) = \frac{1}{\sqrt{N}} \sum_{u=1}^N e^{i\mathbf{k} \cdot \mathbf{R}_j^u} \phi_j(\mathbf{r} - \mathbf{R}_j^u), \quad (j = 1, \dots, n), \quad (2.2)$$

with \mathbf{R}_j^u the position vector of the atomic orbital ϕ_j in unit cell u , with N the

number of unit cells in the lattice, and with n the number of atomic orbitals (and therefore the number of Bloch basis functions) which are taken into account.

In principle a total number of 14 atomic orbitals should be taken into account for monolayer TMDs: 5 transition metal d orbitals, 6 chalcogen p orbitals (3 for each chalcogen atom in the unit cell), 1 transition metal s orbital, and 2 chalcogen s orbitals. This would lead to a 14×14 Hamiltonian. However, the s orbitals account for less than 7% of the total orbital weight of the relevant energy bands [59], which can also be seen in the right panel of Fig. 2.2(c), and are therefore often left out of the model. Furthermore, when taking symmetric and antisymmetric combinations of the p orbitals of the two chalcogen atoms, the 11 remaining orbitals can be divided into two separate groups based on their (anti)symmetry with respect to the x - y mirror plane discussed in the previous subsection: the even group $\{d_{z^2}, d_{x^2-y^2}, d_{xy}, p_{x,s}, p_{y,s}, p_{z,a}\}$ and the odd group $\{d_{xz}, d_{yz}, p_{x,a}, p_{y,a}, p_{z,s}\}$, where the subscript s (a) for the p orbitals indicates the symmetric (antisymmetric) combinations. The Hamiltonian thus consists of a 6×6 block and a 5×5 block which are completely decoupled [59]. Note that a perpendicular electric field would break the mirror symmetry of the system and as such lead to a coupling between these two blocks in the Hamiltonian. Density functional theory calculations, such as those shown in the left panel of Fig. 2.2(c), indicate that the lowest conduction band and highest valence band correspond to the even group of orbitals, meaning that these bands can be described using a 6×6 Hamiltonian in which the tight-binding hopping parameters are fitted to the energy bands calculated from density functional theory. Furthermore, in Ref. [60] it was shown that when including up to third-nearest-neighbor hoppings the three p orbitals in the even group, whose contribution to the lowest conduction band and highest valence band is small as can be seen from the middle panel of Fig. 2.2(c), can be discarded and that therefore these two bands can be well described throughout the entire Brillouin zone (shown in Fig. 2.2(d)) using a 3×3 Hamiltonian. The details of this Hamiltonian are given in appendix A.

2.1.3 Spin-orbit coupling

Another step which needs to be taken en route towards an effective analytical model is the inclusion of spin-orbit coupling. The dominant intra-atomic contribution to these interactions is given by

$$\begin{aligned} H_{so} &= \frac{e}{2m_0^2c^2} \frac{1}{r} \frac{dV(r)}{dr} \mathbf{L} \cdot \mathbf{S} \\ &= \xi(r) (L_z S_z + L_+ S_- + L_- S_+), \end{aligned} \quad (2.3)$$

with $V(r)$ the atomic potential felt by the electron, $L_{\pm} = L_x \pm iL_y$ and $S_{\pm} = (S_x \pm iS_y)/2$ with L_j (S_j) ($j = x, y, z$) the different components of the orbital (spin) angular momentum, and where the scalar prefactor is written as $\xi(r)$. The above expression can be derived from relativistic quantum mechanics. A surprisingly similar result can be found classically by considering the motion of the magnetic moment associated with the electron spin in the potential generated by the nucleus. The classical result differs by a factor 2 from the quantum result, although this can be corrected for. Both approaches are detailed in appendix B. In the basis $\{|d_{z^2}, \uparrow\rangle, |d_{x^2-y^2}, \uparrow\rangle, |d_{xy}, \uparrow\rangle, |d_{z^2}, \downarrow\rangle, |d_{x^2-y^2}, \downarrow\rangle, |d_{xy}, \downarrow\rangle\}$ the above Hamiltonian is block diagonal, i.e. diagonal in spin space, and these blocks are given by

$$H_{so} = \lambda s \begin{pmatrix} 0 & 0 & 0 \\ 0 & 0 & -i \\ 0 & i & 0 \end{pmatrix}, \quad (2.4)$$

with $s = \pm 1$ the spin index, where the relations $|d_{z^2}\rangle = |d_0\rangle$, $|d_{x^2-y^2}\rangle = (|d_2\rangle + |d_{-2}\rangle)/\sqrt{2}$, and $|d_{xy}\rangle = (|d_2\rangle - |d_{-2}\rangle)/(\sqrt{2}i)$ were used, and with

$$\lambda = \hbar^2 \int d\mathbf{r} \xi(r) |d_2(\mathbf{r})|^2, \quad (2.5)$$

with $d_2(\mathbf{r}) = \langle \mathbf{r} | d_2 \rangle$. Note that $d_2(\mathbf{r}) = (d_{-2}(\mathbf{r}))^*$ and that $\xi(r)\mathbb{1}$, with $\mathbb{1}$ the identity operator, preserves the orthogonality between atomic orbital states with the same n and l quantum number but different m quantum number because of its radial symmetry. Equation (2.4) implies that there is spin splitting in the valence band but not in the conduction band. However, taking into account the small contribution from p states leads to a small conduction band spin splitting as well through the second and third term of Eq. (2.3). These terms only couple states whose m quantum numbers differ by ± 1 and therefore give no contribution to Eq. (2.4) but will couple some of the d states with some of the p states. These additional coupling terms are non-diagonal in spin space but, as they are very small due to the small contribution from the p states and the spatial separation between the p and d states, they can be treated in perturbation theory. In general, it can be concluded that spin-orbit coupling is strong in the valence bands of monolayer TMDs because the corresponding Bloch states consist of atomic orbital states with non-zero angular momentum, i.e. $d_{\pm 2}$ states, located on the same atomic sites.

2.2 Life in the valleys

2.2.1 Effective Hamiltonian

In this thesis only low-energy phenomena are of interest and therefore it is useful to construct an effective analytical model to describe the states close to the K and K' points at the corners of the hexagonal first Brillouin zone, which are therefore said to be located in the so-called low-energy *valleys*. There are only two inequivalent low-energy valleys since each of them can be connected to two other valleys in the first Brillouin zone by means of reciprocal lattice vectors, as can be seen in Fig. 2.2(d). As shown in appendix A, a three-band tight-binding model involving only nearest neighbor d - d hoppings in the basis of Bloch functions based on the atomic orbital states $\{|d_{z^2}\rangle, |d_{x^2-y^2}\rangle, |d_{xy}\rangle\}$ leads to a band structure which is in very good agreement with density functional theory calculations for the highest valence band, lowest conduction band, and a higher conduction band around the K and K' point but diverges from the density functional theory calculations when moving away from these points. This higher conduction band can be decoupled from the other two bands by means of the Löwdin partitioning method [61, 62]. Expanding this Hamiltonian around the K and K' point up to second order in the wave vector then leads to an effective Hamiltonian for the highest valence and lowest conduction band in the basis of Bloch functions based on the orbitals $\{|\phi_c\rangle = |d_{z^2}\rangle, |\phi_v\rangle = (|d_{x^2-y^2}\rangle + i\tau |d_{xy}\rangle)/\sqrt{2}\}$ [60, 61]:

$$H_\tau(\mathbf{k}) = \frac{\Delta}{2}\sigma_z + at\mathbf{k}\cdot\boldsymbol{\sigma}_\tau + a^2k^2(\gamma_1 I_2 + \gamma_2\sigma_z) + a^2\gamma_3(\mathbf{k}\cdot\boldsymbol{\sigma}_\tau^*)\sigma_x(\mathbf{k}\cdot\boldsymbol{\sigma}_\tau^*), \quad (2.6)$$

where $\boldsymbol{\sigma}_\tau$ is the Pauli matrix vector $(\tau\sigma_x, \sigma_y)$, I_2 the 2×2 identity matrix, a the lattice constant, and where t , γ_1 , γ_2 , and γ_3 are different tight-binding parameters. The valley index $\tau = 1$ ($\tau = -1$) describes the K (K') valley and the wave vector \mathbf{k} is defined with respect to the K (K') point. The second term in the above Hamiltonian is the massless Dirac Hamiltonian which also describes the low-energy spectrum of graphene. The first term is the mass term leading to the band gap Δ . The third and fourth term lead to electron-hole asymmetry and the last term introduces the trigonal symmetry of the lattice into the low-energy spectrum, which is known as *trigonal warping*. Note that the atomic orbital states used in the Bloch basis can also be written as $|\phi_c\rangle = |d_0\rangle$ and $|\phi_v\rangle = |d_2\rangle$ ($|d_{-2}\rangle$) in the K (K') valley.

Transforming the spin-orbit Hamiltonian (2.4) to the basis of the above Hamiltonian gives

$$H_{so} = \begin{pmatrix} 0 & 0 \\ 0 & \lambda s\tau \end{pmatrix} \quad (2.7)$$

	a (nm)	t (eV)	Δ (eV)	$2\lambda_c$ (eV)	$2\lambda_v$ (eV)
MoS ₂	0.32	1.10	1.66	-0.003	0.15
MoSe ₂	0.33	0.94	1.47	-0.021	0.18
WS ₂	0.32	1.37	1.79	0.027	0.43
WSe ₂	0.33	1.19	1.60	0.038	0.46

Table 2.1: Lattice constant (a) [56], hopping parameter (t) [56], band gap (Δ) [56], and spin splitting of the conduction ($2\lambda_c$) [63] and valence ($2\lambda_v$) [64] band for different monolayer TMDs.

and needs to be added to Eq. (2.6). This leads to a splitting of 2λ between the valence bands of opposite spin. As mentioned in the previous section, the spin-orbit coupling in the conduction band is zero in this basis. However, it can simply be added ad hoc to account for the existence of this effect to give the total spin-orbit Hamiltonian

$$H_{so} = \begin{pmatrix} \lambda_c s\tau & 0 \\ 0 & \lambda_v s\tau \end{pmatrix}. \quad (2.8)$$

This leads to a splitting of $2\lambda_c$ ($2\lambda_v$) between the conduction (valence) bands of opposite spin.

The material constants for the four TMDs studied in this thesis are listed in Table 2.1. The low-energy spectrum of MoS₂ is shown in Fig. 2.3. This shows that the effect from the hopping parameters γ_1 , γ_2 , and γ_3 is small close to the band extrema, i.e. the relative difference between the energy bands obtained from the Hamiltonian (2.6) with and without these parameters does not exceed 18% for energies up to 180 meV above (below) the conduction band maximum (valence band minimum). These extra hopping parameters are not readily available in the literature for other TMDs. However, because of the very similar lattice constants and orbital compositions of the energy bands, similar values are expected for the other TMDs considered in this thesis, in analogy to the t hopping parameters listed in Table 2.1. The terms associated with these hopping parameters will therefore be neglected in the remainder of the thesis. The effective low-energy Hamiltonian is thus given by

$$H_{s,\tau}(\mathbf{k}) = \begin{pmatrix} \frac{\Delta}{2} + \lambda_c s\tau & at(\tau k_x - ik_y) \\ at(\tau k_x + ik_y) & -\frac{\Delta}{2} + \lambda_v s\tau \end{pmatrix}, \quad (2.9)$$

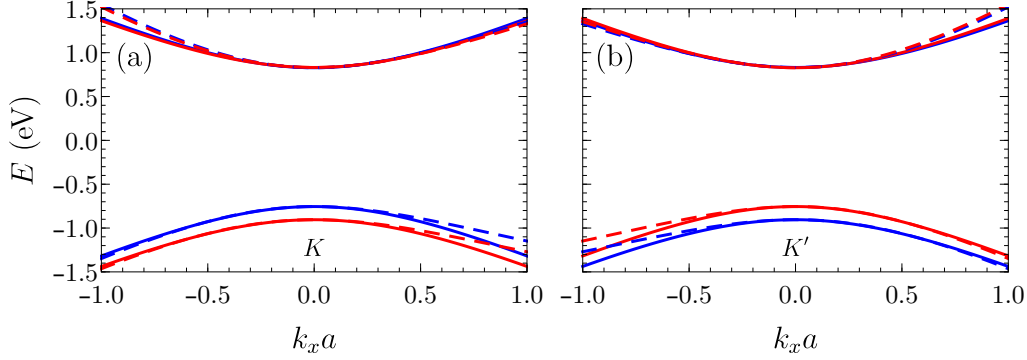


Figure 2.3: Low-energy spectrum of MoS₂ in the K (a) and K' (b) valley as obtained from the Hamiltonian (2.6) (plus the spin-orbit term) (dashed) and (2.9) (solid). Blue and red bands are spin up and spin down bands, respectively. The extra hopping parameters are taken to be $\gamma_1 = 0.066$ eV, $\gamma_2 = -0.011$ eV, and $\gamma_3 = -0.123$ eV [60].

for which the energy spectrum is isotropic and can be written as

$$E_{s,\tau,\alpha}(\mathbf{k}) = \frac{\lambda_c + \lambda_v}{2} s\tau + \alpha \sqrt{a^2 t^2 k^2 + \frac{\Delta_{s,\tau}^2}{4}}, \quad (2.10)$$

with $\Delta_{s,\tau} = \Delta + (\lambda_c - \lambda_v) s\tau$ the effective band gap and with $\alpha = 1$ (-1) describing the conduction (valence) band. The corresponding eigenstates are given by the two-component spinor

$$\begin{aligned} |\psi_{\mathbf{k},s,\tau,\alpha}\rangle &= \sqrt{\frac{(\Delta_{s,\tau} + 2\alpha\varepsilon_{\mathbf{k},s,\tau})^2}{(\Delta_{s,\tau} + 2\alpha\varepsilon_{\mathbf{k},s,\tau})^2 + 4a^2 t^2 k^2}} \begin{pmatrix} 1 \\ \frac{2atk\tau e^{i\tau\varphi_{\mathbf{k}}}}{\Delta_{s,\tau} + 2\alpha\varepsilon_{\mathbf{k},s,\tau}} \end{pmatrix} \\ &= \frac{1}{2\sqrt{\varepsilon_{\mathbf{k},s,\tau}}} \begin{pmatrix} \sqrt{2\varepsilon_{\mathbf{k},s,\tau} + \alpha\Delta_{s,\tau}} \\ \alpha\tau e^{i\tau\varphi_{\mathbf{k}}} \sqrt{2\varepsilon_{\mathbf{k},s,\tau} - \alpha\Delta_{s,\tau}} \end{pmatrix}, \end{aligned} \quad (2.11)$$

with $\varepsilon_{\mathbf{k},s,\tau} = \sqrt{\Delta_{s,\tau}^2 + 4a^2 t^2 k^2}/2$ and $\varphi_{\mathbf{k}} = \arctan(k_y/k_x)$. This can also be written as

$$|\psi_{\mathbf{k},s,\tau,1}\rangle = \begin{pmatrix} \cos\left(\frac{\theta_{\mathbf{k},s,\tau}}{2}\right) \\ \sin\left(\frac{\theta_{\mathbf{k},s,\tau}}{2}\right) \tau e^{i\tau\varphi_{\mathbf{k}}}\end{pmatrix}, \quad |\psi_{\mathbf{k},s,\tau,-1}\rangle = \begin{pmatrix} \sin\left(\frac{\theta_{\mathbf{k},s,\tau}}{2}\right) \\ -\cos\left(\frac{\theta_{\mathbf{k},s,\tau}}{2}\right) \tau e^{i\tau\varphi_{\mathbf{k}}}\end{pmatrix}, \quad (2.12)$$

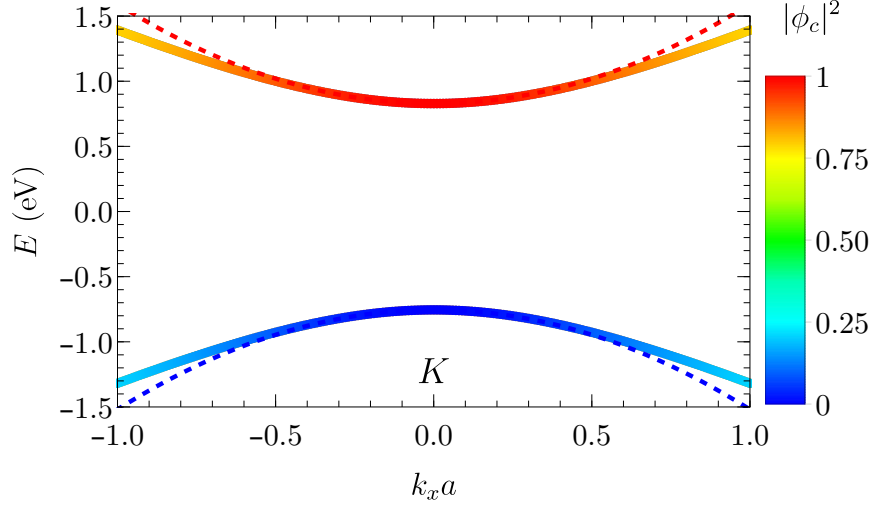


Figure 2.4: Low-energy spectrum of MoS₂ in the K valley for spin up electrons as obtained from the Hamiltonian (2.9) (solid) and (2.13) (dotted). The color indicates the contribution from the first spinor component, i.e. from the d_{z^2} Bloch function.

with $\cos \theta_{\mathbf{k},s,\tau} \equiv \Delta_{s,\tau}/(2\varepsilon_{\mathbf{k},s,\tau})$. The two components of the eigenstates are also referred to as the *pseudospin* components.

The energy spectrum (2.10) is hyperbolic and there is a gradual mixing between the two basis components when moving away from the K or K' point, as is shown in Fig. 2.4. For small k it can be approximated by

$$E_{s,\tau,\alpha}(\mathbf{k}) = \frac{(\lambda_c + \lambda_v)s\tau + \alpha\Delta_{s,\tau}}{2} + \alpha \frac{\hbar^2 k^2}{2m_{s,\tau}}, \quad (2.13)$$

with the effective charge carrier mass given by

$$m_{s,\tau} = \frac{\hbar^2 \Delta_{s,\tau}}{2a^2 t^2}. \quad (2.14)$$

This approximate parabolic energy spectrum is also shown in Fig. 2.4. Note that no state mixing is shown for these energy bands. This is because this approximation is often used in the so-called *single-band model* in which the conduction and valence bands are treated separately. The difference between the two-band Dirac model and the parabolic single-band model will be explained more in depth in the next chapter. Using the parameters given in Table 2.1, the effective band masses of MoS₂, MoSe₂, WS₂, and WSe₂ are given by $0.49m_0$ ($0.53m_0$), $0.54m_0$ ($0.62m_0$), $0.32m_0$ ($0.40m_0$), and $0.34m_0$ ($0.45m_0$), respectively, for $s\tau = 1$ ($s\tau = -1$).

2.2.2 Circular dichroism

The interaction of electrons in monolayer TMDs with a radiation field will now be studied. The radiation field is modeled classically, i.e. as a monochromatic electromagnetic wave with vector potential

$$\mathbf{A}(\mathbf{r}, t) = 2A_0 \mathbf{e} \cos(\mathbf{q} \cdot \mathbf{r} - \omega t), \quad (2.15)$$

with \mathbf{e} the polarization direction and \mathbf{q} the wave vector of the light. Using the Peierls substitution $\mathbf{p} \rightarrow \mathbf{p} - q\mathbf{A}$ this leads to an extra term $ate\mathbf{A}(\mathbf{r}, t) \cdot \boldsymbol{\sigma}_\tau / \hbar$ in the Hamiltonian, with e the elementary charge. This is a harmonic time-dependent perturbation for which the absorption rate $|\mathcal{P}_e(\mathbf{k})|^2$ is, according to Fermi's golden rule, proportional to $|\langle \psi_f | e^{i\mathbf{q} \cdot \mathbf{r}} \mathbf{e} \cdot \boldsymbol{\sigma}_\tau | \psi_i \rangle|^2$. As the light wavelength for transitions in the visible range is much larger than the lattice constant only direct transitions, i.e. $\mathbf{q} = \mathbf{0}$, will be considered. For light polarized in the x -direction the matrix element for an optical transition from the valence band to the conduction band is given by

$$\begin{aligned} \langle \psi_{\mathbf{k},s,\tau,1} | \tau \sigma_x | \psi_{\mathbf{k},s,\tau,-1} \rangle &= -\cos^2 \left(\frac{\theta_{\mathbf{k},s,\tau}}{2} \right) e^{i\tau\varphi_{\mathbf{k}}} + \sin^2 \left(\frac{\theta_{\mathbf{k},s,\tau}}{2} \right) e^{-i\tau\varphi_{\mathbf{k}}} \\ &= -\cos \theta_{\mathbf{k},s,\tau} \cos \varphi_{\mathbf{k}} - i \sin \varphi_{\mathbf{k}}. \end{aligned} \quad (2.16)$$

Similarly, for light polarized in the y -direction the transition matrix element is

$$\begin{aligned} \langle \psi_{\mathbf{k},s,\tau,1} | \sigma_y | \psi_{\mathbf{k},s,\tau,-1} \rangle &= i\tau \cos^2 \left(\frac{\theta_{\mathbf{k},s,\tau}}{2} \right) e^{i\tau\varphi_{\mathbf{k}}} + i\tau \sin^2 \left(\frac{\theta_{\mathbf{k},s,\tau}}{2} \right) e^{-i\tau\varphi_{\mathbf{k}}} \\ &= i\tau \cos \varphi_{\mathbf{k}} - \tau \cos \theta_{\mathbf{k},s,\tau} \sin \varphi_{\mathbf{k}}. \end{aligned} \quad (2.17)$$

As a result, the matrix element for circularly polarized light is given by

$$\langle \psi_{\mathbf{k},s,\tau,1} | \tau \sigma_x + i\gamma \sigma_y | \psi_{\mathbf{k},s,\tau,-1} \rangle = -e^{i\gamma\tau\varphi_{\mathbf{k}}} (\gamma\tau + \cos \theta_{\mathbf{k},s,\tau}), \quad (2.18)$$

where $\gamma = 1$ ($\gamma = -1$) describes left (right) circularly polarized light. The circular polarization is therefore found to be

$$\eta_{s,\tau}(\mathbf{k}) = \frac{|\mathcal{P}_{\gamma=+}^{s,\tau}(\mathbf{k})|^2 - |\mathcal{P}_{\gamma=-}^{s,\tau}(\mathbf{k})|^2}{|\mathcal{P}_{\gamma=+}^{s,\tau}(\mathbf{k})|^2 + |\mathcal{P}_{\gamma=-}^{s,\tau}(\mathbf{k})|^2} = \frac{2\tau \cos \theta_{\mathbf{k},s,\tau}}{1 + \cos^2 \theta_{\mathbf{k},s,\tau}} = \tau \frac{\Delta_{s,\tau} \sqrt{\Delta_{s,\tau}^2 + 4a^2 t^2 k^2}}{\Delta_{s,\tau}^2 + 2a^2 t^2 k^2}. \quad (2.19)$$

This result is shown in Fig. 2.5(a), illustrating that the K (K') valley is strongly dominated by left (right) circularly polarized light transitions. The polarization is

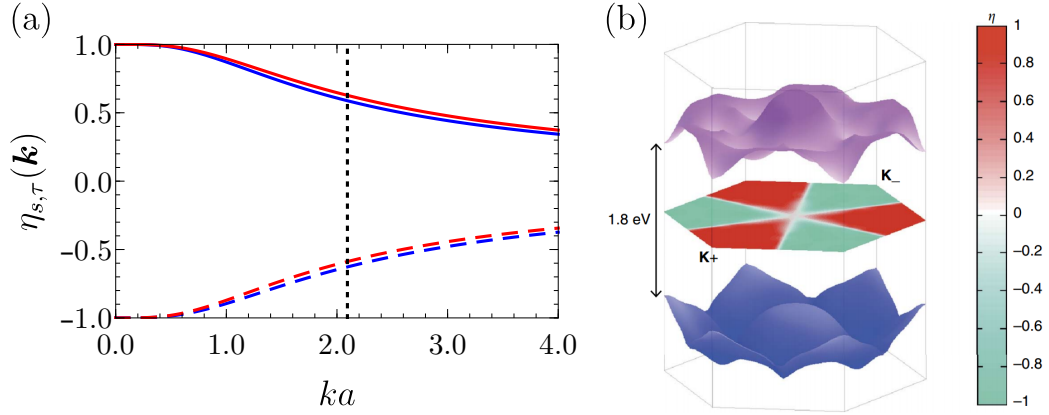


Figure 2.5: (a) Circular polarization of spin up (blue) and spin down (red) electrons in the K (solid) and K' (dashed) valley of MoS₂ as calculated from Eq. (2.19). The dotted black line indicates the halfway point between the K and K' points, i.e. the M point. (b) Circular polarization of electrons in MoS₂ calculated throughout the entire first Brillouin zone from density functional theory. Figure taken from Ref. [65].

opposite for electrons with opposite valley and spin indexes. Moving away from the band extrema the circular polarization decreases very slowly from its extremal value, i.e. to lowest non-zero order in k it is given by $\eta_{s,\tau}(\mathbf{k}) = \tau - 2\tau(ak/\Delta_{s,\tau})^4$. At the M point there is still a polarization of 59% (63%) for spin up (spin down) electrons in the K valley. However, as this point is located halfway between the K and K' point the effective Hamiltonian (2.9) is no longer valid. Density functional theory calculations show that the electrons retain their near-perfect circular polarization throughout almost the entire first Brillouin zone, except along the lines connecting the Γ point with the M points where the polarization vanishes [65]. This is shown in Fig. 2.5(b). This means that charge carriers can be excited selectively in the K (K') valley by means of a left (right) circularly polarized laser. This effect is called *circular dichroism* and was indeed confirmed experimentally [66, 67]. Note that, as the perturbation associated with the electromagnetic wave vector potential (2.15) is diagonal in spin space, optical transitions conserve the spin of the electron [68]. Furthermore, even though the angular momentum of a photon ($\pm\hbar$) is insufficient to allow for a transition between electron states with angular momentum $\pm 2\hbar$ and 0, angular momentum conservation can still be satisfied by taking into account the crystal symmetry. The trigonal symmetry leads to a Bloch phase which can absorb angular momentum in a manner similar to an Umklapp process

and as such provides the system with additional angular momentum in a modulus of $3\hbar$ [68–70]. This effect is associated with transitions between atomic orbital states of transition metal atoms in different unit cells.

2.2.3 Berry curvature

Transporting a system adiabatically along a closed circuit in parameter space causes it to pick up a global gauge-invariant, and therefore physical, phase known as the Berry phase which can be expressed as [71, 72]

$$\gamma_n = \int_S d\mathbf{S} \cdot \boldsymbol{\Omega}_n(\mathbf{R}), \quad (2.20)$$

where the integral is performed over the surface S enclosed by the closed path in the parameter space and where

$$\boldsymbol{\Omega}_n(\mathbf{R}) = \nabla_{\mathbf{R}} \times \langle n(\mathbf{R}) | i \nabla_{\mathbf{R}} | n(\mathbf{R}) \rangle \quad (2.21)$$

is a local gauge-invariant quantity known as the Berry curvature, which is a measure of the coupling of the n^{th} energy level with eigenstate $|n(\mathbf{R})\rangle$ with all the other energy levels in the system. For crystals the parameter space is the first Brillouin zone and as such the Berry curvature depends on the wave vector \mathbf{k} . It is non-zero in all crystals with broken inversion symmetry and is essential in a proper description of the dynamics of Bloch electrons, leading for example to the spin and valley Hall effect in monolayer TMDs [56]. Using the eigenstates (2.11), the Berry curvature is found to be equal to

$$\boldsymbol{\Omega}_{s,\tau,\alpha}(\mathbf{k}) = -\tau\alpha \frac{2a^2t^2\Delta_{s,\tau}}{(\Delta_{s,\tau}^2 + 4a^2t^2k^2)^{\frac{3}{2}}} \mathbf{e}_z, \quad (2.22)$$

with \mathbf{e}_z the unit vector in the z -direction. This shows that it is opposite for the conduction and valence bands and opposite for electrons with opposite spin and valley indexes. Another important physical quantity which is directly related to the Berry curvature is the intrinsic orbital magnetic moment of Bloch particles which is given by [73, 74]

$$\begin{aligned} \mathbf{m}_{s,\tau,\alpha}(\mathbf{k}) &= -i \frac{e}{2\hbar} \langle \nabla_{\mathbf{k}} \psi_{\mathbf{k},s,\tau,\alpha} | \times (H_{s,\tau}(\mathbf{k}) - E_{s,\tau,\alpha}(\mathbf{k})) | \nabla_{\mathbf{k}} \psi_{\mathbf{k},s,\tau,\alpha} \rangle \\ &= \frac{e}{2\hbar} (E_{s,\tau,\alpha}(\mathbf{k}) - E_{s,\tau,-\alpha}(\mathbf{k})) \boldsymbol{\Omega}_{s,\tau,\alpha}(\mathbf{k}). \end{aligned} \quad (2.23)$$

For monolayer TMDs this leads to

$$\mathbf{m}_{s,\tau}(\mathbf{k}) = -\tau \frac{ea^2t^2\Delta_{s,\tau}}{4\hbar a^2t^2k^2 + \hbar\Delta_{s,\tau}^2} \mathbf{e}_z, \quad (2.24)$$

which is opposite for electrons with opposite spin and valley indexes but equal for the conduction and valence bands and therefore does not influence the optical selection rules discussed in the previous subsection. At the K and K' points the above expression reduces to $\mathbf{m}_{s,\tau}(\mathbf{0}) = -\tau\mu_B^* \mathbf{e}_z$ with $\mu_B^* = e\hbar/(2m_{s,\tau})$ the effective Bohr magneton. This magnetic moment plays an important role when a perpendicular magnetic field is applied.

2.2.4 Magnetic field effects

A commonly used experimental manipulation is the application of a magnetic field. In this subsection the effects of both a perpendicular and an in-plane magnetic field will be investigated.

Perpendicular magnetic field

A possible vector potential which leads to a magnetic field oriented perpendicular to the TMD layer, i.e. $\mathbf{B} = \nabla \times \mathbf{A} = B\mathbf{e}_z$, is given by $\mathbf{A} = Bxe_y$. Including this vector potential in the Hamiltonian through the Peierls substitution leads to the breakdown of k_x as a good quantum number. However, it is possible to define an operator

$$\hat{a} = \frac{l_B}{\sqrt{2}} \left(\hat{k}_x - i \left(k_y + \frac{\hat{x}}{l_B^2} \right) \right), \quad (2.25)$$

with $l_B = \sqrt{\hbar/(eB)}$ the magnetic length, for which it is easy to show that $[\hat{a}, \hat{a}^\dagger] = \hat{1}$. The eigenvalue equation for the effective Hamiltonian then becomes

$$\begin{cases} \hat{a} |\phi_v\rangle = \frac{l_B}{\sqrt{2}at} \left(E - \frac{\lambda_c + \lambda_v}{2} s\tau - \frac{\Delta_{s,\tau}}{2} \right) |\phi_c\rangle \\ \hat{a}^\dagger |\phi_c\rangle = \frac{l_B}{\sqrt{2}at} \left(E - \frac{\lambda_c + \lambda_v}{2} s\tau + \frac{\Delta_{s,\tau}}{2} \right) |\phi_v\rangle \end{cases} \quad (2.26)$$

for $\tau = 1$. For $\tau = -1$ the operators in the left hand sides of the above equations are changed to $-\hat{a}^\dagger$ ($-\hat{a}$) for the top (bottom) equation. Substituting one equation into the other shows that both components of the spinor are eigenstates of the number

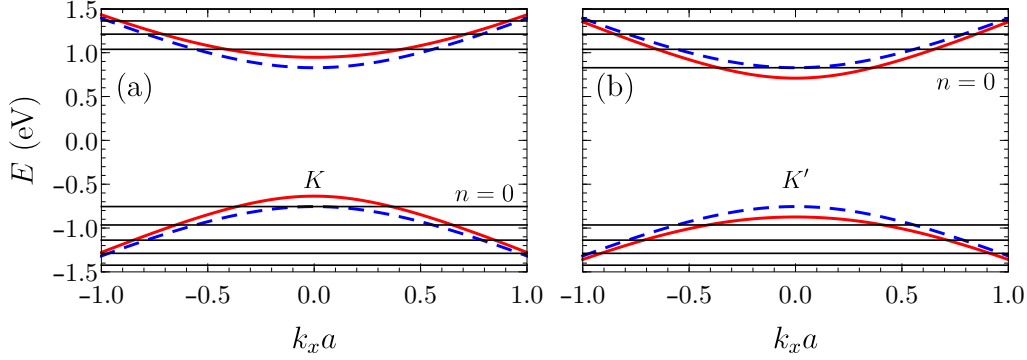


Figure 2.6: Landau level spectrum of MoS₂ in the K (spin up) (a) and K' (spin down) (b) valley. The zero-field bands are shown with (solid, red) and without (dashed, blue) the contribution from (2.24). The $n = 0$ Landau level is indicated in both valleys. A magnetic field of 1000 T is used in the calculation in order to clearly show its effect.

operator $\hat{a}^\dagger \hat{a}$. The energy spectrum is found to be given by

$$E_{n,s,\tau,\alpha} = \frac{(\lambda_c + \lambda_v)}{2} s\tau + \alpha \sqrt{\frac{\tilde{\Delta}_{s,\tau}^2}{4} + \frac{2a^2 t^2}{l_B^2} n}, \quad (2.27)$$

with n a strictly positive integer. The corresponding eigenstates in the K valley are

$$|\psi_{n,s,1,1}\rangle = \begin{pmatrix} \cos\left(\frac{\theta_{n,s,1}}{2}\right) |n-1\rangle \\ i \sin\left(\frac{\theta_{n,s,1}}{2}\right) |n\rangle \end{pmatrix}, \quad |\psi_{n,s,1,-1}\rangle = \begin{pmatrix} \sin\left(\frac{\theta_{n,s,1}}{2}\right) |n-1\rangle \\ -i \cos\left(\frac{\theta_{n,s,1}}{2}\right) |n\rangle \end{pmatrix}, \quad (2.28)$$

with $\cos \theta_{n,s,\tau} \equiv \Delta_{s,\tau} / \sqrt{\Delta_{s,\tau}^2 + 8a^2 t^2 n / l_B^2}$. In the K' valley the kets $|n-1\rangle$ and $|n\rangle$ need to be switched. Special attention needs to be paid to the case when $n = 0$, for which the energy spectrum is given by $E_{0,s,\tau} = -\tau \Delta_{s,\tau} / 2 + (\lambda_c + \lambda_v) s\tau / 2$, meaning that this state is located in the valence (conduction) band in the K (K') valley, and the corresponding eigenstates are given by $|\psi_{0,s,1}\rangle = (0, |0\rangle)^T$ and $|\psi_{0,s,-1}\rangle = (|0\rangle, 0)^T$, respectively.

The Landau level spectrum is shown in Fig. 2.6. The symmetry breaking between the energy levels in the K and K' valley is a consequence of the breaking of time-reversal symmetry in the system due to the presence of the magnetic field. In the valence (conduction) band of the K (K') valley the lowest Landau level is

located at the bottom of the zero-field bands, which would mean that there is no magnetic confinement. However, the energy spectrum can be made to look more intuitive by explicitly taking into account the effect of the intrinsic magnetic moment (2.24). This contributes a term $-\mathbf{m}_{s,\tau}(\mathbf{k}) \cdot \mathbf{B} \approx \tau \mu_B^* B$ to the energy spectrum, i.e. a type of valley Zeeman effect, which is already implicitly included in the Landau level spectrum (2.27). Shifting the zero-field bands by this amount shows that the lowest Landau level is always shifted by the same energy amount with respect to the zero-field band extrema [75].

There are two other types of Zeeman effects present in monolayer TMDs: the orbital Zeeman effect associated with the angular quantum number of the atomic orbital states which shifts the valence bands by an amount $2\tau\mu_B B$ and the spin Zeeman effect which shifts all energy bands by an amount $s\mu_B B$, with μ_B the Bohr magneton. These effects are not included in Fig. 2.6.

Furthermore, using the eigenstates (2.28) and following a procedure analogous to that discussed in subsection 2.2.2 it is possible to show that perfect circular dichroism is retained in the presence of a perpendicular magnetic field but that now only transitions between Landau levels whose indexes differ by ± 1 are allowed.

In-plane magnetic field

A possible vector potential which leads to a magnetic field oriented in the plane of the TMD layer, i.e. $\mathbf{B} = \nabla \times \mathbf{A} = B e_x$, is given by $\mathbf{A} = -B z e_y$. Since the electrons are located within a single layer it is possible to take $z = 0$ and as such the in-plane magnetic field will have no orbital effect. However, it will have an important effect through the spin Zeeman effect, i.e. the term $\mu_B \mathbf{B} \cdot \mathbf{s}$ in the Hamiltonian with \mathbf{s} the vector of Pauli matrices in spin space. When adding this term to the low-energy Hamiltonian (2.9), the in-plane components of the magnetic field prevent it from being diagonal in spin space and as such lead to a 4×4 Hamiltonian instead of a 2×2 Hamiltonian. As this effect is generally small it is possible to treat it in first order perturbation theory [76] and absorb the resulting energy shift in the spin-orbit coupling parameters: $\tilde{\lambda}_{c(v)} = \lambda_{c(v)} + \mu_B^2 B_x^2 / (2\lambda_{c(v)})$. The eigenstates are then given by

$$|\psi_{\mathbf{k},s,\tau,\alpha}\rangle = \frac{1}{\sqrt{1 + \delta_\alpha^2}} \left(|\psi_{\mathbf{k},s,\tau,\alpha}\rangle_0 + s\tau\delta_\alpha |\psi_{\mathbf{k},-s,\tau,\alpha}\rangle_0 \right), \quad (2.29)$$

with $|\psi_{\mathbf{k},s,\tau,\alpha}\rangle_0$ the unperturbed eigenstates, with $\delta_\alpha = \mu_B B_x / (2\lambda_\alpha)$, and with $\lambda_1 = \lambda_c$ and $\lambda_{-1} = \lambda_v$. This is a good approximation as long as $\mu_B B_x$ is small compared to $\lambda_{c(v)}$, which is the case for realistic magnetic field strengths for the four considered TMDs, except for MoS₂ for magnetic fields stronger than 10 T.

Using the above eigenstates, the optical transition amplitudes between valence and conduction band states are found to be

$$\mathcal{P}_\gamma^{s,\tau} = \frac{1}{\sqrt{(1 + \delta_1^2)(1 + \delta_{-1}^2)}} (\mathcal{P}_{\gamma,0}^{s,\tau} + \delta_1 \delta_{-1} \mathcal{P}_{\gamma,0}^{-s,\tau}) \quad (2.30)$$

and

$$\mathcal{P}_\gamma^{s,\tau} = \frac{s\tau}{\sqrt{(1 + \delta_1^2)(1 + \delta_{-1}^2)}} (\delta_1 \mathcal{P}_{\gamma,0}^{-s,\tau} - \delta_{-1} \mathcal{P}_{\gamma,0}^{s,\tau}) \quad (2.31)$$

for transitions between states with the same spin and opposite spin, respectively, with $\mathcal{P}_{\gamma,0}^{s,\tau}$ the optical transition amplitude between the zeroth order eigenstates and with s the spin of the conduction band. This means that the presence of an in-plane magnetic field allows for optical transitions between energy bands associated with opposite spins.

2.3 A hole in the band

The hole was already briefly discussed in section 1.1 in the context of an array of tightly bound electron states, showing that it is a quasiparticle of opposite charge. This concept can be extended to periodic condensed matter systems. In semiconductors such as monolayer TMDs the “normal” state or vacuum state is that in which the valence bands are completely filled and the conduction bands are completely empty. To this vacuum state excitations can be added, i.e. adding an electron to the conduction band or removing an electron from the valence band. Removing an electron with a certain energy, wave vector, and spin can equivalently be described as adding a quasiparticle, i.e. the hole, with opposite energy, wave vector, and spin to the system. This means that the hole quasiparticle Hamiltonian can easily be expressed in terms of the electron Hamiltonian as $H_{s,\tau}^h(\mathbf{k}) = -H_{-s,-\tau}^e(-\mathbf{k})$, or in more general mathematical terms as $H^h = -TH^eT^{-1}$ with $T = is_yK$ the time-reversal operator with s_y a Pauli matrix in spin space and K the complex conjugation [77]. Note that for TMDs, because of the hexagonal Brillouin zone (see Fig. 2.2(d)), a flip in the wave vector implies that the valley index is flipped as well.

It is worth pointing out the difference between a valence electron and a hole. A valence electron is a negatively charged *real* particle with a negative band mass due to the negative second derivative of the energy bands near the valence band maximum. As a result, valence electrons move in the direction opposite to that of an applied force and can form a bound state in the presence of a negatively charged impurity. A hole is a positively charged quasiparticle with a positive band mass

(because of the energy flip) which therefore moves in the direction of an applied force and also forms a bound state in the presence of a negatively charged impurity. This shows how valence electrons and holes can have very similar properties. On the other hand, a conduction electron and a hole (in the valence band) can form a bound state, i.e. an exciton, while a conduction electron and a valence electron can not. This shows the fundamental difference between the two.

2.4 Interparticle interaction potential

When studying few-body or many-body effects knowledge of the interparticle interaction potential is needed. In order to find an expression for this potential in a TMD monolayer Gauss's law is used as a starting point: $\nabla \cdot \mathbf{D} = n_{ext}$, with n_{ext} the charge density of an external point charge located at (\mathbf{r}', z') with charge q_1 . The charge is located in the TMD layer which is located at $z' = 0$. The displacement field \mathbf{D} is given by $\mathbf{D} = \varepsilon_0 \mathbf{E} + \mathbf{P}$, with \mathbf{E} the electric field and $\mathbf{P} = \chi \varepsilon_0 \mathbf{E}$ the polarization density, with χ the polarizability. For homogeneous 3D dielectrics this simplifies to $\mathbf{D} = \tilde{\varepsilon} \mathbf{E}$, with $\tilde{\varepsilon}$ the dielectric tensor of the material. Using $\mathbf{E} = -\nabla \phi(\mathbf{r} - \mathbf{r}', z, z')$, with $\phi(\mathbf{r} - \mathbf{r}', z, z')$ the electrostatic potential, Gauss's law becomes

$$\left(\varepsilon_r^i \left(\frac{\partial^2}{\partial x^2} + \frac{\partial^2}{\partial y^2} \right) + \frac{\partial}{\partial z} \left(\varepsilon_z^i \frac{\partial}{\partial z} \right) \right) \phi^i(\mathbf{r} - \mathbf{r}', z, 0) = -\frac{q_1}{\varepsilon_0} \delta(\mathbf{r} - \mathbf{r}') \delta(z), \quad (2.32)$$

with ε_r^i and ε_z^i the in-plane and out-of-plane relative dielectric constants of the homogeneous 3D region below ($i = b$) and above ($i = t$) the TMD. Here, only isotropic dielectrics, i.e. $\varepsilon_r^i = \varepsilon_z^i = \varepsilon_i$, will be considered. Because monolayer TMDs are 2D materials there will only be an induced charge density in the material plane, i.e. $\chi(z) = \chi_{2D} \delta(z)$ where χ_{2D} has the dimensions of length as opposed to the dimensionless 3D polarizability χ . As a consequence it is no longer possible to write $\mathbf{D} = \tilde{\varepsilon} \mathbf{E}$ and as a result there are non-local dielectric screening effects [78]. Gauss's law becomes $\varepsilon_0 \nabla \cdot \mathbf{E} = n_{ext} + n_{ind}$ with

$$\begin{aligned} n_{ind} &= -\nabla \cdot \mathbf{P} = \varepsilon_0 \chi_{2D} \nabla \cdot (\delta(z) \nabla \phi(\mathbf{r} - \mathbf{r}', z, 0)) \\ &= \varepsilon_0 \chi_{2D} \left(\delta(z) \left(\frac{\partial^2}{\partial x^2} + \frac{\partial^2}{\partial y^2} + \frac{\partial^2}{\partial z^2} \right) + \left(\frac{\partial}{\partial z} \delta(z) \right) \frac{\partial}{\partial z} \right) \phi(\mathbf{r} - \mathbf{r}', z, 0) \end{aligned} \quad (2.33)$$

the induced charge density in the TMD layer. Adding the above induced charge density to Eq. (2.32) and performing an in-plane 2D Fourier transform over $\mathbf{r} - \mathbf{r}'$

gives the equation

$$\begin{aligned} \frac{\partial}{\partial z} \left(\varepsilon_i \frac{\partial}{\partial z} \phi_{\mathbf{q}}^i(z, 0) \right) - \varepsilon_i q^2 \phi_{\mathbf{q}}^i(z, 0) &= -\frac{q_1}{A\varepsilon_0} \delta(z) \\ + \chi_{2D} \left(q^2 \delta(z) - \delta(z) \frac{\partial^2}{\partial z^2} - \left(\frac{\partial}{\partial z} \delta(z) \right) \frac{\partial}{\partial z} \right) \phi_{\mathbf{q}}^i(z, 0), \end{aligned} \quad (2.34)$$

with A the area of the system. This equation has to be solved in both the region below and above the TMD. In these regions the right hand side of the above equation vanishes and the solutions are given by

$$\phi_{\mathbf{q}}^i(z, 0) = A_i e^{qz} + B_i e^{-qz}, \quad (2.35)$$

with A_i and B_i integration constants. Since the external and induced charge densities are located in the TMD layer, i.e. between the two homogeneous 3D regions, they will only enter in the boundary conditions relating the two piecewise solutions $\phi_{\mathbf{q}}^i(z, 0)$ at the interface at $z = 0$. The boundary conditions are given by

$$\begin{aligned} \phi_{\mathbf{q}}^t(0, 0) &= \phi_{\mathbf{q}}^b(0, 0), \\ \varepsilon_t \frac{\partial}{\partial z} \phi_{\mathbf{q}}^t(0, 0) &= \varepsilon_b \frac{\partial}{\partial z} \phi_{\mathbf{q}}^b(0, 0) + q^2 \chi_{2D} \phi_{\mathbf{q}}^b(0, 0) - \frac{q_1}{A\varepsilon_0}. \end{aligned} \quad (2.36)$$

Notice that the last two terms on the right hand side of Eq. (2.34) cancel each other. Furthermore, $B_b = A_t = 0$ needs to be imposed in order to avoid divergences. The first boundary condition then yields $A_b = B_t$ and from the second boundary condition it follows that the interaction potential between the external charge q_1 and a charge q_2 can in general be written as

$$V(q, z, 0) = q_2 \phi_{\mathbf{q}}(z, 0) = \frac{q_1 q_2}{2Aq\varepsilon_0 \varepsilon(q, z)}, \quad (2.37)$$

with $\varepsilon(q, z)$ a relative dielectric function given by

$$\varepsilon(q, z) = \left(\frac{\varepsilon_b + \varepsilon_t}{2} + \frac{\chi_{2D}}{2} q \right) e^{q|z|}. \quad (2.38)$$

Defining the average dielectric constant of the environment $\kappa = (\varepsilon_b + \varepsilon_t)/2$ and the screening length $r_0 = \chi_{2D}/(2\kappa)$, the real space interaction potential in the TMD layer can be found by performing the inverse 2D Fourier transform, which gives

$$\begin{aligned} V(r) &= \frac{A}{(2\pi)^2} \int d^2 q V(q, 0, 0) e^{i\mathbf{q} \cdot (\mathbf{r} - \mathbf{r}')} \\ &= \frac{q_1 q_2}{4\pi \kappa \varepsilon_0} \int_0^\infty dq \frac{J_0(qr)}{1 + r_0 q}, \end{aligned} \quad (2.39)$$

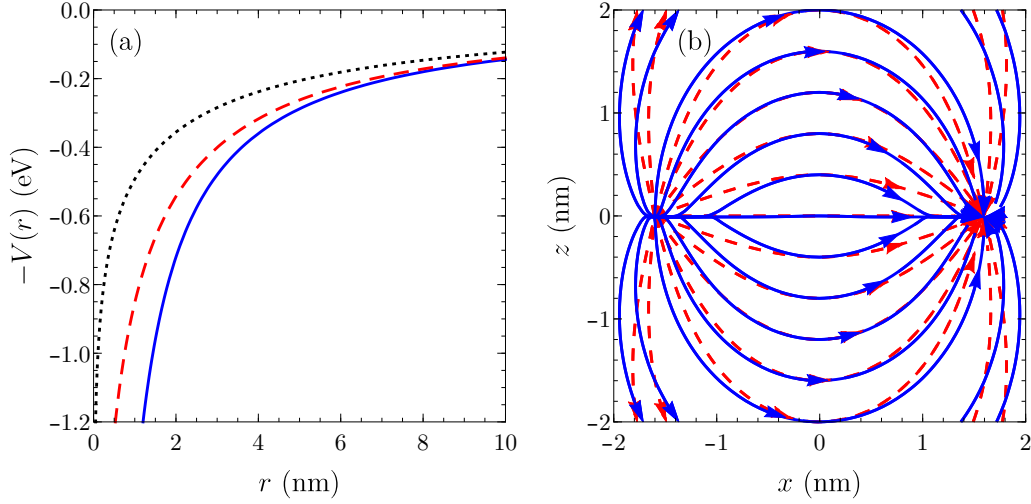


Figure 2.7: (a) Interaction potential between an electron and a hole in monolayer TMDs for $\kappa = 1$ and with screening length $r_0 = 0$ nm (solid, blue), $r_0 = 2$ nm (dashed, red), and $r_0 = 6$ nm (dotted, black). (b) Electric field lines created by a positive and a negative charge separated by a distance of 3.2 nm in a monolayer TMD at $z = 0$ with screening length $r_0 = 10$ nm (solid, blue) and $r_0 = 0$ nm, i.e. a bare Coulomb potential (dashed, red).

with J_0 the zeroth order Bessel function of the first kind and $r = |\mathbf{r} - \mathbf{r}'|$ the distance between the two charges. Performing the integral leads to

$$V(r) = \frac{e^2}{4\pi\kappa\epsilon_0} \frac{\pi}{2r_0} \left(H_0 \left(\frac{r}{r_0} \right) - Y_0 \left(\frac{r}{r_0} \right) \right), \quad (2.40)$$

where Y_0 and H_0 are the Bessel function of the second kind and the Struve function, respectively, and where $q_1 = q_2 = \pm e$ was chosen. This potential is known as the Keldysh potential [79, 80] and is shown in Fig. 2.7(a). For $r_0 = 0$ this potential reduces to the bare Coulomb potential $V(r) = e^2/(4\pi\kappa\epsilon_0 r)$. Increasing the screening length leads to a decrease in the short-range interaction strength while the long-range interaction strength is unaffected. For very large screening lengths $r_0 \rightarrow \infty$ the interaction potential becomes logarithmic, i.e. $V(r) = e^2/(4\pi\kappa\epsilon_0 r_0) \ln(r_0/r)$. Density functional theory calculations show that the 2D polarizability is equal to 8.29 nm, 10.34 nm, 7.58 nm, and 9.02 nm in MoS₂, MoSe₂, WS₂, and WSe₂, respectively [81].

The corresponding electric field lines of this interaction between two

oppositely charged particles are shown in Fig. 2.7(b) and are compared with the electric field lines associated with the bare Coulomb potential. This shows that in the vicinity of the charge carriers the electric field lines associated with the Keldysh potential are located within the TMD layer, i.e. as if the electromagnetic field is confined to the 2D plane as well, whereas when moving further away from the charge carriers they break out of the layer to recover the 3D behavior of the bare Coulomb potential.

The peculiar interaction potential (2.40) leads to series of exciton energy levels in monolayer TMDs which are more shallow, have less degeneracies, and follow a different functional form as compared to the 2D hydrogenic Rydberg series (1.2). These exciton levels will be discussed in more detail in the next chapter.

2.5 Many-body phases in monolayer TMDs

In the following chapters few-body and many-body effects of particles of opposite charge are studied. In this section, many-body effects of same-charge particles are investigated, e.g. the possibility of ferromagnetism. It is known that long-range exchange interactions cause the 3D electron gas to become ferromagnetic at low densities [82–84]. This was later confirmed by Monte Carlo simulations [85, 86], which predicted the same effect in the 2D electron gas [85, 87]. The 2D electron gas has been investigated in detail in semiconductor heterostructures and electrons above liquid helium [88–91], however the discovery of graphene and other related 2D materials such as those discussed in section 1.2 provided new systems with different dispersion relations and topologies for studying the 2D electron gas [92]. The pronounced effect of the dispersion relation on the many-body state of the electron gas was shown by using a variational wave function technique, which found that monolayer graphene does not exhibit a ferromagnetic phase [93] while bilayer graphene does [94].

Monolayer TMDs provide an interesting platform for studying these many-body effects, as it can be expected that the valley-contrasting spin splitting will result in a rich many-body phase diagram with many more possible phases than those predicted for monolayer and bilayer graphene. Recently, ferromagnetic behavior was predicted in numerous different TMD-based systems such as exfoliated TMDs with defects [95], transition metal-doped TMDs [96], intercalated TMDs [97], TMD-based heterostructures [98, 99], and TMDs in which one of the chalcogen layers is either removed [100] or different from the other chalcogen layer [101]. However, in all of these systems the ferromagnetic phase is not driven by many-

body exchange interactions but rather is a single-particle effect in which one of the spin states is energetically preferred over the other, and which is not present in clean monolayer TMDs.

In this section a variational technique, similar to that used in Refs. [93, 94], is used to study the exchange interaction-driven many-body phases of different monolayer TMDs and their dependence on the dielectric constant of the substrate and on a perpendicular magnetic field. This study was published in Physical Review B [102]. After the publication of this work other theoretical studies appeared predicting interaction-driven valley and spin polarized phases in monolayer TMDs [103–105], as briefly discussed at the end of this section.

2.5.1 Many-body Hamiltonian

Due to the large band gap either only conduction band states (n -doped TMDs) or only valence band states (p -doped TMDs) need to be taken into account because interband electron-hole fluctuations are suppressed. The kinetic energy contribution to the many-body Hamiltonian can then be written as

$$\hat{H}_0^\alpha = \alpha \sum_{\mathbf{k}, s, \tau} E_{s, \tau, \alpha}(\mathbf{k}) \hat{a}_{\mathbf{k}, s, \tau}^\dagger \hat{a}_{\mathbf{k}, s, \tau}, \quad (2.41)$$

with $E_{s, \tau, \alpha}(\mathbf{k})$ the single-particle energy spectrum (2.10), with $\alpha = 1$ ($\alpha = -1$) describing electrons (holes), and with $\hat{a}_{\mathbf{k}, s, \tau}^\dagger$ ($\hat{a}_{\mathbf{k}, s, \tau}$) the creation (annihilation) operator of either an electron in the conduction band (n -doped TMDs) or a vacancy in the valence band (p -doped TMDs) with wave vector \mathbf{k} , spin index s , and valley index τ . Recall from section 2.3 that the hole quasiparticle has opposite energy, wave vector, spin index, and valley index as compared to that of the vacant valence band state.

The many-body interaction Hamiltonian is in general given by

$$\hat{V}^\alpha = \frac{1}{2} \sum_{\mathbf{q}, w, \rho} \sum_{\mathbf{k}, s, \tau} \sum_{\mathbf{q}', w', \rho'} \sum_{\mathbf{k}', s', \tau'} \langle \psi_{\mathbf{q}, w, \rho, \alpha} \psi_{\mathbf{k}, s, \tau, \alpha} | V(|\mathbf{r} - \mathbf{r}'|) | \psi_{\mathbf{q}', w', \rho', \alpha} \psi_{\mathbf{k}', s', \tau', \alpha} \rangle \hat{a}_{\mathbf{q}, w, \rho}^\dagger \hat{a}_{\mathbf{k}, s, \tau}^\dagger \hat{a}_{\mathbf{k}', s', \tau'} \hat{a}_{\mathbf{q}', w', \rho'}, \quad (2.42)$$

with $V(r)$ given by (2.40) and with the position representation of the eigenstates $|\psi_{\mathbf{k}, s, \tau, \alpha}\rangle$ given by (2.11) multiplied with $e^{i\mathbf{k}\cdot\mathbf{r}} \eta_s / \sqrt{A}$ with A the surface area and

η_s the orthonormal spin states. Performing the integrals over \mathbf{r} and \mathbf{r}' leads to

$$\langle \psi_{\mathbf{q},w,\rho} \psi_{\mathbf{k},s,\tau} | V(|\mathbf{r} - \mathbf{r}'|) | \psi_{\mathbf{q}',w',\rho'} \psi_{\mathbf{k}',s',\tau'} \rangle = \frac{e^2}{2\varepsilon_0 \kappa A} \delta_{w,w'} \delta_{s,s'} \delta_{\rho,\rho'} \delta_{\tau,\tau'} \delta_{\mathbf{k}'+\mathbf{q}',\mathbf{k}+\mathbf{q}} \frac{\langle \psi_{\mathbf{q},w,\rho,\alpha} | \psi_{\mathbf{q}',w',\rho',\alpha} \rangle_p \langle \psi_{\mathbf{k},s,\tau,\alpha} | \psi_{\mathbf{k}',s',\tau',\alpha} \rangle_p}{|\mathbf{k} - \mathbf{k}'| + r_0 |\mathbf{k} - \mathbf{k}'|^2}, \quad (2.43)$$

where $\langle \rangle_p$ denotes the overlap element of the pseudospin part of the eigenstates (2.11) and where intervalley scattering was neglected due to the large corresponding momentum exchange. When only considering the exchange interactions (the direct interactions are canceled by the interactions with the positive lattice background), this reduces to

$$\hat{V}^\alpha = -\frac{e^2}{4\varepsilon_0 \kappa A} \sum_{s,\tau} \sum_{\mathbf{k},\mathbf{q}} \frac{|\langle \psi_{\mathbf{q},s,\tau,\alpha} | \psi_{\mathbf{k},s,\tau,\alpha} \rangle_p|^2}{|\mathbf{k} - \mathbf{q}| + r_0 |\mathbf{k} - \mathbf{q}|^2} \hat{a}_{\mathbf{q},s,\tau}^\dagger \hat{a}_{\mathbf{q},s,\tau} \hat{a}_{\mathbf{k},s,\tau}^\dagger \hat{a}_{\mathbf{k},s,\tau}, \quad (2.44)$$

i.e. an attractive interaction between particles with the same spin and valley indexes.

The magnetic part of the many-body Hamiltonian can be obtained by summing over the Zeeman effect contributions of all the single-particle states and is therefore given by

$$\hat{H}_B^\alpha = \alpha B \sum_{\mathbf{k},s,\tau} (s\mu_B - \mathbf{e}_z \cdot \mathbf{m}_{s,\tau}(\mathbf{k})) \hat{a}_{\mathbf{k},s,\tau}^\dagger \hat{a}_{\mathbf{k},s,\tau} - 2B \sum_{\mathbf{k},s,\tau} \tau \mu_B \hat{a}_{\mathbf{k},s,\tau}^\dagger \hat{a}_{\mathbf{k},s,\tau}, \quad (2.45)$$

where the three terms describe the spin, valley, and orbital Zeeman effect, respectively, and where the last term thus should only be included for holes. Apart from the different Zeeman effects, a perpendicular magnetic field also leads to confinement of the charge carriers, resulting in discrete Landau levels in the energy spectrum as discussed in subsection 2.2.4. This will have a significant effect on the many-body phase when the confinement region is smaller than the average interparticle distance. The latter can be estimated by $\langle r \rangle = 1/\sqrt{\pi n}$ with n the charge carrier density, while the former is given by the magnetic length $l_B = \sqrt{\hbar/(eB)}$. For $B = 50$ T this gives $l_B = 3.63$ nm, which is less than the average interparticle distance for densities smaller than $n = 0.3 \times 10^{13} \text{ cm}^{-2}$. This means that only at high magnetic field strengths and low densities would the Landau levels significantly affect the many-body phase. Therefore, this effect is not taken into account here.

2.5.2 Variational solution

A variational state is considered in which the four energy bands can be filled independently from each other up to a certain number of particles $N_{s,\tau}$, i.e. the state

$$|\Psi_0\rangle = \left(\prod_{s,\tau} \prod_{k \leq k_F^{s,\tau}} \hat{a}_{\mathbf{k},s,\tau}^\dagger \right) |\emptyset\rangle, \quad (2.46)$$

with $k_F^{s,\tau}$ the band dependent Fermi wave vector and with $|\emptyset\rangle$ the vacuum state, i.e. completely filled valence bands and completely empty conduction bands. This is a Hartree-Fock method in which Fermi correlation is taken into account (through the anticommutation relations of the creation and annihilation operators) but Coulomb correlation is not. The occupation number of a given single-particle state is therefore given by

$$N_{\mathbf{k},s,\tau} = \langle \Psi_0 | \hat{a}_{\mathbf{k},s,\tau}^\dagger \hat{a}_{\mathbf{k},s,\tau} | \Psi_0 \rangle = \begin{cases} 1 & \text{for } k \leq k_F^{s,\tau} \\ 0 & \text{for } k > k_F^{s,\tau} \end{cases}. \quad (2.47)$$

The total number of particles in a given energy band is given by $N_{s,\tau} = \sum_{\mathbf{k}} N_{\mathbf{k},s,\tau}$ and together they form the set of variational parameters. In order to gain more direct physical insight from the variational parameters they are transformed to

$$N = \sum_{s,\tau} N_{s,\tau}, \quad \zeta_s = \frac{\sum_{s,\tau} s N_{s,\tau}}{\sum_{s,\tau} N_{s,\tau}}, \quad \zeta_\tau = \frac{\sum_{s,\tau} \tau N_{s,\tau}}{\sum_{s,\tau} N_{s,\tau}}, \quad \zeta_\beta = \frac{\sum_{s,\tau} s\tau N_{s,\tau}}{\sum_{s,\tau} N_{s,\tau}}. \quad (2.48)$$

The total number of particles in the system N is fixed, meaning that there are three variational parameters: ζ_s , ζ_τ , and ζ_β . These are the spin, valley, and spin-valley polarization, respectively, and can range from -1 to 1 . For example, a state characterized by $(\zeta_s, \zeta_\tau, \zeta_\beta) = (0, 0, 1)$ has an equal number of spin up and spin down particles, has an equal number of particles in both valleys, but all spin up (spin down) particles reside in the K (K') valley. Starting from $N_{s,\tau} = \sum_{\mathbf{k}} N_{\mathbf{k},s,\tau}$, converting the summation over \mathbf{k} to an integral, and using Eq. (2.47) an expression relating $N_{s,\tau}$ and $k_F^{s,\tau}$ is obtained. The set of equations in Eq. (2.48) is then inverted to get

$$k_F^{s,\tau} = \sqrt{4\pi \frac{N_{s,\tau}}{A}} = \sqrt{\pi n (1 + s\zeta_s + \tau\zeta_\tau + s\tau\zeta_\beta)}, \quad (2.49)$$

with $n = N/A$ the total particle density. The expectation value of the kinetic energy (2.41) with respect to the variational state is given by

$$\begin{aligned} \langle \Psi_0 | \hat{H}_0^\alpha | \Psi_0 \rangle &= \alpha \frac{A}{2\pi} \sum_{s,\tau} \int_0^{k_F^{s,\tau}} dk k E_{s,\tau,\alpha}(\mathbf{k}) \\ &= \frac{N}{2\pi n} \sum_{s,\tau} \left(\alpha \frac{\lambda_c + \lambda_v}{2} s\tau (k_F^{s,\tau})^2 + \frac{1}{24a^2 t^2} \left(\left(4a^2 t^2 (k_F^{s,\tau})^2 + \Delta_{s,\tau}^2 \right)^{\frac{3}{2}} - \Delta_{s,\tau}^3 \right) \right). \end{aligned} \quad (2.50)$$

The expectation value of the interparticle interactions (2.44) with respect to the variational state is given by

$$\langle \Psi_0 | \hat{V}^\alpha | \Psi_0 \rangle = -\frac{Ne^2}{4\varepsilon_0 \kappa (2\pi)^3 n} \sum_{s,\tau} I_{s,\tau} (k_F^{s,\tau})^3, \quad (2.51)$$

where the integral

$$\begin{aligned} I_{s,\tau} &= \int_0^1 du u \int_0^1 dv v \int_0^{2\pi} d\theta \left[\left(\frac{1}{2} + \frac{\tilde{\Delta}_{s,\tau}^2}{2f_{s,\tau}(u)f_{s,\tau}(v)} + \frac{uv \cos \theta}{2f_{s,\tau}(u)f_{s,\tau}(v)} \right) / \right. \\ &\quad \left. \left(\sqrt{u^2 + v^2 - 2uv \cos \theta} + c_{s,\tau} (u^2 + v^2 - 2uv \cos \theta) \right) \right], \end{aligned} \quad (2.52)$$

with

$$f_{s,\tau}(x) = \sqrt{\tilde{\Delta}_{s,\tau}^2 + x^2}, \quad \tilde{\Delta}_{s,\tau} = \frac{\Delta_{s,\tau}}{2atk_F^{s,\tau}}, \quad c_{s,\tau} = r_0 k_F^{s,\tau}, \quad (2.53)$$

is evaluated numerically.

The expectation value of the magnetic part of the Hamiltonian (2.45) with respect to the variational state is given by

$$\langle \Psi_0 | \hat{H}_B^\alpha | \Psi_0 \rangle = \alpha N \zeta_s \mu_B B + \alpha \frac{NeB}{16\pi \hbar n} \sum_{s,\tau} \tau \Delta_{s,\tau} \ln \left(1 + \frac{1}{\tilde{\Delta}_{s,\tau}^2} \right) - 2N \zeta_\tau \mu_B B, \quad (2.54)$$

where the last term should only be included for holes.

The sum of the three terms (2.50), (2.51), and (2.54) gives the total variational energy which depends on the three variational parameters and which is minimized brute force to find the variational parameters which define the lowest energy many-body state.

2.5.3 Numerical results

The main results and discussions presented here are for n -doped TMDs. A short discussion of p -doped TMDs follows at the end of this subsection.

n -doped TMDs

In the absence of interactions the many-body state can simply be found by filling up the lowest energy single-particle states. In the absence of a magnetic field this means that both valleys are populated equally and, as a consequence, that both spin states are also populated equally. The many-body state is therefore characterized by $(\zeta_s, \zeta_\tau, \zeta_\beta) = (0, 0, 1)$ at low densities, i.e. there is no global spin and no valley polarization but there is spin polarization in each valley separately (so-called *spin-valley locking*). For densities above some critical value, the electrons will also populate the higher conduction band in both valleys and as such the spin-valley locking will be gradually lost, i.e. there is a second order phase transition. The many-body state is then given by $(\zeta_s, \zeta_\tau, \zeta_\beta) = (0, 0, \beta(n))$ for molybdenum-based TMDs and by $(\zeta_s, \zeta_\tau, \zeta_\beta) = (0, 0, -\beta(n))$ for tungsten-based TMDs with

$$\beta(n) = \frac{\Delta(\lambda_v - \lambda_c) - (\lambda_v + \lambda_c)\sqrt{4a^2t^2\pi n + \Delta^2 - 4\lambda_c\lambda_v}}{2a^2t^2\pi n} \quad (2.55)$$

a function which decreases continuously with increasing density from 1 to 0. The sign difference between molybdenum- and tungsten-based TMDs is the direct consequence of the difference in sign of the conduction band spin-orbit coupling parameter λ_c (see Table 2.1).

When including electron-electron interactions, four different many-body phases are found. These are shown in Fig. 2.8 for WSe₂ but are found in all four of the TMDs considered in this thesis. Phase I is characterized by $(\zeta_s, \zeta_\tau, \zeta_\beta) = (1, 1, 1)$ or $(\zeta_s, \zeta_\tau, \zeta_\beta) = (-1, -1, 1)$ for molybdenum-based TMDs and by $(\zeta_s, \zeta_\tau, \zeta_\beta) = (1, -1, -1)$ or $(\zeta_s, \zeta_\tau, \zeta_\beta) = (-1, 1, -1)$ for tungsten-based TMDs. The system is completely spin polarized and valley polarized, i.e. the many-body state is a truly ferromagnetic state. In the specific case of MoS₂ an additional ferromagnetic phase, phase I', is found characterized by $(\zeta_s, \zeta_\tau, \zeta_\beta) = (-1, 1, -1)$ or $(\zeta_s, \zeta_\tau, \zeta_\beta) = (1, -1, -1)$. The difference with phase I is that the electrons now all occupy one of the upper conduction bands as opposed to one of the lower conduction bands. This is possible because of the very small spin-orbit coupling in the conduction band and because the upper conduction bands have a slightly larger effective mass (2.14) reducing their kinetic energy contribution. Phase II is characterized by $(\zeta_s, \zeta_\tau, \zeta_\beta) = (0, 0, 1)$ for molybdenum-based TMDs and by

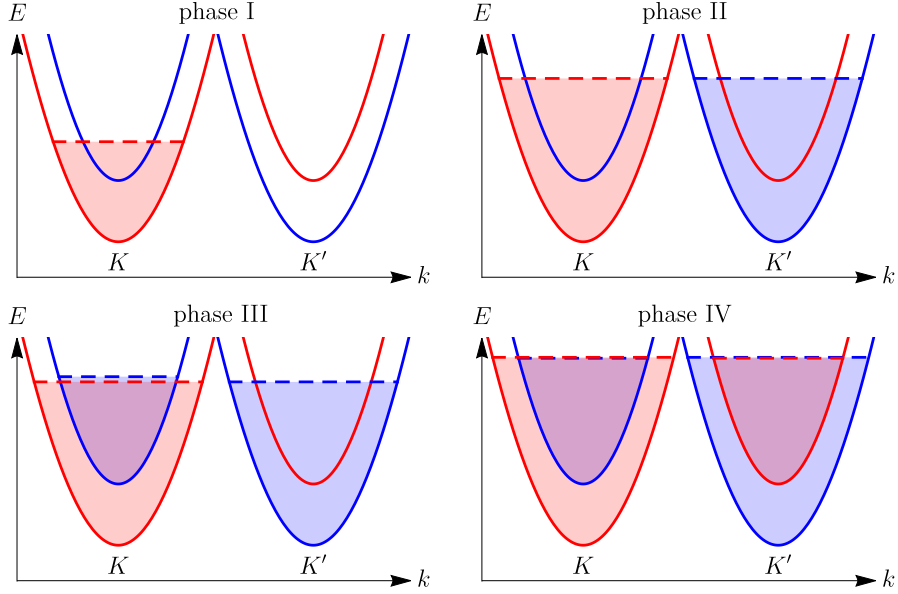


Figure 2.8: The four different obtained phases of monolayer TMDs (shown here for WSe_2) in zero magnetic field. Blue and red bands are spin up and spin down bands, respectively.

$(\zeta_s, \zeta_\tau, \zeta_\beta) = (0, 0, -1)$ for tungsten-based TMDs, i.e. the low-density phase of the non-interacting case discussed above. There is no global spin and valley polarization but there is spin-valley locking. Phase III is characterized by non-zero values between -1 and 1 for all three variational parameters, which vary as a function of the electron density, such that one of the valleys is completely spin polarized whereas the other valley shows little to no spin polarization. Finally, phase IV is characterized by $(\zeta_s, \zeta_\tau, \zeta_\beta) = (0, 0, \beta(n))$ for molybdenum-based TMDs and by $(\zeta_s, \zeta_\tau, \zeta_\beta) = (0, 0, -\beta(n))$ for tungsten-based TMDs. This is the completely unpolarized phase which was also found in the high density limit without interactions.

The energies of these four phases are shown in Fig. 2.9 in an experimentally accessible electron density range [106]. This shows that a step by step decrease in the spin/valley order of the many-body state is found when increasing the density. In the limit of zero density the energy of all these phases converges to $\Delta/2 - \lambda_c$, i.e. the lowest single-particle energy. However, at very low densities the system should transit to a Wigner crystal, which is predicted to occur at densities of the order of $1 \times 10^{11} \text{ cm}^{-2}$ [107], although for such low densities the effects of defects also become increasingly important. Furthermore, the first derivative of the ground

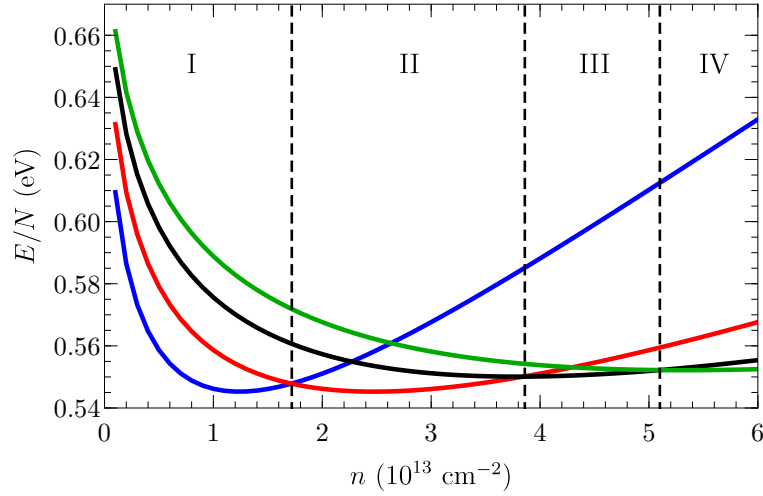


Figure 2.9: Energy per particle for MoSe₂ calculated for zero magnetic field and $\varepsilon_b = \varepsilon_t = 1$ as a function of the total electron density for phase I (blue), phase II (red), phase III (black), and phase IV (green). The phase transitions are indicated by the dashed black vertical lines.

state energy shows discontinuities when transiting between phases, meaning that the transitions between these phases are all first order. In summary, in the non-interacting case there are only two phases (phase II and phase IV) with a second order transition between them, but when interactions are included additional phases are found between them (phase III) and at low densities (phase I) with first order transitions between all phases.

The phase diagram as a function of the electron density and the substrate dielectric constant is shown in Figs. 2.10(a)-(b). All the phase transitions occur at lower densities for larger substrate dielectric constants, meaning that the substrate also leads to a reduction in spin/valley order. This is because the substrate weakens the electron-electron interactions. The phase transition between phase I and II is less dependent on the substrate dielectric constant than those between phase II and III and between phase III and IV. The order in which the four different TMDs change phases is different for the phase transition between phase I and II as compared to those between phase II and III and between phase III and IV.

When a perpendicular magnetic field is added to the system, the phase diagram shown in Fig. 2.11(a) is found. The four phases which are present at zero magnetic field persist for non-zero magnetic field. The magnetic field breaks the valley degeneracy and as a result phase I is now only characterized by $(\zeta_s, \zeta_\tau, \zeta_\beta) =$

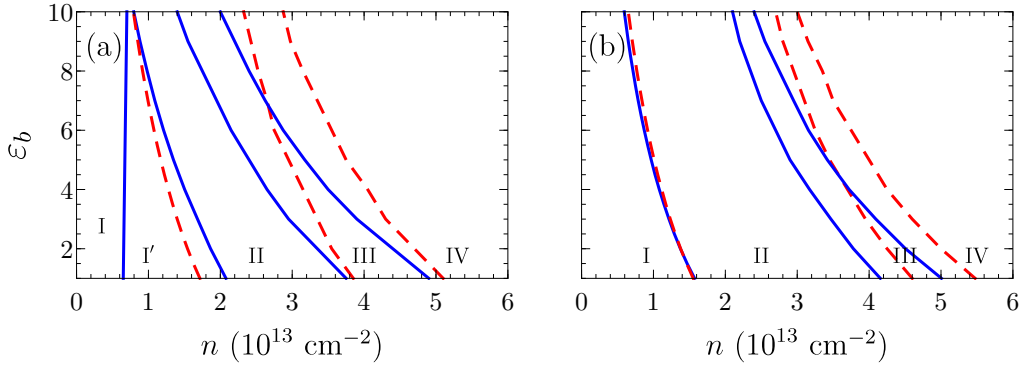


Figure 2.10: (a) Phase diagram calculated for zero magnetic field as a function of the total electron density and the dielectric constant of the substrate below the material ε_b ($\varepsilon_t = 1$) for MoS₂ (solid, blue) and MoSe₂ (dashed, red). (b) The same as (a) but now for WS₂ (solid, blue) and WSe₂ (dashed, red).

$(-1, -1, 1)$ for molybdenum-based TMDs and by $(\zeta_s, \zeta_\tau, \zeta_\beta) = (1, -1, -1)$ for tungsten-based TMDs. For MoS₂ phase I' persists up to magnetic field strengths of 40 T and is characterized by $(\zeta_s, \zeta_\tau, \zeta_\beta) = (1, -1, -1)$. This means that a complete flip in spin polarization, from $\zeta_s = -1$ to $\zeta_s = 1$, occurs when tuning the system from phase I to phase I'. The transition to phase I' occurs at larger densities with increasing magnetic field because the energy difference between the two conduction bands in the lowest energy valley increases with magnetic field. Phase II is now characterized by $(\zeta_s, \zeta_\tau, \zeta_\beta) = (-\delta(n), -\delta(n), 1)$ for molybdenum-based TMDs and by $(\zeta_s, \zeta_\tau, \zeta_\beta) = (\delta(n), -\delta(n), -1)$ for tungsten-based TMDs with $\delta(n)$ a function similar to $\beta(n)$. The exact numerical values of the variational parameters which define phase III and phase IV also change slightly due to the magnetic field but they still represent the same type of phases as those shown in Fig. 2.8. The phase transitions between phase I and phase II and between phase III and phase IV shift to higher densities as the magnetic field increases. The phase transition between phase II and phase III, however, shifts to lower densities as the magnetic field increases.

In Fig. 2.11(b) the spin polarization as a function of the electron density is shown. This clearly shows the transition from phase I with complete spin polarization to phase II with partial spin polarization. In the absence of a magnetic field the spin polarization in phase II is 0, but this value increases with the magnetic field strength. This also shows that the transition occurs at higher densities for stronger magnetic fields.

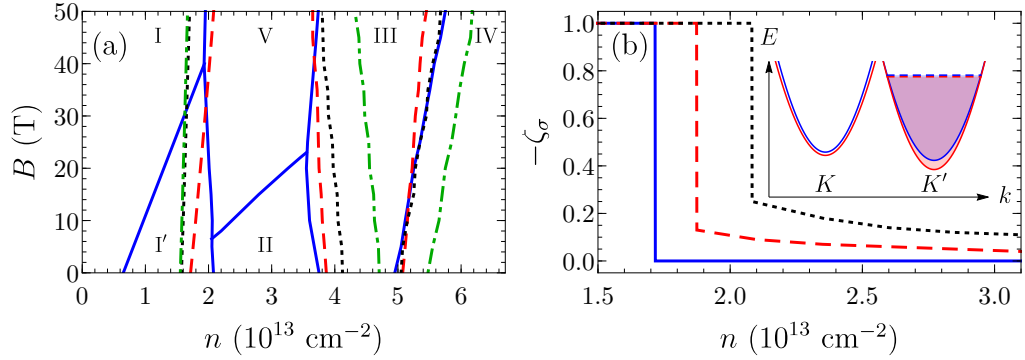


Figure 2.11: (a) Phase diagram calculated for $\varepsilon_b = \varepsilon_t = 1$ as a function of the total electron density and the perpendicular magnetic field for MoS₂ (solid, blue), MoSe₂ (dashed, red), WS₂ (dotted, black), and WSe₂ (dot-dashed, green). (b) Spin polarization calculated for $\varepsilon_b = \varepsilon_t = 1$ for MoSe₂ as a function of the total electron density for a perpendicular magnetic field of 0 T (solid, blue), 20 T (dashed, red), and 50 T (dotted, black). The inset shows phase V which occurs in the presence of strong magnetic fields.

Furthermore, for MoS₂, an additional phase (phase V) for magnetic fields larger than 7 T is found which completely replaces phase II for magnetic fields larger than 23 T. This phase is characterized by $(\zeta_s, \zeta_\tau, \zeta_\beta) = (-\delta(n), -1, \delta(n))$ and is shown in the inset of Fig. 2.11(b). There is complete valley polarization and very little spin polarization, which is a consequence of the fact that the states in the K' valley shift down in energy with respect to those in the K valley. The reason that this phase is only found for MoS₂ is because of the very small spin-orbit coupling in the conduction band. This phase will also occur for the other TMDs but at much stronger magnetic fields.

p-doped TMDs

For *p*-doped TMDs the same four phases as for *n*-doped TMDs are found. The transition between phase I and phase II as a function of the substrate dielectric constant is identical to that for *n*-doped TMDs for MoS₂ and MoSe₂. This is because in both phase I and phase II only the lowest energy bands are occupied and therefore the energy difference with the higher energy bands due to the spin splitting, which is very different for the conduction and valence bands, has no influence on this phase transition. For WS₂ and WSe₂, however, this phase transition occurs at lower densities for *p*-doped TMDs as compared to *n*-doped TMDs. The reason

is that for these materials the highest valence bands have a smaller effective mass than the lowest conduction bands, whereas for MoS₂ and MoSe₂ these bands have the same effective mass. Furthermore, phase III and phase IV occur at much higher densities, above $7 - 15 \times 10^{13} \text{ cm}^{-2}$ depending on the TMD and the substrate, as compared to *n*-doped TMDs. This is a consequence of the much stronger spin splitting in the valence bands as compared to the conduction bands. This strong spin splitting also leads to the absence of phase I' for *p*-doped MoS₂.

In the presence of a perpendicular magnetic field the transition between phase I and phase II depends more strongly on the magnetic field for *p*-doped TMDs as compared to *n*-doped TMDs. This is a consequence of the orbital Zeeman effect, which only occurs for valence band states. Furthermore, phase V only occurs for unrealistically strong magnetic fields for all TMDs, including MoS₂.

2.5.4 Conclusion

A variational technique was used to study the different many-body phases of electrons in different monolayer TMDs. It was found that there are four phases with first order phase transitions between them. When increasing the electron density a step-wise reduction in spin/valley order was found in which the system consecutively exhibits: complete spin and valley polarization, spin-valley locking, spin polarization in only one of the valleys, and no spin or valley polarization. The effect of a substrate below the TMD was studied and it was found that it leads to a reduction in spin/valley order.

Furthermore, the effect of a perpendicular magnetic field was studied and it was found that all four phases persist. For the specific case of MoS₂ an extra phase appears for magnetic fields larger than 7 T. In this phase there is complete valley polarization but little to no spin polarization. Another effect exclusive to this material is that a complete flip in spin polarization, from $\zeta_s = -1$ to $\zeta_s = 1$, occurs at low densities. Both these effects are the consequence of the very small spin-orbit coupling in the conduction band.

Finally, *p*-doped TMDs were considered and it was found that the corresponding phase diagram is less rich than that of *n*-doped TMDs. Phase I' and phase V do not occur and phase III and phase IV only occur at very large densities.

The phase diagrams obtained here could in principle be measured experimentally. Phases with a significant spin polarization, i.e. phases I and III, should be the easiest to observe experimentally by using a magnetometer, although the limited density region in which phase III occurs might hinder observations of this phase. Nevertheless, experimental evidence for a spin polarized electron gas was indeed

found very recently in monolayer MoS₂ [108].

Similar results were obtained in other theoretical works. In Ref. [103] a valley polarized phase was predicted using a variational mean field treatment based on a three-band nearest-neighbor tight-binding Hamiltonian applicable throughout the entire first Brillouin zone. A contact potential was used for the interactions and only *p*-doped TMDs were considered. In Refs. [104] and [105] a spin polarized phase was predicted by studying the time-dependent spin response function and the free energy with explicit inclusion of the intervalley interactions, respectively. The former considered *p*-doped TMDs and used a contact potential, while the latter considered *n*-doped TMDs and used a bare Coulomb potential with the inclusion of dynamical screening effects.

CHAPTER 3

Excitons in monolayer TMDs

In this chapter the properties of excitons in monolayer TMDs are studied. A four-band exciton Hamiltonian is constructed starting from the two-band electron and hole single-particle Hamiltonians derived in the previous chapter. The corresponding eigenvalue equation is solved numerically, exploiting the eigenstates of the conserved exciton angular momentum, to obtain the exciton energies and wave functions and the results are compared with those of the single-band model commonly used in the literature. The chapter ends with an explanation on how some of the exciton properties calculated in this chapter can be measured experimentally.

3.1 Exciton Hamiltonian eigenvalue equation(s)

A two-body exciton Hamiltonian can in general be written as $H^{exc} = H^e \otimes \mathbb{1} + \mathbb{1} \otimes H^h$ with H^e and H^h the single-particle electron and hole Hamiltonians. Using the two-band single-electron Hamiltonian $H_{s^e, \tau^e}^e(\mathbf{k}^e)$ (2.9) and the relation $H_{s^h, \tau^h}^h(\mathbf{k}^h) = -H_{-s^h, -\tau^h}^e(-\mathbf{k}^h)$ discussed in section 2.3 results in a four-band exciton Hamiltonian which acts on states in the product Hilbert space $\mathcal{H}^{exc} = \mathcal{H}^e \otimes \mathcal{H}^h$. A possible set of basis states which span the exciton Hilbert space is given by $\{|\Phi_c^e\rangle \otimes |\Phi_c^h\rangle, |\Phi_c^e\rangle \otimes |\Phi_v^h\rangle, |\Phi_v^e\rangle \otimes |\Phi_c^h\rangle, |\Phi_v^e\rangle \otimes |\Phi_v^h\rangle\}$ with $|\Phi_c^{e(h)}\rangle$ and $|\Phi_v^{e(h)}\rangle$ the electron (hole) Bloch state (2.2) based on the atomic orbital states d_0 and $d_{2\tau}$, respectively. Writing out the exciton Hamiltonian in this basis by explic-

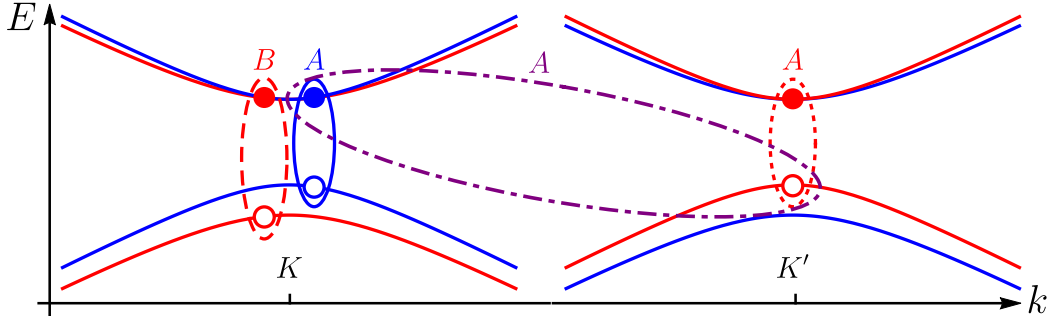


Figure 3.1: Schematic representation of the different types of excitons in monolayer TMDs. The circles and dots indicate holes and electrons, respectively. The solid blue ellipse and the dotted red ellipse indicate intravalley A excitons in the K and K' valley, respectively. The dashed red ellipse indicates an intravalley B exciton in the K valley. The large dot-dashed purple ellipse indicates an intervalley A exciton.

itly working out the tensor products in the above general expression then gives

$$H_{\sigma}^{exc}(\mathbf{k}^e, \mathbf{k}^h) = \begin{pmatrix} 0 & at(-\tau^h k_x^h - ik_y^h) & at(\tau^e k_x^e - ik_y^e) & 0 \\ at(-\tau^h k_x^h + ik_y^h) & \Delta_{s^h, \tau^h} & 0 & at(\tau^e k_x^e - ik_y^e) \\ at(\tau^e k_x^e + ik_y^e) & 0 & -\Delta_{s^e, \tau^e} & at(-\tau^h k_x^h - ik_y^h) \\ 0 & at(\tau^e k_x^e + ik_y^e) & at(-\tau^h k_x^h + ik_y^h) & \lambda(s^e \tau^e - s^h \tau^h) \end{pmatrix}. \quad (3.1)$$

Note that in this entire chapter the spin splitting in the conduction bands is neglected, i.e. $\lambda_c = 0$, since it only has a small quantitative effect on the exciton energies and wave functions, while the spin splitting in the valence bands $\lambda_v = \lambda$ is retained. As a result $\Delta_{s, \tau}$ now reduces to $\Delta - \lambda s \tau$. The subscript σ is shorthand notation for s^e, τ^e, s^h, τ^h and defines the type of exciton. Excitons consisting of a hole in the upper (lower) valence band, i.e. $s^h \tau^h = 1$ ($s^h \tau^h = -1$), are commonly known as A excitons (B excitons) [81]. Excitons with $\tau^e = -\tau^h$ ($\tau^e = \tau^h$) are referred to as *intervalley* (*intravalley*) excitons, i.e. these names refer to whether the electron is in the same or opposite valley as compared to the absence of the electron, not compared to the hole quasiparticle. Since light cannot induce a spin flip, optically excited excitons have $s^e \tau^e = s^h \tau^h$. The different types of excitons are illustrated in Fig. 3.1.

The energy spectrum of the above exciton Hamiltonian is in general given by

$E_{\sigma, \alpha^e, \alpha^h}^{exc}(\mathbf{k}^e, \mathbf{k}^h) = E_{s^e, \tau^e, \alpha^e}(\mathbf{k}^e) + E_{s^h, \tau^h, \alpha^h}(\mathbf{k}^h)$ with $E_{s, \tau, \alpha}(\mathbf{k})$ the single-particle energy spectrum (2.10). For $k^e = k^h$ the energy band with $\alpha^e = \alpha^h = 1$ is given by the single-particle conduction band multiplied with a factor 2. This band corresponds to excitons composed of an electron (hole) in the conduction (valence) band, i.e. the classical type of exciton. This band will lead to bound states when interparticle interactions are included. Similarly, the energy band with $\alpha^e = \alpha^h = -1$ is twice the single-particle valence band and corresponds to excitons composed of an electron (hole) in the valence (conduction) band. The energy bands with $\alpha^e = -\alpha^h = \pm 1$ are located in between the other two bands and are completely flat in the case of optically excited excitons. These bands correspond to excitons composed of an electron and hole in the same band (conduction or valence).

The interaction potential between the electron and hole can be added to the exciton Hamiltonian through the term $V(|\mathbf{r}_e - \mathbf{r}_h|)I_4$ with $V(r)$ given by Eq. (2.40) and I_4 the 4×4 identity matrix. As a result, the Hamiltonian does not commute with the single-particle momentum operators. This means that the components of the single-particle wave vectors \mathbf{k}^e and \mathbf{k}^h are not good quantum numbers and should be replaced by their corresponding differential operators when solving the eigenvalue problem in the position representation. However, if the single-particle coordinates are transformed to center of mass and relative coordinates,

$$\mathbf{R} = \frac{\mathbf{r}_e + \mathbf{r}_h}{2}, \quad \mathbf{r} = \mathbf{r}_e - \mathbf{r}_h, \quad \mathbf{K} = \mathbf{k}^e + \mathbf{k}^h, \quad \mathbf{k} = \frac{\mathbf{k}^e - \mathbf{k}^h}{2}, \quad (3.2)$$

the interaction term becomes $V(r)I_4$. As a consequence, the Hamiltonian does not commute with the relative momentum operator but does commute with the center of mass momentum operator. Therefore, \mathbf{K} is a conserved quantity and its components are good quantum numbers. Note that the above definitions are written as a function of the single-particle wave vectors which are relative with respect to the valley wave vector $\tau \mathbf{D}$, i.e. $\mathbf{k}^i = \mathbf{q}^i - \tau^i \mathbf{D}^i$ with \mathbf{q}^i the absolute wave vector in the Brillouin zone. This means that in these coordinates the center of mass wave vector of an intervalley exciton can still be zero, i.e. when both the electron and hole are located at their respective band extrema, even though the absolute center of mass wave vector is $\pm 2\mathbf{K}$ (or $\mp \mathbf{K}$ when reduced to the first Brillouin zone).

At this point the exciton eigenvalue equation is a differential equation as a function of two variables, i.e. the two components of the relative position vector. In polar coordinates the angular part can be separated from the radial part by exploiting the fact that the single-electron Hamiltonian (2.9) commutes with the angular

momentum operator

$$\frac{1}{\hbar} J_{z,\tau^e}^e(\mathbf{k}^e) = (x_e k_y^e - y_e k_x^e) I_2 + \frac{\tau^e}{2} \sigma_z = \frac{1}{i} \frac{\partial}{\partial \varphi_e} I_2 + \frac{\tau^e}{2} \sigma_z, \quad (3.3)$$

where the first and second term correspond to the contributions from the orbital angular momentum and the pseudospin, respectively. Using $(A \otimes B)(C \otimes D) = (AC) \otimes (BD)$ and $\partial_{\varphi_e} V(r_{eh}) = -\partial_{\varphi_h} V(r_{eh})$ it can be shown that the total exciton angular momentum operator

$$\begin{aligned} \frac{1}{\hbar} J_{z,\tau^e,\tau^h}^{exc} &= \frac{1}{\hbar} J_{z,\tau^e}^e(\mathbf{k}^e) \otimes I_2 + I_2 \otimes \frac{1}{\hbar} J_{z,-\tau^h}^h(\mathbf{k}^h) \\ &= (x k_y - y k_x + X K_y - Y K_x) I_4 + \frac{1}{2} \text{diag}(\tau_-^{eh}, \tau_+^{eh}, -\tau_+^{eh}, -\tau_-^{eh}), \end{aligned} \quad (3.4)$$

with $\tau_{\pm}^{eh} = \tau^e \pm \tau^h$, commutes with the exciton Hamiltonian (3.1). Note that the separate electron, hole, relative, and center of mass angular momentum operators all do not commute with the exciton Hamiltonian. In the single-band Schrödinger-like model based on the single-particle energy spectrum (2.13), which is often used in the literature and which will be discussed in subsection 3.1.3, the latter two angular momentum operators do commute with the exciton Hamiltonian, but this is prevented in the four-band Dirac model due to the coupling between the momentum and the pseudospin.

3.1.1 Exact solution for $\mathbf{K} = \mathbf{0}$ excitons

Considering first the simplest case in which $\mathbf{K} = \mathbf{0}$, i.e. excitons with no translational kinetic energy. The center of mass orbital angular momentum now vanishes and as a result the eigenvalues of the exciton angular momentum operator (3.4) are all non-degenerate and the eigenstates are eigenstates of the exciton Hamiltonian (3.1) as well. This allows the exciton wave function to be written as

$$\Psi_{\sigma}^{exc}(r) = \begin{pmatrix} \phi_{c,c}^{e,h}(r) e^{i(j-\frac{1}{2}\tau_-^{eh})\varphi} \\ i\phi_{c,v}^{e,h}(r) e^{i(j-\frac{1}{2}\tau_+^{eh})\varphi} \\ i\phi_{v,c}^{e,h}(r) e^{i(j+\frac{1}{2}\tau_+^{eh})\varphi} \\ \phi_{v,v}^{e,h}(r) e^{i(j+\frac{1}{2}\tau_-^{eh})\varphi} \end{pmatrix}, \quad (3.5)$$

with j the angular quantum number (which needs to be an integer in order to satisfy single-valuedness of the wave function) and where the diagonal nature of the exciton angular momentum operator allows separate prefactors (in this case a factor i

in the second and third component) to be included for convenience. The subscripts of the radial wave functions denote the bands in which the particles denoted in the corresponding superscripts are located. Using the above ansatz the exciton Hamiltonian eigenvalue equation in relative coordinates and in position representation, in which

$$\tau k_x \pm ik_y = \frac{1}{i} \tau e^{\pm i\tau\varphi} \left(\frac{\partial}{\partial r} \pm \frac{i\tau}{r} \frac{\partial}{\partial \varphi} \right), \quad (3.6)$$

becomes

$$\left\{ \begin{array}{l} \tau^h \left(\frac{\partial}{\partial r} - \frac{\tau^h}{r} \left(j - \frac{1}{2} \tau_+^{eh} \right) \right) \phi_{c,v}^{e,h}(r) + \tau^e \left(\frac{\partial}{\partial r} + \frac{\tau^e}{r} \left(j + \frac{1}{2} \tau_+^{eh} \right) \right) \phi_{v,c}^{e,h}(r) \\ \quad = \frac{1}{at} (E_\sigma^{exc} + V(r)) \phi_{c,c}^{e,h}(r) \\ \tau^h \left(\frac{\partial}{\partial r} + \frac{\tau^h}{r} \left(j - \frac{1}{2} \tau_-^{eh} \right) \right) \phi_{c,c}^{e,h}(r) + \tau^e \left(\frac{\partial}{\partial r} + \frac{\tau^e}{r} \left(j + \frac{1}{2} \tau_-^{eh} \right) \right) \phi_{v,v}^{e,h}(r) \\ \quad = -\frac{1}{at} (E_\sigma^{exc} + V(r) - \Delta_{s^h, \tau^h}) \phi_{c,v}^{e,h}(r) \\ \tau^e \left(\frac{\partial}{\partial r} - \frac{\tau^e}{r} \left(j - \frac{1}{2} \tau_-^{eh} \right) \right) \phi_{c,c}^{e,h}(r) + \tau^h \left(\frac{\partial}{\partial r} - \frac{\tau^h}{r} \left(j + \frac{1}{2} \tau_-^{eh} \right) \right) \phi_{v,v}^{e,h}(r) \\ \quad = -\frac{1}{at} (E_\sigma^{exc} + V(r) + \Delta_{s^e, \tau^e}) \phi_{v,c}^{e,h}(r) \\ \tau^e \left(\frac{\partial}{\partial r} - \frac{\tau^e}{r} \left(j - \frac{1}{2} \tau_+^{eh} \right) \right) \phi_{c,v}^{e,h}(r) + \tau^h \left(\frac{\partial}{\partial r} + \frac{\tau^h}{r} \left(j + \frac{1}{2} \tau_+^{eh} \right) \right) \phi_{v,c}^{e,h}(r) \\ \quad = \frac{1}{at} (E_\sigma^{exc} + V(r) - \lambda(s^e \tau^e - s^h \tau^h)) \phi_{v,v}^{e,h}(r) \end{array} \right. \quad (3.7)$$

This set of equations can be solved numerically ‘exact’ using the finite element method (FEM).

3.1.2 Approximate solution for $K \neq 0$ excitons

When $K \neq 0$, the center of mass orbital angular momentum $\mathbf{R} \times \hbar \mathbf{K}$ can be non-zero and the eigenvalues of the total exciton angular momentum operator are in general given by the sum of the relative and center of mass quantum numbers $j = j_r + j_R$, both of which are integers, meaning that these eigenvalues are all infinitely degenerate and that the eigenstates are not necessarily eigenstates of the exciton Hamiltonian. In order to find the common eigenstates of the angular momentum and the Hamiltonian the latter would have to be diagonalized in the infinite dimensional subspace spanned by all the angular momentum eigenstates corresponding to a given eigenvalue j . This is practically impossible and as such

this prevents the separation of the angular problem from the radial one. Since the momentum-pseudospin coupling lies at the heart of this problem, this can be resolved by decoupling the exciton eigenvalue equation to a single equation following a procedure analogous to earlier works [109–111]. Defining

$$\mathcal{O}_e = at(\tau^e k_x^e - ik_y^e)I_2, \quad \mathcal{O}_h = at(-\tau^h k_x^h \sigma_x + k_y^h \sigma_y), \quad (3.8)$$

the exciton eigenvalue equation can be rewritten as

$$\begin{cases} \left(\mathcal{O}_h - V(r)I_2 + \frac{\Delta_{s^h, \tau^h}}{2}(I_2 - \sigma_z) \right) |\Psi_{c'}^e\rangle + \mathcal{O}_e |\Psi_v^e\rangle = E_{\sigma}^{exc} |\Psi_{c'}^e\rangle \\ \mathcal{O}_e^\dagger |\Psi_{c'}^e\rangle + \left(\mathcal{O}_h - V(r)I_2 - \frac{\Delta_{s^e, \tau^e}}{2}(I_2 + \sigma_z) \right. \\ \left. + \frac{\lambda(s^e \tau^e - s^h \tau^h)}{2}(I_2 - \sigma_z) \right) |\Psi_v^e\rangle = E_{\sigma}^{exc} |\Psi_v^e\rangle \end{cases}, \quad (3.9)$$

with $|\Psi_{c'}^e\rangle = (|\phi_{c,c}^{e,h}\rangle, |\phi_{c,v}^{e,h}\rangle)^T$ and $|\Psi_v^e\rangle = (|\phi_{v,c}^{e,h}\rangle, |\phi_{v,v}^{e,h}\rangle)^T$. It follows from the second equation that

$$\begin{aligned} |\Psi_v^e\rangle \approx & \left(E_{\sigma}^{exc} I_2 + V(r)I_2 + \frac{\Delta_{s^e, \tau^e}}{2}(I_2 + \sigma_z) \right. \\ & \left. - \frac{\lambda(s^e \tau^e - s^h \tau^h)}{2}(I_2 - \sigma_z) \right)^{-1} \mathcal{O}_e^\dagger |\Psi_{c'}^e\rangle, \end{aligned} \quad (3.10)$$

where the hole kinetic energy was assumed to be small compared to the band gap and the exciton energy, which is a good approximation for monolayer TMDs since for a high photo-induced charge carrier density of $5 \times 10^{12} \text{ cm}^{-2}$ [112–114] the Fermi energy is on average 0.03 eV with respect to the band extrema for the considered TMDs, which compares with a band gap of on average 1.5 eV (and an exciton energy which is lower but of the same order as the band gap). Using this result, the first equation of (3.9) can be written as

$$\begin{cases} (-V(r) + a^2 t^2 k_-^e (g_1^\sigma(E_{\sigma}^{exc}, r) k_+^e)) |\phi_{c,c}^{e,h}\rangle - at k_+^h |\phi_{c,v}^{e,h}\rangle = E_{\sigma}^{exc} |\phi_{c,c}^{e,h}\rangle \\ (-V(r) + \Delta_{s^h, \tau^h} + a^2 t^2 k_-^e (g_2^\sigma(E_{\sigma}^{exc}, r) k_+^e)) |\phi_{c,v}^{e,h}\rangle - at k_-^h |\phi_{c,c}^{e,h}\rangle = E_{\sigma}^{exc} |\phi_{c,v}^{e,h}\rangle \end{cases} \quad (3.11)$$

with $k_{\pm}^j = \tau^j k_x^j \pm ik_y^j$ and with

$$\begin{aligned} g_1^\sigma(E_{\sigma}^{exc}, r) &= (E_{\sigma}^{exc} + V(r) + \Delta_{s^e, \tau^e})^{-1}, \\ g_2^\sigma(E_{\sigma}^{exc}, r) &= (E_{\sigma}^{exc} + V(r) - \lambda(s^e \tau^e - s^h \tau^h))^{-1}. \end{aligned} \quad (3.12)$$

The first equation now leads to

$$|\phi_{c,c}^{e,h}\rangle \approx -\frac{atk_+^h}{E_\sigma^{exc} + V(r)} |\phi_{c,v}^{e,h}\rangle, \quad (3.13)$$

now assuming the electron kinetic energy to be small compared to the exciton energy, which is a good approximation for the same reason as explained below Eq. (3.10). Inserting this in the second equation of (3.11), transforming to center of mass and relative coordinates, and going to position representation results in

$$\begin{aligned} & \left(-\frac{2a^2t^2}{E_\sigma^{exc} + V(r)} \left(\frac{\partial^2}{\partial r^2} + \frac{1}{r} \frac{\partial}{\partial r} + \frac{1}{r^2} \frac{\partial^2}{\partial \varphi^2} - \frac{K^2}{4} \right) - V(r) + \Delta_{s^h, \tau^h} \right. \\ & - a^2t^2 \left(\frac{\partial}{\partial r} \frac{1}{E_\sigma^{exc} + V(r)} \right) \left(2 \frac{\partial}{\partial r} + i \frac{\tau^e + \tau^h}{r} \frac{\partial}{\partial \varphi} \right. \\ & \left. \left. + \delta_{\tau^h, -\tau^e} \tau^h (K_y \cos(\varphi) - K_x \sin(\varphi)) \right) \right) \phi_{c,v}^{e,h}(r, \varphi) = E_\sigma^{exc} \phi_{c,v}^{e,h}(r, \varphi). \end{aligned} \quad (3.14)$$

In the last step it was assumed that $s^e \tau^e = s^h \tau^h$ since in this chapter only optically excited excitons are considered. The disadvantages of using this equation are the fact that it needs to be solved self-consistently and that the other three components of the exciton wave function still need to be calculated explicitly from Eqs. (3.10) and (3.13) after solving this equation whereas a numerical solution of the coupled set of equations (3.7) immediately yields all four components. The last two terms in this equation, which only appear for intravalley excitons and not for intervalley ones, still prevent the separation of the angular and the radial part. In principle these terms could be treated within perturbation theory. In such a case the angular part of the zeroth order wave function is simply given by $\exp(ij\varphi)$ with j an integer quantum number. This implies that these terms give no contribution in first order perturbation theory, whereas in second order perturbation theory they only couple states whose angular momentum quantum numbers differ by ± 1 . Because of the large energy difference between such states (for not too highly excited states), which will be seen in subsection 3.2.2, these corrections will be negligibly small. They will therefore be neglected in the remainder of the calculations and the angular part of the wave function is thus assumed to be given by $\exp(ij\varphi)$.

3.1.3 Single-band model

Starting from the parabolic single-particle energy spectrum (2.13), absorbing the constant terms into the exciton energy, and performing the more general transfor-

mation to center of mass and relative coordinates, i.e. with

$$\mathbf{R} = \frac{m_e \mathbf{r}_e + m_h \mathbf{r}_h}{m_e + m_h}, \quad \mathbf{k} = \frac{m_h \mathbf{k}_e - m_e \mathbf{k}_h}{m_e + m_h}, \quad (3.15)$$

as compared to Eq. (3.2), the exciton eigenvalue equation reduces to a typical Schrödinger equation:

$$\left(\frac{\hbar^2 K^2}{2M_\sigma} - \frac{\hbar^2}{2\mu_\sigma} \left(\frac{\partial^2}{\partial r^2} + \frac{1}{r} \frac{\partial}{\partial r} + \frac{1}{r^2} \frac{\partial^2}{\partial \varphi^2} \right) - V(r) \right) \psi_\sigma^{exc}(r, \varphi) = E_\sigma^{exc} \psi_\sigma^{exc}(r, \varphi), \quad (3.16)$$

with $M_\sigma = m_{s^e, \tau^e} + m_{s^h, \tau^h}$ the total exciton mass and $\mu_\sigma = m_{s^e, \tau^e} m_{s^h, \tau^h} / (m_{s^e, \tau^e} + m_{s^h, \tau^h})$ the reduced exciton mass and where the angular part of the wave function is again of the form $\exp(ij\varphi)$ with j an integer quantum number. This equation is often used in the literature as it is easier to solve numerically, for example using the FEM, than the set of equations (3.7) or the decoupled equation (3.14). Furthermore, it has the important advantage that it is always a single equation, even when studying complexes consisting of more than two particles. It will be used in the next two chapters to study trions and biexcitons. The Dirac model on the other hand leads to a set of 2^N coupled equations for an N -particle complex. The disadvantage of the single-band model is that the coupling between the conduction and valence bands, which is inherently present in the multi-band Dirac model through the Berry curvature, is not taken into account. Different properties of excitons in monolayer TMDs will now be calculated using the four-band model and the differences with the single-band model will be investigated. This study was published in Physical Review B [115]. Unless specified otherwise, the results are shown for intravalley A excitons with $\mathbf{K} = \mathbf{0}$ and are obtained from the set of equations (3.7).

3.2 Numerical results

3.2.1 Ground state binding energy

Solving either the set of equations (3.7), the decoupled equation (3.14), or the single-band model equation (3.16) yields the exciton energy E_σ^{exc} , which from now on is written as E , dropping the subscript σ and the superscript exc for notational simplicity. However, a physically more relevant quantity is the exciton binding energy E_b . This quantity is defined as the difference between the energy of the constituent electron and hole and the exciton energy, i.e. $E_b = E^e + E^h - E$. In the multi-band model this reduces to $E_b = \Delta_{s^h, \tau^h} - E$ whereas in the single-band model it is simply given by $E_b = -E$.

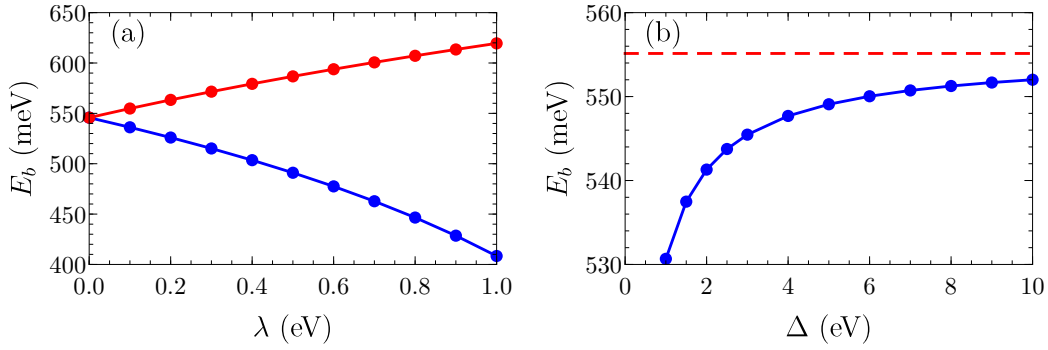


Figure 3.2: (a) Binding energy for A (blue) and B (red) excitons in MoS_2 suspended in vacuum as a function of the spin-orbit coupling strength. (b) Binding energy for A excitons in MoS_2 suspended in vacuum as a function of the band gap for fixed charge carrier mass. The dashed red line is the single-band result.

In Fig. 3.2(a) the ground state binding energy for A and B excitons as a function of the spin-orbit coupling strength is shown. In the absence of spin-orbit coupling the binding energies for both kinds of excitons are equal since there is no spin splitting of the energy bands. With increasing spin-orbit coupling the A (B) exciton binding energy decreases (increases). This is to be expected since increasing λ will cause the A exciton band gap to become smaller whereas the B exciton band gap becomes larger. It follows from Eq. (2.14) that an increasing (decreasing) band gap leads to an increasing (decreasing) effective charge carrier mass. This reduces (enhances) the kinetic energy and therefore enhances (reduces) the binding energy, thus explaining the results in the figure. For the realistic value of the spin-orbit coupling strength of MoS_2 given in Table 2.1 the difference in binding energy of the A and B exciton is 14 meV and the difference in the ground state energy of the A and B exciton is 136 meV, i.e. 2λ minus the difference in binding energy.

The ground state binding energy as a function of the band gap is shown in Fig. 3.2(b). In order to facilitate comparison with the single-band model result, for each value of the band gap the value of at is calculated according to Eq. (2.14) such that it fixes the charge carrier mass at $0.5m_0$. The figure shows that the binding energy calculated in the multi-band model converges to the binding energy calculated in the single-band model in the limit of an infinite band gap. As discussed in the previous chapter, in the multi-band model there is a mixing between the conduction and valence band states, which is clear from the eigenstates (2.12). This mixing increases with decreasing band gap and as such the conduction (valence) band state increasingly loses its electron-like (hole-like) character. This causes the exciton

binding energy to decrease with decreasing band gap. In the single-band model the charge carrier mass replaces the role of the parameter at in the multi-band model as the parameter that determines the curvature of the energy bands. However, the band gap parameter is effectively lost. Only pure electron- and hole-like states are considered in the single-band eigenvalue equation (3.16), which can therefore be viewed as an infinite band gap approximation. This is why the multi-band result converges to the single-band result in the infinite band gap limit. At the realistic value of the band gap of MoS₂ given in Table 2.1 the difference in binding energy of the multi- and single-band model is 16 meV. It should be noted that, in the multi-band model, when the band gap is smaller than the exciton binding energy the ground state is no longer a true bound state. However, this is not the case for the materials considered in this thesis.

In Table 3.1 the exciton ground state binding energy is shown for different monolayer TMDs and different substrates as calculated using both the single- and multi-band model. For the single-band results the effective masses given in Ref. [81], which are equal to those calculated in subsection 2.2.1 (except for MoS₂ for which $0.50m_0$ is used instead of $0.49m_0$), were used. The calculated values are compared with other theoretical studies based on the single-band model using ground state diffusion Monte Carlo [116], path-integral Monte Carlo [117], and the stochastic variational method [118], as well as experimental results. It is clear that excitons in monolayer TMDs have exceptionally large binding energies. The origin for these large binding energies is threefold: the (quasi-)perfect 2D nature of the charge carriers, the relatively large effective masses, and the reduced dielectric screening, i.e. for a monolayer TMD in vacuum only charges in the material plane itself contribute to the screening, as described by the Keldysh potential (2.40). As discussed in section 1.1, non-perfect 2D confinement, small effective masses, and large dielectric constants limit the exciton binding energy in conventional semiconductor heterostructures such as GaAs/AlGaAs. The calculated values also show that the presence of a substrate reduces the exciton binding energy, which is a result of the additional dielectric screening. In general the values are in good agreement with the other theoretical results, differing at most 16%. However, it should be noted that in Ref. [117] a value of $\varepsilon_b = 3.0$ was used for SiO₂, leading to consistently larger binding energies. Assuming $\varepsilon_b = 3.0$, a single-band (multi-band) binding energy of 365.3 meV (352.1 meV), 323.6 meV (316.8 meV), 328.6 meV (315.2 meV), and 301.6 meV (292.1 meV) for MoS₂, MoSe₂, WS₂, and WSe₂, respectively, is found. This is in considerably better agreement with the results of Ref. [117]. The agreement with the experimental results is less satisfactory. With some references there is reasonable agreement while other references find

		Substrate	Literature		This thesis	
			Theory	Experiment	SB	MB
MoS ₂	Vacuum		551.4 [116]	570 [122]	555.1	538.6
			526.5 [117]			
			555.0 [118]			
			614 [119]			
	SiO ₂		348.6 [117]	-	320.6	308.4
			301 [120]			
	hBN	222.0 [121]	-	191.9	183.5	
MoSe ₂	Vacuum		477.8 [116]	-	480.4	471.8
			476.9 [117]			
			480.4 [118]			
	SiO ₂		322.9 [117]	590 ± 50 [123]	286.2	279.9
		BLG	-	550 ± 40 [124]	256.7	250.9
				580 ± 60 [125]		
WS ₂	Vacuum		519.1 [116]	-	523.3	505.7
			509.8 [117]			
			523.5 [118]			
	SiO ₂		322.9 [117]	320 ± 40 [126]	284.0	271.8
				312 [127]		
				710 ± 10 [128]		
			410 [129]			
			700 [130]			
WSe ₂	Vacuum		466.7 [116]	-	470.2	457.8
			456.4 [117]			
			470.2 [118]			
	SiO ₂		294.6 [117]	370 [131]	262.5	253.8
				720 ± 70 [123]		
				482 [132]		
			198 [133]			
			600 ± 200 [134]			

Table 3.1: Exciton ground state binding energy (meV) for different monolayer TMDs and different substrates calculated using the single-band (SB) and multi-band (MB) model, compared with theoretical and experimental results from the literature. The following dielectric constants were used: $\varepsilon_b = 3.8$ ($\varepsilon_b = 4.58$) and $\varepsilon_t = 1$ for SiO₂ (bilayer graphene, BLG) below and vacuum above the TMD and $\varepsilon_b = \varepsilon_t = 4.4$ for encapsulating hBN.

binding energies which are almost a factor 3 larger. These large discrepancies and the non-consistency between different experimental results for the same systems can potentially be attributed to surface roughness of the substrate, which can lead to local detachment of the TMD from the substrate and as such to considerably larger binding energies. Another possible explanation is the fact that in experiments the excitons can potentially be confused with excitons which are bound to defects, which leads to higher predicted binding energies. The procedure of these experiments is discussed in section 3.3.

3.2.2 Exciton energy spectrum

Up to now only results for the ground state were shown. This state is characterized by a principal quantum number $n = 1$ and an angular momentum quantum number $j = 0$ and is referred to as the $1s$ state in analogy to the 2D hydrogen atom. However, similar to the 2D hydrogen atom, there is an infinite spectrum of bound exciton states which pile up towards the edge of the continuum, which for the case of monolayer TMDs lies at Δ_{s^h, τ^h} . These will be discussed in this subsection, starting with s states. However, in contrast to the (2D) hydrogen atom in which states with the same principal quantum number but different angular momentum are degenerate, the non-local screening effects in monolayer TMDs which lead to the Keldysh potential (2.40) also result in the breaking of this degeneracy, as will be seen shortly. The higher angular momentum states cannot be observed by means of one-photon transitions which are most commonly used in experiments. However, two-photon transitions can give optical access to these states, as was shown successfully for p states [130, 131]. Even higher angular momentum states, such as d states, have so far not been experimentally measured in monolayer TMDs. Even though these non-zero angular momentum states are optically inactive, they do play an important role in exciton relaxation and valley dynamics [135] and are therefore worth investigating. The results are shown in this subsection and this study was published in Physical Review B [136].

In Fig. 3.3(a) the five lowest s state energy levels for excitons in WSe₂ and WS₂ on a SiO₂ substrate are shown and compared with an analytical model based on an effective Hamiltonian and a bare coulomb potential [77] and experimental results [126, 131]. This shows that the agreement of the multi-band model with the experimental results is better than that of the analytical model. The results obtained from the multi-band model always overestimate the experimental results except for the ground state of WS₂ for which a smaller value is found.

The dependence on the 2D polarizability of the three lowest s state energy levels

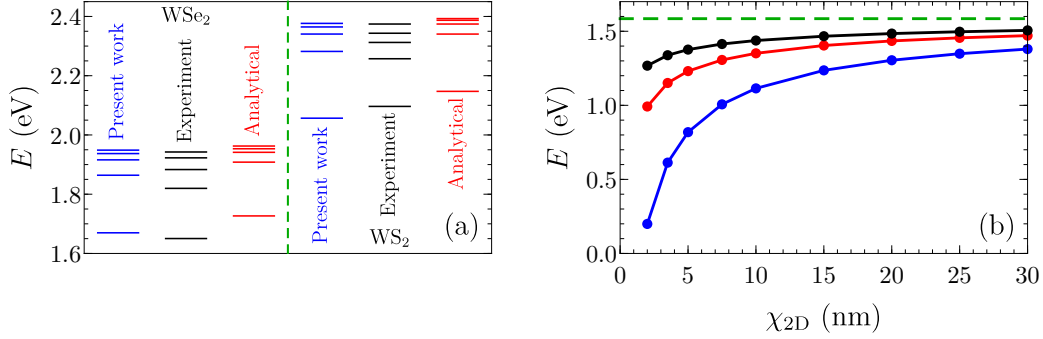


Figure 3.3: (a) Five lowest s state energy levels for excitons in WSe_2 and WS_2 on a SiO_2 substrate, compared with the analytical model of Ref. [77] (red), and the experimental results of Refs. [131] (WSe_2) and [126] (WS_2) (black). The parameters specified in Ref. [77] were used in the calculation, i.e. $\Delta_{s,\tau} = 1.97$ eV, $a = 3.310$ Å, and $t = 1.13$ eV for WSe_2 and $\Delta_{s,\tau} = 2.4$ eV, $a = 3.197$ Å, and $t = 1.25$ eV for WS_2 , and a dielectric constant of $\epsilon_r = 3.9$ for the SiO_2 substrate. (b) Three lowest s state energy levels calculated for excitons in MoS_2 suspended in vacuum as a function of the 2D polarizability. The dashed green line indicates the edge of the continuum.

for excitons in MoS_2 is shown in Fig. 3.3(b). As the 2D polarizability increases, and thus the interaction strength decreases, all the energy levels converge towards the edge of the continuum. As the 2D polarizability decreases, the ground state disappears in the negative continuum, at which point it is no longer a true bound state.

The exciton bound state spectrum of MoS_2 , now also including p and d states, is shown in Fig. 3.4. Note that the degeneracy between states with the same principal quantum number but different orbital angular momentum is broken, such that those with higher (absolute value of) orbital angular momentum have lower energy. The energy difference between the energy levels is larger when the material is suspended in vacuum as compared to when it is placed on a substrate, which is due to the stronger interactions in the former case. The results are compared with those of Refs. [119] and [120], which use a first-principles (meaning without tunable parameters, phenomenological models, or other assumptions) and a tight-binding formulation, respectively, of the Bethe-Salpeter equation approach, which is a many-body formulation of the exciton problem which takes into account two-particle interactions up to infinite order and is therefore expected to give reliable results. These studies also found that $E_{2p} < E_{2s}$, which was experimentally found

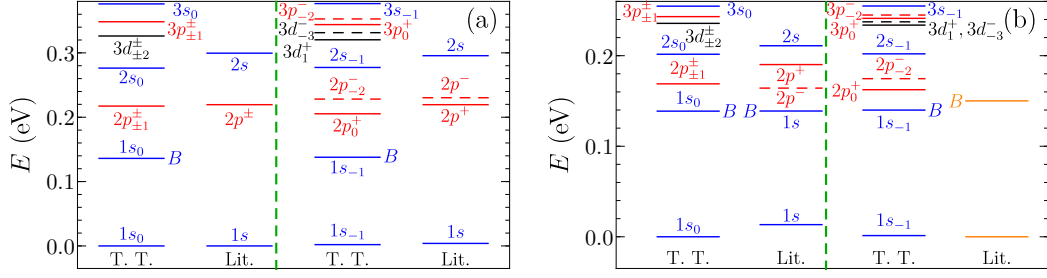


Figure 3.4: Intravalley ($\tau^e = -\tau^h = 1$, left) and intervalley ($\tau^e = \tau^h = -1$, right) exciton energy levels for MoS₂ suspended in vacuum (a) and placed on a SiO₂ substrate ($\varepsilon_b = 3.8$) (b). The results of this thesis (T. T.) are compared with results from the literature (Lit.), i.e. from Ref. [119] (a) and Ref. [120] (b). The obtained results are labeled on the figure according to $n[L]_j$, where $[L]$ represents s (blue), p (red), or d (black) depending on the orbital angular momentum of the dominant component of the wave function. No labeling was given in Ref. [120] for intervalley excitons. Exciton states with negative orbital angular momentum are indicated with dashed lines. When two states with opposite orbital angular momentum are degenerate only the solid line is shown. B exciton states are indicated with the letter B . To facilitate comparison, the energy levels are uniformly shifted downwards in energy such that the ground state (which can be either intravalley or intervalley) has zero energy.

as well in Ref. [130] for WS₂. Furthermore, the results show that $E_{3d} < E_{3p} < E_{3s}$, which was also theoretically predicted in Ref. [130] for WS₂.

The lowest energy intravalley exciton is found to have slightly lower energy than the lowest energy intervalley exciton, which again agrees with Ref. [119] but not with Ref. [120]. However, whether the intravalley or intervalley exciton has lowest energy will also depend on the effect of exchange interactions. This effect is not taken into account here and therefore it is not possible to give a definite answer on which type of exciton has the lowest ground state energy. However, the exact strength of the exchange interactions is difficult to predict and therefore even when including this effect it is still practically impossible to estimate which exciton has the lowest ground state energy [120].

The most remarkable result is the ordering of the intervalley exciton energy levels with different j , with as the most striking example the fact that the ground state has angular momentum $j = -1$. The reason for this is related to the orbital angular momenta of the different components of the total exciton wave function.

The second component, which corresponds to an exciton consisting of an electron in the conduction band and a hole in the valence band as discussed in the previous section, is the most dominant one. As can be seen from Eq. (3.5), the dominant component of an intravalley exciton ($\tau^e = -\tau^h$) with total angular momentum j also has orbital angular momentum j . For an intervalley exciton ($\tau^e = \tau^h = \tau$), however, the dominant component of an exciton with angular momentum j has orbital angular momentum $j - \tau$. Therefore, the total wave function of an intervalley exciton with angular momentum $j = \tau$ resembles that of an s -like state and thus has the lowest energy. Looking at Eq. (3.4), this remarkable result can be interpreted as the exciton having approximately zero orbital angular momentum (and hence an s -like wave function, even though this is not a good quantum number) but non-zero contribution from the pseudospin of the electron and hole, which cancels for intravalley excitons but adds up for intervalley excitons. This is why the energy levels in Fig. 3.4 are labeled according to the orbital angular momentum of the dominant component of the exciton wave function. From now on, the subscript j in these labels will be omitted for intravalley excitons, as in this case the total angular momentum and the (approximate) orbital angular momentum are equal. In Ref. [119] it was found that the intervalley exciton ground state is a $1s$ state, although the origin of the angular momentum labeling used in that work is not entirely clear, whereas in Ref. [120] no statement was made about the angular momentum of the intervalley exciton states.

Finally, it is found that intravalley excitons with angular momenta $\pm j$ are degenerate, which is in agreement with Ref. [119] but not with Ref. [120]. This degeneracy is broken for intervalley excitons, again in agreement with Ref. [119], but is restored when taking opposite intervalley excitons into account, i.e. (τ, j) and $(-\tau, -j)$ excitons are degenerate. This may suggest that the (non-)degeneracy between the states with opposite j arises from the coupling between the orbital angular momentum of the exciton and the intrinsic angular momentum of the exciton. The single-particle intrinsic angular momentum (which is associated with the Berry curvature and gives rise to the intrinsic magnetic moment (2.24)) is opposite for electrons and holes, as well as in the two valleys. This means that the total intrinsic angular momentum for intravalley excitons is zero and therefore it cannot couple with the orbital angular momentum. For intervalley excitons, however, the total intrinsic angular momentum is non-zero and opposite for the two opposite intervalley excitons. This causes a valley-opposing splitting between intervalley excitons with opposite j , which explains the degeneracy between (τ, j) and $(-\tau, -j)$ exciton states. The non-degeneracy between opposite j intravalley excitons found in Ref. [120] could be explained by many-body Berry curvature

	Substrate	1s	2p	2s	3d	3p	3s
MoS ₂	Vacuum	539	321	262	212	190	163
	SiO ₂	308	139	107	73	65	54
	hBN	183	61	46	26	25	20
MoSe ₂	Vacuum	472	291	241	199	179	154
	SiO ₂	280	135	104	74	66	55
	hBN	172	63	48	28	26	22
WS ₂	Vacuum	506	283	226	176	157	132
	SiO ₂	272	110	83	52	48	39
	hBN	152	44	34	17	17	14
WSe ₂	Vacuum	458	265	214	170	152	129
	SiO ₂	254	108	82	54	49	40
	hBN	146	45	34	19	18	15

Table 3.2: Binding energy (meV) calculated for different exciton states in different monolayer TMDs for different substrates. The following dielectric constants were used: $\varepsilon_b = 3.8$ and $\varepsilon_t = 1$ for SiO₂ below and vacuum above the TMD and $\varepsilon_b = \varepsilon_t = 4.4$ for encapsulating hBN.

effects [137], which are not taken into account in this thesis.

In Table 3.2 the binding energy of different exciton states is shown for different monolayer TMDs and different substrates. The results show that, for all exciton states, the binding energy is largest in MoS₂ and smallest in WSe₂. Remarkably, the binding energy is larger in MoSe₂ than in WS₂ for all states except for the ground state. For comparison, results from the literature are summarized in Table 3.3. In the case of MoS₂, for which the results from the literature are theoretical, the agreement with the calculated values is good, differing at most by 17%. In the case of WS₂ and WSe₂ experimental results are available (except for the 2s, 3d, and 3s states of Ref. [130] which are theoretical) and the agreement with the calculated values is less satisfactory, differing at least by 15% and at most by a factor 9 (with the 3s state of Ref. [134]). The results of Refs. [130] and [134] in particular are remarkable, with 1s state binding energies which are significantly larger than the range of commonly accepted theoretical ground state exciton binding energies in vacuum (see Table 3.1), even though in both works a SiO₂ substrate is used which should reduce the binding energy. However, the difference in energy between the 1s and 2s state found in Ref. [134] is 13% smaller than the value obtained here, whereas the result found in Ref. [130] is 38% larger than said value. This may

	Substrate	Ref.	1s	2p	2s	3d	3p	3s
MoS ₂	Vacuum	[119]	614	395	315	-	-	-
	SiO ₂	[120]	301	150(-)/125(+)	99	-	-	-
WS ₂	SiO ₂	[126]	320	-	156	-	-	96
	SiO ₂	[130]	621	423	314	266	205	136
WSe ₂	SiO ₂	[131]	364	-	199	-	-	133
	SiO ₂	[134]	650	500	500	-	370	370

Table 3.3: Binding energy (meV) for different exciton states in different monolayer TMDs for different substrates as found in the literature. Results for MoS₂ are theoretical whereas the results for WS₂ and WSe₂ are experimental.

indicate that in Ref. [134] the band gap was overestimated, which was already suggested in the manuscript itself, whereas in Ref. [130] there may have been issues with the substrate as discussed in the previous subsection.

3.2.3 Wave function and interparticle distance

In Fig. 3.5 the different components of the 1s state exciton wave function are shown for two values of the band gap. For the realistic value of the band gap the second component of the exciton wave function (blue curves), which represents the contribution of an exciton composed of an electron in the conduction band and a hole in the valence band, is significantly larger than the other three components. This component as well as the third component (black curves) show *s*-like behavior, whereas the first and fourth component (red curves) show *p*-like behavior. This is in agreement with Eq. (3.5), in which for $j = 0$ and $\tau^e = -\tau^h = 1$ the second and third component have zero orbital angular momentum and the first (fourth) component has orbital angular momentum -1 (1). The single-band model wave function, which has only one component since in this model only conduction particles are considered, is in good agreement with the dominant component. It is precisely the other components, representing the contribution of excitons consisting partly or entirely of valence particles, which lead to the decreasing binding energy with decreasing band gap shown in Fig. 3.2(b). For the case of a very large band gap the valence components are completely suppressed and the dominant conduction component agrees perfectly with the single-band model wave function, which is in correspondence with the fact that the binding energy in the multi-band model converges to the single-band model binding energy in the limit of an infinite band

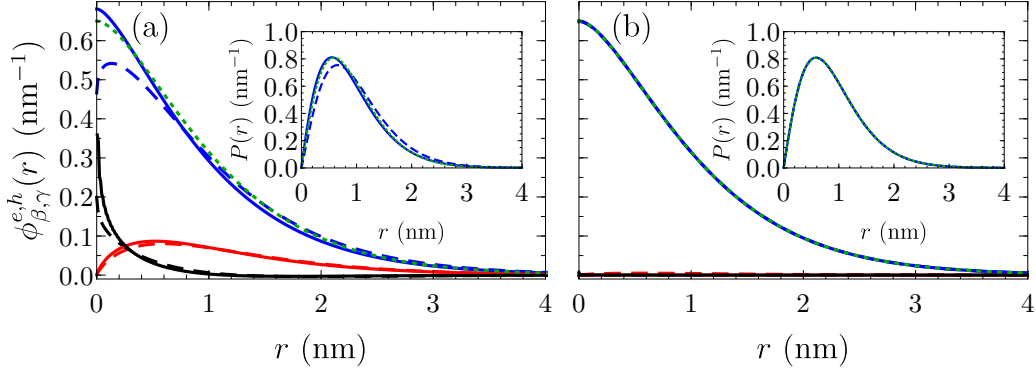


Figure 3.5: Different components ($\beta = c, \gamma = v$: blue curve, $\beta = c, \gamma = c$ and $\beta = v, \gamma = v$: red curve, $\beta = v, \gamma = c$: black curve) of the $1s$ state wave function for excitons in MoS_2 suspended in vacuum obtained from Eq. (3.14) (solid) and Eq. (3.7) (dashed) for $\Delta = 1.66$ eV (a) and $\Delta = 500$ eV (b) for fixed charge carrier mass. The dotted green curve is the single-band result. The inset shows the corresponding total radial probability distribution.

gap.

It is also worth comparing the results of the decoupled eigenvalue equation (3.14) with those of the set of equations (3.7). Using the decoupled eigenvalue equation for an exciton in MoS_2 suspended in vacuum results in a binding energy of 556 meV, 274 meV, and 330 meV for the $1s$, $2s$, and $2p$ state, respectively. This compares with the values 539 meV, 262 meV, and 321 meV, respectively, obtained from equation (3.7) listed in Table 3.2. This amounts to a difference of 3-4% between the results of the two equations. When comparing the wave functions obtained from both equations, the largest difference between the two is found in the second component for small r . The wave function obtained from Eq. (3.7) has a maximum at small non-zero r while the solution obtained from Eq. (3.14) has its maximum in the origin. This additional curvature of the wave function for the former leads to a higher energy and as such a lower binding energy, in agreement with the values mentioned above. The total radial probability distributions as obtained from the two equations are in good agreement, with the probability distribution obtained from Eq. (3.7) being slightly more spread out, which is in agreement with the lower binding energy which is found using this equation.

Solving the decoupled eigenvalue equation (3.14) allows to calculate the exciton energy as a function of the center of mass wave vector. This dependence is approximately parabolic at low energy. From the curvature of the exciton disper-

sion the total exciton mass can be obtained through the expression

$$M = \frac{\hbar^2}{m_0} \left(\frac{\partial^2 E(K)}{\partial K^2} \Big|_{K=0} \right)^{-1}. \quad (3.17)$$

This results in $M = 1.14m_0$, $M = 1.24m_0$, $M = 0.70m_0$, and $M = 0.77m_0$ for the $1s$ state exciton in, respectively, MoS₂, MoSe₂, WS₂, and WSe₂ suspended in vacuum. These values are 9-14% larger than the non-interacting exciton masses $M_\sigma = m_{s^e, \tau^e} + m_{s^h, \tau^h}$, with $m_{s, \tau}$ calculated from Eq. (2.14), which results in, respectively, $M = 0.98m_0$, $M = 1.08m_0$, $M = 0.64m_0$, and $M = 0.68m_0$. The interaction between the electron and the hole thus causes the exciton to become heavier. These interacting exciton masses differ very little for higher excited exciton states: they have slightly smaller masses, e.g. $M = 1.12m_0$ and $M = 1.09m_0$ for the $2p$ and $2s$ state in MoS₂, respectively. Furthermore, there is also a very weak dependence on the substrate dielectric constant, i.e. a decreasing exciton mass with increasing dielectric constant, e.g. $M = 1.09m_0$ for the $1s$ state exciton in MoS₂ on a SiO₂ substrate. These two observations are in correspondence with the fact that a lower binding energy leads to a smaller exciton mass.

It should be noted that in this thesis the exchange interactions between the electrons and holes, which actually stem from the exchange interactions between the conduction and valence electrons and are therefore weak because of the small overlap between these states, are not taken into account. These couple the intravalley exciton bands originating from direct transitions in the K and K' valley and as such lead to a splitting of these originally degenerate bands into a parabolic lower band and a linear upper band [119, 120]. This leads to a correction on the total exciton mass of the lower parabolic band, which is the ground state. Using the effective model and the parameters given in Ref. [119] leads to a correction factor of 1.26 for the total exciton mass for MoS₂ suspended in vacuum. Similar results are expected for other TMDs. It should be noted that in Ref. [119] the bare Coulomb potential was used instead of the Keldysh potential to study the exchange effects. When using the latter potential the above correction factor is expected to be even closer to 1. The presence of a substrate will also reduce the correction factor. The exchange interactions reduce the binding energy of excitons in MoS₂ suspended in vacuum by 20 meV in the case of a bare Coulomb potential [119]. In the case of the Keldysh potential this effect will be even smaller, which is why it is neglected in this thesis.

For a general N -particle complex the correlation function between particles i and j is defined as

$$C_{ij}(\mathbf{r}) = \langle \Psi | \delta(\mathbf{r}_i - \mathbf{r}_j - \mathbf{r}) | \Psi \rangle, \quad (3.18)$$

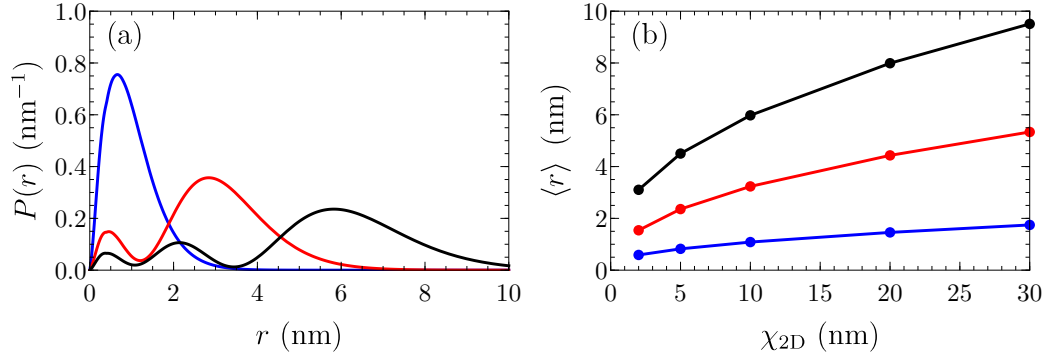


Figure 3.6: Radial probability distribution (a) and average interparticle distance as a function of the 2D polarizability (b) calculated for the three lowest s states for excitons in MoS₂ suspended in vacuum.

with $\Psi(\mathbf{r}_1, \mathbf{r}_2, \dots, \mathbf{r}_N)$ the total N -particle wave function. For excitons in a translational invariant system this simply reduces to the total probability distribution. The radial probability distributions for the three lowest s states for excitons in MoS₂ suspended in vacuum are shown in Fig. 3.6(a). This shows that the excited states have a larger probability for the particles being at a larger distance from each other. In general, the radial probability distribution of the n^{th} state exhibits n maxima. In Fig. 3.6(b) the average interparticle distances for the three lowest s states as a function of the 2D polarizability are shown. These are calculated from

$$\langle r_{ij} \rangle = 2\pi \int_0^\infty r^2 C_{ij}(r) dr. \quad (3.19)$$

The results show that the average interparticle distance increases with the 2D polarizability, which is a consequence of the reduced interaction strength, as well as with increasingly excited states.

In Table 3.4 the average interparticle distance of different exciton states is shown for different monolayer TMDs and different substrates. The results show that the average interparticle distances exhibit opposite behavior as compared to the binding energies listed in Table 3.2, as can be expected. It can be seen that the average interparticle distance is mostly determined by the type of transition metal in the TMD, while changing the chalcogen atom between sulfur and selenium has very little influence on the interparticle distance. Furthermore, in vacuum the average interparticle distance in MoS₂ (WS₂) is slightly smaller than that in MoSe₂ (WSe₂) for all states, while in the presence of a substrate this behavior holds for the lowest states, whereas for higher excited states the opposite is true.

	Substrate	1s	2p	2s	3d	3p	3s
MoS ₂	Vacuum	1.00	2.05	2.97	3.43	4.39	5.53
	SiO ₂	1.11	2.57	3.86	4.87	6.31	8.09
	hBN	1.27	3.47	5.22	7.49	9.52	11.99
MoSe ₂	Vacuum	1.04	2.11	3.05	3.48	4.46	5.59
	SiO ₂	1.14	2.57	3.83	4.71	6.12	7.83
	hBN	1.28	3.32	5.02	6.92	8.85	11.27
WS ₂	Vacuum	1.23	2.56	3.75	4.42	5.69	7.21
	SiO ₂	1.41	3.43	5.18	6.87	8.84	11.32
	hBN	1.66	4.93	7.36	11.33	14.05	17.52
WSe ₂	Vacuum	1.27	2.62	3.82	4.45	5.72	7.23
	SiO ₂	1.43	3.40	5.12	6.62	8.56	10.97
	hBN	1.66	4.73	7.11	10.58	13.24	16.65

Table 3.4: Average interparticle distance (nm) calculated for different exciton states in different monolayer TMDs for different substrates. The following dielectric constants were used: $\varepsilon_b = 3.8$ and $\varepsilon_t = 1$ for SiO₂ below and vacuum above the TMD and $\varepsilon_b = \varepsilon_t = 4.4$ for encapsulating hBN.

3.2.4 Absorbance spectrum

When both the excitonic energy spectrum as well as the wave functions are known it is also possible to calculate the absorbance spectrum from the valence band continuum to the bound exciton states resulting from the presence of a radiation field. Similar to the discussion in subsection 2.2.2, the absorption rate is obtained from Fermi's golden rule. Because now transitions between two-particle states are considered the perturbation is proportional to $(\mathbf{e} \cdot \boldsymbol{\sigma}) \otimes I_2 - I_2 \otimes (\mathbf{e} \cdot \boldsymbol{\sigma})$, again assuming that $\mathbf{q} = \mathbf{0}$ because of the large light wavelength compared to the lattice constant. The density of states of the final state, which appears in Fermi's golden rule but is a constant for the continuum bands at low energy, is now for a bound exciton state with energy E_j given by

$$\delta(E_j - \hbar\omega) = \lim_{\gamma \rightarrow 0} \frac{1}{\pi\gamma} \frac{\gamma^2}{(E_j - \hbar\omega)^2 + \gamma^2} = \lim_{\gamma \rightarrow 0} \frac{1}{\pi} \text{Im} \left(\frac{1}{E_j - \hbar\omega - i\gamma} \right), \quad (3.20)$$

with $\hbar\omega$ the photon energy. Due to thermal effects the broadening factor γ will be non-zero and the limit in the above expression can be left out. The absorbance is given by the ratio of the absorbed energy per unit time to the energy flux of the radiation field and, calculating the matrix element of the perturbation term between

the valence band continuum state and an exciton bound state, can be expressed as [138, 139]

$$\alpha(\omega) \propto \frac{1}{\omega} \text{Im} \left(\sum_j \frac{|\mathcal{P}_e(\mathbf{0})|^2 |\phi_{c,v}^{e,h,j}(0) - \phi_{v,c}^{e,h,j}(0)|^2}{E_j - \hbar\omega - i\gamma} \right), \quad (3.21)$$

with $\phi_{c,v}^{e,h,j}(r)$ and $\phi_{v,c}^{e,h,j}(r)$ components of the exciton wave function (3.5) and $\mathcal{P}_e(\mathbf{0})$ the absorption rate between the valence and conduction band continuum states discussed in subsection 2.2.2 at the band edges. The wave function of higher angular momentum states is zero in the origin, thus explaining why these states cannot be observed in one-photon experiments as discussed earlier. The above formula can also be derived more rigorously from quantum field theory. This lies outside the scope of this thesis but the derivation can be found in Ref. [140] and the different steps can be summarized as follows. The electromagnetic field is treated classically and the electronic part of the Hamiltonian is written out in second quantization, expanding the field operators in the Bloch functions in the term describing the interactions between the electrons and the electric field. The Heisenberg equations for the creation and annihilation operators lead to an equation for the interband polarization, which is defined as the expectation value of the electric dipole and can also be expanded in Bloch functions. Assuming a filled valence band and an empty conduction band, this equation can be solved by means of a Fourier transform and by subsequently expanding the interband polarization in the exciton wave functions. The absorbance is defined as the imaginary part of the polarizability, which follows directly from the interband polarization.

The excitonic absorbance spectrum is shown in Fig. 3.7. The calculated results are in good agreement with results obtained from numerically solving the Bethe-Salpeter equation, which means that the higher-order interaction effects taken into account in the Bethe-Salpeter equation do not have a significant effect on the exciton properties. The most noticeable difference between the two is the height of the peak around 2.27 eV, which corresponds to the $2s$ state of the B exciton, which is about 50% of the peak of the $1s$ state of the B exciton in the results obtained from the Bethe-Salpeter equation whereas it is about 20% of this peak in the results obtained here. The splitting between the peaks of the $1s$ state of the A and the B exciton is similar for the three different results shown in this figure. However, both the current results and the Bethe-Salpeter equation predict that the B exciton peak is higher than the A exciton peak whereas in the experimental results the A exciton peak is more pronounced than the B exciton peak. It should be noted that the experimental absorbance was not measured up to high enough photon energies to clearly distinguish the excited states.

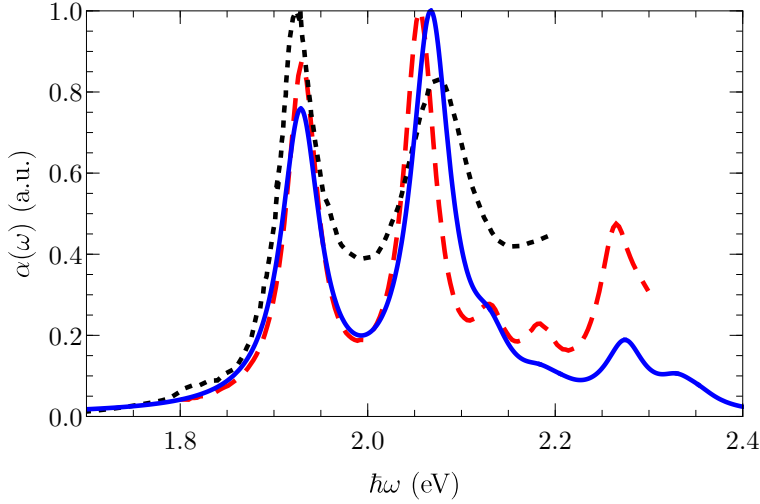


Figure 3.7: Excitonic absorbance spectrum calculated for MoS₂ on a SiO₂ substrate using a broadening of $\gamma = 25$ meV (solid, blue), compared with the numerical solution of the Bethe-Salpeter equation of Ref. [120] (dashed, red) and the experimental results of Ref. [141] (dotted, black). The two theoretical results are shifted such that they match the *A* exciton energy of the experimental results. The results are also rescaled to facilitate comparison.

3.3 Experimental measurement of the exciton binding energy

In Tables 3.1 and 3.3 numerous experimental exciton binding energies were listed. In this section the most important methods for measuring these binding energies are briefly discussed.

Charge carriers are excited from the valence band by means of a continuous wave laser operating at a fixed wavelength of about 500 nm (often 532 nm, i.e. green light) in order to ensure that the electrons reach the conduction band. The radius of the focused laser spot is of the order of a few μm . Note that charge carriers can only be excited to a state within the light cone defined by $k = E/(\hbar c)$ with E the photon energy, which gives $ka = 0.0026$ for the transition between the band extrema in MoS₂. The electrons and holes then form excitons and perform a cascade-like relaxation through energetically lower lying exciton states by means of phonon emissions. After a few ps almost all the excitons reside in the exciton ground state [135]. After a few hundred ps the excitons radiatively recombine

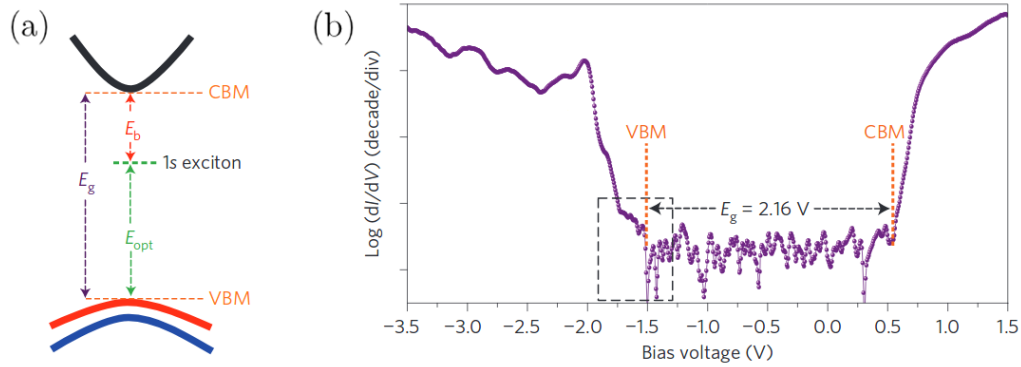


Figure 3.8: (a) Energy diagram schematically indicating the electronic band gap or transport gap (E_g), the optical band gap or transition energy (E_{opt}), and the exciton binding energy (E_b). (b) Logarithm of the scanning tunneling spectroscopy differential conductance of MoSe₂ on a bilayer graphene substrate. Both figures are taken from Ref. [124].

and emit photons with energy E_{opt} . This backscattered photoluminescence (PL) is guided to a spectrometer and detected using a CCD camera. As such the photon energy E_{opt} , also known as the optical band gap or the transition energy, can be experimentally measured.

An alternative way of obtaining the optical band gap is by doing an absorption measurement. In such an experiment a broadband radiation source is used to impinge light on the sample and the reflected radiation is collected on a CCD camera in a spectrometer. This results in an absorbance spectrum such as that shown in Fig. 3.7, which is similar to the PL spectrum [141]. In both types of experiments the energy at which the peak occurs gives the optical band gap.

Knowledge of the optical band gap is not sufficient for obtaining the exciton binding energy. As illustrated in Fig. 3.8(a) the exciton binding energy is given by $E_b = E_g - E_{opt}$, meaning that the electronic band gap E_g , also known as the transport gap, needs to be measured as well. This can be done by means of scanning tunneling spectroscopy measurements. A scanning tunneling microscope tip is placed at a fixed height above the sample and the electron tunneling current I between the tip and the sample is measured as a function of the voltage V between the tip and the sample. This allows to obtain the differential conductance dI/dV , which eliminates the dependence on the properties of the tip. The logarithm of an experimentally obtained differential conductance is shown in Fig. 3.8(b). In the band gap region the differential conductance is significantly lower and as such the

band gap can immediately be obtained as the width of this near-zero differential conductance interval.

It is also possible for excitons to bind to defects, which will be present in any realistic sample. These defect-bound excitons also lead to a peak in the PL spectrum which is located at energies lower than the free exciton peak and which at low laser power dominates over the free exciton peak [142]. As such the free exciton might be inadvertently allocated to the bound exciton peak, which would lead to an overestimation of the exciton binding energy. At high laser power, on the other hand, the free exciton peak dominates over the bound exciton peak since the number of bound excitons is limited by the number of defects whereas the number of free excitons is in theory unlimited. Note that the free excitons are not affected by the defects since the average electron-hole interparticle distance for excitons in TMDs is typically of the order of a few nm (see Table 3.4), which is less than the typical average distance between defects in realistic samples.

An alternative way of experimentally obtaining the exciton binding energy is through photocurrent spectroscopy. In this type of experiments the sample is illuminated using a broadband radiation source and the resulting photocurrent is measured as a function of the photon energy. The advantage of such measurements is that the optical and electronic band gap can be obtained simultaneously, while the disadvantage is the fact that electrical contacts need to be fabricated on the sample [122].

Excited s state excitons have much lower absorption than the ground state, which is associated with the lower value of the exciton wave function in the origin in Eq. (3.21) and can be seen in Fig. 3.7. Therefore, they can best be detected by means of reflectance contrast measurements, i.e. the difference in reflected radiation from the sample and from the substrate, both following broad band illumination, normalized by the reflected radiation from the substrate. Taking the derivative of this reflectance contrast reveals the excited s states [126]. Higher angular momentum exciton states, which do not appear in the absorbance spectrum because their wave function is zero in the origin, can be measured in two-photon absorbance experiments by means of a tunable pulsed infrared radiation source [131].

3.4 Conclusion

In this chapter excitons in monolayer TMDs were studied and a comparison was made between the single-band model, which is often used in the literature, and the multi-band model constructed in this thesis. It was shown how the latter can be

solved by exploiting the eigenstates of the exciton total angular momentum operator with which the exciton Hamiltonian commutes. It was found that the multi-band result for the exciton binding energy is lower than the single-band result, which is a consequence of the Dirac nature of the low-energy charge carriers in monolayer TMDs. This Dirac nature persists in the excitons and manifests itself in the extra components of the exciton wave function.

The spectrum of excited exciton states was calculated in the multi-band model, which confirmed the broken degeneracies between states with the same principal quantum number but different (approximate) orbital angular momentum previously found in the literature, which is a consequence of the non-local dielectric screening effects which are included in the Keldysh potential.

It was discovered that for intravalley excitons the approximate orbital angular momentum, i.e. that of the dominant wave function component, coincides with the conserved total angular momentum, whereas for intervalley excitons they differ by plus or minus one. This can be attributed to the electron and hole pseudospin which do (intravalley) or do not (intervalley) cancel with each other and leads to an intervalley exciton ground state with angular momentum $j = \tau$, with $\tau = \pm 1$ the valley index.

Furthermore, it was found that states with opposite approximate orbital angular momentum are degenerate for intravalley excitons, whereas for intervalley excitons they are not. However, this degeneracy is restored when taking opposite intervalley excitons into account, which suggests that this effect may arise as a result of coupling between the orbital angular momentum of the exciton and the intrinsic angular momentum of the exciton, which is associated with the Berry curvature. These results are in agreement with those of Ref. [119] and were extended here to higher excited states. In Ref. [120] this degeneracy was also found to be broken for intravalley excitons, which might be due to many-body Berry curvature effects [137].

The calculated values of the exciton ground state binding energy, which are of the order of half an eV in monolayer TMDs, were found to be in good agreement with theoretical results from the literature. On the other hand, significant differences were found with experimental results, for which substrate surface roughness and defect-bound excitons were proposed as possible explanations.

CHAPTER 4

Trions and biexcitons in monolayer TMDs

In this chapter excitonic complexes consisting of three (trions) and four (biexcitons) particles are studied. It is demonstrated that the FEM is unsuitable for solving the eigenvalue equations of the corresponding Hamiltonians, showing the need for another numerical solution method. Hence the stochastic variational method is introduced and used to calculate the binding energy and the structural properties of trions and biexcitons in monolayer TMDs. A short discussion is given at the end of the chapter on the experimental detection of these excitonic complexes.

4.1 A short history of trions and biexcitons

Up to now only excitons, i.e. two-particle bound states, have been considered in this thesis. However, it is possible for an exciton to bind an additional particle, either an electron or a hole, to form a stable three-particle state which is known as a trion or a charged exciton, or even for two excitons to bind to form a so-called biexciton. The binding energies, in vacuum, of both excitonic complexes were first calculated in 1946 using a variational method [143].

The stability of trions in 3D semiconductors was first predicted in 1958 [144]. Since then, they have been thoroughly studied theoretically in 3D semiconductors [145] and in semiconductor heterostructures [146–148]. However, the first experimental observation, in a CdTe/CdZnTe heterostructure, followed more than thirty years later [149]. Subsequently they have mostly been measured in GaAs/AlGaAs

heterostructures [150–153]. The trion binding energies predicted and measured in these systems, which generally increase with decreasing quantum well width for the same reason as discussed in section 1.1 for excitons, never exceed 3 meV in the absence of a magnetic field. The effects of a perpendicular magnetic field on the binding energy of excitonic complexes will be discussed in the next chapter.

Stable biexcitons in 3D semiconductors were only first suggested in 1972, predicting a binding energy of 0.13 meV for bulk GaAs [154]. Later, theoretical studies were also presented for biexcitons in GaAs/AlGaAs heterostructures, predicting a biexciton binding energy up to 2 meV [155], and in CdTe/CdZnTe heterostructures, predicting a biexciton binding energy of almost 4 meV [156]. The first experimental observation of stable biexcitons had been done in 1978 in bulk silicon [157], followed shortly by observation of biexcitons in a GaAs/AlGaAs heterostructure [158]. Both works predicted a biexciton binding energy of 1-1.5 meV. Later, however, a significantly larger binding energy of 10 meV was measured [159] in a CdTe/CdZnTe heterostructure with a quantum well width more than a factor two smaller than that of Ref. [158].

Analogous to the discussions on the exciton binding energy in section 1.1 and subsection 3.2.1, the above mentioned trion and biexciton binding energies are limited by the non-perfect 2D confinement in the quantum wells, the small effective masses of the charge carriers, and the large dielectric constant of the environment. Therefore, similar to the very strongly bound excitons discussed in the previous chapter, trions and biexcitons in monolayer TMDs are expected to exhibit binding energies of the order of tens of meVs.

4.2 Trions in monolayer TMDs: a first attempt

In this chapter only negative trions will be considered, i.e. an exciton with an additional electron. However, the two kinds of trions exhibit very similar properties and the procedure presented below can very easily be modified to describe positive trions. In the case of equal electron and hole effective masses the properties of the two types of trions are even identical out of symmetry. In the multi-band model, again starting from the two-band single-electron Hamiltonian (2.9), the trion Hamiltonian can be constructed in the basis $\mathcal{B}^{tri} = \{\mathcal{B}^{exc} \otimes |\Phi_c^{e2}\rangle, \mathcal{B}^{exc} \otimes |\Phi_v^{e2}\rangle\}$ with \mathcal{B}^{exc} the exciton basis given in section 3.1. This results in

$$H_{\sigma, s^{e2}, \tau^{e2}}^{tri} = \begin{pmatrix} H_{\sigma}^{exc} + V_1 & \mathcal{O}_{e2} \\ \mathcal{O}_{e2}^{\dagger} & H_{\sigma}^{exc} + V_2^{s^{e2}, \tau^{e2}} \end{pmatrix}, \quad (4.1)$$

with H_σ^{exc} the exciton Hamiltonian (3.1) and with

$$\mathcal{O}_{e_2} = at \left(\tau^{e_2} k_x^{e_2} - ik_y^{e_2} \right) I_4, \quad (4.2)$$

$$V_1 = \left(\frac{\Delta}{2} - V(r_{he_2}) + V(r_{e_1e_2}) \right) I_4, \quad (4.3)$$

$$V_2^{s^{e_2}, \tau^{e_2}} = \left(-\frac{\Delta}{2} + \lambda s^{e_2} \tau^{e_2} - V(r_{he_2}) + V(r_{e_1e_2}) \right) I_4, \quad (4.4)$$

with $r_{ij} = |\mathbf{r}_i - \mathbf{r}_j|$. The eigenvalue problem of this trion Hamiltonian thus leads to a set of eight coupled differential equations, which is practically near-impossible to solve. Therefore, it is better to decouple this set of equations. From the second equation of the eigenvalue problem it follows that

$$|\Psi_v^{e_2}\rangle \approx \left(E_{\sigma, s^{e_2}, \tau^{e_2}}^{tri} I_4 - V_2^{s^{e_2}, \tau^{e_2}} - D_\sigma^{exc} \right)^{-1} \mathcal{O}_{e_2}^\dagger |\Psi_c^{e_2}\rangle, \quad (4.5)$$

with $|\Psi_{c(v)}^{e_2}\rangle = \left(|\phi_{c,c,c(v)}^{e_1, h, e_2}\rangle, |\phi_{c,v,c(v)}^{e_1, h, e_2}\rangle, |\phi_{v,c,c(v)}^{e_1, h, e_2}\rangle, |\phi_{v,v,c(v)}^{e_1, h, e_2}\rangle \right)^T$ and with D_σ^{exc} the 4×4 diagonal matrix containing the diagonal elements of the exciton Hamiltonian (3.1). In this approximation, the kinetic energy of the first electron and the hole is assumed to be small compared to the band gap and the trion energy, which is a good approximation for the same reason as explained below Eq. (3.10) and because the trion energy is even larger than the exciton energy. Inserting the above relation in the first equation of the eigenvalue problem leads to

$$\begin{aligned} \left(H_\sigma^{exc} + \mathcal{O}_{e_2} \left(E_{\alpha, s^{e_2}, \tau^{e_2}}^{tri} I_4 - V_2^{s^{e_2}, \tau^{e_2}} - D_\alpha^{exc} \right)^{-1} \mathcal{O}_{e_2}^\dagger \right. \\ \left. + V_1 \right) |\Psi_c^{e_2}\rangle = E_{\sigma, s^{e_2}, \tau^{e_2}}^{tri} |\Psi_c^{e_2}\rangle. \end{aligned} \quad (4.6)$$

This eigenvalue problem is similar to the exciton eigenvalue problem, but now with additional terms on the diagonal. Therefore, this 4×4 matrix equation can be decoupled in a similar fashion as described in subsection 3.1.2 for excitons, in which it is again useful to transform to center of mass and relative coordinates (3.2) and where the conserved center of mass momentum is now assumed to be equal to zero. Going to position representation for an extra electron with $s^{e_2} \tau^{e_2} = s^{e_1} \tau^{e_1} = s^h \tau^h$, meaning that it can be optically excited simultaneously with the other electron and the hole, the resulting decoupled differential equation is given

by

$$\begin{aligned}
& \left(-\mathcal{V}(E_\beta^{tri}, r_{e_1h}, r_{he_2}) \left(\nabla_{\mathbf{r}_{e_1h}}^2 + \nabla_{\mathbf{r}_{he_2}}^2 - \nabla_{\mathbf{r}_{e_1h}} \cdot \nabla_{\mathbf{r}_{he_2}} \right) - V(r_{e_1h}) - V(r_{he_2}) \right. \\
& - \left(\frac{\partial}{\partial r_{e_1h}} \mathcal{V}(E_\beta^{tri}, r_{e_1h}, r_{he_2}) \right) \frac{\partial}{\partial r_{e_1h}} - \left(\frac{\partial}{\partial r_{he_2}} \mathcal{V}(E_\beta^{tri}, r_{e_1h}, r_{he_2}) \right) \frac{\partial}{\partial r_{he_2}} \\
& + \frac{1}{2} \left(\frac{\partial}{\partial r_{e_1h}} \mathcal{V}(E_\beta^{tri}, r_{e_1h}, r_{he_2}) \right) \frac{\partial}{\partial r_{he_2}} + \frac{1}{2} \left(\frac{\partial}{\partial r_{he_2}} \mathcal{V}(E_\beta^{tri}, r_{e_1h}, r_{he_2}) \right) \frac{\partial}{\partial r_{e_1h}} \\
& \left. + V(r_{e_1h} + r_{he_2}) + \Delta_{s^h, \tau^h} + \frac{\Delta}{2} \right) \phi_{c,v,c}^{e_1,h,e_2}(r_{e_1h}, r_{he_2}) = E_\beta^{tri} \phi_{c,v,c}^{e_1,h,e_2}(r_{e_1h}, r_{he_2}), \tag{4.7}
\end{aligned}$$

with

$$\mathcal{V}(E_\beta^{tri}, r_{e_1h}, r_{he_2}) = \frac{2a^2t^2}{E_\beta^{tri} + V(r_{e_1h}) + V(r_{he_2}) - V(r_{e_1h} + r_{he_2}) - \frac{\Delta}{2}} \tag{4.8}$$

and where β is shorthand notation for $\sigma, s^{e_2}, \tau^{e_2}$. The electron-electron interaction term depends on $|\mathbf{r}_{e_1h} + \mathbf{r}_{he_2}|$, which means that the angular parts of the equation cannot be decoupled from the radial parts. A FEM solution of a differential equation with four variables is very time consuming and uses a very large amount of computer memory. Therefore, as a rough approximation, it is assumed that $\varphi_{e_1h} = \varphi_{he_2}$ such that $|\mathbf{r}_{e_1h} + \mathbf{r}_{he_2}| = r_{e_1h} + r_{he_2}$, the accuracy of which will be checked in subsection 4.4.1. In that case, the angular part of the trion wave function is approximately of the form $\exp(ij_1\varphi_{e_1h} + ij_2\varphi_{he_2})$ and in the above differential equation j_1 and j_2 were already taken to be zero. The differential equation again has to be solved self-consistently to determine the trion energy E_β^{tri} and the component $\phi_{c,v,c}^{e_1,h,e_2}(r_{e_1h}, r_{he_2})$ of the trion wave function. The other components of the wave function can be determined from Eq. (4.5) and equations which are analogous to Eqs. (3.10) and (3.13) and which follow from decoupling the trion eigenvalue problem. The trion binding energy is given by $E_b = \Delta/2 + E_\sigma^{exc} - E_\beta^{tri}$, i.e. the difference in energy between the trion and the exciton plus a free electron.

As a comparison the trion Hamiltonian eigenvalue equation will also be solved in the single-band model, i.e. starting from the parabolic single-particle energy spectrum (2.13). Analogous to the exciton single-band differential equation (3.16), performing the transformation (3.15) and taking the center of mass momentum to

be zero results in the trion single-band differential equation

$$\left(-\frac{\hbar^2}{2\mu_\sigma} \left(\nabla_{\mathbf{r}_{e_1h}}^2 + \nabla_{\mathbf{r}_{he_2}}^2 \right) + \frac{\hbar^2}{m_h} \nabla_{\mathbf{r}_{e_1h}} \cdot \nabla_{\mathbf{r}_{he_2}} - V(r_{e_1h}) - V(r_{he_2}) + V(r_{e_1h} + r_{he_2}) \right) \psi_\beta^{tri}(r_{e_1h}, r_{he_2}) = E_\beta^{tri} \psi_\beta^{tri}(r_{e_1h}, r_{he_2}), \quad (4.9)$$

with the reduced mass μ_σ defined below Eq. (3.16). Again the approximation $|\mathbf{r}_{e_1h} + \mathbf{r}_{he_2}| = r_{e_1h} + r_{he_2}$ was made, in order to allow for a practical solution using the FEM, and $j_1 = j_2 = 0$ was taken for the angular part of the wave function. In the single-band model the trion binding energy is given by $E_b = E_\sigma^{exc} - E_\beta^{tri}$. The biexciton single-band Hamiltonian eigenvalue equation will not be given here. Their binding energy is given by $E_b = 2E_\sigma^{exc} - E_{\beta, s^{h_2}, \tau^{h_2}}^{bi}$ since they dissociate into two excitons.

It can be concluded that the trion Hamiltonian eigenvalue problem presents a few challenges, i.e. the fact that in the multi-band model it is a set of eight coupled equations and the fact that, in both the multi- and the single-band model, the angular dependence in the interaction potential needs to be neglected in order to allow for a practical solution using the FEM. For biexcitons these challenges are even more significant, i.e. the biexciton Hamiltonian eigenvalue problem is a set of sixteen coupled equations in the multi-band model and there are three angular coordinates which need to be neglected in the interaction potential. It can be expected, although this will be checked in subsection 4.4.1, that this is not a good approximation. This shows the need for another numerical method which allows to solve the trion and biexciton Hamiltonian eigenvalue equations without neglecting the angular dependences in a reasonable computation time and without needing an excessive amount of memory. This numerical method will be introduced now.

4.3 Stochastic variational method

In the stochastic variational method (SVM), which was first proposed in 1976 [160], the many-body wave function $\Psi(\mathbf{r}_1, \dots, \mathbf{r}_N)$ of an N -particle complex is expanded in a basis of size K :

$$\Psi_{S, M_S}(\mathbf{r}_1, \dots, \mathbf{r}_N) = \sum_{n=1}^K c_n \varphi_{S, M_S}^n(\mathbf{r}_1, \dots, \mathbf{r}_N), \quad (4.10)$$

where the basis functions are taken as correlated Gaussians [161, 162]:

$$\varphi_{S, M_S}^n(\mathbf{r}_1, \dots, \mathbf{r}_N) = \mathcal{A} \left(e^{-(\vec{x}^T A_n \vec{x} + \vec{y}^T A_n \vec{y})/2} \chi_{S, M_S}^n \right), \quad (4.11)$$

where \vec{x} and \vec{y} are N -dimensional vectors containing, respectively, the x - and y -components of the positions of the different particles. The matrices A_n are symmetric and positive definite and contain variational parameters. χ_{S,M_S}^n is the total spin state of the excitonic complex corresponding to the total spin S and z -component of the spin M_S , which are conserved quantities. This total spin state is obtained by adding step by step single-particle spin states. Therefore, multiple total spin states belonging to the same S and M_S value are possible, as these can be obtained by different intermediate spin states. For example, the spin state of an exciton is either a triplet state ($S = 1, M_S = 1, 0, -1$) or a singlet state ($S = 0, M_S = 0$), i.e. there is only one possible spin state associated with a certain value of (S, M_S) . Trions, however, have a total spin of either $S = 1/2$ or $S = 3/2$ and the former can be realised by either adding a third spin to the exciton singlet state or to the exciton triplet state. As such there are two possible $(S, M_S) = (1/2, 1/2)$ trion doublet states given by

$$\begin{aligned} \left| \frac{1}{2}, \frac{1}{2} \right\rangle_1 &= -\sqrt{\frac{2}{3}} |\uparrow\uparrow\downarrow\rangle + \sqrt{\frac{1}{6}} (|\uparrow\downarrow\uparrow\rangle + |\downarrow\uparrow\uparrow\rangle), \\ \left| \frac{1}{2}, \frac{1}{2} \right\rangle_0 &= \frac{1}{\sqrt{2}} (|\uparrow\downarrow\uparrow\rangle - |\downarrow\uparrow\uparrow\rangle), \end{aligned} \quad (4.12)$$

where the subscripts of the kets in the left hand sides of the equations correspond to the total spin of the exciton to which the third spin was added. In this thesis the $(S, M_S) = (0, 0)$ singlet state is considered for excitons and biexcitons and the $(S, M_S) = (1/2, 1/2)$ doublet state is considered for trions. Finally, \mathcal{A} is the antisymmetrization operator for the indistinguishable particles.

The energy of the excitonic complex is estimated by means of a stochastic trial and error procedure. First, a matrix A_1 and a spin function χ_{S,M_S}^1 are randomly generated multiple times and the variational energy is calculated using each of them. The wave function with the set of parameters that gives the lowest variational energy is then retained as the first basis function, i.e. $K = 1$. Subsequently, a new matrix A_2 and spin function χ_{S,M_S}^2 are randomly generated multiple times and the variational energy is calculated in the $K = 2$ basis consisting of the previously determined first basis function and the new trial basis function. The wave function with the set of parameters that gives the lowest variational energy is then retained as the second basis function. Following this procedure, the variational principle ensures that each addition of a new basis function guarantees a lower variational energy value and the basis size is increased until convergence of the energy value is reached.

The result is virtually exact in the limit of an infinite basis size [162, 163].

For the calculations done in this thesis, a basis size of $K = 50$ for excitons and $K = 250$ for trions and biexcitons was used, resulting in a typical energy difference between the results for a basis size of $K - 1$ and K of $0.001 \mu\text{eV}$, $0.1 \mu\text{eV}$, and $1 \mu\text{eV}$, for excitons, trions, and biexcitons, respectively. However, a better estimate for the statistical error associated with the stochastic nature of the SVM can be obtained by calculating the energy for a given excitonic complex, TMD, and substrate \mathcal{N} times and calculating the standard deviation

$$\mathcal{S} = \sqrt{\frac{1}{\mathcal{N}} \sum_{i=1}^{\mathcal{N}} (E_i - E_a)^2}, \quad \text{with} \quad E_a = \frac{1}{\mathcal{N}} \sum_{i=1}^{\mathcal{N}} E_i, \quad (4.13)$$

for the set of calculated energies E_i . For example, for excitons in WS_2 on a SiO_2 substrate (for which a binding energy of 284.0 meV is obtained, i.e. identical to the value obtained with the FEM in the single-band model listed in Table 3.1), a standard deviation of $\mathcal{S} = 0.04 \text{ meV}$ is obtained for $\mathcal{N} = 10$. For the same system and \mathcal{N} value, standard deviations of $\mathcal{S} = 0.3 \text{ meV}$ and $\mathcal{S} = 1.7 \text{ meV}$ are obtained for trions and biexcitons, respectively. Values of the same order are expected for other combinations of TMDs and substrates.

One of the major advantages of the correlated Gaussian basis functions (4.11) is the fact that the matrix elements between these basis functions of a lot of operators, including those of the Hamiltonian, can be calculated analytically. For example, the overlap of the x -dependent part of the Gaussian basis functions, i.e. the matrix element of the identity operator between basis functions with parameter matrices A and A' , is given by

$$\begin{aligned} \langle \mathbf{1} \rangle_x &\equiv S_0 = \int d\vec{x} e^{-(\vec{x}^T (A+A') \vec{x})/2} = \int d\vec{x} e^{-(\vec{x}^T U D U^T \vec{x})/2} = \int d\vec{t} e^{-(\vec{t}^T D \vec{t})/2} \\ &= \prod_{i=1}^N \int dt_i e^{-\lambda_i t_i^2/2} = \prod_{i=1}^N \sqrt{\frac{2\pi}{\lambda_i}} = \left(\frac{(2\pi)^N}{\det(A+A')} \right)^{\frac{1}{2}}, \end{aligned} \quad (4.14)$$

with U the unitary transformation matrix which transforms the matrix $A + A'$ to the diagonal matrix D with the eigenvalues λ_i of $A + A'$ on the diagonal. Because U is unitary, the absolute value of the Jacobian determinant of the coordinate transformation $\vec{t} = U^T \vec{x}$ is equal to 1. Also including the y -dependent part of the Gaussian basis functions leads to the final result $\langle \mathbf{1} \rangle = S_0^2$. The matrix element of numerous other operators can be calculated in a similar way and the results are listed in Table 7.1 of Ref. [161]. The derivation for two important operators, i.e.

the kinetic energy and the delta function, is given in appendix C. The importance of the delta function lies in the fact that a general potential can be written as

$$V\left(\sum_{k=1}^N w_k \mathbf{r}_k\right) = \int d\mathbf{r}_0 V(\mathbf{r}_0) \delta\left(\sum_{k=1}^N w_k \mathbf{r}_k - \mathbf{r}_0\right), \quad (4.15)$$

with w_k real constants. As such the expectation value of such a potential between the correlated Gaussian basis functions is reduced to that of the delta function, the result of which is proportional to $e^{-c\mathbf{r}_0^2}$ with c a constant depending on the variational parameters, as shown in appendix C. Therefore, the expectation value of the potential is known analytically as long as the integral

$$\int d\mathbf{r}_0 V(\mathbf{r}_0) e^{-c\mathbf{r}_0^2} \quad (4.16)$$

can be performed analytically. This is the case for the Keldysh potential, as shown in appendix C.

The expectation value of all the different terms in the Hamiltonian can thus be calculated analytically for a general N -particle complex. This allows for a relatively short computation time, i.e. of the order of 15 minutes, 12 hours, and 2 days for excitons, trions, and biexcitons, respectively, on a 3.60 GHz Intel Xeon E5-1650 v4 processor (calculations with different input parameters are run in parallel on different cores). However, the real gain by using the SVM lies in the very small amount of memory which is needed. For biexcitons and $K = 250$ the wave function is characterized by 3000 variational parameters which need to be stored. This compares with the FEM in which the wave function is defined by its value at n^6 different mesh points with n the number of mesh points for each coordinate. This number is already larger than 3000 for $n = 4$.

The SVM will now be used to calculate different properties of trions and biexcitons in monolayer TMDs and for trions the comparison will be made with the FEM results. These results were published in Physical Review B, partly in Ref. [115] and partly in Ref. [164]. In this thesis, and in all works in the literature, the SVM is only applied to the single-band model. In principle, however, it could also be applied to the multi-band model by using a different correlated Gaussian basis function for each of the components.

	MoS ₂	MoSe ₂	WS ₂	WSe ₂
m_e	0.47	0.55	0.32	0.34
m_h	0.54	0.59	0.35	0.36

Table 4.1: Charge carrier masses in units of m_0 for different monolayer TMDs, taken from Ref. [117].

4.4 Numerical results

4.4.1 Binding energy

In Table 4.2 the trion binding energy is shown for different monolayer TMDs and different substrates in the single-band model, obtained with both the SVM and the FEM, and in the multi-band model. For the FEM solution of the single-band model the effective masses of Ref. [81] were used whereas for the SVM the masses given in Table 4.1 were used in order to account for the small differences between the electron and hole masses. The FEM results (for both the single- and the multi-band model) were obtained by neglecting angular correlations. The calculated values are compared with other theoretical studies based on the single-band model using ground state diffusion Monte Carlo [116, 165], path-integral Monte Carlo [117], and the SVM [118], as well as experimental results. It is clear that trions in monolayer TMDs exhibit exceptionally large binding energies, i.e. an order of magnitude larger than those in semiconductor heterostructures as discussed in section 4.1. This is again due to the perfect 2D confinement, the large effective masses, and the reduced dielectric screening. For TMDs suspended in vacuum the results obtained with the multi-band model are a few meV larger than the single-band SVM results. On the other hand, for TMDs placed on a SiO₂ substrate the multi-band model results are considerably smaller than the SVM results. Furthermore, the single-band FEM results agree very badly with the SVM results, even predicting unstable trions in WS₂ on a SiO₂ substrate and in WSe₂ encapsulated by hBN. This clearly shows the importance of angular correlations in trions, which can therefore not be neglected.

The calculated SVM values differ by at most 10% with the results from the different theoretical approaches for both vacuum and SiO₂. Again, as was already the case for excitons, note that $\varepsilon_b = 3.0$ was used for SiO₂ in Ref. [117], explaining their consistently larger binding energies. Assuming $\varepsilon_b = 3.0$, an SVM binding energy of 24.9 meV, 21.6 meV, 24.0 meV, and 20.5 meV is obtained for MoS₂, MoSe₂, WS₂, and WSe₂, respectively. This is in considerably better agreement

		Substrate	Literature		This thesis		
			Theory	Experiment	SVM	FEM	MB
MoS ₂	Vacuum		33.8 [116]	-	33.4	23.1	37.9
			32.0 [117]				
			33.7 [118]				
			32 [165]				
	SiO ₂	24.7 [117]	18 ± 1.5 [141]	22.9	3.4	14.5	
MoSe ₂	Vacuum		28.4 [116]	-	27.7	21.1	32.5
			27.7 [117]				
			28.2 [118]				
			31 [165]				
	SiO ₂	22.1 [117]	30 [166]	20.3	5.3	14.2	
WS ₂	Vacuum		34.0 [116]	-	32.4	18.8	35.2
			33.1 [117]				
			33.8 [118]				
			31 [165]				
	SiO ₂	24.3 [117]	30 [167] 30 [168] 18-45 [169] 26 [170]	21.3	-1.9	9.4	
WSe ₂	Vacuum		29.5 [116]	-	28.8	18.3	32.1
			28.5 [117]				
			29.5 [118]				
			27 [165]				
	SiO ₂	21.5 [117]	30 [171] 30 [133]	19.6	0.4	10.4	
	hBN	26 [172]	32 [172]	12.4	-5.3	5.7	

Table 4.2: Negative trion binding energy (meV) for different TMD materials and different substrates in the single-band model obtained using both the SVM and the FEM and in the multi-band model (MB), compared with theoretical and experimental results from the literature. The following dielectric constants were used: $\varepsilon_b = 3.8$ and $\varepsilon_t = 1$ for SiO₂ below and vacuum above the TMD and $\varepsilon_b = \varepsilon_t = 4.4$ for encapsulating hBN. The FEM and MB results were obtained by neglecting angular correlations.

	Substrate	Literature		This thesis
		Theory	Experiment	
MoS ₂	Vacuum	22.7 [116]	-	19.0
		22.7 [117]		
		22.5 [118]		
		24 [165]		
	SiO ₂	20.3 [117]	-	14.0
Al ₂ O ₃	-	70 [173]	10.0	
		60 [174]		
MoSe ₂	Vacuum	17.7 [116]	-	15.5
		19.3 [117]		
		18.4 [118]		
		23 [165]		
	SiO ₂	17.4 [117]	-	11.3
Al ₂ O ₃	-	20 [175]	9.5	
WS ₂	Vacuum	23.3 [116]	-	19.5
		23.9 [117]		
		23.6 [118]		
		23 [165]		
	SiO ₂	20.9 [117]	65 [167] 69 [176]	14.5
WSe ₂	Vacuum	20.0 [116]	-	15.9
		20.7 [117]		
		20.2 [118]		
		20 [165]		
	SiO ₂	18.1 [117]	52 [177]	12.5
Al ₂ O ₃	19.8 [178]	18.3 ± 0.5 [178]	5.4	

Table 4.3: Biexciton binding energy (meV) for different TMD materials and different substrates in the single-band model obtained using the SVM, compared with theoretical and experimental results from the literature. The following dielectric constants were used: $\epsilon_b = 3.8$ ($\epsilon_b = 10$) and $\epsilon_t = 1$ for SiO₂ (Al₂O₃) below and vacuum above the TMD.

with the results of Ref. [117]. There is a very small difference, i.e. at most 1.4 meV, between the calculated SVM values and the SVM results of Ref. [118]. The latter used the equal electron and hole effective masses of Ref. [81] and it can thus be concluded that the small difference in the electron and hole masses has a very limited effect on the trion binding energy. In general, the calculated SVM values underestimate the experimental results by a factor of about 2/3, except for MoS₂.

In Table 4.3 the biexciton binding energy is shown for different monolayer TMDs and different substrates in the single-band model obtained with the SVM. The results are compared with the same theoretical studies as for trions, as well as with experimental results. The theoretically predicted biexciton binding energies are smaller than the corresponding trion binding energies but are still considerably larger than the biexciton binding energies in semiconductor heterostructures as discussed in section 4.1. The calculated values are about 15-20% smaller than the other theoretical results for vacuum. For SiO₂ the difference is slightly larger, which is again due to the smaller dielectric constant which was used in Ref. [117]. The reason for the significant difference with the theoretical value for Al₂O₃ is not immediately clear. Very large biexciton binding energies, which can be up to a factor of 2-4 larger than predicted by theory, have been found in multiple experiments. However, there is some discussion on whether these are truly biexcitons which are being measured. It was argued in Ref. [118] that this disagreement is due to a misinterpretation of the experimental results and that in experiment the particular biexciton peak is in fact the one from an excited state of the biexciton. In Ref. [179], on the other hand, it was demonstrated that these experimental results can be related to the coupling of excitons with intervalley plasmons.

One possible explanation for the consistently larger experimental trion and biexciton binding energies as compared to theoretical predictions is local potential fluctuations as a result of the substrate. These can be modeled by means of a circular potential well $V(r) = V_0\Theta(r - a_w)$, with V_0 (a_w) the height (radius) of the potential well, acting on all the particles. In Fig. 4.1 the negative trion and biexciton binding energies are shown as a function of the potential well radius for a fixed potential height. The binding energy increases with decreasing potential well radius due to the confinement for both excitonic complexes, with the effect being slightly more pronounced for biexcitons. The binding energies of both complexes are approximately doubled at a well radius of 5 nm as compared to the absence of a potential well.

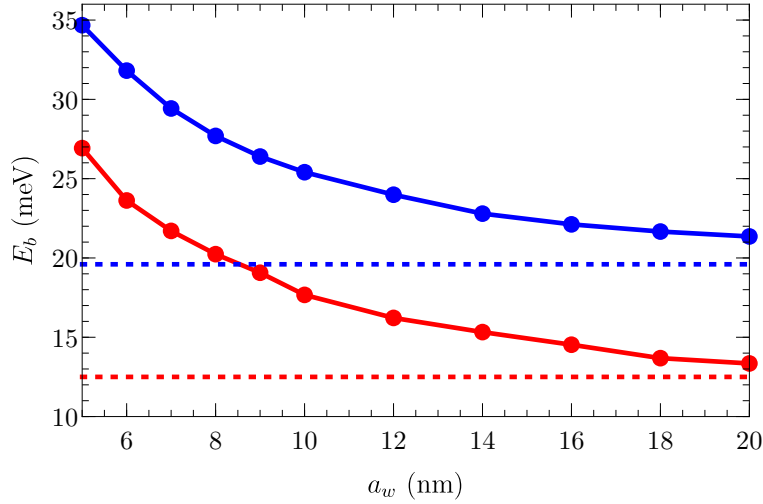


Figure 4.1: Negative trion (blue) and biexciton (red) binding energy calculated as a function of the potential well radius for WSe₂ on a SiO₂ substrate. The height of the circular potential well is $V_0 = 300$ meV. The dotted lines indicate the binding energy in the absence of a potential well.

4.4.2 Wave function

In Fig. 4.2 the different components of the multi-band trion ground state wave function are shown. Similar to the case of the exciton shown in Fig. 3.5, there is now one dominant component which represents a trion consisting of two electrons in the conduction band and a hole in the valence band, and three considerably smaller components representing a trion in which one of the particles is in its sea, i.e. an electron in the valence band or a hole in the conduction band. In Fig. 4.2, only these four largest components are shown. There are however four more components which are even smaller, i.e. three components representing a trion in which two of the particles are in their sea and one component representing a trion in which all three particles are in their sea.

The wave function as a function of the hole x -coordinate when its y -coordinate and the two electrons are fixed is shown in Fig. 4.2(a). This shows that the hole localizes equally around the two electrons. The component $\phi_{c,c,c}^{e_1,h,e_2}$ of the wave function also shows extrema around the electron positions whereas the main contribution of the other two non-dominant components is in between the two electrons. Furthermore, the SVM wave function shows qualitatively the same behavior as the dominant component of the multi-band wave function and as the single-band

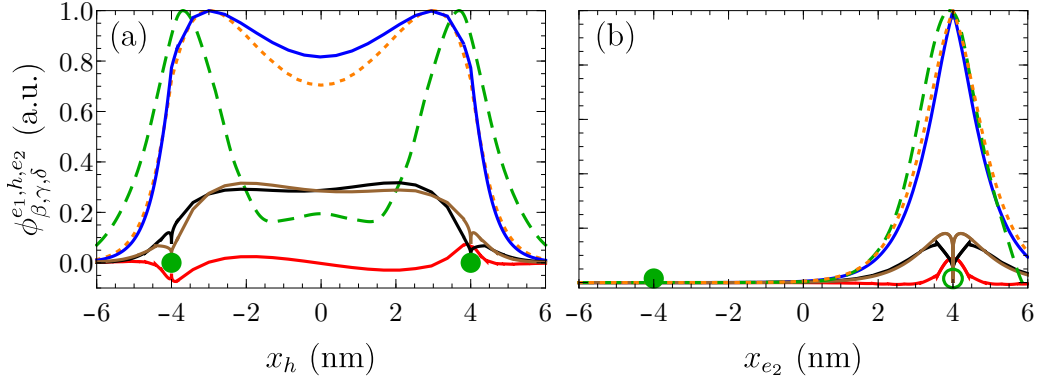


Figure 4.2: (a) Different components ($\beta = c, \gamma = v, \delta = c$: blue curve, $\beta = c, \gamma = c, \delta = c$: red curve, $\beta = c, \gamma = v, \delta = v$: black curve, $\beta = v, \gamma = v, \delta = c$: brown curve) of the ground state wave function for trions in MoS₂ suspended in vacuum as a function of the hole coordinate x_h for $y_h = 0$ and for fixed electrons calculated in the multi-band model. The dashed green curve and dotted orange curve are the single-band SVM and FEM result, respectively. (b) Same as (a) but now as a function of the electron coordinate x_{e_2} for $y_{e_2} = 0$ and for a fixed electron and hole. Circles and dots indicate the position of holes and electrons, respectively. All the wave functions are scaled to their respective maxima.

FEM wave function but there are substantial quantitative differences. These differences are a consequence of the fact that the dependence of the wave function on the angular coordinates was neglected when using the FEM. In Fig. 4.2(b) the wave function is shown as a function of the electron x -coordinate when its y -coordinate and the hole and the other electron are fixed, which shows that the electron localizes around the hole. The other components show a similar behavior as the dominant component. In this case the agreement between the SVM and FEM wave functions is better than in the case of fixed electrons.

The dominant component of the ground state wave function and the second excited state wave function is shown as a function of the relative coordinates in Fig. 4.3. The ground state wave function has a single maximum at $r_{e_1h} = r_{he_2} = 0$, meaning that the three particles form one symmetric system with comparable average interparticle distances between all the particles. The calculated interparticle distances using Eq. (3.19) are $\langle r_{eh} \rangle = 0.96$ nm and $\langle r_{ee} \rangle = 1.40$ nm, yielding a ratio of $\langle r_{eh} \rangle / \langle r_{ee} \rangle = 0.69$. The second excited state however has two maxima: one at $r_{e_1h} = 0$ and $r_{he_2} \approx 3$ nm and one at $r_{e_1h} \approx 3$ nm and $r_{he_2} = 0$. This means that the structure of the trion is now given by an exciton, consisting of one of the

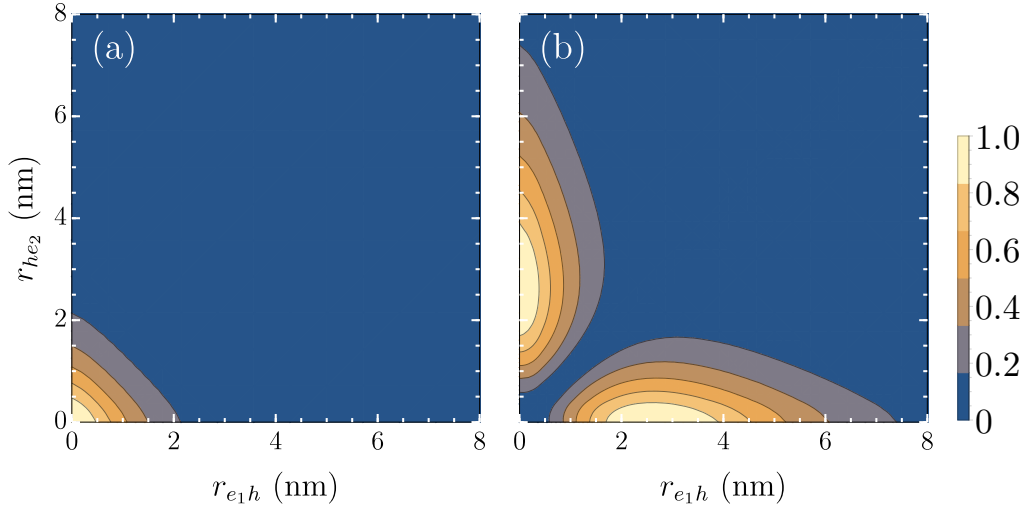


Figure 4.3: Dominant component $\phi_{c,v,c}^{e_1,h,e_2}(r_{e_1h}, r_{he_2})$, scaled to its maximum, of the ground state (a) and second excited state (b) wave function for trions in MoS₂ suspended in vacuum as a function of the relative coordinates calculated in the multi-band model.

electrons and the hole, with the additional electron circling around it. In this case Eq. (3.19) gives $\langle r_{eh} \rangle = 2.31$ nm and $\langle r_{ee} \rangle = 3.81$ nm. However, since the two electrons are identical, this implies that $\langle r_{eh} \rangle$ is the average of the average distance between the hole and the inner electron and the average distance between the hole and the outer electron. Approximating the latter by the average electron-electron distance leads to an average distance between the hole and the inner electron of $\langle r_{eh}^{in} \rangle = 0.80$ nm. This gives $\langle r_{eh}^{in} \rangle / \langle r_{ee} \rangle = 0.21$, i.e. the second excited state is more asymmetric than the ground state.

The biexciton wave function is shown in the next chapter.

4.5 Experimental measurement of the trion and biexciton binding energy

In this section it will be explained how the experimental trion and biexciton binding energies listed in Tables 4.2 and 4.3 can be measured.

Trions are typically measured in monolayer TMDs placed on a thin substrate, for example 300 nm of SiO₂, which in turn rests on a heavily doped silicon sub-

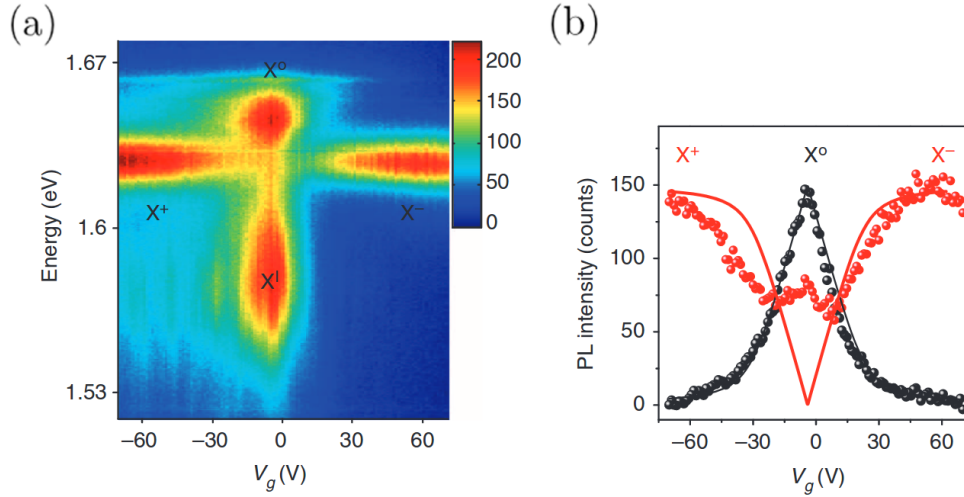


Figure 4.4: (a) PL spectrum of MoSe₂ on a SiO₂ substrate as a function of the back gate voltage. The exciton (X^0), positive and negative trion (X^+ and X^-), and impurity trapped exciton (X^I) are indicated on the figure. (b) Exciton and trion peak intensity as a function of the back gate voltage. Solid lines are fits to the experimental results. Both figures are taken from Ref. [166].

strate. Furthermore, electron beam lithography is used to fabricate source and drain contacts which are grounded. Applying a back gate potential to the doped silicon then allows to electrostatically dope the monolayer TMD. Measuring the PL spectrum, as described in section 3.3, for a range of back gate voltages leads to a result such as that shown in Fig. 4.4(a). The trion binding energy is simply given by the difference between the exciton peak energy and the trion peak energy. Therefore, the value of the band gap does not need to be known and thus no scanning tunneling spectroscopy measurements are necessary. This removes an element of uncertainty from the experiment and might help explain why there is less discrepancy between different experimentally obtained trion binding energies for the same system as compared to between different experimentally obtained exciton binding energies. Furthermore, the results of Fig. 4.4(a) can be explained as follows.

When there are an equal number of electrons and holes, which is the case when optically exciting electrons from the valence to the conduction band, the energetically most favorable situation is that in which all of these charge carriers pair up and form excitons. Therefore, in this case little to no trions will be present in the

system. When there is an excess of one of the charge carriers, however, the energetically most favorable situation is that in which all the minority charge carriers pair up with one of the majority charge carriers to form excitons, and the remaining majority charge carriers are bound by the excitons to form trions. An excess of electrons (holes) leads to the formation of negative (positive) trions. When the number of majority charge carriers is less than twice the number of minority charge carriers there will be a coexistence of excitons and trions because not all excitons will be able to bind an additional particle. When there are more than twice as many majority charge carriers as compared to minority charge carriers all excitons are able to bind an additional particle to form a trion and as a result little to no excitons will be present in the system.

This qualitative picture can be confirmed by measuring the intensity of the exciton and trion peaks, which is a measure of the number of excitons and trions in the system, as a function of the back gate voltage, as shown in Fig. 4.4(b). This indicates that the number of excitons decreases with increasing absolute value of the gate voltage, whereas the number of trions increases such that the sum of the two is approximately constant. The residual trions at zero gate voltage are due to a background electron density which can be attributed to the large contact resistance of the sample preventing the carrier concentration from reaching equilibrium on the experimental time scale. This effect should be eliminated by improved contact technologies [166].

The formation of biexcitons, i.e. the binding of two excitons, is a process which becomes increasingly important with increasing exciton density. In optical experiments this corresponds to high laser intensities and biexcitons have indeed been reported in standard PL measurements under these conditions [167, 177]. However, as mentioned in section 4.4, there is some debate on whether these PL features, which occur at energies lower than the trion energy, are truly stemming from biexcitons.

On the other hand, biexcitons have also been observed in pump-probe experiments [173, 176, 178] in which the output of a laser is split into two pulses with a controllable time delay between them. Tuning the first pulse (the pump pulse) to the exciton energy and measuring the differential absorption as a function of the energy of the second pulse (the probe pulse) and the time difference between the two pulses then leads to a result such as that shown in Fig. 4.5. The differential absorption, i.e. the difference in absorption between the pump and the probe pulse, is negative for excitons and trions because these states are partly saturated due to the pump pulse and are therefore less likely to absorb the probe pulse. For the biexciton, however, the differential absorption is positive because the absorption of

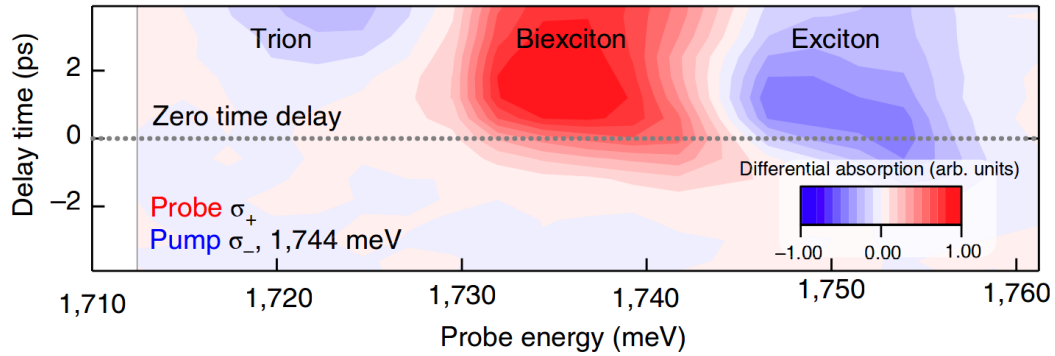


Figure 4.5: Differential absorption for WSe₂ on a Al₂O₃ substrate obtained by means of a pump-probe measurement as a function of the probe pulse energy and the time difference between the pump and the probe pulse for a fixed pump pulse energy of 1.744 eV. Figure taken from Ref. [178].

the probe pulse leads to a transition from two excitonic states to a biexcitonic state.

Both in standard PL and in pump-probe experiments the biexciton peak is associated with a transition between an exciton and a biexciton state and as such the peak energy gives the difference between the exciton and biexciton energy. Therefore, the biexciton binding energy, which is given by the difference between two times the exciton energy and the biexciton energy, can be obtained as the difference between the exciton peak energy and the biexciton peak energy. In Fig. 4.5 the biexciton peak is found between the exciton and trion peaks, meaning that the biexciton binding energy is found to be smaller than the trion binding energy.

4.6 Conclusion

In this chapter trions and biexcitons in monolayer TMDs were studied. An attempt was made to calculate the trion binding energies in the single-band model using the FEM by neglecting angular correlations (a full solution being practically infeasible), but comparison with theoretical results from the literature showed that this is not a good approximation. Therefore, the SVM based on correlated Gaussian basis functions was introduced and used to calculate the trion and biexciton binding energies for different monolayer TMDs and different substrates and very large values were found, i.e. up to 30 meV and up to 20 meV for trions and biexcitons, respectively. Good agreement was obtained with other theoretical studies and reasonably good agreement was found with experimental results for trions. For

biexcitons there are very large differences with experimental results but it was explained that this may be the consequence of misinterpretation of the experimental results [118, 179]. It was also shown that the trion and biexciton binding energies can be approximately doubled by adding in-plane confinement to the system.

CHAPTER 5

Magnetic field effects on excitonic complexes in monolayer TMDs

In this chapter the presence of a uniform magnetic field is considered and its effect on excitonic complexes in monolayer TMDs is investigated. For excitons the Hamiltonian in the presence of a perpendicular magnetic field is constructed in the four-band model and the corresponding eigenvalue equation is solved numerically in order to obtain the exciton Landau level spectrum. Next, it is shown how so-called dark excitons, which brighten as a result of an in-plane magnetic field, exhibit a strong valley Zeeman effect when applying a tilted magnetic field. Finally, the SVM is used to study the effects of a perpendicular magnetic field on trions and biexcitons.

5.1 Exciton Landau levels

The presence of a perpendicular magnetic field again needs to be taken into account by means of the Peierls substitution $\mathbf{\Pi} = \mathbf{k} - q\mathbf{A}/\hbar$, leading to the magnetic electron Hamiltonian $H_{s,\tau}^{e,q}(\mathbf{\Pi})$ and hole Hamiltonian $H_{s,\tau}^{h,q}(\mathbf{\Pi}) = -H_{-s,-\tau}^{e,-q}(-\mathbf{\Pi})$. In this chapter, the symmetric gauge $\mathbf{A} = (-By/2, Bx/2, 0)^T$ is chosen for the vector potential. As a result, the components of the center of mass momentum are no longer good quantum numbers and, similar to the discussion in subsection 3.1.2, the exciton Hamiltonian eigenvalue equation will again have to be decoupled in or-

der to separate the angular part from the radial part, even though the total exciton angular momentum operator (3.4) still commutes with the (magnetic) Hamiltonian. Furthermore, as discussed in subsection 2.2.4, the spin Zeeman effect and the Zeeman effect due to the orbital angular momentum m of the single-particle states around their atomic sites, i.e. $m = 0$ and $m = 2\tau$ for conduction and valence band states, respectively, also needs to be taken into account explicitly. Following the same procedure as explained in subsection 3.1.2 leads to the decoupled equation

$$\begin{aligned} & \left(\Pi_-^e \left(\frac{1}{g^\sigma(E_\sigma^{exc}, r_{eh}) - \lambda_v \beta} \Pi_+^e \right) + \Pi_-^h \left(\frac{1}{g^\sigma(E_\sigma^{exc}, r_{eh}) - \lambda_c \beta} \Pi_+^h \right) \right) |\phi_{c,v}^{e,h}\rangle \\ &= \frac{g^\sigma(E_\sigma^{exc}, r_{eh}) - \Delta_\sigma}{a^2 t^2} |\phi_{c,v}^{e,h}\rangle, \end{aligned} \quad (5.1)$$

with $\Pi_\pm^j = \tau^j \Pi_x^j \pm i \Pi_y^j$, $\beta = s^e \tau^e - s^h \tau^h$, $g^\sigma(E_\sigma^{exc}, r_{eh}) = E_\sigma + V(r) - (s^e + s^h) \mu_B B - 2\tau^h \mu_B B$, $\Delta_\sigma = \Delta + \lambda_c s^e \tau^e - \lambda_v s^h \tau^h$, and where $|\phi_{c,v}^{e,h}\rangle$ is again the component of the exciton eigenstate representing an exciton consisting of an electron in the conduction band and a hole in the valence band. It was again assumed that the electron and hole kinetic energies are small compared to the band gap and the exciton energy. Switching to position representation, transforming to center of mass and relative coordinates (3.2), and taking $\beta = 0$, $\lambda_c = 0$, and $\lambda_v = \lambda$ eventually leads to the differential equation

$$\begin{aligned} & \left((s^e + s^h) \mu_B B + 2\tau^h \mu_B B - \frac{2a^2 t^2}{g^\sigma(E_\sigma^{exc}, r)} \left(\frac{\partial^2}{\partial r^2} + \frac{1}{r} \frac{\partial}{\partial r} + \frac{1}{r^2} \frac{\partial^2}{\partial \varphi_r^2} \right. \right. \\ & + \frac{1}{4} \frac{\partial^2}{\partial R^2} + \frac{1}{4} \frac{1}{R} \frac{\partial}{\partial R} + \frac{1}{4} \frac{1}{R^2} \frac{\partial^2}{\partial \varphi_R^2} - \frac{1}{16l_B^4} (r^2 + 4R^2) + \frac{i}{2l_B^2} \left(\frac{\partial}{\partial \varphi_r} + \frac{\partial}{\partial \varphi_R} \right) \\ & - \left. \frac{\tau^e + \tau^h}{2l_B^2} \right) - a^2 t^2 \left(\frac{\partial}{\partial r} \frac{1}{g^\sigma(E_\sigma^{exc}, r)} \right) \left(2 \frac{\partial}{\partial r} + i \frac{\tau^e + \tau^h}{r} \frac{\partial}{\partial \varphi_r} - (\tau^e + \tau^h) \frac{r}{4l_B^2} \right. \\ & + \delta_{\tau^h, -\tau^e} \tau^h \cos(\varphi_R - \varphi_r) \left(\frac{R}{l_B^2} - i \tan(\varphi_R - \varphi_r) \frac{\partial}{\partial R} - \frac{i}{R} \frac{\partial}{\partial \varphi_R} \right) \left. \right) \\ & - V(r) + \Delta - \lambda s^h \tau^h \Big) \phi_{c,v}^{e,h}(r, R, \varphi_r, \varphi_R) = E_\sigma^{exc} \phi_{c,v}^{e,h}(r, R, \varphi_r, \varphi_R). \end{aligned} \quad (5.2)$$

There are now three terms which only appear for intravalley excitons and not for intervalley excitons and which prevent the equation from being separable into an angular and a radial part. These terms are small because they are related to magnetic field effects and it can again be argued that they can be neglected because

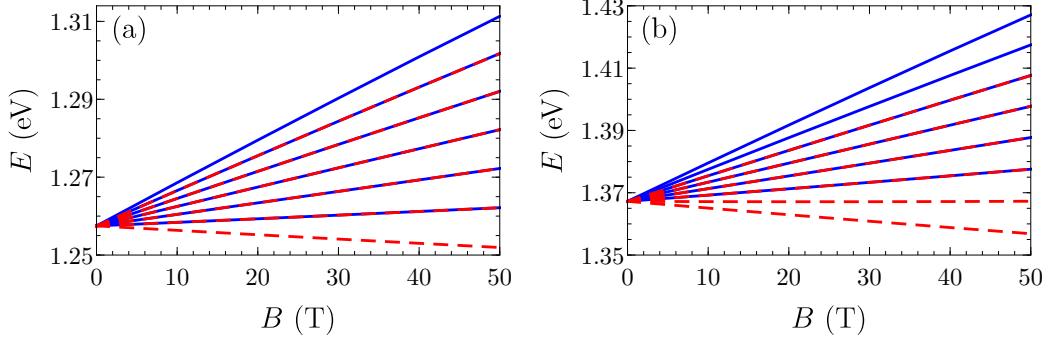


Figure 5.1: Six lowest Landau levels of the intravalley ($\tau^e = -\tau^h = 1$) $2p$ state (a) and $3d$ state (b) calculated for excitons in MoS_2 suspended in vacuum. Solid blue (dashed red) lines indicate positive (negative) relative angular momentum states.

they will only contribute in second order perturbation theory, similar to the discussion below Eq. (3.14), where they now only couple states whose relative (center of mass) angular momentum quantum numbers differ by ± 1 (∓ 1). It is therefore assumed that the angular part of the wave function is given by $\exp(ij_r\varphi_r + ij_R\varphi_R)$, with j_r and j_R integer quantum numbers. Furthermore, the terms corresponding to the magnetic angular momentum (i.e. the last one on the second line of the equation) and the Zeeman effect related to the intrinsic magnetic moment of the individual Bloch particles (2.24) (i.e. the first one on the third line of the equation) can now be distinguished.

Solving the above differential equation leads to discrete energy levels, i.e. the Landau levels, which depend on a total of four integer indexes, i.e. the principal and angular quantum numbers $n_R \geq 0$ and j_R ($n_r > 0$ and j_r) associated with the center of mass (relative) degree of freedom. The Landau levels for the exciton $2p$ and $3d$ states of MoS_2 are shown in Fig. 5.1. The Landau levels show a linear behavior as a function of the magnetic field strength and correspond qualitatively to the Landau levels of a 2D charged Schrödinger particle, i.e. [180]

$$E_\sigma^{exc} \simeq \left(n_R + \frac{j_R + |j_R|}{2} + \frac{1}{2} \right) \hbar\omega_c, \quad (5.3)$$

with $\omega_c = 2eB/M$ the center of mass cyclotron frequency with M the total exciton mass (3.17). This means that for each n_R the corresponding Landau levels are infinitely degenerate for all $j_R \leq 0$ and that for each n_R and j_R all the states with quantum numbers $(n_R + q, j_R - q)$, with q an integer for which $n_R + q \geq 0$ and $j_R - q \geq 0$, are degenerate. Note that some of the lowest Landau levels decrease as

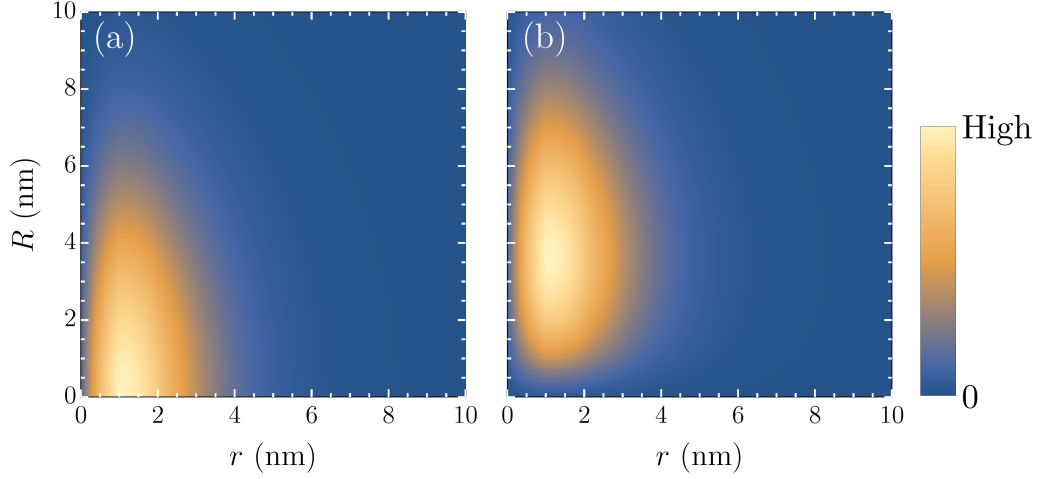


Figure 5.2: Dominant component of the intravalley ($\tau^e = -\tau^h = 1$) $2p$ state $n_R = 0$ wave function for the degenerate states with $(j_r, j_R) = (1, 0)$ (a) and $(j_r, j_R) = (-1, 1)$ (b) calculated for excitons in MoS₂ suspended in vacuum in the presence of a magnetic field of $B = 50$ T.

a function of the magnetic field, which is a consequence of the Zeeman effect due to the orbital angular momentum of the single-particle states around their atomic sites. Furthermore, the magnetic field breaks the degeneracy between states with opposite relative angular momentum $\pm j_r$, which is to be expected. However, there is still a degree of degeneracy in the relative angular momentum quantum number in the sense that Landau level number k of the state with relative angular momentum j_r is degenerate with Landau level number $k + j_r$ of the state with opposite relative angular momentum $-j_r$. As a result, only the lowest $|j_r|$ Landau levels of the state with negative relative angular momentum are non-degenerate with the Landau levels of the state with opposite relative angular momentum. This is a remarkable result since it is not immediately clear from Eq. (5.2) that this should be the case.

The exciton wave functions of two degenerate states of which both the relative and the center of mass angular momentum quantum numbers are different are shown in Fig. 5.2. The wave function in Fig. 5.2(a) shows s -like behavior as a function of the center of mass coordinate whereas the wave function in Fig. 5.2(b) shows p -like behavior. Both wave functions show p -like behavior as a function of the relative coordinate. This also shows that, even for a high magnetic field strength of 50 T, the exciton wave functions are more localized as a function of the relative coordinate as compared to the center of mass coordinate.

Note that the exchange interactions for p and d states are expected to be negligible since these are proportional with the value of the exciton wave function squared in the relative coordinate origin [120]. Therefore, it is to be expected that the inclusion of exchange interaction effects would have little to no effect on the results presented here. For s states the slopes of the Landau levels are altered by the inverse of the correction factor discussed in subsection 3.2.3.

The results presented in this section were published in Physical Review B [136]. In principle it should be possible to measure these exciton Landau levels experimentally by means of photoluminescence experiments. However, due to the small energy separation between the different Landau levels, high magnetic field strengths, high laser powers, and low temperatures would be needed to try and resolve the different states. Landau level-like features were found in Ref. [127], although the origin of these features was not discussed.

5.2 Strong valley Zeeman effect of dark excitons in a tilted magnetic field

5.2.1 Influence of the different Zeeman effects on the exciton energies

As mentioned in subsection 2.2.4, a perpendicular magnetic field breaks time-reversal symmetry and as such lifts the degeneracy between the K and K' valley, as can be seen from the Landau level spectrum shown in Fig. 2.6. Aside from leading to Landau quantization, however, a magnetic field also leads to Zeeman shifts in the energy spectrum. As discussed earlier, there are three types of Zeeman effects in monolayer TMDs: the Zeeman effect associated with the angular momentum of the atomic orbital states (which will be referred to in this section as the orbital Zeeman effect), the spin Zeeman effect, and the Zeeman effect related to the intrinsic magnetic moment of the individual Bloch particles (2.24) (which will be referred to in this section as the Bloch Zeeman effect). They are schematically depicted in Fig. 5.3(a). The spin and Bloch Zeeman effects do not influence the energy gap between states with the same spin and valley indexes. The orbital Zeeman effect, however, decreases (increases) the energy gap in the K (K') valley by an amount of $2\mu_B B_z$. As a result, the exciton transition energy, which is measured in PL experiments and scales with the band gap, is different in the two valleys as well. Due to the circular dichroism in monolayer TMDs this means that the exciton resonances in the PL spectra for left and right circularly polarized light shift from each other

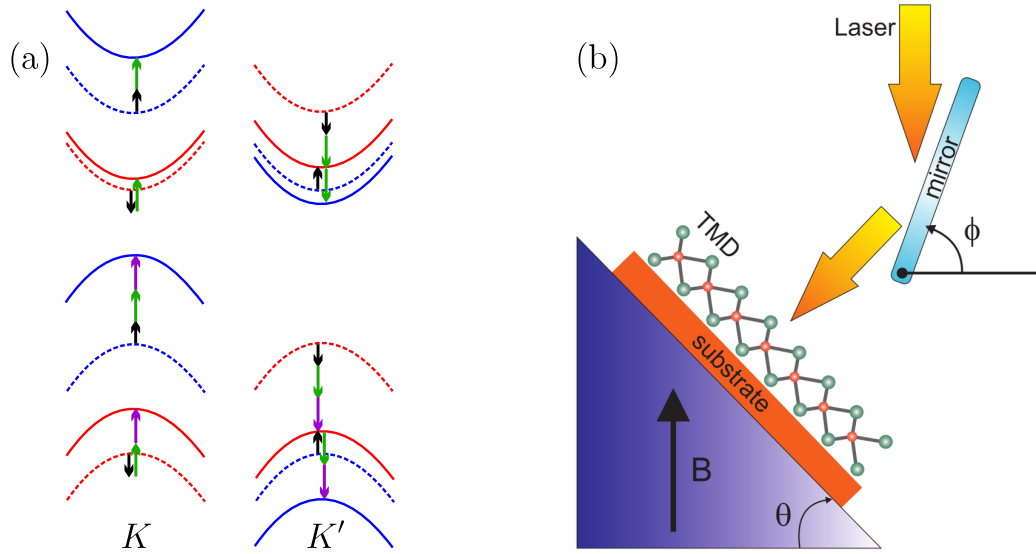


Figure 5.3: (a) Schematic representation of the energy bands of tungsten-based monolayer TMDs in the absence (dashed) and presence (solid) of a perpendicular magnetic field. Landau levels are not shown here. Blue and red curves are spin up and spin down bands, respectively. The black, purple, and green arrows indicate the effect of the spin, orbital, and Bloch Zeeman effect, respectively. (b) Schematic illustration of an experimental setup for studying the effects of a tilted magnetic field on the optical properties of a TMD monolayer.

in the presence of a perpendicular magnetic field by an amount of $4\mu_B B_z$. This is referred to in the literature as the exciton valley Zeeman effect and has indeed been experimentally observed in monolayer TMDs [127, 181–185].

Depending on the relative sign of the spin-orbit couplings in the conduction and valence bands in monolayer TMDs, the constituent electron and hole of the lowest-energy exciton can be located in energy bands which either have the same spin or opposite spin. Since optical transitions conserve spin, the former are referred to as *bright excitons* while the latter are known as *dark excitons*. Theoretical studies predict that $\lambda_c < 0$ for molybdenum-based TMDs and $\lambda_c > 0$ for tungsten-based TMDs [60, 63, 186, 187], as was shown in Table 2.1. Since $\lambda_v > 0$ for all monolayer TMDs, the lowest-energy *A* exciton in tungsten-based TMDs is dark. As discussed in subsection 2.2.4, an in-plane magnetic field, aside from leading to small additional shifts in the energy bands, couples the different spin states and as a result leads to a non-zero amplitude for previously forbidden interband transitions

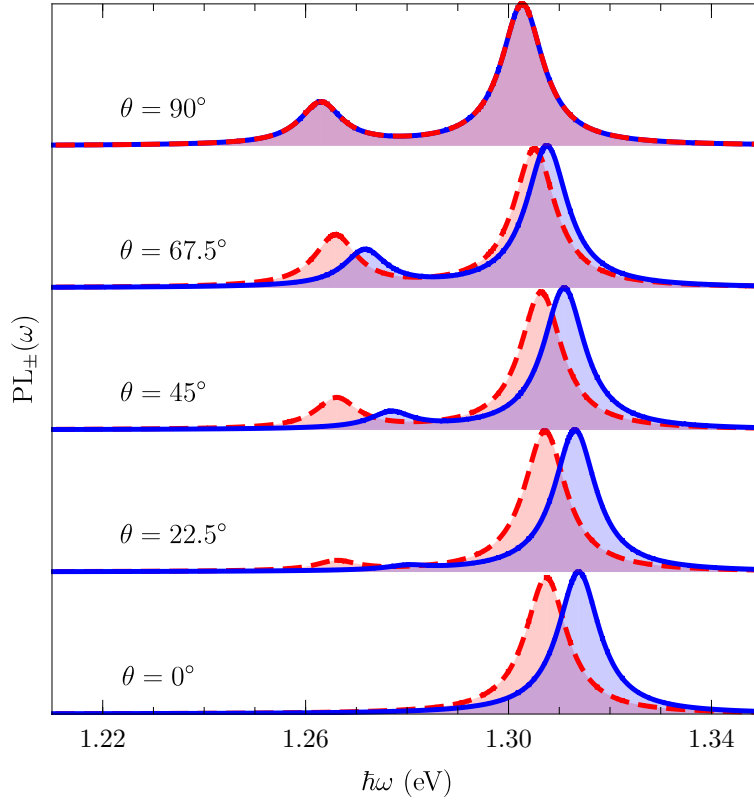


Figure 5.4: Excitonic PL spectra calculated for WS_2 on a SiO_2 substrate for right (solid, blue) and left (dashed, red) circularly polarized light for different tilt angles of the sample in the presence of a magnetic field of 30 T. A broadening of $\gamma = 5$ meV was used.

(2.31). This causes the dark excitons to *brighten* and as such leads to additional peaks in the PL spectrum, which was indeed observed experimentally [76].

Fig. 5.3(a) shows that the spin Zeeman effect leads to an additional increase (decrease) of $2\mu_B B_z$ of the energy gap between the highest valence band and the conduction band with opposite spin in the K (K') valley. The Bloch Zeeman effect further adds to this difference in size of the energy gap since it is slightly stronger for states with $s\tau = 1$ as compared to states with $s\tau = -1$, as can be seen from Eq. (2.24). Therefore, in a tilted magnetic field the peaks in the PL spectrum due to these brightened dark excitonic states will also split between the two circular polarizations of the laser and this splitting is expected to be more than twice as

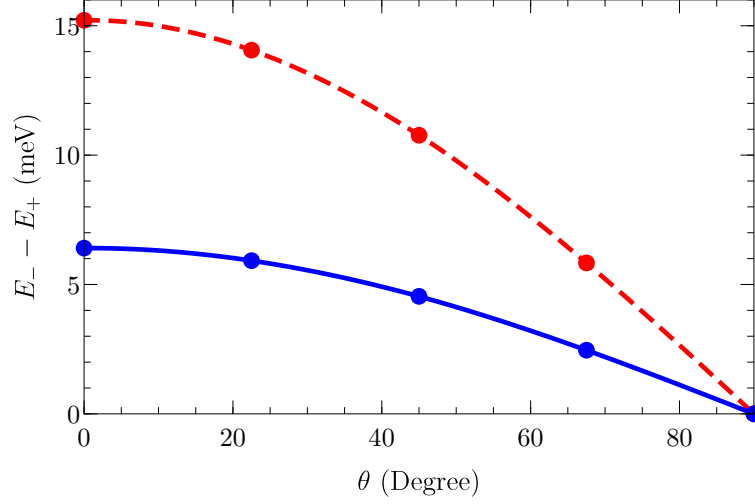


Figure 5.5: Splitting of the bright (solid, blue) and dark (dashed, red) excitonic peaks in the PL spectrum calculated for WS_2 on a SiO_2 substrate in the presence of a magnetic field of 30 T as a function of the tilt angle of the sample.

large as the splitting between the bright exciton peaks. For materials with $\lambda_c > 0$, i.e. tungsten-based TMDs, the dark A exciton energy is lower than the bright A exciton energy and therefore these resonances can be detected in the PL spectrum as their intensity is further thermally increased by a factor $\exp(\Delta E_{bd}/(k_B T))$, with ΔE_{bd} the difference between the bright and the dark exciton energy. A possible experimental setup to measure this effect is shown in Fig. 5.3(b). The magnetic field is oriented along the z -direction and the sample can be tilted over an arbitrary angle θ . The mirror should be tilted over an angle $\phi = (\pi - \theta)/2$ in order to have perpendicular incidence of the laser beam which is pointed along the z -direction.

5.2.2 PL spectrum in a tilted magnetic field

It will now be investigated how these different Zeeman effects and brightenings of dark excitons manifest themselves in the PL spectrum in different monolayer TMDs in the presence of a tilted magnetic field. The PL spectrum is calculated by adding a factor $\exp(-E_j/(k_B T))$ to each term in the expression of the absorbance spectrum (3.21) in order to take into account thermalization effects which occur between the formation and the recombination of the excitons. The exciton energies and wave functions, which are needed to obtain the PL spectrum, are calculated

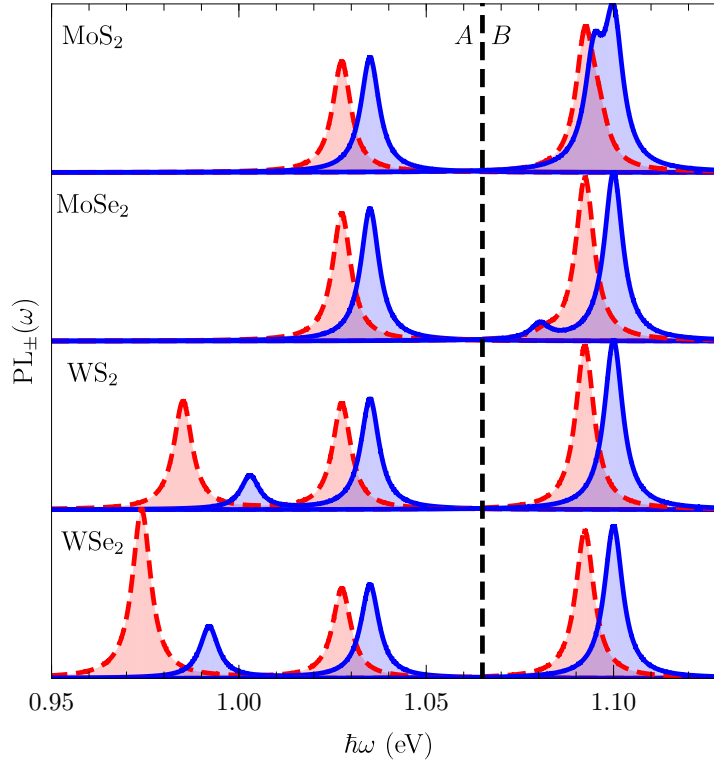


Figure 5.6: Excitonic PL spectra for right (solid, blue) and left (dashed, red) circularly polarized light calculated for different TMD monolayers on a SiO_2 substrate with tilt angle $\theta = 45^\circ$ in the presence of a magnetic field of 50 T. A broadening of $\gamma = 3$ meV was used. Note that for the A and the B exciton the bright peaks in the right circularly polarized PL spectra of the different materials have been artificially aligned at 1.035 eV and 1.1 eV, respectively, to facilitate comparison.

from a differential equation, similar to Eq. (5.2), derived from Eq. (5.1) for the more general case $\beta \neq 0$. The results presented in this section were published in Physical Review B Rapid Communication [188].

The excitonic PL spectrum of WS_2 is shown for different tilt angles in Fig. 5.4. The results clearly show the above predicted effects, i.e. the splitting of the dark exciton peaks is more than twice as large as compared to the splitting of the bright exciton peaks, which should be detectable experimentally. However, although the splitting of the dark exciton peak increases as the tilt angle decreases, the intensity of the dark exciton peaks decreases as well, making them more difficult to observe. Therefore, this effect can be best measured at intermediate tilt angles. The splitting

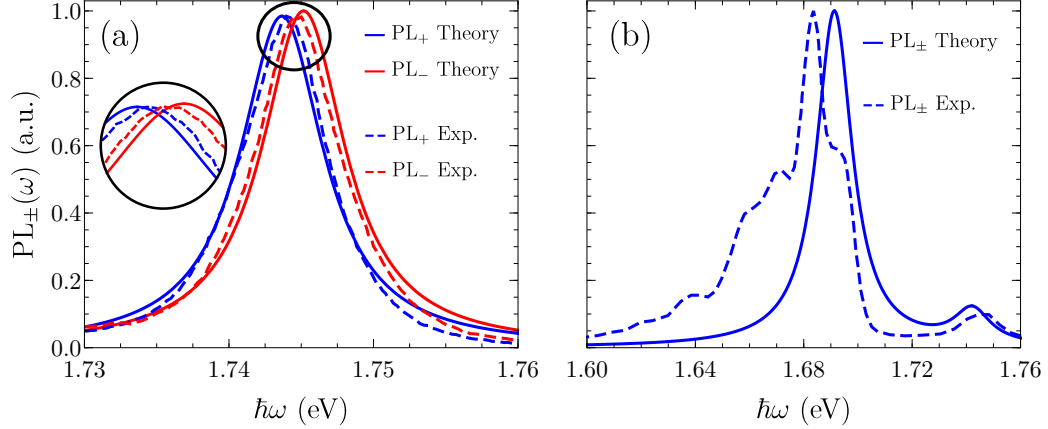


Figure 5.7: Excitonic PL spectra for left and right circularly polarized light calculated for WSe₂ on a SiO₂ substrate for $B = 7$ T, $\theta = 0^\circ$, $\gamma = 3.5$ meV (a) and $B = 14$ T, $\theta = 90^\circ$, $\gamma = 8$ meV (b). Comparison is made with the experimental results of Ref. [183] (a) and Ref. [76] (b). The calculated results are shifted to match the A exciton energy of the experimental results and the maxima are rescaled to facilitate comparison.

of the bright and dark excitonic peaks in the PL spectrum is shown in Fig. 5.5 as a function of the tilt angle of the sample. Notice that the splitting of both excitonic peaks increases with decreasing angle and that the splitting of the dark excitonic peak is more than twice as large as compared to the splitting of the bright peak.

For materials with $\lambda_c < 0$, i.e. molybdenum-based TMDs, the dark A exciton energy is higher than that of the bright A exciton and as such these states are, in addition to their already lower intensity, further thermally suppressed by a factor $\exp(\Delta E_{bd}/(k_B T))$ and are therefore not detected experimentally. This can be seen in Fig. 5.6, where no brightened dark A exciton peaks are seen in the PL spectra of MoS₂ and MoSe₂. For B excitons the situation is reversed: in materials with $\lambda_c < 0$ the dark exciton has a lower energy than the bright exciton and can be detected whereas in materials with $\lambda_c > 0$ the dark exciton has a higher energy than the bright exciton and is thermally suppressed. However, in this case the spin and orbital Zeeman effects cancel each other and the only (small) change in the energy gap comes from the Bloch Zeeman effect. Therefore, the splitting of the dark B exciton peaks in the PL spectrum will be smaller than that of the bright excitons and thus more difficult to detect. This can be seen in the figure, where the brightened dark B exciton peak of MoSe₂ and that of MoS₂ are difficult to observe. Although, for the latter, the treatment of the in-plane component of the

magnetic field within first order perturbation theory, as discussed above and below Eq. (2.29), might have smaller accuracy due to the very small λ_c .

In Figs. 5.7(a) and (b) the calculated results are compared with experimental results for the case of a perpendicular and an in-plane magnetic field, respectively. For a perpendicular magnetic field a slightly larger splitting of the excitonic peak is found, which is possibly due to the fact that the magnetic quantum numbers in the conduction and valence bands of monolayer TMDs deviate somewhat from the values $m = 0$ and $m = 2\tau$ due to mixing of the transition metal d orbitals that make up the single-particle states at the band edges with the chalcogen p orbitals [127]. In the case of an in-plane magnetic field there are additional features in the experimental PL spectrum at energies lower than the brightened dark exciton energy which have been attributed to localized or defect-related excitons [167,189].

5.3 Magnetic field dependence of the ground state properties of excitonic complexes

In general, the Hamiltonian for an N -particle excitonic complex in the presence of a uniform perpendicular magnetic field is in the single-band model given by

$$H = \sum_{i=1}^N \frac{\hbar^2}{2m_i} \left(\mathbf{k}_i + \frac{e}{\hbar} \mathbf{A}_i \right)^2 + \sum_{i<j}^N \text{sgn}(q_i q_j) V(|\mathbf{r}_i - \mathbf{r}_j|), \quad (5.4)$$

with q_i and m_i the charge and effective mass of particle i . Again the symmetric gauge $\mathbf{A} = (-By/2, Bx/2, 0)^T$ is chosen for the vector potential. In this section, the different Zeeman terms are not taken into account because they do not influence the binding energy and the structural properties of the excitonic complexes. The Hamiltonian can be rewritten as

$$H = \sum_{i=1}^N \left(-\frac{\hbar^2}{2m_i} \nabla_i^2 + \frac{e^2 B^2}{8m_i} r_i^2 + \frac{eB}{2m_i} L_{z_i} \right) + \sum_{i<j}^N \text{sgn}(q_i q_j) V(|\mathbf{r}_i - \mathbf{r}_j|), \quad (5.5)$$

with L_{z_i} the z -component of the angular momentum of particle i . The energies and wave functions are obtained from the above Hamiltonian using the SVM and the results, which are presented in this section, were published in Physical Review B [164]. The matrix elements of the r_i^2 terms between the correlated basis functions can be obtained by exploiting Eq. (4.15). The expectation value of the sum of the single-particle angular momenta vanishes for the ground state [161].

In addition to the SVM approach, and in order to get a better physical insight, it is also useful to construct a simplified variational method for excitons in a magnetic field. Transforming to center of mass and relative coordinates (3.15) leads to the exciton Hamiltonian

$$H_{ex} = \frac{P^2}{2M} + \frac{e^2 B^2}{8\mu} R^2 + \frac{p^2}{2\mu} + \frac{e^2 B^2}{8M^2} \left(\frac{m_h^3 + m_e^3}{m_h m_e} \right) r^2 + \frac{e^2 B^2 (m_e - m_h)}{4 M \mu} \mathbf{R} \cdot \mathbf{r} - V(r), \quad (5.6)$$

with $M = m_h + m_e$ and $1/\mu = 1/m_h + 1/m_e$. Here it was used that the sum of the two single-particle angular momentum operators is equal to the sum of the center of mass and the relative angular momentum operators, which was also used in Eq. (3.4). The latter two commute with the Hamiltonian and are zero for the ground state. For equal electron and hole masses $m_e = m_h = m$ the above Hamiltonian decouples into a center of mass part and a relative part, i.e. $H_{ex} = H_{CM} + H_{rel}$, $\Psi_{ex}(\mathbf{R}, \mathbf{r}) = \psi_{CM}(\mathbf{R})\psi_{rel}(\mathbf{r})$, and $E_{ex} = E_{CM} + E_{rel}$. The center of mass part can be solved exactly. Its Hamiltonian can be rewritten as

$$H_{CM} = \frac{P^2}{2M} + \frac{1}{2} M \omega^2 R^2, \quad (5.7)$$

with $\omega = eB/(2\sqrt{M\mu}) = eB/M$. This is the Hamiltonian of the 2D harmonic oscillator, which has an energy spectrum given by Eq. (5.3), yielding a ground state energy of $E_{CM}^0 = \hbar eB/M = \hbar^2/(2ml_B^2)$. The corresponding ground state wave function is given by

$$\psi_{CM}^0(\mathbf{R}) = \frac{1}{\sqrt{\pi} l_B} e^{-R^2/(2l_B^2)}. \quad (5.8)$$

Note that this implies that a difference in electron and hole mass would only lead to corrections of the order of $(m_e - m_h)^2$ since first order perturbation theory implies that the lowest order correction of the corresponding term in the Hamiltonian is proportional to $\langle \psi_{CM}^0 | R | \psi_{CM}^0 \rangle = 0$.

The relative part of the Hamiltonian can be written as

$$H_{rel} = -\frac{\hbar^2}{2\mu} \nabla^2 + \frac{e^2 B^2}{32\mu} r^2 - V(r). \quad (5.9)$$

In the case of zero magnetic field the Hamiltonian reduces to that of a hydrogen-like problem which, in the absence of non-local screening, has an exponential ground state wave function. Without the Coulomb-like interaction term, on the other hand,

the Hamiltonian reduces to that of an harmonic oscillator which has a Gaussian ground state wave function. Therefore, to interpolate between these limiting cases, the following variational wave function is considered:

$$\psi_{rel}^0(\mathbf{r}) = N e^{-a^2 r^2 - br}, \quad (5.10)$$

with a and b variational parameters and N a normalization constant. The variational ground state energy of the relative part of the Hamiltonian is

$$E_{rel}^0(a, b) = \frac{\langle \psi_{rel}^0 | H_{rel} | \psi_{rel}^0 \rangle}{\langle \psi_{rel}^0 | \psi_{rel}^0 \rangle}, \quad (5.11)$$

and the best approximation for the total exciton energy is therefore given by

$$E_{ex} = \frac{\hbar^2}{2m l_B^2} + E_{rel}^0(a_{min}, b_{min}), \quad (5.12)$$

with a_{min} and b_{min} the variational parameters which minimize the variational energy.

Furthermore, in the simplified variational model for the exciton, it is possible to show that the correlation function between the electron and hole (3.18) is given by

$$C_{eh}(r) = \frac{1}{2\pi} \frac{8a^3}{2a - \gamma b} e^{-2a^2 r^2 - 2br}, \quad (5.13)$$

leading to an average electron-hole distance (3.19) given by

$$\langle r_{eh} \rangle = \frac{\gamma(a^2 + b^2) - 2ab}{2a^2(2a - \gamma b)}, \quad (5.14)$$

with $\gamma = \sqrt{2\pi} e^{b^2/(2a^2)} \text{Erfc}(b/(\sqrt{2}a))$ and where the magnetic field and 2D polarizability dependence is reflected in the variational parameters a and b which have to be chosen such that they minimize the variational energy.

5.3.1 Binding energy

In the presence of a magnetic field the binding energies for excitons, negative trions, and biexcitons are, respectively, given by

$$E_b^{ex}(B, \chi_{2D}) = E_0^e(B) + E_0^h(B) - E_{ex}(B, \chi_{2D}), \quad (5.15)$$

$$E_b^{tr}(B, \chi_{2D}) = E_0^e(B) + E_{ex}(B, \chi_{2D}) - E_{tr}(B, \chi_{2D}), \quad (5.16)$$

$$E_b^{bi}(B, \chi_{2D}) = 2E_{ex}(B, \chi_{2D}) - E_{bi}(B, \chi_{2D}), \quad (5.17)$$

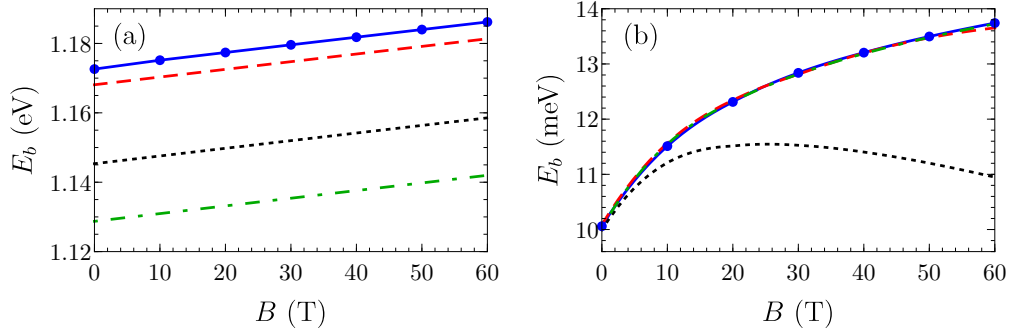


Figure 5.8: Exciton binding energy as a function of the magnetic field strength for a 2D polarizability of $\chi_{2D} = 2$ nm (a) and $\chi_{2D} = 1000$ nm (b). The system is suspended in vacuum and the effective masses are taken to be $m_e = m_h = 0.26m_0$. The solid blue curves are obtained with the SVM, the dashed red curves are the results from the simplified variational model (5.10), the dotted black curves are obtained with the simplified model in which a is set to 0, and the dot-dashed green curves are obtained with the simplified model in which b is set to 0.

where $E_0^{e(h)}$, E_{ex} , E_{tr} and E_{bi} are the free electron (hole), exciton, trion, and biexciton energy, respectively. Again only negative trions will be considered.

In Fig. 5.8 the exciton binding energy is shown as a function of the magnetic field strength for two different 2D polarizabilities. An increased 2D polarizability leads to a decreased binding energy as a consequence of the decreased short-range interactions, as was shown in Fig. 2.7. For small 2D polarizabilities, the binding energy increases linearly with the magnetic field strength, whereas for large 2D polarizabilities the binding energy initially increases linearly with the magnetic field strength but at higher magnetic field strengths the increase becomes slower than linear. This can be understood since a perpendicular magnetic field leads to in-plane confinement of the particles, for which the length scale is the magnetic length. At low magnetic field strengths this length scale is much larger than the average interparticle distance and as such the exciton energy depends very weakly on the magnetic field. Free electrons and holes, however, do immediately feel the influence of the magnetic field and this confinement leads to an increase in the first two terms of Eq. (5.15) and therefore in the binding energy as well. As the magnetic field strength increases, the magnetic length decreases and eventually becomes of the same order as the interparticle distance. Increasing the magnetic field strength even further will cause the particles to be pushed closer towards each other which increases the kinetic energy of the exciton. This effect decreases the bind-

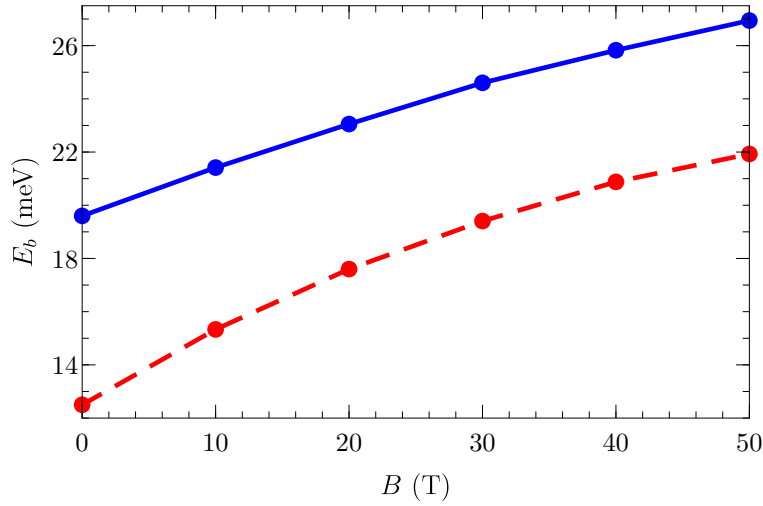


Figure 5.9: Trion (solid, blue) and biexciton (dashed, red) binding energy as a function of the magnetic field strength calculated for WSe₂ on a SiO₂ substrate.

ing energy and adds up with the increase in binding energy stemming from the magnetic confinement of the free electrons and holes to yield a deviation from the linear magnetic field dependence of the binding energy. At larger 2D polarizabilities the interparticle distance is larger due to the decreased Coulomb interactions and therefore the deviation from the linear behavior starts at lower magnetic field strengths.

Figure 5.8 also shows that the results obtained with the simplified variational method agree well with those obtained with the SVM. In the absence of screening, which is not shown here, the SVM results can be reproduced with high accuracy in the chosen magnetic field range, i.e. 0 T up to 60 T, by using an exponential variational wave function (i.e. $a = 0$). When using a Gaussian wave function (i.e. $b = 0$), binding energies which are 21.5% smaller than the SVM values are found. This implies that in this magnetic field range the Coulomb term dominates over the magnetic field term and therefore the relative part of the exciton is described by an exponential wave function. For small 2D polarizabilities Fig. 5.8(a) shows that the results obtained using the full variational wave function are about 5 meV, or 0.4%, smaller than the SVM results, that the results obtained using an exponential wave function ($a = 0$) are about 28 meV, or 2.3%, smaller than the SVM results, and that the results obtained using a Gaussian wave function ($b = 0$) are about 39 meV, or 3.4%, smaller than the SVM results. This implies that the interaction term, which is now given by the Keldysh potential (2.40) instead of the bare Coulomb potential,

	Subst.	Exciton			Trion			Biexciton		
		0 T / 10 T / 20 T			0 T / 10 T / 20 T			0 T / 10 T / 20 T		
MoS ₂	Vac.	555.7	556.9	558.1	33.4	34.9	36.1	19.0	22.3	23.5
	SiO ₂	321.1	322.3	323.5	22.9	24.7	25.9	15.5	17.8	19.5
MoSe ₂	Vac.	486.7	487.8	488.8	27.7	29.3	30.4	15.5	17.6	19.3
	SiO ₂	291.4	292.5	293.5	20.3	21.7	22.8	13.3	15.3	16.7
WS ₂	Vac.	530.1	532.0	533.7	32.4	35.7	37.4	19.5	22.4	25.0
	SiO ₂	289.2	291.0	292.7	21.3	24.0	25.6	14.5	17.1	19.7
WSe ₂	Vac.	473.8	475.5	477.2	28.8	31.3	32.7	15.9	19.3	20.7
	SiO ₂	265.2	267.1	268.7	19.6	21.4	23.1	12.5	15.3	17.6

Table 5.1: Exciton, trion, and biexciton binding energies (meV) calculated for different TMD materials and different substrates. The dielectric constants $\epsilon_b = 3.8$ and $\epsilon_t = 1$ were used for SiO₂ below and vacuum above the TMD.

still dominates over the magnetic field term. However, the corresponding exciton state cannot be described by an exponential or a Gaussian wave function or even a product of the two, although the latter gives the best approximation. In the presence of strong screening Fig. 5.8(b) shows that the SVM results can be reproduced with high accuracy by using a Gaussian variational wave function ($b = 0$). When using an exponential wave function ($a = 0$), however, the results agree at low magnetic field strengths but deviate from the SVM results for higher magnetic field strengths, even resulting in a decrease in binding energy. This implies that, due to the strong screening and therefore weak interactions, the magnetic field term now dominates over the interaction term and therefore the relative part of the exciton is described by a Gaussian wave function.

The trion and biexciton binding energies are shown as a function of the magnetic field strength in Fig. 5.9. For both excitonic complexes it shows qualitatively the same behavior as that of the exciton binding energy, however the deviation from the linear behavior is less pronounced as compared to that in Fig. 5.8(b). This is because the corresponding trion and biexciton interparticle distances are smaller than the exciton interparticle distance corresponding to Fig. 5.8(b) because different parameters were used. Furthermore, notice that the biexciton binding energy is smaller than the trion binding energy.

In Table 5.1 the exciton, trion, and biexciton binding energies are shown for different monolayer TMDs, different substrates, and different magnetic field strengths. The binding energy of the different excitonic complexes increases with the mag-

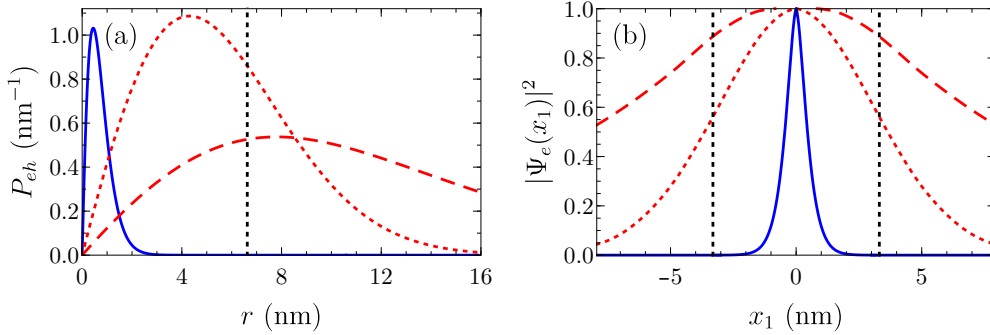


Figure 5.10: (a) Interparticle distance probability distribution between the electron and hole of an exciton calculated for the same parameters as in Fig. 5.8 and for a 2D polarizability of $\chi_{2D} = 2$ nm (solid, blue) and $\chi_{2D} = 1000$ nm (red, scaled up by a factor of 8), in the absence (dashed) and presence (dotted) of a magnetic field of $B = 60$ T. The dotted black vertical line indicates twice the magnetic length. (b) The modulus squared of the exciton wave function $\Psi_e(x_1) \equiv \Psi_{0,0}((x_1, y_1 = 0), \mathbf{0})$ for a hole fixed in the origin for the same cases as in (a). The calculated wave functions are rescaled relative to their respective maxima.

netic field strength, with the increase being in general slightly larger at low fields, i.e. going from 0 T to 10 T as compared to going from 10 T to 20 T. This is in correspondence with the non-linear behavior discussed above. Furthermore, the materials with smaller effective electron and hole masses (WS_2 and WSe_2) exhibit a stronger magnetic field dependence than those with larger effective electron and hole masses (MoS_2 and MoSe_2). This is because a smaller effective mass, and therefore larger kinetic energy, leads to a smaller binding energy and therefore a larger excitonic complex which is more susceptible to magnetic confinement. Furthermore, the magnetic field dependence is also more pronounced for trions and biexcitons as compared to that for excitons, which again is a consequence of the fact that the former two excitonic complexes are less strongly bound and therefore larger.

5.3.2 Wave function and interparticle distance

In Fig. 5.10 the interparticle distance probability distribution and the modulus squared of the wave function for an exciton with the hole fixed at $x = y = 0$ are shown, as obtained from the SVM. When the screening is weak these quantities are unaffected by the presence of a magnetic field since the exciton is localized in

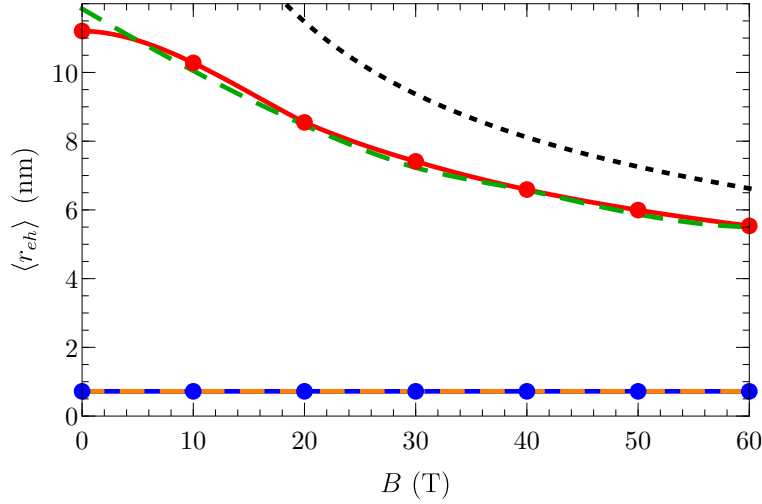


Figure 5.11: Average interparticle distance between the electron and hole of an exciton as a function of the magnetic field strength calculated for the same parameters as in Fig. 5.8 and for a 2D polarizability of $\chi_{2D} = 2$ nm (SVM: solid, blue and simplified model: dashed, orange) and $\chi_{2D} = 1000$ nm (SVM: solid, red and simplified model: dashed, green). The dotted black curve is twice the magnetic length.

a region smaller than the magnetic confinement region. In the presence of strong screening, however, the exciton is larger than this magnetic confinement region and therefore becomes compressed when a magnetic field is applied. In Fig. 5.11 the average interparticle distance is shown as a function of the magnetic field strength. For larger 2D polarizabilities the exciton is larger, which is again a consequence of the decreased interaction. As the magnetic field increases, the exciton in the presence of strong screening decreases considerably in size. This is because the magnetic length already becomes comparable to the size of the exciton at a relatively small magnetic field strength of 10 T. Moreover, the average interparticle distance converges to twice the magnetic length for high magnetic field strengths. The size of the exciton in the presence of small screening remains constant at 0.72 nm because it is significantly smaller than the magnetic length for the considered magnetic field strengths. The figure also shows good agreement between the results obtained from the SVM and the simplified variational model (5.10).

Using Eq. (3.19), average interparticle distances of $\langle r_{ee} \rangle = 3.56$ nm and $\langle r_{eh} \rangle = 2.25$ nm are found for the trion of Fig. 5.9 (WSe₂ on a SiO₂ substrate), approximately independent of the magnetic field for realistic field strengths. For

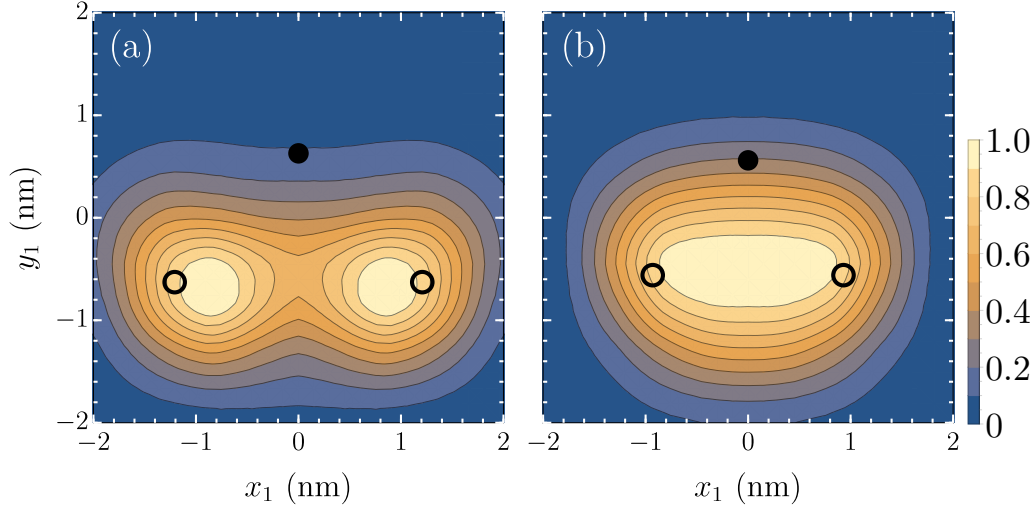


Figure 5.12: Modulus squared of the biexciton wave function $\Psi_{0,0}((x_1, y_1), \mathbf{r}_2^0, \mathbf{r}_3^0, \mathbf{r}_4^0)$ calculated for a 2D polarizability of $\chi_{2D} = 5.3$ nm and a magnetic field strength of $B = 0$ T (a) and $B = 60$ T (b). The circles and dots indicate the location of the fixed holes and electrons, respectively.

biexcitons in the same system average interparticle distances of $\langle r_{ee} \rangle = 2.78$ nm and $\langle r_{eh} \rangle = 2.05$ nm are obtained, again approximately independent of the magnetic field for realistic field strengths. This shows that the biexciton is smaller than the trion despite the fact that its binding energy is also smaller. This may be explained due to the fact that for biexcitons there is an extra hole, as compared to negative trions, to screen the repulsive electron-electron interaction.

In Fig. 5.12 the modulus squared of the biexciton wave function for a fixed electron and fixed holes, i.e. the conditional electron probability distribution, is shown for the previously used parameters $m_e = m_h = 0.26m_0$ and $\kappa = 1$. Notice that for $B = 0$ T the other electron localizes predominantly around the fixed holes. The presence of a strong magnetic field causes the localized regions around the fixed holes to merge, which is a manifestation of the fact that $\langle r_{hh} \rangle$ has decreased due to the magnetic field.

5.3.3 Diamagnetic shift

For excitons, the center of mass part of the Hamiltonian leads to a linear magnetic field term in the energy spectrum (5.12). It can be shown that this term is in general given by $N\hbar^2/(2Ml_B^2)$ for an N -particle excitonic complex with equal effective

electron and hole masses. The quadratic magnetic field term in the excitonic energy spectrum, the so-called diamagnetic shift [190], is approximately given by σB^2 with $\sigma = e^2 \langle r^2 \rangle / 32\mu$, where the expectation value is taken with respect to the wave function in the absence of a magnetic field. It is possible to show that, up to first order in the electron-hole mass difference, the center of mass part can be decoupled from the relative part of the Hamiltonian (5.5) and that the diamagnetic shift of the energy of the N -particle excitonic complex is in general given by

$$\sigma = \frac{e^2}{8M} \sum_{i>j}^N \langle r_{ij}^2 \rangle. \quad (5.18)$$

This value can be experimentally obtained by fitting the results of the transition energy as a function of the magnetic field and as such it provides information about the size of the excitonic complex. The transition energy, which was schematically shown for excitons in Fig. 3.8(a), is in general defined as the energy of the photon resulting from the recombination process of an electron and a hole in the excitonic complex [147]. It can therefore be written as

$$E_t^{ex}(B, \chi_{2D}) = E_g + E_{ex}(B, \chi_{2D}), \quad (5.19)$$

$$E_t^{tr}(B, \chi_{2D}) = E_g + E_{tr}(B, \chi_{2D}) - E_0^e(B), \quad (5.20)$$

$$E_t^{bi}(B, \chi_{2D}) = E_g + E_{bi}(B, \chi_{2D}) - E_{ex}(B, \chi_{2D}), \quad (5.21)$$

for excitons, trions, and biexcitons, respectively, with E_g the band gap. Since the diamagnetic shift describes the quadratic dependence on the magnetic field and since E_g and $E_0^e(B)$ are, respectively, constant and linear as a function of the magnetic field it follows that $\sigma_t^{ex} = \sigma^{ex}$, $\sigma_t^{tr} = \sigma^{tr}$, and $\sigma_t^{bi} = \sigma^{bi} - \sigma^{ex}$. Therefore, σ_t can be obtained by measuring and fitting the transition energy of a given excitonic complex, from which in turn σ can be found which then gives an estimate of the size of the excitonic complex by means of Eq. (5.18). The different Zeeman terms are linear as a function of the magnetic field and therefore do not influence the diamagnetic shift.

In Table 5.2 the exciton, trion, and biexciton diamagnetic shifts, as determined from fitting the magnetic field dependence of the transition energy, are shown and compared with the values obtained from the calculated interparticle distances by means of Eq. (5.18). Here equal electron and hole masses of $0.5m_0$, $0.54m_0$, $0.32m_0$, and $0.34m_0$ for MoS₂, MoSe₂, WS₂, and WSe₂, respectively, were assumed. Only experimental results for excitons are shown in the table. There are no experimental results for biexcitons and only one for trions, i.e. $\sigma = 5.7 \mu\text{eV}$

	Exciton			Trion		Biexciton	
	This thesis Fit	(5.18)	Literature	This thesis Fit	(5.18)	This thesis Fit	(5.18)
MoS ₂	0.033	0.035	-	0.319	0.282	0.271	0.292
MoSe ₂	0.032	0.030	-	0.263	0.286	0.302	0.287
WS ₂ <i>A</i>	0.080	0.080	0.9 [127]	0.756	0.700	0.633	0.744
			0.32 ± 0.02 [129]				
WS ₂ <i>B</i>	0.047	0.047	0.11 ± 0.02 [129]				
WSe ₂	0.081	0.080	0.18 ± 0.02 [132]	0.992	0.709	0.849	0.790

Table 5.2: Exciton, trion, and biexciton diamagnetic shifts σ ($\mu\text{eV T}^{-2}$) for different TMD materials on a SiO₂ substrate ($\varepsilon_b = 3.8$, $\varepsilon_t = 1$) found by fitting the magnetic field dependence of the transition energy, compared with values calculated from the interparticle distances using Eq. (5.18). Experimental results from the literature are shown for excitons. For WS₂ results are shown for both the *A* and the *B* exciton.

T^{-2} for WS₂ on a SiO₂ substrate [127], which differs almost an order of magnitude from the results calculated here. The trion and biexciton diamagnetic shifts are comparable, whereas the corresponding exciton diamagnetic shift is almost an order of magnitude smaller. For excitons excellent agreement is found between the results obtained with the fit and from Eq. (5.18). For trions and biexcitons a relative discrepancy between the fit and the results from Eq. (5.18) between 5% and 28% is found. This implies that the estimated size of the excitonic complex will differ between 2.5% and 15% from the theoretical size calculated from Eq. (5.18). The agreement between the fit and the results obtained from Eq. (5.18) can be further improved by increasing the number of variational basis functions but this will lead to an exponential increase of the computation time. It can also be concluded that the value of the diamagnetic shift for excitons, trions, and biexcitons depends strongly on the type of transition metal, whereas the type of chalcogen atom is of less importance.

For excitons, the calculated results obtained from both the fit and Eq. (5.18) underestimate the experimental results by about a factor 4 for *A* excitons in WS₂ (and by more than a factor 10 when comparing with Ref. [127]) and by a factor 2 for *B* excitons in WS₂ and for *A* excitons in WSe₂. *A* (*B*) excitons consist of a hole stemming from the upper (lower) valence band and have slightly different effective masses. For *B* excitons in WS₂ $m_e = m_h = 0.405m_0$ was used. These experimen-

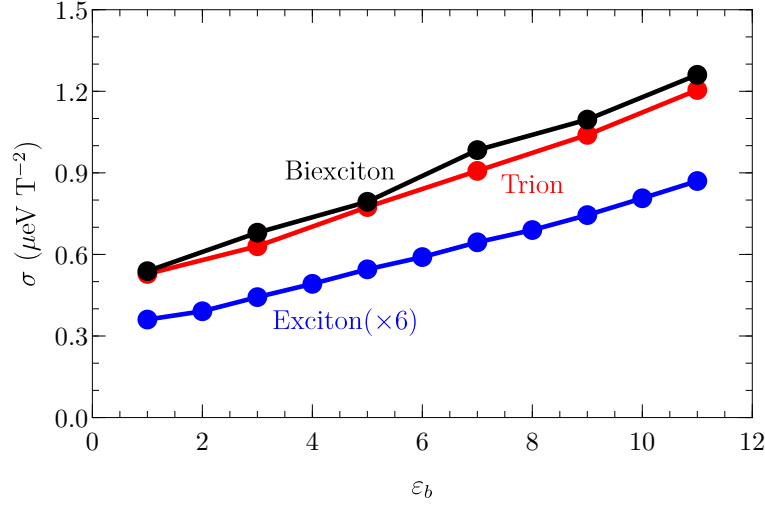


Figure 5.13: Exciton (blue), trion (red), and biexciton (black) diamagnetic shift obtained from Eq. (5.18) for WS_2 as a function of the dielectric constant of the substrate. The exciton results are scaled up by a factor 6.

tal results depend significantly on the exact value of the dielectric constant of the substrate and in Ref. [132] the high frequency value for the dielectric constant of SiO_2 was used instead of the static one, i.e. $\epsilon_b = 2.1$ instead of $\epsilon_b = 3.8$. When using $\epsilon_b = 2.1$ diamagnetic shifts of $\sigma = 0.067 \mu\text{eV T}^{-2}$ and $\sigma = 0.069 \mu\text{eV T}^{-2}$ are found using the fit and Eq. (5.18), respectively. Furthermore, it is remarkable that the experimental results for these two materials differ by about a factor 2 while their effective charge carrier masses and 2D polarizabilities are very similar.

The diamagnetic shift obtained from Eq. (5.18) is shown for excitons, trions, and biexcitons in WS_2 as a function of the dielectric constant of the substrate in Fig. 5.13. This shows that the diamagnetic shift increases approximately linearly with the dielectric constant of the substrate and that its value can be more than doubled as compared to the value in vacuum by choosing an appropriate substrate. The substrate dependence of the trion and biexciton diamagnetic shifts is stronger than that of the exciton diamagnetic shift. More specifically, the results can be fitted by a linear curve, i.e. $\sigma = a\epsilon_b + b$, and the fitting parameters are $(a, b) = (0.0085, 0.04887) \mu\text{eV T}^{-2}$, $(a, b) = (0.0678, 0.4408) \mu\text{eV T}^{-2}$, and $(a, b) = (0.0721, 0.4593) \mu\text{eV T}^{-2}$ for excitons, trions, and biexcitons, respectively.

5.4 Conclusion

In this chapter the effects of uniform magnetic fields on excitons, trions, and biexcitons in monolayer TMDs were studied. It was found that a perpendicular magnetic field leads to exciton Landau levels which correspond qualitatively to those of the 2D charged Schrödinger particle. As expected, the degeneracy between states with opposite angular momentum was found to be broken as a result of the magnetic field. However, this degeneracy is only partly broken since only the lowest $|j_r|$ Landau levels of the state with negative relative angular momentum are non-degenerate with the Landau levels of the state with opposite relative angular momentum.

Next, it was shown how two known effects from the literature, i.e. the exciton valley Zeeman effect in the presence of a perpendicular magnetic field and the brightening of dark excitons in the presence of an in-plane magnetic field, can be combined in the presence of a tilted magnetic field. More specifically, it was found that this dark exciton valley Zeeman effect is more than twice as strong as compared to that of the bright exciton. It was also demonstrated that, as a result of the sign of the spin-orbit coupling in the conduction band, this strong effect is only present for A excitons in tungsten-based TMDs.

Finally, the SVM was used to study the ground state properties of excitons, trions, and biexcitons in a perpendicular magnetic field and it was shown that the binding energy of all three excitonic complexes increases as a function of the magnetic field strength. More specifically, the biexciton binding energy can be almost doubled in the presence of a magnetic field of 50 T. Furthermore, the diamagnetic shift of trions and biexcitons was found to be almost an order of magnitude larger than that of excitons and the diamagnetic shift of all three excitonic complexes was shown to increase as a function of the substrate dielectric constant.

CHAPTER 6

Excitonic complexes in anisotropic 2D materials

In this chapter two new materials are considered, i.e. monolayer black phosphorus and monolayer TiS_3 . These materials exhibit an anisotropic energy spectrum and the effect of this anisotropy on the binding energy and the structural properties of excitons, trions, and biexcitons in these materials is investigated by means of the SVM. It is shown that excitonic complexes in black phosphorus are strongly anisotropic whereas in TiS_3 they are almost isotropic, which is a consequence of the relative anisotropy of the constituent electrons and holes. Finally, the effect of tensile and compressive strain in different directions on the properties of excitons in black phosphorus is studied.

6.1 Anisotropic 2D materials

Monolayer TMDs, like graphene, have trigonal lattice symmetry which persists in the electronic band structure. However, at low energies this trigonal warping effect, described by the parameter γ_3 in the low-energy Hamiltonian (2.6), is very small and as such it is a good approximation to consider the low-energy spectrum of these materials to be perfectly isotropic. As a result, excitonic complexes in these materials are isotropic as well.

As mentioned in section 1.2, numerous 2D materials, including materials with non-trigonal symmetry, can be fabricated using the same methods which are used to obtain graphene and monolayer TMDs. As such, another possible type of 2D

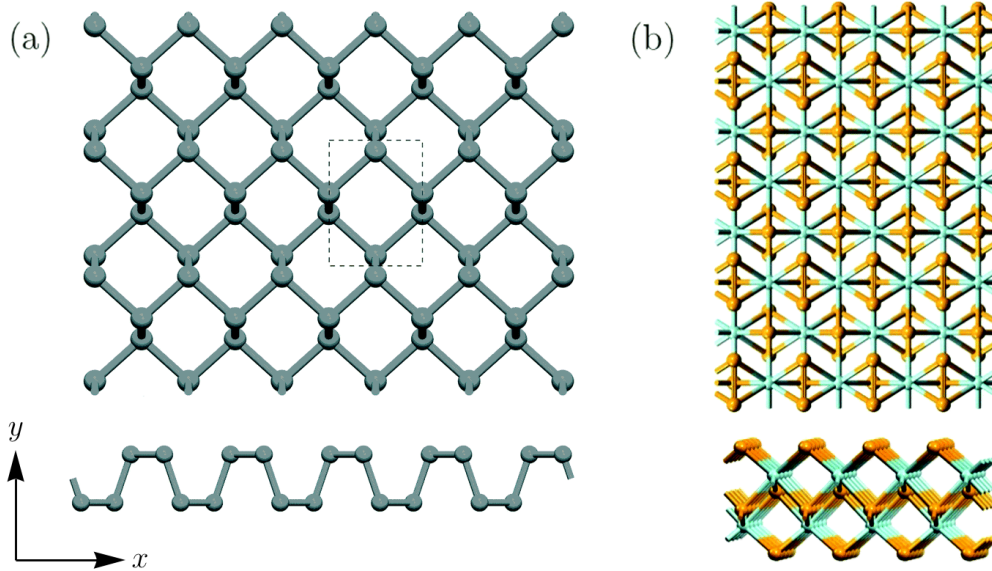


Figure 6.1: Top view (top) and side view (bottom) of the lattice of monolayer bP (a) and TiS_3 (b). The unit cell of bP is indicated by the dashed rectangle. Ti (S) atoms are indicated in light blue (orange). Figures taken from Ref. [191] (a) and [192] (b).

semiconductor is monolayer black phosphorus (bP) [37, 38], for which the lattice structure is shown in Fig. 6.1(a). This material is also commonly referred to in the literature as phosphorene, which is slightly misleading since electrons in bP form sp^3 bonds as opposed to the sp^2 bonds in graphene and in benzene-like structures (from which graphene got its “ene”). As a result of the strong symmetry breaking between the x - and y -direction, this material exhibits a highly anisotropic band structure [193, 194], i.e. the effective masses in the k_x -direction are different from those in the k_y -direction. Since bP is a semiconductor with a band gap similar to that of TMDs, it is also well-suited for technological applications such as field effect transistors [195] and photodetector devices [196, 197].

Another class of anisotropic 2D semiconductors is formed by the transition metal trichalcogenides [198, 199]. Monolayer TiS_3 , the prototypical representative of this class for which the lattice structure is shown in Fig. 6.1(b), has recently been synthesized and proposed as a candidate material for use in transistors [200, 201]. This material exhibits a peculiar anisotropic band structure in which the conduction band is flatter in the k_x -direction whereas the valence band is flatter in the k_y -direction [202]. Thus the anisotropy directions of electrons and holes are different

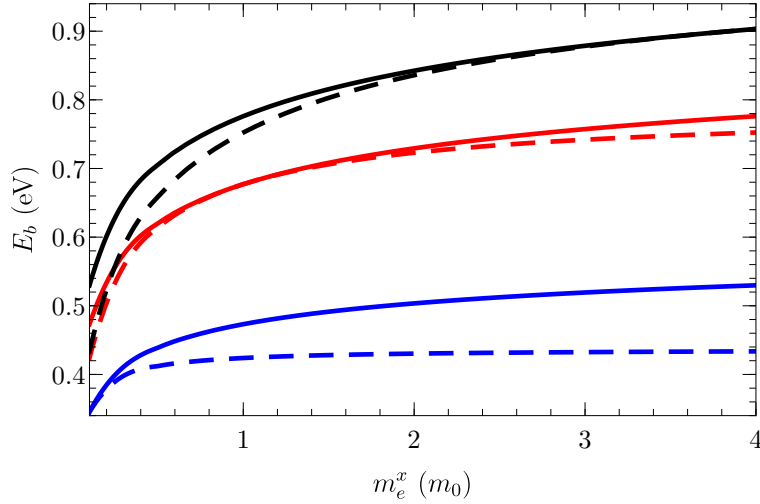


Figure 6.2: Exciton binding energy calculated for a general system as a function of m_e^x for $m_e^y = 0.1m_0$ (blue), $m_e^y = m_0$ (red), and $m_e^y = 4m_0$ (black) for $(m_h^x, m_h^y) = (m_e^x, m_e^y)$ (solid) and $(m_h^x, m_h^y) = (m_e^y, m_e^x)$ (dashed). The following parameters were used: $\chi_{2D} = 8$ nm and $\varepsilon_b = \varepsilon_t = 1$.

from each other. This is in contrast to bP in which both the conduction and valence bands are flatter in the k_y -direction. As a result of their anisotropic band structure, both bP and TiS₃ show interesting properties such as linear dichroism [203–205] and Faraday rotation [206].

The binding energy and structural properties of excitonic complexes in both monolayer bP and monolayer TiS₃ will now be studied using the SVM in the single-band model. The same procedure as explained in section 4.3 can be used, with the only difference being that now the matrices containing the variational parameters in the correlated Gaussian basis functions (4.11) are different for the x - and y -dependence. The results presented in this chapter were published in Physical Review B [207].

6.2 Binding energy

In order to better understand the influence of the anisotropic band structure, the exciton binding energy is shown in Fig. 6.2 for a general system as a function of the electron band mass in the k_x -direction for different values of the electron band mass in the k_y -direction. Two distinct situations are considered: *i*) identical electron and

	$m_e^x (m_0)$	$m_e^y (m_0)$	$m_h^x (m_0)$	$m_h^y (m_0)$	χ_{2D} (nm)
bP	0.20	6.89	0.20	6.89	5.49 [208]
TiS ₃	1.52	0.40	0.30	0.99	8.87 [209]

Table 6.1: Charge carrier masses [202] and 2D polarizabilities for bP and TiS₃.

hole masses and *ii*) opposite electron and hole masses, i.e. the k_x -component of one equals the k_y -component of the other and vice versa. The binding energy for identical electron and hole masses is always larger than that for opposite masses except when the masses in the k_x - and k_y -direction are equal, i.e. at $m_e^x = 0.1m_0$, $m_e^x = m_0$, and $m_e^x = 4m_0$ for the blue, red, and black curves, respectively, as in this case the two situations are identical. This can be explained by the fact that the reduced mass $\mu^{x(y)} = m_e^{x(y)} m_h^{x(y)} / (m_e^{x(y)} + m_h^{x(y)}) \leq \min(m_e^{x(y)}, m_h^{x(y)})$, implying that in the opposite mass case, i.e. the electron and hole anisotropy directions are perpendicular with respect to each other, $\mu^x = \mu^y$ will remain small when $m_e^x = m_h^y$ becomes large. Since excitonic properties are determined by the reduced mass and not the individual masses, this means that excitons in this system are isotropic and always 2D (even though the constituent particles are quasi-1D in the limit of large $m_e^x = m_h^y$) because of the limited reduced masses and therefore have limited binding energy. On the other hand, in the identical mass case, i.e. the electron and hole anisotropy directions are parallel with respect to each other, $\mu^{x(y)} = m_e^{x(y)} / 2 = m_h^{x(y)} / 2$ and therefore μ^x increases linearly with increasing $m_e^x = m_h^x$ whereas μ^y remains constant. Excitons in this system are anisotropic and are quasi-1D in the limit of large $m_e^x = m_h^x$ and therefore their binding energy is large due to the additional confinement.

For the remainder of this chapter the focus will lie on monolayer bP and monolayer TiS₃, for which the effective band masses and 2D polarizabilities used in the calculations are given in Table 6.1. The binding energies for excitons, negative and positive trions, and biexcitons are shown in Table 6.2 for bP and TiS₃ both suspended in vacuum and placed on a SiO₂ substrate. The calculated values are compared with other theoretical studies using diffusion Monte Carlo [210], the Numerov approach [211], a simple variational method [208], and first-principles Bethe-Salpeter calculations [209, 212, 213]. For bP, the calculated values differ at most 16% from those of Ref. [210]. More specifically for excitons the agreement is best with the results of Ref. [212] (a difference of 0.3% for vacuum) and least good with the results of Ref. [208] (a difference of 21% for SiO₂), which are obtained using a simple variational method. There are no other theoretical results for

Substrate		bP		TiS ₃			
		This thesis	Literature	This thesis	Literature		
X	Vacuum	832.4	743.9 [210] 760 [211] 710 [208] 830 [212]	537.1	560, 590 [209] 920 [213]		
		SiO ₂	483.6		405.0 [210] 400 [211] 380 [208]	314.7	330 [209]
		hBN	443.7		-	289.0	-
		hBN×2	293.8		-	191.7	-
	X^-	Vacuum	56.3	51.6 [210]	34.9	32 [209]	
SiO ₂		39.6	34.2 [210]	25.3	23 [209]		
hBN		37.3	-	23.9	-		
hBN×2		27.2	-	17.8	-		
X^+	Vacuum	56.3	53 [210]	34.0	36 [209]		
	SiO ₂	39.6	-	24.2	26 [209]		
	hBN	37.3	-	22.8	-		
	hBN×2	27.2	-	16.7	-		
X_2	Vacuum	40.1	40.9 [210]	25.8	-		
	SiO ₂	33.0	-	21.8	-		
	hBN	31.8	-	21.1	-		
	hBN×2	25.9	-	17.5	-		

Table 6.2: Exciton (X), negative (X^-) and positive (X^+) trion, and biexciton (X_2) binding energies (meV) for bP and TiS₃ and for different substrates obtained using the SVM, compared with theoretical results from the literature. The following dielectric constants were used: $\varepsilon_b = 3.8$ ($\varepsilon_b = 4.4$) and $\varepsilon_t = 1$ for SiO₂ (hBN) below and vacuum above the material and $\varepsilon_b = \varepsilon_t = 4.4$ for encapsulating hBN (denoted by hBN×2).

biexcitons in bP on a SiO_2 substrate. The binding energies for TiS_3 are in general smaller than those for bP. The calculated values agree very well, i.e. differing at most 9%, with those from Ref. [209], which are obtained by numerically solving the relative Schrödinger equation either directly for excitons or using an imaginary time evolution operator for trions. The authors also calculate the exciton binding energy for TiS_3 in vacuum by solving the Bethe-Salpeter equation and find 590 meV, which is still in good agreement. However, the result from Ref. [213], which was obtained using first-principles Bethe-Salpeter calculations, differs by almost a factor 2 from both the calculated result and those of Ref. [209].

The results for both bP and TiS_3 on an hBN substrate are, due to the similar dielectric constant, close to those for a SiO_2 substrate. However, when the materials are encapsulated in hBN the binding energies of the excitonic complexes are considerably smaller. Furthermore, the biexciton binding energy is almost always smaller than the trion binding energy. However, the difference between them decreases with increasing substrate screening and for TiS_3 encapsulated in hBN the biexciton is more tightly bound than the positive trion. This is consistent with the general results of Ref. [165] which found that both a difference in electron and hole band masses and a reduced screening length (in this case due to an increased κ) lead to an increase of the biexciton binding energy with respect to the trion binding energy. This may be explained due to the fact that biexcitons are smaller than trions (as discussed in subsection 5.3.2), making them more susceptible to the increase in short-range interactions associated with the reduced screening length. The dependence on the difference in electron and hole band masses is not immediately clear. Finally, note that the negative and positive trion binding energies are equal in bP because equal electron and hole band masses were assumed. In Ref. [210] a difference of 2.6% between these two excitonic complexes was found. For TiS_3 the negative trion binding energy is larger than the positive trion binding energy, which is to be expected because the electron effective masses are larger than the hole effective masses, whereas the opposite behavior was found in Ref. [209].

There are only few experimental works studying excitonic complexes in monolayer bP. An exciton binding energy of 900 ± 120 meV and 300 meV was found in Ref. [214] and Ref. [215], respectively. Both studies used a SiO_2 substrate. The former differs by about a factor 2 from the value calculated here (and even more from the other theoretical results), although it is remarkable that this value is in good agreement with the theoretical results for bP suspended in vacuum. It is possible that the experiment was performed on a part of the material which was locally detached from the substrate. The result of Ref. [215] is in reasonable agreement with the value calculated here, i.e. a difference of 21%. This study also found a

	bP			TiS ₃		
	r_{eh}	r_{ee}	r_{hh}	r_{eh}	r_{ee}	r_{hh}
	x_{eh}	x_{ee}	x_{hh}	x_{eh}	x_{ee}	x_{hh}
	y_{eh}	y_{ee}	y_{hh}	y_{eh}	y_{ee}	y_{hh}
Exciton	0.68	-	-	0.92	-	-
	0.82	-	-	0.78	-	-
	0.23	-	-	0.74	-	-
Trion	1.22	2.01	-	1.52	2.43	-
	1.61	2.34	-	1.31	1.83	-
	0.35	0.50	-	1.33	1.97	-
Biexciton	1.06	1.47	1.47	1.32	1.75	1.78
	1.36	1.75	1.75	1.13	1.31	1.50
	0.32	0.38	0.38	1.12	1.46	1.35

Table 6.3: Exciton, negative trion, and biexciton average interparticle distances (nm), total and in the x/y -direction, calculated for bP and TiS₃ suspended in vacuum.

trion binding energy of 100 meV, again on a SiO₂ substrate, which differs by about a factor 3 from both the calculated value and that of Ref. [210]. There are no experimental results available for biexcitons in bP and for monolayer TiS₃ in general.

6.3 Correlation function and interparticle distance

Similar to the average interparticle distance in the isotropic case (3.19), the average distance between particles i and j is in the anisotropic case obtained by

$$\langle r_{ij} \rangle = \int_{-\infty}^{\infty} \int_{-\infty}^{\infty} \sqrt{x^2 + y^2} C_{ij}(x, y) dx dy, \quad (6.1)$$

where the correlation function (3.18) is now anisotropic. Analogously the interparticle distance in the x - and y -direction are defined as

$$\begin{aligned} \langle x_{ij} \rangle &= \sqrt{\int_{-\infty}^{\infty} \int_{-\infty}^{\infty} x^2 C_{ij}(x, y) dx dy}, \\ \langle y_{ij} \rangle &= \sqrt{\int_{-\infty}^{\infty} \int_{-\infty}^{\infty} y^2 C_{ij}(x, y) dx dy}. \end{aligned} \quad (6.2)$$

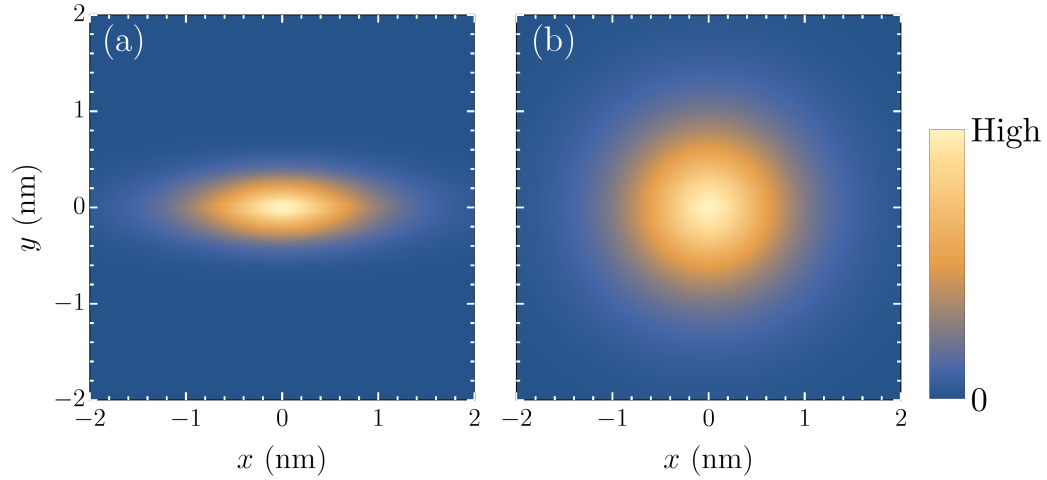


Figure 6.3: Electron-hole correlation functions calculated for excitons in bP (a) and TiS₃ (b) suspended in vacuum.

In Table 6.3 the average interparticle distances, total as well as resolved in the x/y -direction, are shown for excitons, negative trions, and biexcitons in bP and TiS₃. In general, the interparticle distances are larger in TiS₃ as compared to bP, which is in correspondence with the smaller binding energies found in Table 6.2. Excitons exhibit the smallest interparticle distance, as can be expected. More remarkably, trions show larger interparticle distances than biexcitons, even though their binding energy is larger. This is similar to what was found for monolayer transition metal dichalcogenides, as discussed in subsection 5.3.2. Furthermore, the average distance between particles of equal charge is larger than that between particles of opposite charge. Looking at the x/y -resolved interparticle distances, it is clear that the excitonic complexes in bP are strongly anisotropic, with the interparticle distances in the x -direction a factor 4-5 larger than those in the y -direction, whereas the excitonic complexes in TiS₃ are almost isotropic. This is because, in the discussion related to Fig. 6.2 on the reduced masses, bP is an example of the identical mass case whereas TiS₃ is an example of the opposite mass case. It is also interesting to note that the electron-electron and hole-hole interparticle distances are identical in bP, due to the identical electron and hole band masses, whereas they are slightly different in TiS₃. More specifically, in TiS₃, the difference between the electron-electron and hole-hole interparticle distances in the x/y -direction is more pronounced than the difference between the total electron-electron and hole-hole

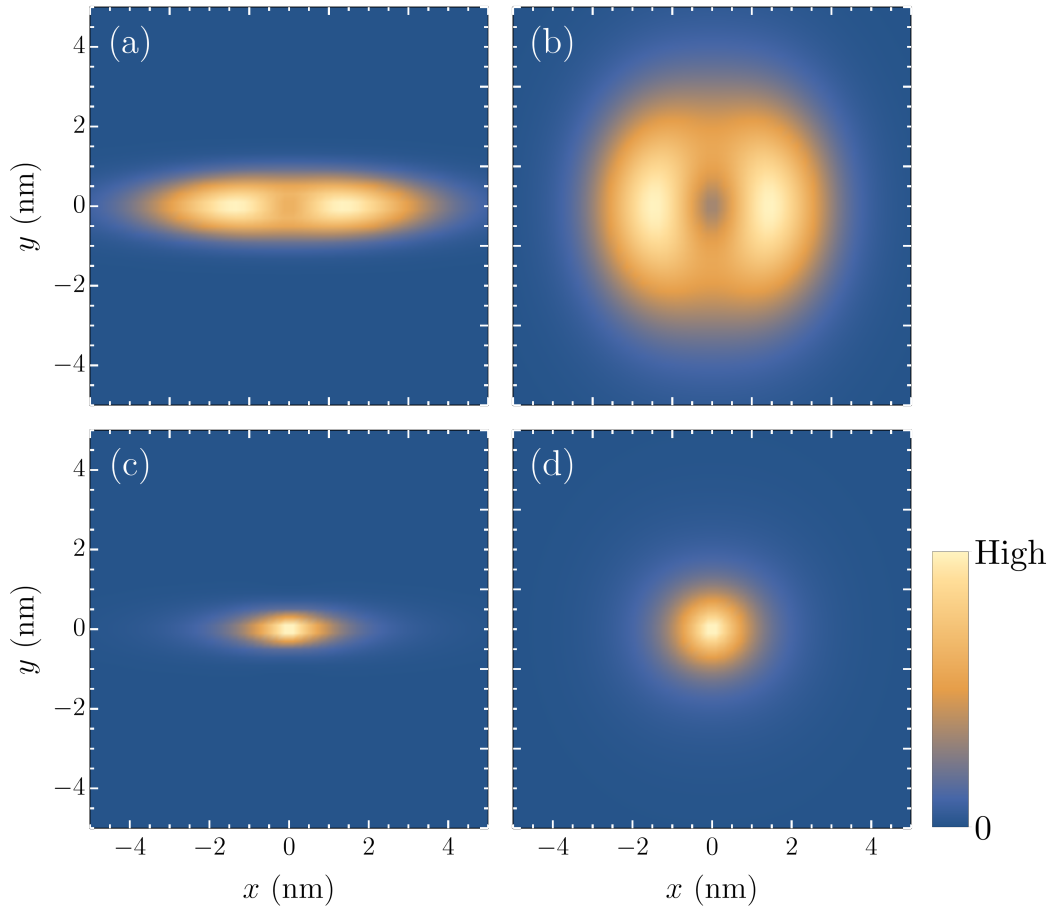


Figure 6.4: Electron-electron (a)-(b) and electron-hole (c)-(d) correlation functions calculated for negative trions in bP (a)+(c) and TiS_3 (b)+(d) suspended in vacuum.

interparticle distances. Furthermore, in the x -direction the electrons are located closer together than the holes whereas in the y -direction the opposite is true. This agrees with the band masses in Table 6.1, i.e. a larger electron band mass in the x -direction and a larger hole band mass in the y -direction.

The electron-hole correlation functions for excitons in bP and TiS_3 are shown in Fig. 6.3. This clearly demonstrates the strongly anisotropic behavior of excitons in bP and the almost isotropic excitons in TiS_3 , as well as the fact that excitons in TiS_3 are in general larger than those in bP, even though in bP they are slightly more spread out in the x -direction.

The electron-electron and electron-hole correlation functions for negative trions

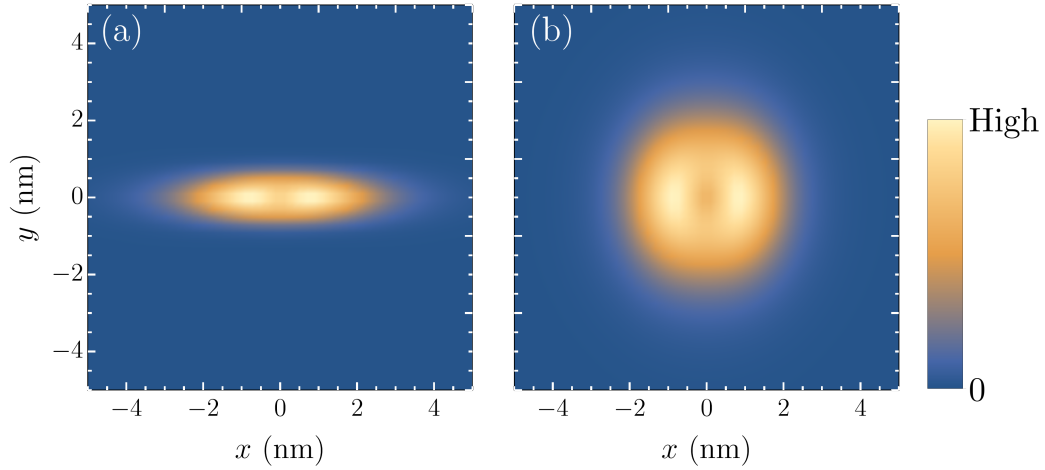


Figure 6.5: Electron-electron correlation functions calculated for biexcitons in bP (a) and TiS₃ (b) suspended in vacuum.

in bP and TiS₃ are shown in Fig. 6.4. This again demonstrates the difference in (an)isotropy between the two materials, although now the slight anisotropy in TiS₃ is also apparent in the electron-electron correlation function. The electron-electron correlation functions show two maxima along the x -direction, instead of one in the origin. This is a consequence of the Coulomb repulsion between the two electrons [147,210] and this effect is therefore not present in the electron-hole correlation functions. This figure also clearly shows the larger spatial extent of the electron-electron correlation functions as compared to the electron-hole correlation functions, which is consistent with the average interparticle distances shown in Table 3.4.

For biexcitons the electron-electron correlation functions for bP and TiS₃ are shown in Fig. 6.5. This shows that the electron-electron correlation functions for biexcitons are qualitatively similar to those for negative trions, except that the system is more compact. This is related to the smaller interparticle distances for biexcitons as compared to negative trions found in Table 6.3.

6.4 Excitons in strained bP

In this section the influence of in-plane uniaxial strain on excitons in monolayer and bilayer bP is investigated. To this end, the effective band masses are calculated from a numerical four-band tight-binding method [193]. The 2D polarizability of

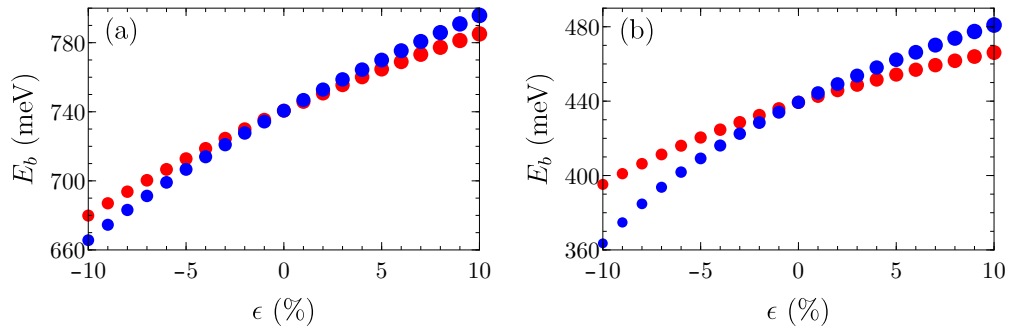


Figure 6.6: Exciton binding energy calculated for monolayer (a) and bilayer (b) bP suspended in vacuum as a function of the strain in the x -direction (blue) and y -direction (red). The size of the dots indicates the value of the exciton wave function in the relative coordinate origin, scaled relatively to the value for 10% strain in the x -direction.

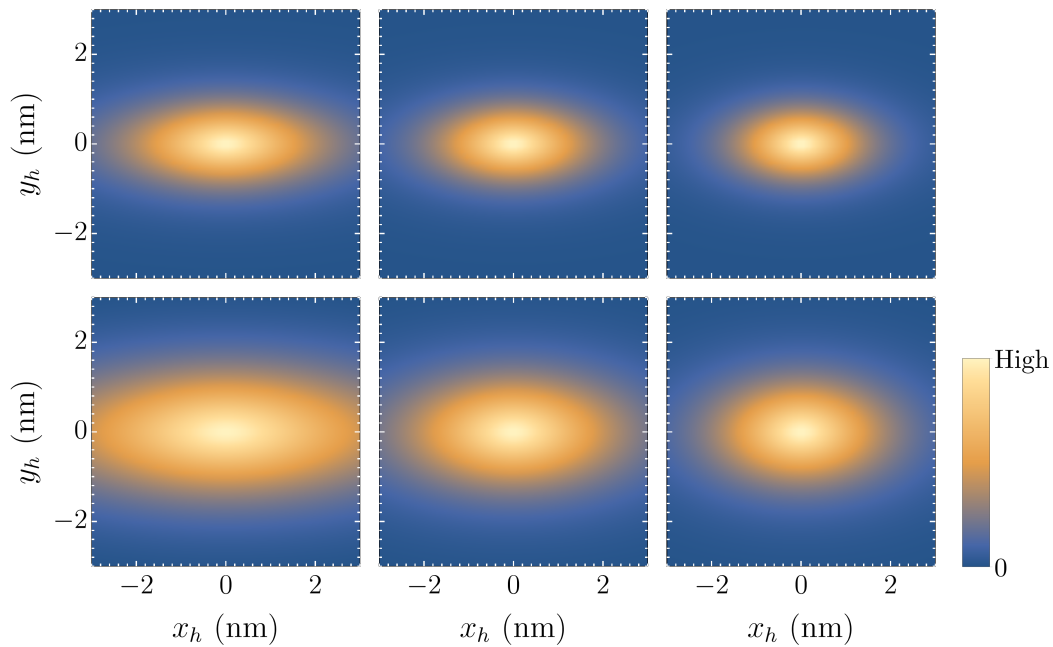


Figure 6.7: Exciton wave function calculated for monolayer (top) and bilayer (bottom) bP suspended in vacuum as a function of the hole coordinates for an electron fixed in the origin. Three different strain values in the x -direction were considered: -10% (left), 0% (middle), and 10% (right).

	-10%	0%	10%
Monolayer	2.60	2.18	1.94
Bilayer	2.92	2.09	1.75

Table 6.4: Anisotropy ratio x_{eh}/y_{eh} of the exciton average interparticle distance calculated for both monolayer and bilayer bP for three different strain values in the x -direction.

bilayer bP is taken to be twice that of monolayer bP [209, 210]. A paper which includes the results presented in the remainder of this section is currently being written.

In Fig. 6.6 the exciton binding energy is shown as a function of strain. The results show that the binding energy increases (decreases) in a non-linear way as a result of tensile (compressive) strain. The wave function in the electron-hole relative coordinate origin, which is a measure of the absorbance of the corresponding exciton state as shown in Eq. (3.21), follows the same pattern as the binding energy. This is because a larger binding energy is associated with a more compact wave function, which has a relatively larger value in the relative coordinate origin. Applying strain in the x -direction has a more pronounced effect as compared to applying strain in the y -direction. As such, it can be concluded that applying tensile strain, particularly in the x -direction, makes excitons in bP optically more active. Furthermore, excitons in bilayer bP are less strongly bound and are more susceptible to applied strain than their counterparts in monolayer bP. Notice that the exciton binding energy for monolayer bP differs somewhat from the value given in Table 6.2 because there is a small difference between the calculated band masses and those from the literature.

The exciton wave function is shown for different strain values in the x -direction in Fig. 6.7. This clearly shows the anisotropic nature of the excitons in both monolayer and bilayer bP. Furthermore, it is clear that applying tensile strain leads to a more compact wave function, which is related to the larger binding energy. For the same reason, the monolayer bP exciton wave functions are more compact than those in bilayer bP. Remarkably, tensile strain leads to a more symmetric exciton wave function, i.e. it partly restores the isotropy in the energy band structure. Compressive strain, on the other hand, increases this anisotropy even further. This is quantified in Table 6.4, where the ratio of the average interparticle distances in the x - and y -direction is shown. This clearly demonstrates that this effect is more pronounced in bilayer bP, for which in the case of 10% compressive strain the ex-

citons are almost three times more spread out in the x -direction as compared to the y -direction, while for 10% tensile strain the excitons are less than two times more spread out in the x -direction as compared to the y -direction. The same qualitative effect, although less pronounced, was found in the case of strain in the y -direction.

6.5 Conclusion

In this chapter the properties of excitons, trions, and biexcitons were studied in 2D materials with anisotropic band structures, more specifically monolayer bP and monolayer TiS₃. For all three excitonic complexes the binding energies were calculated using the SVM and good agreement was found with theoretical results from the literature when available. The binding energies for excitonic complexes in TiS₃ are comparable to those in TMDs, whereas in bP they can be almost twice as large.

Next, the pair correlation functions and average interparticle distances were calculated, which showed an important difference between the two materials. In bP the electron and hole anisotropy directions are parallel and therefore excitonic complexes in bP are anisotropic as well. In TiS₃, however, the electron and hole anisotropy directions are perpendicular and as a result excitonic complexes in TiS₃ are almost isotropic.

Finally, the effect of uniaxial tensile and compressive strain in different directions on the properties of excitons in bP was studied and it was found that applying tensile strain increases the exciton binding energy and restores the isotropy in the excitonic complexes, whereas compressive strain decreases the exciton binding energy and increases the anisotropy even further.

CHAPTER 7

Interlayer excitons in TMD heterostructures

In this chapter the properties of interlayer excitons in TMD heterostructures, i.e. excitons which consist of an electron in one layer and a hole in the other layer, are studied in the multi-band Dirac model. An expression for the electron-hole interaction potential in these systems is derived, taking into account the effect of the dielectric environment above, below, and between the two TMDs as well as polarization effects both in the transition metal layer and in the chalcogen layers of the TMDs. The interlayer exciton binding energy is calculated and its dependence on the dielectric environment is investigated. Finally, the excitonic absorbance spectrum is obtained and it is shown that the interlayer exciton signature is influenced by a perpendicular electric field.

7.1 TMD heterostructures: band alignment and interlayer coupling

Up to now only the monolayer form of TMDs has been considered in this thesis. However, as mentioned in section 1.2, it is also possible to stack different kinds of monolayer TMDs on top of each other and as such create a so-called van der Waals heterostructure [39]. Depending on the materials which are combined, this stacking can result in different types of energy band alignment, as is shown in Fig. 7.1. When the bands of the two combined TMDs are staggered, which

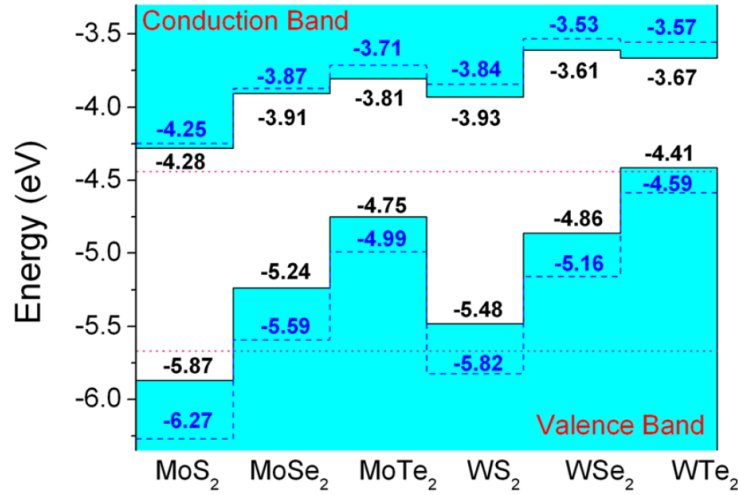


Figure 7.1: Band alignment of different monolayer TMDs obtained using two different numerical methods (solid, black and dashed, blue). Figure taken from Ref. [221].

is known as *type-II band alignment*, low-energy electrons naturally reside in one TMD while low-energy holes are located in the other TMD. These electrons and holes can then form so-called *interlayer excitons*, which were detected in recent experiments [216–219] and were found to have a binding energy of the order of hundred meV and a lifetime which is one to two orders of magnitude larger than that of intralayer excitons [217, 220]. These interlayer excitons also play a crucial role in excitonic superfluidity, as will be seen in the next chapter. Type-II band alignment has been theoretically predicted [221–224] and experimentally found [225] to occur in a wide range of TMD heterostructures, i.e. Fig. 7.1 shows that this is the case for all possible combinations of the four most common TMDs studied in this thesis except for MoSe₂/WS₂ for which different alignment types are predicted by different numerical methods. Therefore, the properties of interlayer excitons in all these TMD heterostructures will now be investigated. The results presented in this chapter were published in Physical Review B [226].

The interlayer coupling between different TMDs will be discussed in more detail in the next chapter. In this chapter it is only important to note that the interlayer hopping energy between the valence bands of the different TMDs is of the order of 0.1 eV [227], while between the conduction bands this hopping energy is considerably smaller still [228]. Since these energies are much smaller than the band offsets there is very little hybridization between the two layers and it is a good approxima-

tion to assume that the TMDs in a TMD heterostructure are completely decoupled from each other. The interlayer exciton Hamiltonian can therefore be written as

$$H_{\sigma}^{exc}(\mathbf{k}^e, \mathbf{k}^h) = \begin{pmatrix} \delta_1 - V(r_{eh}, h) & -a^h t^h k_+^h & a^e t^e k_-^e & 0 \\ -a^h t^h k_-^h & \delta_2 - V(r_{eh}, h) & 0 & a^e t^e k_-^e \\ a^e t^e k_+^e & 0 & \delta_3 - V(r_{eh}, h) & -a^h t^h k_+^h \\ 0 & a^e t^e k_+^e & -a^h t^h k_-^h & \delta_4 - V(r_{eh}, h) \end{pmatrix}, \quad (7.1)$$

with $V(r_{eh}, h)$ the interlayer interaction potential, with h the interlayer distance, which will be derived in the next section and with

$$\begin{aligned} \delta_1 &= \frac{\Delta^e - \Delta^h}{2}, & \delta_2 &= \frac{\Delta^e + \Delta^h}{2} - \lambda^h s^h \tau^h, \\ \delta_3 &= -\frac{\Delta^e + \Delta^h}{2} + \lambda^e s^e \tau^e, & \delta_4 &= -\frac{\Delta^e - \Delta^h}{2} + \lambda^e s^e \tau^e - \lambda^h s^h \tau^h, \end{aligned} \quad (7.2)$$

and $k_{\pm}^j = \tau^j k_x^j \pm i k_y^j$. The superscript e or h denotes a parameter from the electron or hole TMD, respectively. The band offset between the two TMDs appears as a diagonal term in the above Hamiltonian and can therefore be absorbed into the exciton energy. Analogous to the discussion on excitons in monolayer TMDs, the eigenvalue equation of this Hamiltonian can either be solved by exploiting the commutation with the exciton angular momentum operator and numerically solving the resulting set of coupled equations as explained in subsection 3.1.1, or by decoupling this set of equations to a single equation and solving it self-consistently as explained in subsection 3.1.2. In this chapter the latter method is chosen and attention is focused on bright intravalley s state A excitons with zero center of mass momentum. Following the decoupling procedure of subsection 3.1.2 then leads to the equation in relative coordinates

$$\begin{aligned} &\left(- (a^e t^e)^2 \left(\frac{\partial}{\partial r} g_4(E_{\sigma}^{exc}, r) \right) \frac{\partial}{\partial r} - (a^h t^h)^2 \left(\frac{\partial}{\partial r} g_1(E_{\sigma}^{exc}, r) \right) \frac{\partial}{\partial r} + \delta_2 - V(r, h) \right. \\ &\quad \left. - (a^e t^e)^2 g_4(E_{\sigma}^{exc}, r) \nabla_{\mathbf{r}}^2 - (a^h t^h)^2 g_1(E_{\sigma}^{exc}, r) \nabla_{\mathbf{r}}^2 \right) \phi_{c,v}^{e,h}(r) = E_{\sigma}^{exc} \phi_{c,v}^{e,h}(r), \end{aligned} \quad (7.3)$$

with

$$g_{1(4)}(E_{\sigma}^{exc}, r) = (E_{\sigma}^{exc} + V(r, h) - \delta_{1(4)})^{-1}. \quad (7.4)$$

Solving the above differential equation gives the interlayer exciton energy which can then be used to find the interlayer exciton binding energy which is given by

$$E_b = \frac{\Delta^e + \Delta^h}{2} - \lambda^h s^h \tau^h - E_\sigma^{exc}. \quad (7.5)$$

7.2 Interlayer interaction potential

An expression for the interlayer interaction potential can be derived from Gauss's law, analogous to the derivation of the interaction potential in monolayer TMDs in section 2.4. In order to take into account the possibility of a layered substrate between the two TMDs and of polarization effects in the chalcogen layers of each TMD [229], Gauss's law is now solved for a stack of N 2D layers. Placing a test charge in one of these layers leads to induced charge densities in all N layers. Including the possibility of anisotropic dielectrics between the 2D layers, i.e. $\varepsilon_r^i \neq \varepsilon_z^i$ for the homogeneous 3D region i , the general solution for the electrostatic potential in such a 3D region can be written as

$$\phi_{\mathbf{q}}^i(z, z') = A_i(z')e^{\sqrt{\varepsilon_r^i/\varepsilon_z^i}qz} + B_i(z')e^{-\sqrt{\varepsilon_r^i/\varepsilon_z^i}qz}, \quad (7.6)$$

with A_i and B_i integration constants which are also dependent on which layer the test charge is placed in. These piecewise solutions need to be matched at each of the N 2D layers [230] and the corresponding boundary conditions are given by

$$\begin{aligned} \phi_{\mathbf{q}}^{i+1}(z_i, z') &= \phi_{\mathbf{q}}^i(z_i, z'), \\ \varepsilon_z^{i+1} \frac{\partial}{\partial z} \phi_{\mathbf{q}}^{i+1}(z_i, z') &= \varepsilon_z^i \frac{\partial}{\partial z} \phi_{\mathbf{q}}^i(z_i, z') + q^2 \chi_{2D}^i \phi_{\mathbf{q}}^i(z_i, z') - \frac{q_1}{A\varepsilon_0} \delta_{z', z_i}, \end{aligned} \quad (7.7)$$

with z' equal to one of the z_i . Furthermore, assuming region i ($i = 1, \dots, N+1$) to be located between z_{i-1} and z_i , which implies that $z_0 = -\infty$ and $z_{N+1} = +\infty$, $B_1 = A_{N+1} = 0$ has to be imposed in order to avoid divergences. As such the electrostatic potential can be uniquely determined, from which the reciprocal interaction potential in turn is immediately found by means of Eq. (2.37) (with in this case a general z' instead of $z' = 0$). The interlayer interaction potential is found by taking $z = -z' = \pm h/2$. The result will depend on how the total system is modeled.

Two possible models of a TMD heterostructure are shown in Fig. 7.2. In (a) the TMDs are modeled by monolayers and the barrier between the two TMDs is modeled by a 3D homogeneous material. The substrates above (t) and below (b) the

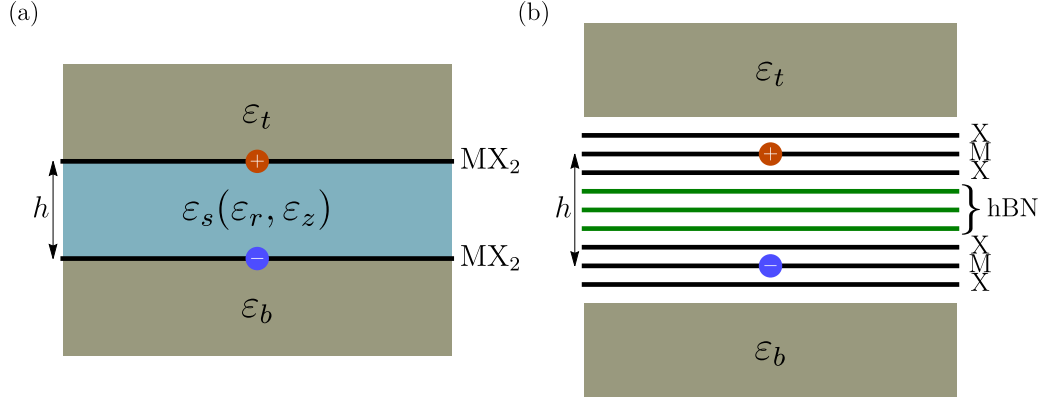


Figure 7.2: Schematic illustration of a TMD heterostructure with substrates with isotropic dielectric constants ε_b and ε_t below and above the system, respectively. (a) The TMDs are modeled by monolayers with 2D polarizabilities χ_{2D}^b and χ_{2D}^t for the bottom and top TMD layer, respectively. The barrier between the two layers has a dielectric constant ε_r and ε_z parallel and perpendicular to the plane, respectively. (b) The TMDs are modeled by trilayers with 2D polarizabilities $\chi_{2D}^{i,M}$ and $\chi_{2D}^{i,X}$ for the transition metal and chalcogen layers, respectively, with $i = b, t$. In between the two TMDs are hBN layers with 2D polarizability χ_{2D}^{hBN} . The interlayer distance h is defined as the separation between the transition metal layers of the two TMDs.

TMD heterostructure are assumed to be isotropic, i.e. $\varepsilon_r^{t/b} = \varepsilon_z^{t/b} = \varepsilon_{t/b}$, whereas for the barrier between the two TMDs the more general case in which ε_r and ε_z can differ from each other is considered. The following dielectric function is found for the interlayer interaction:

$$\varepsilon\left(q, -\frac{h}{2}, \frac{h}{2}\right) = \frac{\varepsilon_b + \varepsilon_t + (\chi_{2D}^b + \chi_{2D}^t)q}{2} \cosh\left(\sqrt{\frac{\varepsilon_r}{\varepsilon_z}} hq\right) + \frac{\varepsilon_r \varepsilon_z + (\varepsilon_b + \chi_{2D}^b q)(\varepsilon_t + \chi_{2D}^t q)}{2\sqrt{\varepsilon_r \varepsilon_z}} \sinh\left(\sqrt{\frac{\varepsilon_r}{\varepsilon_z}} hq\right), \quad (7.8)$$

with χ_{2D}^b (χ_{2D}^t) the 2D polarizability of the bottom (top) TMD. The real space interaction potential can be found by taking the inverse 2D Fourier transform of the reciprocal potential. In general, however, no analytic expression can be found and it has to be obtained by numerical integration. The only limits for which an analytic expression for the real space interaction potential can be found are: 1) $h = 0$, for which $\varepsilon(q) = \kappa + \chi_{2D}q/2$ and the interaction potential reduces to the

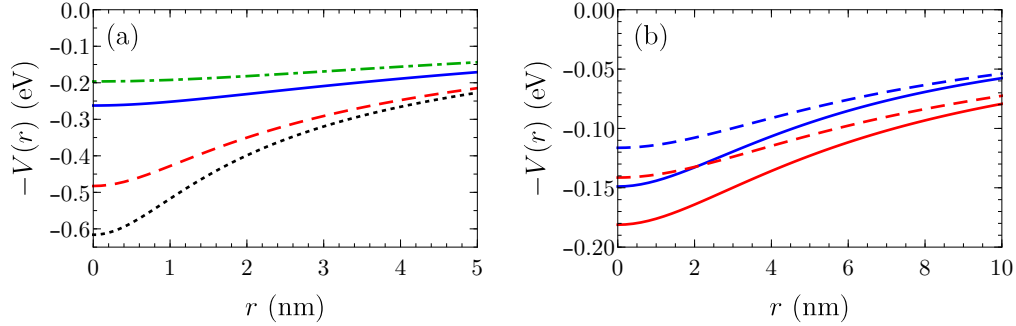


Figure 7.3: (a) Solid, blue: Interlayer interaction potential between a hole and an electron in a TMD heterostructure calculated for $\varepsilon_b = \varepsilon_t = \varepsilon_s = 1$, interlayer distance $h = 1$ nm, and with 2D polarizabilities $\chi_{2D}^b = \chi_{2D}^t = 8$ nm. Dashed, red: Same as the previous but now for $\chi_{2D}^t = 0$. Dot-dashed, green: Interlayer interaction potential taking into account the polarizabilities of the chalcogen layers with $\chi_{2D}^{b,X} = \chi_{2D}^{t,X} = 2$ nm. Dotted, black: Intralayer interaction potential (2.40) with $r \rightarrow \sqrt{r^2 + h^2}$. (b) Interlayer interaction potential calculated for a MoS₂/WS₂ heterostructure on SiO₂ (blue) and between hBN layers (red) and with 1 layer of hBN between the two TMDs which are modeled by trilayers with (dashed) and without (solid) polarization effects in the chalcogen layers with $\chi_{2D}^X = \chi_{2D}^M/4$. Dielectric constants of $\varepsilon_b = 3.8$ for SiO₂ and ($\varepsilon_r = 4.5, \varepsilon_z = 1$) for the hBN substrates were used, as well as a 2D polarizability of $\chi_{2D}^{\text{hBN}} = 1.17$ nm for the hBN layer in the barrier.

intralayer potential (2.40) (when one of the 2D polarizabilities is set to 0) and 2) $\chi_{2D}^b = \chi_{2D}^t = 0$ and $\varepsilon_b = \varepsilon_t = \varepsilon_r = \varepsilon_z = 1$, for which $\varepsilon(q, h) = e^{hq}$ and the interaction potential reduces to $q_1 q_2 / (4\pi\varepsilon_0 \sqrt{r^2 + h^2})$.

In Fig. 7.2(b) the TMDs are modeled by trilayers, i.e. a transition metal layer between two chalcogen layers, and the barrier between the two TMDs is modeled by a stack of 2D layers. The interlayer distance h is defined as the separation between the transition metal layers of the two TMDs and is therefore given by $h = (N_s + 3)d$ with N_s the number of layers in the barrier and $d = 0.333$ nm the elementary distance between the different layers in the system (for simplicity it is assumed that the distance between the transition metal and chalcogen layers of a TMD is also equal to d). Therefore, when there is no barrier between the two TMDs, the interlayer distance h equals 1 nm. In principle an analytic expression for $\varepsilon(q, -h/2, h/2)$ for the interaction between a charge in the transition metal layer of the top TMD and a charge in the transition metal layer of the bottom TMD can

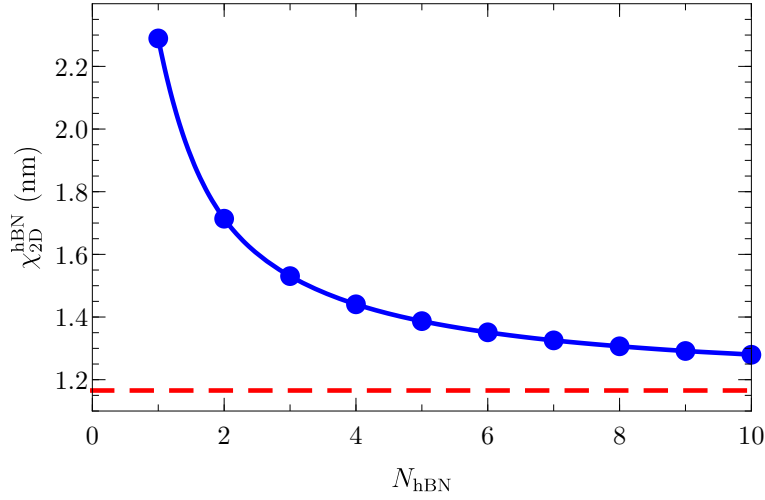


Figure 7.4: 2D polarizability of the hBN layers for which the interaction potential is identical to that when a homogeneous barrier is present between the TMDs, which are modeled by monolayers, with $\varepsilon_r = 4.5$ and $\varepsilon_z = 1$, calculated as a function of the number of hBN layers. The parameters $\varepsilon_b = \varepsilon_t = 1$ and $\chi_{2D}^b = \chi_{2D}^t = 8$ nm are chosen. The thickness of the homogeneous barrier is modified according to the number of hBN layers. The dashed red line indicates the in-plane 2D polarizability $\chi_{2D}^{\text{hBN}} = d(\varepsilon_r - 1)$. The blue curve is a guide to the eye.

be found. This expression is, even in the simple case of a single hBN layer barrier and the absence of polarization in the chalcogen layers, very lengthy and therefore not given here. The real space interaction potential can again only be determined numerically.

The results for the real space interaction potential are shown in Fig. 7.3. This shows that the interaction potential is considerably weaker than what is found by simply substituting $r \rightarrow \sqrt{r^2 + h^2}$ in the intralayer interaction potential (2.40). This is partly due to the additive effect of the screening in the two layers since assuming the 2D polarizability to be zero in one of the layers leads to a potential which is closer to that obtained with the simple substitution in the intralayer potential. Furthermore, the additional dielectric screening effect in the chalcogen layers reduces the interaction strength as expected. The dielectric environment above and below the heterostructure only leads to an approximately constant shift of the interaction potential.

Furthermore, there are also two possible ways of modeling the presence of hBN as a barrier: as a homogeneous 3D slab with a relative dielectric constant ε_s or as

	MoS ₂	MoSe ₂	WS ₂	WSe ₂
MoS ₂	119.5/103.1	112.3/97.1	117.1/101.4	112.1/97.1
MoSe ₂	113.9/98.7	107.4/93.2	111.4/96.9	106.9/93.0
WS ₂	116.4/100.7	109.3/94.7	114.8/99.6	109.7/95.3
WSe ₂	112.7/97.7	106.1/92.1	110.9/96.5	106.3/92.5

Table 7.1: Interlayer exciton binding energy (meV) calculated for different TMD heterostructures modeled by two monolayers on top of a SiO₂ substrate ($\epsilon_b = 3.8$) with interlayer distance $h = 0.6$ nm (left) and $h = 1$ nm (right) (i.e. no barrier between the two TMDs). The rows and columns indicate the n -doped (bottom layer) and p -doped (top layer) materials, respectively.

a stack of 2D layers with 2D polarizability χ_{2D}^{hBN} . The relation between these two parameters is approximately given by $\chi_{2D}^{\text{hBN}} = d(\epsilon_s - 1)$ [78]. When calculating the interlayer interaction potential in both models it is found that they can never be identical when hBN is assumed to be isotropic in the 3D model. It turns out that the out-of-plane relative dielectric constant needs to be set equal to 1 in order to have equal interaction potentials in the two models. In Fig. 7.4 the 2D polarizability is shown for which the interaction potential in the 2D model is identical to that in the 3D model with $\epsilon_z = 1$ and $\epsilon_r = 4.5$ as a function of the number of hBN layers. This shows that for an increasing number of hBN layers the equivalent 2D polarizability converges to the result found using the formula of Ref. [78]. For a finite number of layers the 2D polarizability is always larger than this limiting value, with a maximum difference of a factor 2 for a single hBN layer.

The above real space interaction potentials are plugged into Eq. (7.3) in order to obtain the interlayer exciton (binding) energy, wave function, and other associated properties, the results of which are discussed now.

7.3 Numerical results

In Table 7.1 (Table 7.2) the binding energy (average in-plane interparticle distance) of interlayer excitons in different TMD heterostructures is given for two different interlayer distances: $h = 0.6$ nm, which is the lower bound from density functional theory predictions [233, 234], and the above mentioned theoretical value $h = 1$ nm. As such this leads to a range of binding energies and interparticle distances which are relevant for experiments. It is important to note that in these tables all the possible combinations of TMDs are shown, including those where both TMDs

	MoS ₂	MoSe ₂	WS ₂	WSe ₂
MoS ₂	2.37/2.67	2.43/2.75	2.57/2.89	2.62/2.95
MoSe ₂	2.41/2.72	2.47/2.79	2.63/2.95	2.67/3.00
WS ₂	2.58/2.91	2.66/3.00	2.75/3.09	2.81/3.16
WSe ₂	2.61/2.93	2.68/3.02	2.79/3.13	2.84/3.19

Table 7.2: Average interlayer exciton in-plane interparticle distance (nm) calculated for the same systems as in Table 7.1.

are identical, for the sake of completeness. For heterostructures which do not have a type-II band alignment the electron is artificially put in one TMD and the hole in the other TMD. In theory, the necessary band alignment can always be created for any combination of TMDs using a perpendicular electric field, however the required electric field strengths may be unrealistically large depending on the band offsets. It is also possible to create interlayer excitons by external doping of the different TMDs of choice but in that case a dielectric barrier is required between the two TMDs to prevent immediate electron-hole recombination.

In Table 7.1, the difference between the maximum (MoS₂/MoS₂) and minimum (WSe₂/MoSe₂) binding energy is 13.4 meV for $h = 0.6$ nm and 11 meV for $h = 1$ nm. The binding energies for $h = 1$ nm are smaller than those for $h = 0.6$ nm because of the reduced interaction strength. Heterostructures consisting of two TMD layers containing sulfur have noticeably larger binding energies than heterostructures consisting of two TMD layers containing selenium. The difference between the maximum (WSe₂/WSe₂) and minimum (MoS₂/MoS₂) interparticle distance in Table 7.2 is 0.47 nm for $h = 0.6$ nm and 0.52 nm for $h = 1$ nm. The interparticle distances for $h = 1$ nm are larger than those for $h = 0.6$ nm because of the reduced interaction strength. Heterostructures consisting of two TMD layers containing tungsten have noticeably larger interparticle distances than heterostructures consisting of two TMD layers containing molybdenum. Therefore it can be concluded that the chalcogen atoms mostly influence the binding energy whereas the transition metal atoms mostly influence the interparticle distance. Notice also that the result for e.g. MoS₂/MoSe₂ is slightly different from that for MoSe₂/MoS₂ because of the asymmetric dielectric environment. The intralayer exciton binding energies are, respectively, 320.9 meV, 290.1 meV, 284.6 meV, and 265.1 meV for monolayer MoS₂, MoSe₂, WS₂, and WSe₂ on a SiO₂ substrate. These are about a factor 3 larger than the interlayer exciton binding energies. The corresponding intralayer exciton average interparticle distances are 1.02 nm, 1.05 nm, 1.21 nm,

	Substrate	State	This thesis		Literature
			0.6 nm	1 nm	
MoS ₂ /WS ₂	Vacuum	1s	221	197	430 [231]
		2s	134	124	-
		3s	91	86	-
	SiO ₂	1s	117/139	101/120	-
		2s	56/65	51/59	-
		3s	32/36	30/34	-
MoSe ₂ /WSe ₂	Vacuum	1s	195	175	320 [231]
		2s	123	114	-
		3s	86	81	-
	SiO ₂	1s	107/124	93/108	173 [232]
		2s	54/62	49/57	69 [232]
		3s	32/36	30/33	35 [232]

Table 7.3: Interlayer exciton binding energy (meV) calculated for the lowest three s states for two different TMD heterostructures in vacuum and on top of a SiO₂ substrate ($\epsilon_b = 3.8$), modeled by two monolayers (left) and two trilayers with no polarization effects in the chalcogen layers (right), with interlayer distance $h = 0.6$ nm and $h = 1$ nm (i.e. no barrier between the two TMDs) compared with theoretical results from the literature. Molybdenum- and tungsten-based TMDs are n -doped (bottom layer) and p -doped (top layer), respectively.

and 1.22 nm, respectively. These are about a factor 2.5 smaller than the interlayer exciton average interparticle distances.

In Table 7.3 the interlayer exciton binding energies for two different TMD heterostructures are compared with other theoretical studies based on first-principles many-body perturbation theory with the Bethe-Salpeter equation [231] and on a solution of the effective mass Wannier equation [232]. Here, considerably smaller binding energies are found which is possibly due to the fact that other models for the interaction potential are used in the other theoretical works. The agreement is better for higher excited states, which is because the binding energy converges to 0 in this limit, and for smaller interlayer distances. In Ref. [231] interlayer distances between 0.6 nm and 0.65 nm were used whereas in Ref. [232] an interlayer distance of 0.645 nm was used. Little to no details on the interaction potential are given in Ref. [231] but the authors claim that their large interlayer exciton binding energies, which are only 20% smaller than the intralayer exciton binding energies,

	Substrate t/b	$N_{\text{hBN}} = 1$	$N_{\text{hBN}} = 2$	$N_{\text{hBN}} = 3$
MoS ₂ /WS ₂	Vacuum/SiO ₂	103/83	90/74	81/68
	hBN/hBN	133/107	118/97	107/88
MoSe ₂ /WSe ₂	Vacuum/SiO ₂	94/75	83/68	75/62
	hBN/hBN	121/96	108/87	98/81

Table 7.4: Interlayer exciton binding energy (meV) calculated for two different TMD heterostructures in two different dielectric environments for 1 up to 3 layers of hBN between the two TMDs which are modeled by trilayers with (right) and without (left) polarization effects in the chalcogen layers with $\chi_{2\text{D}}^X = \chi_{2\text{D}}^M/4$. Dielectric constants of $\varepsilon_b = 3.8$ for SiO₂ and ($\varepsilon_r = 4.5, \varepsilon_z = 1$) for the hBN substrates were used, as well as a 2D polarizability of $\chi_{2\text{D}}^{\text{hBN}} = 1.17$ nm for the hBN layers in the barrier. Molybdenum- and tungsten-based TMDs are n -doped (bottom layer) and p -doped (top layer), respectively.

are the result of reduced out-of-plane screening. However, as mentioned earlier, it is shown in Fig. 7.3 that the interlayer interaction potential is considerably weaker than what would be expected from a simple substitution $r \rightarrow \sqrt{r^2 + h^2}$ in the intralayer interaction potential because there is a screening effect in both TMDs. In Ref. [232] a model similar to that of this thesis was used for the interlayer interactions, except that the TMDs are modeled by homogeneous slabs with a certain thickness and constant dielectric constant, meaning that there can be a spacing between the charge carriers and the substrate, whereas here the TMDs are modeled by strictly 2D materials with a 2D polarizability. To facilitate comparison the calculations are therefore also done for the case in which the TMDs are modeled by trilayers without polarization effects in the chalcogen layers, meaning that there is a spacing of 0.666 nm between the transition metal layer and the SiO₂ substrate, in accordance with Fig. 7.2(b). These results are also shown in Table 7.3 and the interlayer exciton binding energies are found to be larger due to the reduced influence of the substrate and as such the results are closer to those of Ref. [232].

In Table 7.4 the interlayer exciton binding energy is shown for two different heterostructures, modeled by two trilayers with and without polarization effects in the chalcogen layers, in two different dielectric environments and for a different number of hBN layers between the two TMDs. As expected, the binding energy decreases with increasing number of layers in the barrier and when there are polarization effects in the chalcogen layers, with the latter effect being stronger than the former. Even though the in-plane dielectric constant of hBN is larger than that

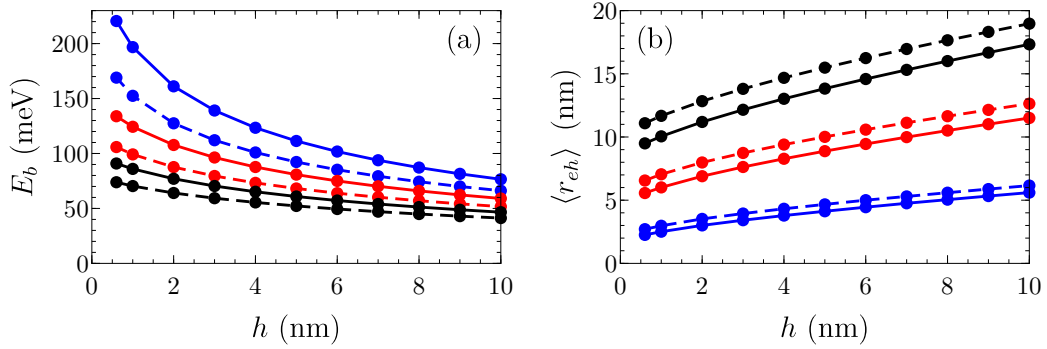


Figure 7.5: Binding energy (a) and average in-plane interparticle distance (b) calculated for the $1s$ (blue), $2s$ (red), and $3s$ state (black) interlayer excitons in a MoS_2/WS_2 heterostructure suspended in vacuum, modeled by two monolayers (solid) and two trilayers with $\chi_{2D}^X = \chi_{2D}^M/4$ (dashed). There is no barrier between the two TMDs. Molybdenum- and tungsten-based TMDs are n -doped (bottom layer) and p -doped (top layer), respectively.

of SiO_2 , the interlayer exciton binding energy of a system with hBN both above and below the heterostructure is larger than that of a system with vacuum (SiO_2) above (below) the heterostructure. This is because, due to the smaller out-of-plane dielectric constant of hBN as compared to that of SiO_2 , the total dielectric constant $\varepsilon = \sqrt{\varepsilon_r \varepsilon_z}$ of the former is smaller than that of the latter for the chosen parameters.

In Fig. 7.5 the interlayer exciton binding energy (a) and average in-plane interparticle distance (b) are shown as a function of the interlayer distance and a comparison is made between the monolayer and the trilayer model for the TMDs. The binding energy decreases in both models with increasing interlayer distance due to the reduced interaction strength, with the binding energy at $h = 10$ nm being more than twice as small as the value at $h = 1$ nm for the ground state. The additional polarization in the chalcogen layers in the double trilayer model reduces the binding energy by an amount of the order of tens of meV, with the effect being more pronounced at small interlayer distances. For higher excited states, which have smaller binding energy, the additional polarization effect in the chalcogen layers is less pronounced. Correspondingly, the average interparticle distance of the interlayer exciton increases with increasing interlayer distance, reaching more than twice the value of $h = 1$ nm at $h = 10$ nm for the ground state. The polarization in the chalcogen layers increases the average interparticle distance by about 0.5 nm,

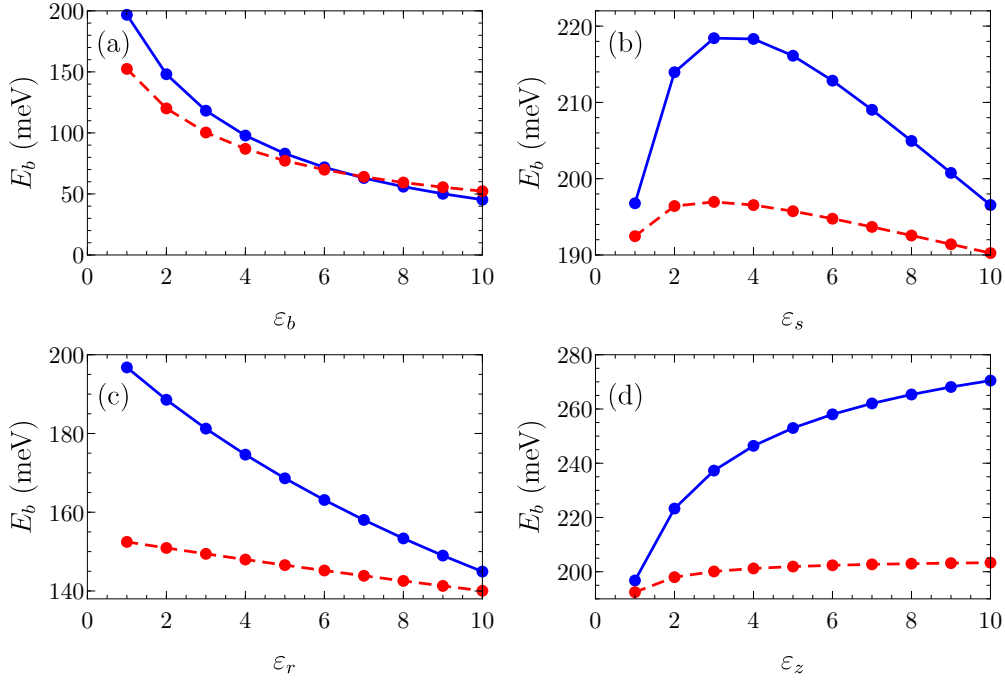


Figure 7.6: Binding energy calculated for interlayer excitons in a MoS₂/WS₂ heterostructure with interlayer distance $h = 1$ nm, modeled by two monolayers (solid, blue) and two trilayers with $\chi_{2D}^X = \chi_{2D}^M/4$ (dashed, red) as a function of ϵ_b (a), ϵ_s (b), ϵ_r (c), and ϵ_z (d). The dielectric constants which are not varied are set to 1 for each figure. The dashed red curves in (b) and (d) are shifted upwards by 40 meV for clarity. Molybdenum- and tungsten-based TMDs are n -doped (bottom layer) and p -doped (top layer), respectively.

1 nm, and 1.5 nm for the $1s$, $2s$, and $3s$ state exciton, respectively. This means that the polarization in the chalcogen layers leads to a larger absolute increase in the average interparticle distance of higher excited states, although the relative increase in interparticle distance is smaller for higher excited states. Remarkably, in absolute terms, the effect of this additional polarization on the interparticle distance is approximately independent on the interlayer distance.

The dependencies of the interlayer exciton binding energy on the different relative dielectric constants of the system are shown in Fig. 7.6. The exciton binding energy decreases by a factor 4 when the dielectric constant of the substrate below the TMD heterostructure increases from 1 to 10, as shown in Fig. 7.6(a). When the polarization in the chalcogen layers is taken into account in the double trilayer

model the decrease in binding energy is limited to a factor 3 for the same dielectric constant range. For small dielectric constants this additional polarization leads to a decrease in binding energy. However, for dielectric constants above $\varepsilon_b \approx 7$ the additional polarization leads to an increase in binding energy. This can be explained due to the fact that, although the chalcogen layers themselves weaken the interactions, they also screen the effect of the substrate. When the effect of the substrate is stronger than that of the chalcogen layers, i.e. for large values of ε_b , this screening of the substrate can enhance the total interaction strength.

A remarkable dependence on the isotropic dielectric constant $\varepsilon_s = \varepsilon_r = \varepsilon_z$ of the barrier between the two TMD layers is found, as shown in Fig. 7.6(b). At first the binding energy increases with increasing ε_s , before reaching a maximum at $\varepsilon_s \approx 4$ after which it starts to decrease. When the additional polarization in the chalcogen layers is taken into account this dependence changes quantitatively, i.e. the binding energy is reduced, the dependence on ε_s is less pronounced, and the maximum binding energy is reached at a slightly smaller value of ε_s , but qualitatively it remains the same. To gain more insight into this behavior the anisotropic case is also studied. The ε_r -dependence, as shown in Fig. 7.6(c), is similar to the ε_b -dependence but it is less pronounced. At some value of ε_r between 12 and 13 the additional polarization in the chalcogen layers again leads to an increase in the exciton binding energy. It is not entirely clear what physical mechanism is behind this increase. Finally, the ε_z -dependence of the exciton binding energy is shown in Fig. 7.6(d). In contrast to what might be expected, the binding energy is found to increase as a function of ε_z . In the limit of large ε_z it converges to a fixed value. When the polarization in the chalcogen layers is taken into account this convergence occurs at smaller values of ε_z . Limiting values of $E_b = 315$ meV and $E_b = 165$ meV are found in the absence and presence of the polarization in the chalcogen layers, respectively. It can be concluded that ε_r and ε_z are in competition with each other for the ε_s -dependence of the binding energy. It is the increase as a function of ε_z which causes the binding energy in (b) to increase for small values of ε_s , whereas the decrease as a function of ε_r and the convergence at large ε_z lead to the subsequent decrease in binding energy for large values of ε_s .

The excitonic absorbance spectrum is shown in Fig. 7.7. The highest energy peak corresponds to intralayer excitons in the WSe₂ layer. The peak next to it corresponds to intralayer excitons in the MoSe₂ layer. The small low-energy peak corresponds to interlayer excitons. The band gap parameters are modified in order to align the different peaks with those from the experimental results. As such an offset of 515 meV is found between the conduction bands of the two TMDs and an offset of 453 meV is found between the valence bands. These results are in-

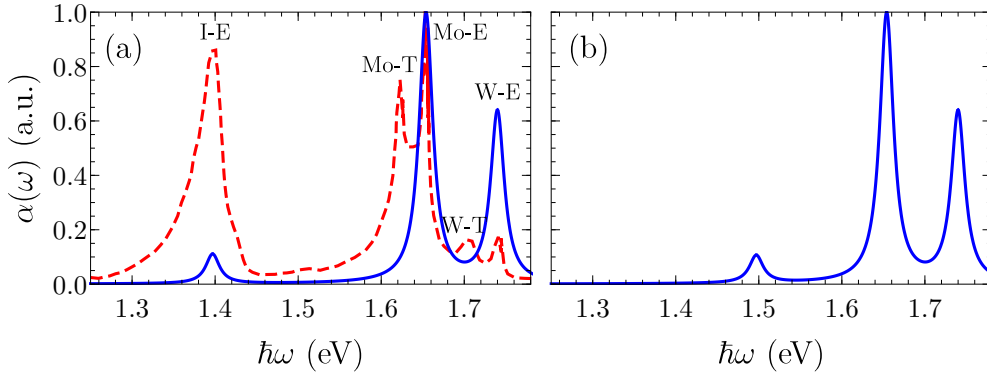


Figure 7.7: Excitonic absorbance spectra calculated for a $\text{MoSe}_2/\text{WSe}_2$ heterostructure modeled by two monolayers on a SiO_2 substrate ($\varepsilon_b = 3.8$) with vacuum on top, in the absence (a) and presence (b) of a perpendicular electric field of -0.1 V/nm and with interlayer distance $h = 1$ nm (i.e. no barrier between the two TMDs). A broadening of $\gamma = 10$ meV was used. The dashed red curve is the experimental photoluminescence result from Ref. [217]. The interlayer (I) and intralayer (Mo/W) exciton (E) and trion (T) peaks are indicated on the figure. Molybdenum and tungsten-based TMDs are n -doped (bottom layer) and p -doped (top layer), respectively.

deed larger than the lower bounds of 310 meV and 230 meV for the conduction band offset and valence band offset, respectively, which were found in Ref. [217], and are also slightly larger than the values of 300-340 meV and 380-430 meV for the conduction and valence band offset, respectively, shown in Fig. 7.1. The additional peaks which are present in the experimental results correspond to trions, which are not considered in the calculations in this chapter. There are considerable differences in the intensities of the interlayer exciton and the WSe_2 intralayer exciton peaks between the calculated absorbance spectrum and the experimental photoluminescence spectrum. The difference lies in the degree of occupation of the different excitonic states. This depends on multiple factors such as the temperature, laser power, recombination times, . . . , and is therefore difficult to predict.

Finally, the results are also shown in the presence of a perpendicular electric field of -0.1 V/nm, i.e. pointing from WSe_2 to MoSe_2 , which is added as a constant term to the diagonal elements of the exciton Hamiltonian (7.1). The intralayer exciton peaks are unaffected, but the interlayer exciton peak shifts upwards in energy by about 0.1 eV. Mathematically, this can be understood since the electric field shifts the energy bands of the two TMDs with respect to each other, thus enhancing

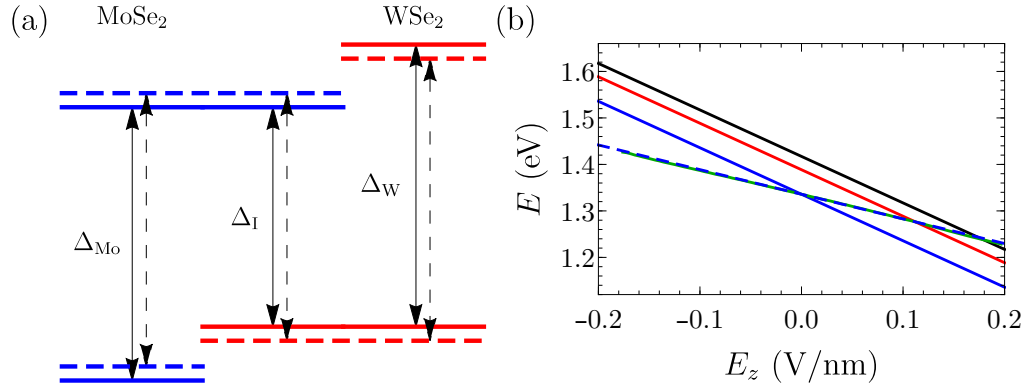


Figure 7.8: (a) Schematic representation of the band diagram of a MoSe₂/WSe₂ heterostructure with (dashed) and without (solid) a perpendicular electric field pointing from WSe₂ to MoSe₂. Δ_{Mo} (Δ_{W}) indicates the intralayer exciton band gap in MoSe₂ (WSe₂) and Δ_{I} indicates the interlayer exciton band gap. (b) 1s (blue), 2s (red), and 3s state (black) interlayer exciton energy calculated as a function of the perpendicular electric field pointing from MoSe₂ to WSe₂ in the case of a hBN substrate above and below the heterostructure. The TMDs are modeled by monolayers. The green curve is the experimental result for the 1s state interlayer exciton from Ref. [235]. The dashed, blue curve is the calculated result when the interlayer distance is reduced from 1 nm to 0.53 nm.

the interlayer exciton band gap, while the intralayer exciton band gaps remain the same. This is shown schematically in Fig. 7.8(a). Physically, this is because the interlayer excitons form an electric dipole pointing (partly) in the perpendicular direction and as such couple to a perpendicular electric field. In this case the electric field is oriented opposite to the interlayer exciton dipole moment which points from the negative to the positive charges, i.e. from MoSe₂ to WSe₂, and as such the interlayer exciton energy is increased. This is very different for intralayer excitons which have an electric dipole pointing completely in the material plane and as such do not couple to a perpendicular electric field. This effect was also found in Ref. [235] in which a bottom and top gate were placed on the hBN substrate above and below the material, respectively. In Fig. 7.8(b) these experimental results, for which a positive electric field means that it points from MoSe₂ to WSe₂, are compared with the results which are calculated here. The interlayer exciton energy depends linearly on the perpendicular electric field, which corresponds with the energy of a electric dipole in an electric field. However, the slopes of the calculated curves, which are determined by the interlayer distance, do not agree with the slope

found in the experimental results. When the interlayer distance is considered as a fitting parameter excellent agreement is found with the experimental results when an interlayer distance of 0.53 nm is assumed, as opposed to the theoretical interlayer distance of 1 nm. This indicates that interlayer exciton formation may cause the electrons and holes to be pulled out of the transition metal layer. This effect is not taken into account in the monolayer TMD single-particle Hamiltonian (2.9) which describes a strictly 2D system. Notice that the slopes for the $1s$, $2s$, and $3s$ states are all equal. A similar experiment was carried out in Ref. [217], in which vacuum (SiO_2) was placed above (below) the heterostructure and where only a top gate and a back gate were used, which is more difficult to model theoretically. The authors found non-linear behavior as a function of the back gate potential, however they mention explicitly that the use of top and bottom gates may elucidate this phenomenon.

7.4 Conclusion

In this chapter interlayer excitons in TMD heterostructures were studied. The appropriate electron-hole interaction potential was derived, which allows to take into account both a homogeneous and a layered substrate between the two TMDs as well as additional polarization effects in the chalcogen layers of the TMDs.

The interlayer exciton binding energy and average interparticle distance were calculated for all combinations of TMDs, which led to the conclusion that the chalcogen atoms mostly influence the binding energy whereas the transition metal atoms mostly influence the interparticle distance. The binding energies were compared with results from the literature when available, showing significant differences which may be the consequence of a difference in interlayer interaction potential.

Next, the effect of different dielectric environments on the exciton binding energy was investigated and a remarkable dependence on the dielectric constant of the barrier between the two TMDs was found, resulting from competing effects as a function of the in-plane and out-of-plane dielectric constants of the barrier. Furthermore, the polarization effects in the chalcogen layers, which in general reduce the exciton binding energy, can lead to an increase in binding energy in the presence of strong substrate effects by screening out the substrate.

Finally, the excitonic absorbance spectrum was calculated and it was shown that the interlayer exciton peak shifts linearly in the presence of a perpendicular electric field, whereas the intralayer exciton peaks are unaffected. This can be at-

tributed to the differently oriented intralayer and interlayer exciton electric dipoles. Furthermore, the dependence of the interlayer exciton peak energy on the perpendicular electric field was found to be in good agreement with experiment, although a slightly lower than usual interlayer distance was needed to obtain near-perfect agreement.

CHAPTER 8

Excitonic superfluidity in TMD heterostructures

In this chapter the possible formation of an interlayer exciton superfluid in TMD heterostructures is investigated. A superlattice of these TMD heterostructures is considered in order to have a 3D superfluid and as such avoid the Berezinskiĭ-Kosterlitz-Thouless transition which limits the critical temperatures in 2D superfluids. The appropriate unscreened interaction potential is derived and polarization effects are taken into account by means of the RPA approximation. The superfluid gap, perpendicular pair correlation length, and condensate fraction are calculated by solving the self-consistent gap equation and very high critical temperatures of up to 270 K are obtained.

8.1 A short history of (conventional) superfluidity

In 1911 Heike Kamerlingh Onnes made a very remarkable discovery: the electrical resistivity of mercury suddenly drops to zero below a critical temperature of 4.2 K, i.e. it becomes a superconductor [236]. In 1938 another exotic low-temperature effect was stumbled upon: liquid helium can flow without viscosity when it is cooled down below a critical temperature of around 2 K, i.e. it becomes a superfluid [237, 238]. In the same year, Fritz London proposed Bose-Einstein condensation as the mechanism underlying the formation of superfluidity in liquid helium [239]. A Bose-Einstein condensate (BEC) is a fourth phase of matter in

which a single-particle state is macroscopically occupied with global phase coherence between the particles, as such leading to an expression of quantum mechanics on a macroscopic scale. This new phase of matter was first theoretically described by Satyendra Nath Bose [240] and Albert Einstein [241] in 1924 in the context of a dilute non-interacting monatomic gas of bosons (atoms for which the total spin of the constituent particles is even, i.e. atoms consisting of an even number of fermions). However, a similar mathematical description can be applied to liquid helium (more specifically helium-4, which consists of two protons, two neutrons, and two electrons), although interactions play a much more prominent role in this system due to the considerably smaller interatomic distance.

It is also possible for a superfluid to form in a system of fermions through a pairing mechanism. A famous example of such a system is helium-3, which lacks a neutron as compared to helium-4 and is therefore a fermion. In this case the interaction potential which leads to the pairing is simply the interatomic potential, which can be modeled by the Lennard-Jones potential. A superfluid with a critical temperature in the mK range was found both experimentally [242, 243] and theoretically [244] in this system in 1972, leading to Nobel Prizes in Physics in 1996 and 2003, respectively. However, the most important example is that of electrons in certain solids which can have an effective attraction between them as a result of electron-phonon interaction, which was shown by Fröhlich in 1950 [245]. The physical picture behind this effective attraction is that of electrons moving in the lattice and leaving behind a trail of lattice deformations behind them. These temporarily displaced positive lattice ions then attract other electrons and as such the electrons can form so-called *Cooper pairs* [246]. These pairs can then condense at low temperatures to form a charged superfluid and as such make the material superconducting. In 1957, Bardeen, Cooper, and Schrieffer presented a minimal theory based on the formation of Cooper pairs which can exhibit superconductivity [247]. It turned out that this BCS theory could qualitatively explain all effects related to conventional superconductors, i.e. for which the pairing is driven by electron-phonon interaction, and could even provide reasonable quantitative agreement with experimental results. This earned them the Nobel Prize in Physics in 1972.

Over the years superconductivity has been detected in many different materials. However, for a long time the critical temperatures which were found never exceeded 40 K. The main reason for this is the rather weak electron-phonon effective interaction which, due to energy conservation, limits the range of electron single-particle states which can contribute to the superconductivity to a window of at most $\hbar\omega_{LO}$ above and below the Fermi level, with ω_{LO} the longitudinal op-

tical phonon frequency. In the 1980s and 1990s new copper-based superconductors were found with critical temperatures of up to 150 K. Much more recently iron-based superconductors appeared with similarly high critical temperatures. For both these new types of superconductors the mechanism behind the pairing is not electron-phonon interaction. However, as for what exactly is the glue that holds the electrons together in these materials remains an open question.

8.2 Excitonic superfluidity

Given the fact that the superfluid critical temperature in fermionic systems is limited by the strength, or rather the weakness, of the interactions between the constituent fermions, it seems natural to consider excitons as a candidate for high-temperature superfluidity. After all, the attractive interaction between the constituent electrons and holes is mediated by the strong long-range Coulomb potential. As such, excitonic superfluidity was first theoretically predicted in 1962 [248]. The price to pay is the fact that this type of superfluidity is strongly hindered by the short radiative lifetime of the excitons.

Therefore, it is advantageous for the superfluid if the electrons and holes are spatially separated in order to prevent this very fast recombination, as was first suggested in Ref. [249]. The first practical realizations of such a system took the form of coupled GaAs/AlGaAs quantum wells, for which a drastic reduction in the width of the peaks in the PL spectrum [250] or a dramatic resonant enhancement of the zero bias tunneling conductance [251] indicated a transition to an ordered state below some critical temperature. However, definitive experimental evidence of excitonic superfluidity in these systems was provided only in 2012, showing a critical temperature of about 1 K [252]. The reason for this low critical temperature is threefold: (1) For experimentally achievable well and barrier thicknesses the electron-hole separation is larger than the effective Bohr radius. (2) The barrier between the two quantum wells (i.e. AlGaAs) has a relatively large dielectric constant which screens the attractive interaction. (3) The reduced exciton mass is small and there is a large mismatch between the electron and hole effective masses.

The discovery of graphene and other 2D materials provided a number of new candidate systems for observing excitonic superfluidity. The combination of an n -doped and a p -doped graphene layer solves almost all of the above problems: the use of hBN allows to create barriers which are a factor 4 thinner as compared to AlGaAs and as such allow for electron-hole separations smaller than the effective Bohr radius, the dielectric constant of hBN is almost a factor 3 smaller as

compared to AlGaAs, and the conduction and valence bands are almost perfectly symmetric. As such, interlayer excitonic superfluidity was predicted to occur in a double monolayer graphene system with critical temperatures up to room temperature [253–255]. Unfortunately, this was never confirmed experimentally because the linear dispersion of graphene implies that the ratio of potential energy to kinetic energy cannot be tuned by means of the electron and hole density and the system is effectively stuck in the weakly interacting regime. Later on it was realized that it is possible to resolve this issue by considering a double bilayer graphene system, which has a parabolic low-energy dispersion. The critical temperature in this system was predicted to be about 20 K [256] and experimental evidence for excitonic superfluidity was indeed recently found [257]. Furthermore, it was shown that the critical temperature can be enhanced by increasing the number of graphene layers [258] and that high-temperature interlayer excitonic superfluidity can also occur in TMD heterostructures [259]. However, it is very important to note that the excitonic superfluidity in these 2D materials could have reached much higher critical temperatures if it had not been for a fundamental thermodynamic argument.

8.3 Berezinskii-Kosterlitz-Thouless transition

In general, the second quantization Hamiltonian of interacting electrons and holes in solids obeys U(1) symmetry, i.e. it is invariant under a transformation $\hat{a} \rightarrow \exp(i\theta)\hat{a}$, as can be seen from the equations (2.41) and (2.42). As will be seen in appendix E, however, the superfluid ground state does not obey this symmetry: the above transformation only holds for $\theta = 0$ and for $\theta = \pi$. Therefore, when the temperature is decreased below the critical temperature T_c the continuous symmetry associated with the phase θ is spontaneously broken, as such allowing for the formation of long-range order with a fixed phase θ , which is necessary for the existence of a superfluid. In mathematical terms: the phase correlation is a constant for $T < T_c$, falls off exponentially with the distance for $T > T_c$, and falls off according to a power law for $T = T_c$, the latter indicating quasi-long-range order. However, as discussed in section 1.2, a spontaneous breaking of a continuous symmetry is not possible in 2D (or lower dimensions) because at non-zero temperature the system can thermally fluctuate to a state with any possible phase θ and as such destroy the long-range order. This effect, which appears at lower dimensions because of the higher density of states, seems to preclude the existence of 2D superfluidity.

However, in 2D systems it is possible for a phase which does not break any symmetry and which exhibits quasi-long-range order, in which the phase correla-

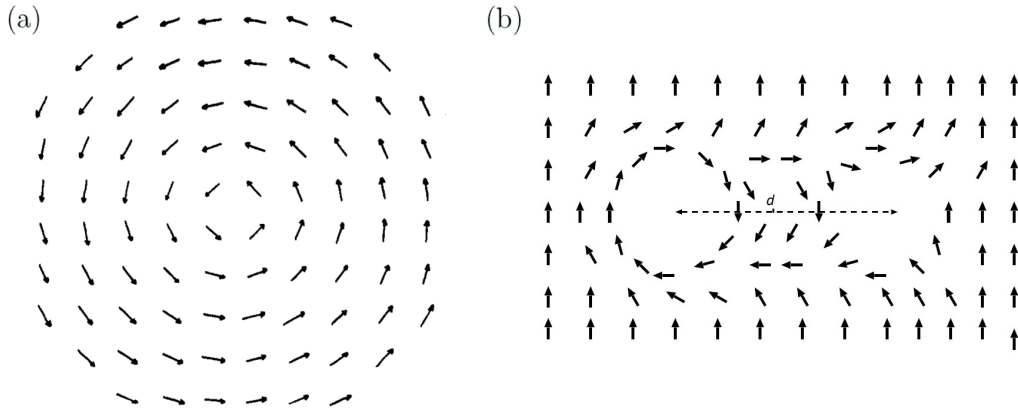


Figure 8.1: Phase of the superfluid in the presence of (a) a vortex and (b) a vortex-antivortex pair separated by a distance d .

tion falls off according to a power law for any non-zero temperature, to exist below some critical temperature. The corresponding phase transition is associated with the dissociation of bound *vortex-antivortex* pairs into unbound vortices and antivortices. A vortex is the flow of the condensate around a region of depleted density known as the vortex core, as shown in Fig. 8.1(a). It is clear that a single vortex or antivortex destroys the phase ordering in the system. For a vortex-antivortex pair, however, there is still a uniform phase order at distances far enough from the pair, as is shown in Fig. 8.1(b). Therefore, the formation of a bound vortex-antivortex pair does not destroy the superfluidity but the formation of a single vortex or antivortex does. It can be shown that the kinetic energy of a free vortex or antivortex is given by $E_{kin} = E_0 \ln(R/\xi)$, with R the size of the system, ξ the size of the vortex core, and $E_0 = \pi n_s \hbar^2/m$ with n_s the superfluid density of particles with mass m . On the other hand, the energy of a bound vortex-antivortex pair is given by $E_{kin} = E_0 \ln(d/2\xi)$, with d the separation distance between the vortex and the antivortex. The details of these calculations are given in appendix D. Furthermore, the entropy S of a vortex is directly related to the number of possible positions of the vortex in the system and is therefore given by $S = 2k_B \ln(R/\xi)$. Equivalently, the entropy of a vortex-antivortex pair is, using $\xi \ll R$, simply given by $S = 4k_B \ln(R/\xi)$. As a result, it is clear that at any non-zero temperature the free energy $F = E_{kin} - TS$ of a bound vortex-antivortex pair is dominated by the entropic contribution and as such thermal excitations of these pairs can always be formed. For a single vortex or antivortex, however, both terms in the free energy

are of the same order and it follows that above a temperature

$$T_c^{\text{BKT}} = \frac{\pi n_s \hbar^2}{2mk_B} \quad (8.1)$$

it is energetically favorable to form single vortices and antivortices and as such to destroy the quasi-long-range order, and the superfluidity with it, in the system. Note that the size of the system and the size of the vortex core do not enter in the above result. This phase transition was first described by Berezinskiĭ [260] and Kosterlitz and Thouless [261] and is therefore referred to as the BKT transition. The critical temperature T_c^{BKT} only depends on the interaction type and strength through the superfluid density and since it is typically lower than the critical temperatures calculated from BCS theory for systems with Coulomb interactions between the particles, this mechanism can limit the effective critical temperature below which superfluidity can be observed in 2D Coulombic systems.

In order to circumvent this problem, a superlattice of alternating monolayer TMDs of two different types with type-II band alignment, where one type is n -doped and the other type is p -doped, will be studied in the remainder of this chapter. A schematic illustration of this system is shown in Fig. 8.2. This is a possible type of system in which the superfluid can act 3D, and as such bypass the BKT transition, but nevertheless can still exhibit the high critical temperatures calculated from BCS theory associated with 2D systems. In order to estimate whether the superfluid acts 3D or 2D the phase coherence length should be known, which represents the length scale over which the superfluid is reduced as a result of a local fluctuation and is related to the size of the vortex core in the above discussion. If the phase coherence length in the perpendicular direction $\xi_z \gg 2d$, with d the interlayer distance and $2d$ therefore the distance between same-type TMDs, the superfluid acts completely 3D, whereas in the opposite case $\xi_z \ll 2d$ it acts completely 2D. A paper on the results presented in the remainder of this chapter has been submitted to Nature Physics.

8.4 Superlattice of TMD heterostructures

8.4.1 Energy spectrum and eigenstates

As mentioned earlier, subsequent layers in bulk TMDs are AB stacked and the corresponding energy spectrum exhibits an indirect band gap. Switching over to TMD heterostructure superlattices, i.e. infinite stacks of alternating monolayer TMDs of two different types, the indirect gap is retained for all combinations of the four

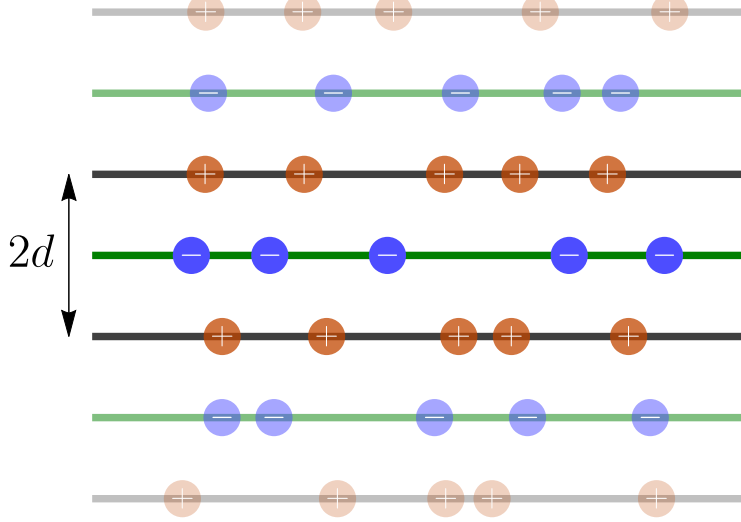


Figure 8.2: Schematic illustration of an infinite superlattice of alternating monolayer TMDs of two different types, indicated by the black and green lines, where one type is n -doped and the other type is p -doped. The periodic distance $2d$, with d the interlayer distance, is indicated by the arrow.

best-known TMDs in the case of AB stacking [223]. As a result, interlayer excitons in these systems would acquire a large center of mass momentum which would complicate matters. Another possible stacking for the heterostructure superlattice is AA stacking, in which all the transition metal atoms are horizontally aligned, as well as all the chalcogen atoms. For this stacking type all combinations of the four best-known TMDs exhibit a direct band gap at the K and K' points except for MoS_2/WS_2 and $\text{MoSe}_2/\text{WSe}_2$ which have an indirect gap [223]. Three of the remaining TMD heterostructures show a type-II band alignment, with the exception being $\text{MoSe}_2/\text{WSe}_2$ as was shown in Fig. 7.1. For a general combination of TMDs the low-energy single-particle Hamiltonian for this system can be written as

$$H_{\mathbf{k},s,\tau} = \begin{pmatrix} H_{s,\tau}^1(k_x, k_y) + \frac{\delta_b}{2} I_2 & T(k_z) \\ T^\dagger(k_z) & H_{s,\tau}^2(k_x, k_y) - \frac{\delta_b}{2} I_2 \end{pmatrix}, \quad (8.2)$$

with $H_{s,\tau}^\ell(k_x, k_y)$ the monolayer Hamiltonian (2.9) for the TMD of type ℓ and with the bias potential δ_b chosen such that the band alignment agrees with that of Ref. [221]. The interlayer coupling part of the Hamiltonian is given by

$$T(k_z) = \begin{pmatrix} 2t_c \cos(k_z d) & 0 \\ 0 & 2t_v \cos(k_z d) \end{pmatrix}, \quad (8.3)$$

with $d = 0.65$ nm the interlayer distance and t_c (t_v) the interlayer hopping parameter between the conduction band d_0 states (valence band $d_{2\tau}$ states) of the different layers. Note that in the case of AB stacking the hopping between the d_0 states vanishes at the K and K' points (and increases linearly with the in-plane wave vector when moving away from these points) because of the trigonal arrangement of the interlayer nearest neighbors and the cylindrical symmetry of the d_0 orbitals. The interlayer hopping between the $d_{2\tau}$ states does not vanish at the K and K' points due to the C_2 symmetry around the z -axis of the $d_{2\tau}$ orbitals. Rather there is an effective interlayer coupling strength $2t_v$ which is given by 0.086 eV, 0.106 eV, 0.109 eV, and 0.134 eV for MoS₂, MoSe₂, WS₂, and WSe₂, respectively [227]. When the stacking between the different TMDs is AA the interlayer nearest neighbors share the same in-plane coordinates. As a result, the interlayer hopping between the d_0 states does not vanish. It was shown in Ref. [228] that the coupling strength between the $d_{2\tau}$ states is almost identical to that in the case of AB stacking and that the coupling strength between the d_0 states is about a factor 1/7 of that between the $d_{2\tau}$ states in the case of bilayer MoS₂. Since this is only determined by the type of orbitals and the spatial separation, which is the same for all TMDs, it will therefore be assumed that $t_c = t_v/7$ is true in general. For TMD heterostructures the effective hopping parameter is assumed to be given by the average value of the hopping parameters of each of the two TMDs, which in general is a good approximation [228] and particularly so when the transition metal atoms of the two TMDs are the same.

The energy spectrum of the system is obtained by numerically solving the eigenvalue equation of the Hamiltonian (8.2) and the result is shown in Fig. 8.3 for a WS₂/WSe₂ heterostructure superlattice. Note that the lowest conduction band is the WS₂ spin down band and the highest valence band is the WSe₂ spin up band. The influence of the interlayer hopping on the energy bands is small as a result of the energy mismatch between the bands of the different TMDs. The band width in the k_z -direction is 1 meV for the lowest conduction band and 27 meV for the highest valence band. The band width of the two-particle electron-hole band is therefore equal to 28 meV.

In the remainder of this chapter the results are shown for the WS₂/WSe₂ su-

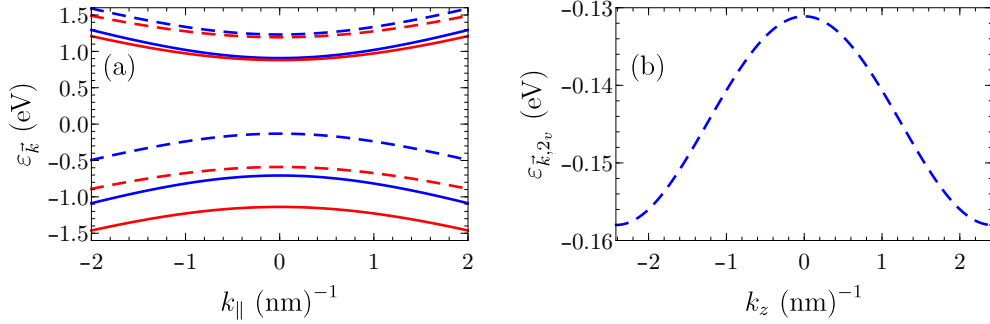


Figure 8.3: (a) Energy spectrum of a WS₂/WSe₂ heterostructure superlattice calculated as a function of the in-plane wave vector component. Solid and dashed bands are associated with WS₂ and WSe₂, respectively. Blue and red bands are spin up and spin down bands, respectively. (b) Highest valence band of a WS₂/WSe₂ heterostructure superlattice calculated as a function of the perpendicular wave vector component.

perlattice because of the relatively large spin splitting in the WS₂ conduction band, i.e. 27 meV, as a result of which the spin up band will only be significantly filled for temperatures above room temperature for the densities considered here and can therefore be neglected. For the WSe₂ valence band the extremely large spin splitting, i.e. 460 meV, assures that neglecting the spin down band is an excellent approximation. As such, for both electrons and holes there are only two low-energy bands, i.e. spin down in the K valley and spin up in the K' valley. In superlattices containing MoS₂ this symmetry between electrons and holes would be broken because the very small spin-orbit coupling in the conduction band of MoS₂ would lead to four low-energy electron bands as opposed to two low-energy hole bands.

For a given spin and valley quantum number, each of the single-particle eigenstates $|\psi_{\mathbf{k},\beta}\rangle$ is a four-component spinor which can be written as

$$|\psi_{\mathbf{k},\beta}\rangle = \begin{pmatrix} C_{1c,\beta}^{\mathbf{k}} |\Phi_{\mathbf{k},1}\rangle \\ C_{1v,\beta}^{\mathbf{k}} |\Phi_{\mathbf{k},1}\rangle \\ C_{2c,\beta}^{\mathbf{k}} |\Phi_{\mathbf{k},2}\rangle \\ C_{2v,\beta}^{\mathbf{k}} |\Phi_{\mathbf{k},2}\rangle \end{pmatrix}, \quad (8.4)$$

where the coefficients $C_{i,\beta}^{\mathbf{k}}$ associated with the pseudospin i of the energy band β are obtained by numerically solving the eigenvalue equation of the Hamiltonian (8.2). The subscript 1(2)_{c(v)} denotes the pseudospin associated with the conduction or valence band of the TMD of type 1 (WS₂) or 2 (WSe₂). These coefficients

reflect the hybridization between the different TMD types. This effect is strongest at the K and K' points and in the valence band, for which the WSe_2 state has 4.67% contribution from the WS_2 layer. At the edge of the Brillouin zone, i.e. for $|k_z| = \pi/2d$, the layers are completely decoupled, which follows from Eq. (8.3).

The position representation of the states $|\Phi_{\mathbf{k},\ell}\rangle$ is obtained by solving the differential eigenvalue equation of the Hamiltonian (8.2). For the in-plane wave vector the low-energy approximation is equivalent to assuming $k_{\parallel}a \ll 1$, which implies that the wavelength of the particles is much larger than the lattice constant and the corresponding solution is given by a plane wave. This approximation is also referred to as the *continuum approximation*. However, because of the small band width in the k_z -direction, states with all possible k_z -values in the first Brillouin zone will be of importance and no continuum approximation, i.e. $k_zd \ll 1$, can be assumed in the perpendicular direction. In the limit of weak interlayer coupling the total solution can therefore be written as

$$\Phi_{\mathbf{k},\ell}(r) = \frac{1}{\sqrt{NA}} e^{i\mathbf{k}_{\parallel}\cdot\boldsymbol{\rho}} \sum_{j=-N/2}^{N/2} \delta^{1/2}(z - j2d - z_{\ell}d) e^{i(2j+z_{\ell})k_zd}, \quad (8.5)$$

with N the number of TMD heterostructures, $\boldsymbol{\rho}$ the in-plane coordinate vector and with $z_{\ell} = 0$ and $z_{\ell} = 1$ for the TMD of the first and second type, respectively.

8.4.2 Coulomb matrix elements between superlattice eigenstates

In this subsection an expression is derived for the bare Coulomb interaction matrix elements for scattering between the eigenstates of the superlattice, i.e.

$$\langle \psi_{\boldsymbol{\kappa}',\alpha'} \psi_{\mathbf{k}',\beta'} | V(r) | \psi_{\boldsymbol{\kappa},\alpha} \psi_{\mathbf{k},\beta} \rangle, \quad \text{with} \quad V(r) = \frac{e^2}{4\pi\epsilon_r\epsilon_0 r}. \quad (8.6)$$

This represents a first particle with wave vector $\boldsymbol{\kappa}$ in band α and a second particle with wave vector \mathbf{k} in band β which interact through the Coulomb potential and as such respectively end up with wave vector $\boldsymbol{\kappa}'$ in band α' and with wave vector \mathbf{k}' in band β' . The relative dielectric constant $\epsilon_r = \sqrt{\epsilon_z\epsilon_{\parallel}}$ accounts for the static screening effects of the ions and the filled valence bands. It is equal to 10.9, 12.3, 9.9, and 11.2 for bulk MoS_2 , MoSe_2 , WS_2 , and WSe_2 , respectively [55]. In the limit of no hybridization between the different TMD types the system effectively consists of two decoupled bulk TMDs whose interlayer distance is twice that of their normal bulk forms. It is shown in Ref. [81] that the dielectric constant of MoS_2 is approximately halved when the interlayer distance is doubled. Therefore,

the heterostructure superlattice dielectric constant is assumed to be given by the average of half the dielectric constants of the two constituent TMDs, which results in a value of 5.5 for the WS_2/WSe_2 superlattice. Note that the bare Coulomb potential, as opposed to the Keldysh potential which is valid for monolayer TMDs, is expected to be appropriate here because for the densities considered in this chapter the average interparticle distance is considerably larger than the interlayer distance and therefore the screening of the interactions is that of a 3D dielectric, which can be quantified by a multiplicative dielectric constant ε_r , instead of a single 2D layer.

As a starting point, the matrix elements between the states $|\Phi_{\mathbf{k},\ell}\rangle$ are given by

$$\begin{aligned} &\langle \Phi_{\mathbf{k}',\ell'_2} \Phi_{\mathbf{k}',\ell'_1} | V(r) | \Phi_{\mathbf{k},\ell_2} \Phi_{\mathbf{k},\ell_1} \rangle = \\ &\delta_{\ell_1,\ell'_1} \delta_{\ell_2,\ell'_2} \delta_{\mathbf{k}+\mathbf{\kappa},\mathbf{k}'+\mathbf{\kappa}'} \frac{e^2}{4\pi\varepsilon_r\varepsilon_0 N A} \frac{2\pi}{q_{\parallel}} \sum_{w=-N}^N e^{i(2w-z_{\ell_1}+z_{\ell_2})q_z d} e^{-|2w-z_{\ell_1}+z_{\ell_2}|q_{\parallel} d}, \end{aligned} \quad (8.7)$$

with A the surface area of the TMD layers and with $\mathbf{q} = \mathbf{k} - \mathbf{k}' = \mathbf{\kappa}' - \mathbf{\kappa}$. Performing the summation in the limit $N \rightarrow \infty$ for the case $\ell_1 = \ell_2$ leads to the known expression [262, 263] for the interaction potential between the same TMD types

$$V^S(q_{\parallel}, q_z) = \frac{e^2}{4\pi\varepsilon_r\varepsilon_0 N A} \frac{2\pi}{q_{\parallel}} \frac{\sinh(2q_{\parallel} d)}{\cosh(2q_{\parallel} d) - \cos(2q_z d)}. \quad (8.8)$$

This expression interpolates between the 2D and 3D limits. In the limit $d \rightarrow \infty$ the last fraction becomes equal to 1 and the 2D interaction potential for N layers of surface area A is recovered. In the limit $d \rightarrow 0$ a Taylor expansion of the trigonometric and hyperbolic functions transforms the last fraction to $2q_{\parallel}/(2d(q_{\parallel}^2 + q_z^2))$ and as such the 3D interaction potential for a volume of $AN2d$ is recovered. This result is shown in Fig. 8.4. A completely analogous procedure for the case $\ell_1 \neq \ell_2$ leads to the interaction potential between the different TMD types

$$V^D(q_{\parallel}, q_z) = \frac{e^2}{4\pi\varepsilon_r\varepsilon_0 N A} \frac{2\pi}{q_{\parallel}} \frac{2 \sinh(q_{\parallel} d) \cos(q_z d)}{\cosh(2q_{\parallel} d) - \cos(2q_z d)}, \quad (8.9)$$

which also reduces to the standard 3D interaction potential in the limit $d \rightarrow 0$ and includes the factor $2e^{-q_{\parallel} d}$ in the limit $d \rightarrow \infty$. This result is also shown in Fig. 8.4.

Because of the large energy gaps between the different bands only the dominant intraband interactions between the lowest conduction band and highest valence band need to be considered in Eq. (8.6), i.e. $\alpha = \alpha' = 1_c$ and $\beta = \beta' = 2_v$ with 1_c and 2_v referring to the dominant component of the state in Eq. (8.4). Retaining

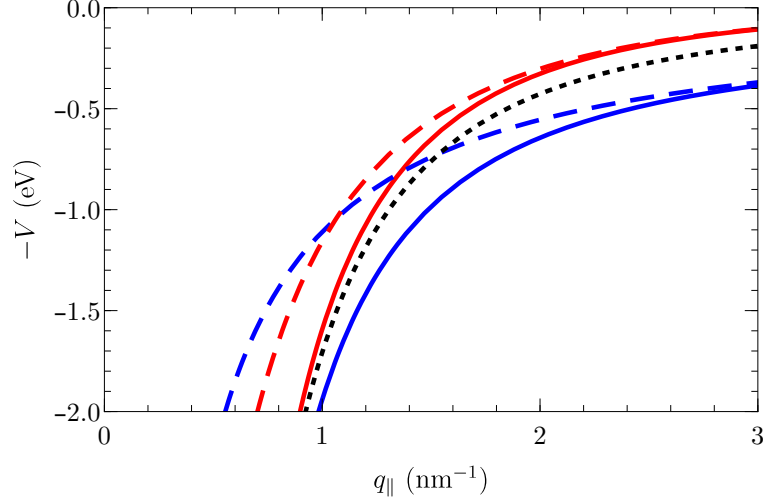


Figure 8.4: Intralayer (solid, blue) and interlayer (solid, red) interaction potential calculated as a function of q_{\parallel} for $q_z = 0$. The corresponding dashed curves are the 2D intralayer ($\propto 1/q_{\parallel}$) and 2D interlayer ($\propto 2e^{-q_{\parallel}d}/q_{\parallel}$) interaction potentials. The dotted black curve is the 3D interaction potential ($\propto 1/q_{\parallel}^2$).

only the dominant zero center of mass momentum electron-hole pairs, Eq. (8.6) can be written as

$$\langle \psi_{-\mathbf{k}',1_c} \psi_{\mathbf{k}',2_v} | V(r) | \psi_{-\mathbf{k},1_c} \psi_{\mathbf{k},2_v} \rangle = F_{\mathbf{k},\mathbf{k}'}^H V^S(q_{\parallel}, q_z) + F_{\mathbf{k},\mathbf{k}'}^0 V^D(q_{\parallel}, q_z). \quad (8.10)$$

The pseudospin overlap factors are given by

$$F_{\mathbf{k},\mathbf{k}'}^0 = C_{\mathbf{k},\mathbf{k}'}^{1,1_c} C_{\mathbf{k},\mathbf{k}'}^{2,2_v} + C_{\mathbf{k},\mathbf{k}'}^{2,1_c} C_{\mathbf{k},\mathbf{k}'}^{1,2_v}, \quad F_{\mathbf{k},\mathbf{k}'}^H = C_{\mathbf{k},\mathbf{k}'}^{1,1_c} C_{\mathbf{k},\mathbf{k}'}^{1,2_v} + C_{\mathbf{k},\mathbf{k}'}^{2,1_c} C_{\mathbf{k},\mathbf{k}'}^{2,2_v}, \quad (8.11)$$

with

$$C_{\mathbf{k},\mathbf{k}'}^{l,\alpha} = \sum_{j=c,v} \left(C_{l_j,\alpha}^{\mathbf{k}'} \right)^* C_{l_j,\alpha}^{\mathbf{k}}, \quad (8.12)$$

and are known as the *form factors*. The form factor $F_{\mathbf{k},\mathbf{k}'}^0$ represents the contribution of both particles being located in their original TMD types or of both particles having hopped to the other TMD type, whereas $F_{\mathbf{k},\mathbf{k}'}^H$ represents the contribution of one of the particles having hopped to the other TMD type. As such, Eq. (8.10) expresses the fact that, due to the hybridization between the bands of the different TMD types, there is a (small) intralayer contribution to the total electron-hole interaction potential. At small q_{\parallel} this total potential is dominated by 3D interactions

between different TMD types. At large q_{\parallel} , however, it is dominated by 2D interactions between the same TMD types. Since the interaction is strongest at small q_{\parallel} , this means that the superfluid will predominantly be driven by 3D interactions, which is physically expected.

8.4.3 Superfluid properties

Assuming the WS_2 layers to be n -doped and the WSe_2 layers to be p -doped, the many-body interacting Hamiltonian in one of the valleys of the heterostructure superlattice is given by

$$\begin{aligned} \hat{H} = & \sum_{\mathbf{k}} \left((\varepsilon_{\mathbf{k},1c} - \mu_e) \hat{a}_{\mathbf{k},1c}^\dagger \hat{a}_{\mathbf{k},1c} + (-\varepsilon_{\mathbf{k},2v} - \mu_h) \hat{b}_{\mathbf{k},2v}^\dagger \hat{b}_{\mathbf{k},2v} \right) \\ & - \sum_{\mathbf{k}, \mathbf{k}'} \langle \psi_{-\mathbf{k}',1c} \psi_{\mathbf{k}',2v} | V(r) | \psi_{-\mathbf{k},1c} \psi_{\mathbf{k},2v} \rangle \hat{a}_{-\mathbf{k}',1c}^\dagger \hat{b}_{\mathbf{k}',2v}^\dagger \hat{b}_{\mathbf{k},2v} \hat{a}_{-\mathbf{k},1c}, \end{aligned} \quad (8.13)$$

which is written as a function of $\hat{a}_{\mathbf{k},1c}^\dagger$ ($\hat{b}_{\mathbf{k},2v}^\dagger$) and $\hat{a}_{\mathbf{k},1c}$ ($\hat{b}_{\mathbf{k},2v}$), the creation and annihilation operators for electrons in the lowest conduction band $\varepsilon_{\mathbf{k},1c}$ (holes in the highest valence band $\varepsilon_{\mathbf{k},2v}$). In this form the states $|\psi_{\mathbf{k},2v}\rangle$ are actually hole states in the hole conduction band, which can be obtained by substituting $\mathbf{k} \rightarrow -\mathbf{k}$ in the corresponding electron valence band state (which has no effect on the total interaction potential), and both chemical potentials μ_e and μ_h are positive. Furthermore, the electron-electron and hole-hole interaction terms are not included in the above Hamiltonian because they do not play a role in the electron-hole pairing mechanism but rather only lead to a correction on the kinetic energy which cancels with other terms, as is shown in appendix E.

The presence of superfluidity in a system is associated with a *superfluid gap* $\Delta_{\mathbf{k}}$, which is related to the energy required to break up an electron-hole Cooper pair. In appendix E it is shown that this superfluid gap can be determined from the zero-temperature self-consistent equation

$$\Delta_{\mathbf{k}} = \sum_{\mathbf{k}'} V^{RPA}(\mathbf{k}, \mathbf{k}') \frac{\Delta_{\mathbf{k}'}}{2E_{\mathbf{k}'}} \quad (8.14)$$

with

$$E_{\mathbf{k}} = \sqrt{\xi_{\mathbf{k}}^2 + \Delta_{\mathbf{k}}^2}, \quad \xi_{\mathbf{k}} = \frac{\varepsilon_{\mathbf{k},1c} - \varepsilon_{\mathbf{k},2v}}{2} - \mu, \quad \mu = \frac{\mu_e + \mu_h}{2}, \quad (8.15)$$

the quasiparticle dispersion, average electron-hole dispersion, and average chemical potential of the 3D system, respectively. Note that this is a mean field result,

i.e. it does not include fluctuations. Because the single-particle energies increase rapidly with increasing k_{\parallel} , results with arbitrarily good accuracy can be obtained by limiting the summation over the in-plane wave vector to a suitable cut-off k_c . For the summation over the perpendicular wave vector component, however, no such cut-off can be used because of the small band widths in the k_z -direction and therefore the summation runs over the entire first Brillouin zone, i.e. from $-\pi/2d$ to $\pi/2d$.

Furthermore, the interaction between an electron and a hole will be screened due to the polarization of the other electrons and holes. Therefore, these effects are taken into account by means of the random phase approximation (RPA), in which the interaction potential is given by [264]

$$V^{RPA}(\mathbf{k}, \mathbf{k}') = \frac{F_{\mathbf{k}, \mathbf{k}'}^0 V^D(q_{\parallel}, q_z) + F_{\mathbf{k}, \mathbf{k}'}^H V^S(q_{\parallel}, q_z)}{1 - 2V^S(q_{\parallel}, q_z)(\Pi_{n, \mathbf{q}}^0 + \Pi_{a, \mathbf{q}}^H) - 2V^D(q_{\parallel}, q_z)(\Pi_{n, \mathbf{q}}^H + \Pi_{a, \mathbf{q}}^0)}, \quad (8.16)$$

which takes into account the intraband polarizations in the presence of a superfluid which are given by [265]

$$\begin{aligned} \Pi_{n, \mathbf{q}}^{0(H)} &= -2 \sum_{\mathbf{k}} \frac{F_{\mathbf{k}+\mathbf{q}, \mathbf{k}}^{0(H)}}{E_{\mathbf{k}+\mathbf{q}} + E_{\mathbf{k}}} \left((u_{\mathbf{k}+\mathbf{q}} v_{\mathbf{k}})^2 + (u_{\mathbf{k}} v_{\mathbf{k}+\mathbf{q}})^2 \right), \\ \Pi_{a, \mathbf{q}}^{0(H)} &= 2 \sum_{\mathbf{k}} \frac{F_{\mathbf{k}+\mathbf{q}, \mathbf{k}}^{0(H)}}{E_{\mathbf{k}+\mathbf{q}} + E_{\mathbf{k}}} (2u_{\mathbf{k}+\mathbf{q}} v_{\mathbf{k}} u_{\mathbf{k}} v_{\mathbf{k}+\mathbf{q}}), \\ u_{\mathbf{k}}^2 &= \frac{1}{2} \left(1 + \frac{\xi_{\mathbf{k}}}{E_{\mathbf{k}}} \right), \quad v_{\mathbf{k}}^2 = \frac{1}{2} \left(1 - \frac{\xi_{\mathbf{k}}}{E_{\mathbf{k}}} \right). \end{aligned} \quad (8.17)$$

The terms $\Pi_{n, \mathbf{q}}^{0(H)}$ represent the normal state screening which is modified due to the presence of the superfluidity. The terms $\Pi_{a, \mathbf{q}}^{0(H)}$, on the other hand, represent the anomalous screening which only appears as a result of the presence of the superfluidity.

8.4.4 Numerical results

The gap equation (8.14) is solved for two different values of μ and the resulting superfluid gaps are shown in Fig. 8.5. Note that from now on the chemical potential is defined relative to the minimum of the average electron-hole energy, i.e. the transformation $\mu \rightarrow \mu - (\varepsilon_{0,1c} - \varepsilon_{0,2v})/2$ is performed. For $\mu = -20$ meV the superfluid gap has its maximum in the origin, whereas for $\mu = 10$ meV the maximum is located at an in-plane wave vector component of about half of the inverse

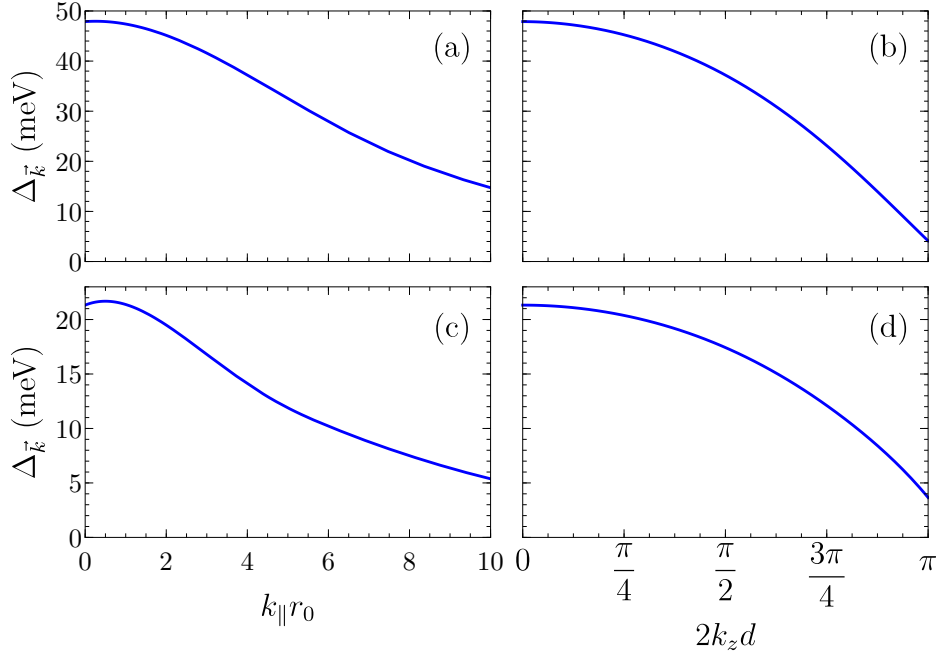


Figure 8.5: Superfluid gaps calculated for $\mu = -20$ meV (top) and $\mu = 10$ meV (bottom) as a function of the in-plane (left) and perpendicular (right) wave vector component, scaled with the average in-plane interparticle distance and the perpendicular periodic distance, respectively.

average in-plane interparticle distance, which is defined as $r_0 = 1/\sqrt{\pi n_{2D}}$ with n_{2D} the effective 2D density (see below). In the in-plane direction, the superfluid gap is wider for $\mu = -20$ meV than for $\mu = 10$ meV, but in both cases it is much wider than $1/r_0$. Since the superfluid gap is related to the pair correlation function of the electron-hole Cooper pair, this indicates that the pairs are compact with respect to the average interparticle distance. In the perpendicular direction, however, the superfluid gap for the lower value of the chemical potential is narrower than that for the higher value. In both cases the size of the pairs is of the order of the interlayer distance.

The chemical potential enters in the gap equation as a parameter. However, an experimentally more relevant parameter is given by the electron and hole density, which is given by

$$n_e = n_h = \frac{2}{AN2d} \sum_{\mathbf{k}} v_{\mathbf{k}}^2 \equiv n, \quad (8.18)$$

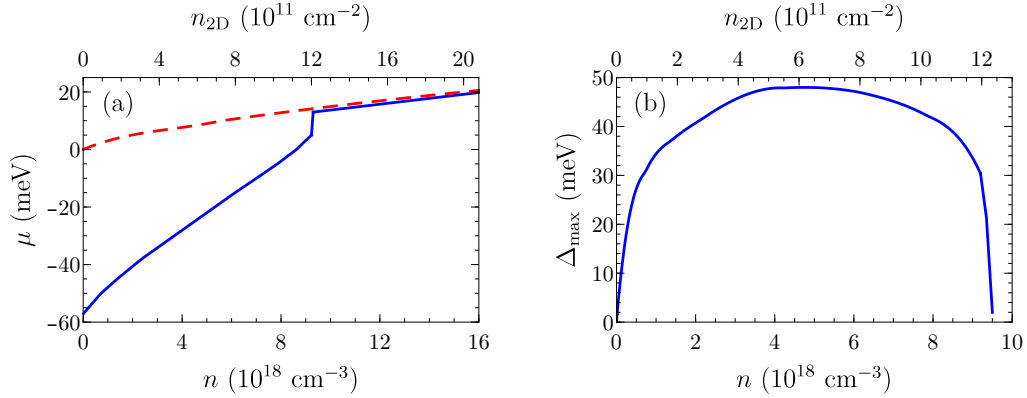


Figure 8.6: Chemical potential (a) and maximum superfluid gap (b) calculated as a function of the 3D and effective 2D density. The dashed red curve in (a) is the average Fermi level.

which is derived in appendix E and from which an effective 2D density n_{2D} can be obtained by multiplying it with $2d$. Note that the electron and hole densities are equal per construction, which is preferable for the formation of a superfluid since an excess of either would increase the screening and as such reduce the interaction strength. Because of the difference in effective mass of the lowest conduction band and highest valence band this implies that the electron and hole Fermi levels are in general not equal. The relation between the chemical potential and the density is shown in Fig. 8.6(a). At low densities the chemical potential is negative. This is to be expected since in the limit of zero density there is an energy gain of half the exciton binding energy when a particle is added to the system. This region in which the chemical potential is negative is referred to as the BEC regime. In the high-density limit, on the other hand, the chemical potential converges to the Fermi level and this region is known as the BCS regime. The region between these two limiting cases is known as the crossover regime.

An alternative way of defining the different regimes is through the condensate fraction, which gives the fraction of the particles which are in the superfluid state and is determined through

$$c = \frac{\sum_{\mathbf{k}} (u_{\mathbf{k}} v_{\mathbf{k}})^2}{\sum_{\mathbf{k}} (v_{\mathbf{k}})^2}, \quad (8.19)$$

as discussed in appendix E. The boundary between the BEC and the crossover regimes is usually assumed to be given by $c = 0.8$, which for this systems corresponds to a density of around $8 \times 10^{18} \text{ cm}^{-3}$. The BCS regime is defined as $c < 0.2$.

However, this regime is never reached in this system, as will be explained in the next paragraph. The shape of the superfluid gap can also give a clue about the regime. In the BEC regime the superfluid gap is wide and has its maximum in the origin, as shown in Fig. 8.5(a). Moving into the crossover regime, the maximum shifts away from the origin and the superfluid gap becomes narrower, as shown in Fig. 8.5(c). In the BCS regime, which is not reached in this system, the superfluid gap is narrow and centered around the Fermi wave vector.

In Fig. 8.6(b) the maximum value of the superfluid gap is shown as a function of the density. The maximum gap initially increases as a function of the density, before reaching a maximum at a density of around $5 \times 10^{18} \text{ cm}^{-3}$. The maximum gap then gradually decreases and, at a density of around $9.5 \times 10^{18} \text{ cm}^{-3}$, almost instantly vanishes. The density at which it vanishes is known as the onset density. This effect can be attributed to the many-body screening of the interaction potential which becomes more efficient at higher densities. At low densities, when the superfluid gap is much larger than the Fermi level, the low-lying states which are normally responsible for the screening, are not available due to the presence of the gap in the energy spectrum. Therefore it can be said that at low densities the superfluidity kills the screening, while at high densities the screening kills the superfluidity. The condensate fraction is found to jump from 0.65 to a near-zero value at the onset density and as a result the BCS regime is never reached in this system. Note that this abrupt disappearance of the superfluidity is also reflected in the chemical potential, which shows a jump towards the Fermi level at the onset density.

The property of the superfluid which is of most interest is the critical temperature T_c , which is defined as the temperature at which the superfluid gap vanishes. At non-zero temperature the electron-hole Cooper pairs can thermally break up, and by assuming these broken up pairs to be non-interacting the temperature-dependent gap equation (E.19) can be derived, as explained in appendix E. At high densities, i.e. in the BCS regime, the condensate fraction is small and therefore the interactions between the broken up pairs only constitute a small fraction of the total interactions. As a result, the critical temperature can be obtained from Eq. (E.19). This is a challenging numerical calculation since close to T_c the solution is not well-behaved. However, there is an alternative way in which the critical temperature can be found much more efficiently. For temperatures close to T_c , the temperature-dependent gap equation (E.19) can be rewritten as

$$\Delta_{\mathbf{k}}(T) \approx \sum_{\mathbf{k}'} V^{RPA}(\mathbf{k}, \mathbf{k}', T) \frac{\Delta_{\mathbf{k}'}(T)}{2|\xi_{\mathbf{k}'}|} \tanh\left(\frac{|\xi_{\mathbf{k}'}|}{2k_B T}\right), \quad (8.20)$$

where it was used that $\Delta_{\mathbf{k}} \ll \xi_{\mathbf{k}}$ and $\xi_{\mathbf{k}}^{\delta} \ll k_B T_c$. The latter still needs to be checked for consistency with the obtained results: it is a good approximation if $T_c > 200$ K. The temperature-dependent superfluid gap can approximately be written as $\Delta_{\mathbf{k}}(T) = g(T)\Delta_{\mathbf{k}}$, i.e. the superfluid will not change from one regime to another with increasing temperature. Furthermore, in the RPA interaction potential the superfluid gap can be assumed to be that at zero temperature since for temperatures close to T_c the role of the vanishing superfluid gap in the screening is taken over by the *pseudogap*. This pseudogap represents an intermediate phase in which there is a gap in the excitation spectrum, i.e. there is pairing, but there is no phase coherence [266]. At T_c this pseudogap is of the same order as the superfluid gap at zero temperature [267]. Multiplying both sides of the above equation with $\Delta_{\mathbf{k}}$ and summing over \mathbf{k} then allows to define a function

$$\lambda(T) = \frac{\sum_{\mathbf{k}} \sum_{\mathbf{k}'} V^{RPA}(\mathbf{k}, \mathbf{k}') \frac{\Delta_{\mathbf{k}} \Delta_{\mathbf{k}'}}{2|\xi_{\mathbf{k}'}|} \tanh\left(\frac{|\xi_{\mathbf{k}'|}}{2k_B T}\right)}{\sum_{\mathbf{k}} (\Delta_{\mathbf{k}})^2} \quad (8.21)$$

whose value is close to 1. The critical temperature can then be obtained by solving for $\lambda(T_c) = 1$. Note that the calculation is performed for fixed density and therefore the chemical potential needs to be adjusted appropriately with increasing temperature. The results obtained from the above expression become less accurate with decreasing density as phase fluctuations of the superfluid and interactions between the broken up pairs become increasingly important. At very low densities, i.e. in the BEC regime, there are no broken up pairs because of the large pseudogap. Phase fluctuations of the superfluid, on the other hand, are important and can in principle be included in order to get very accurate results [268, 269]. However, in the deep BEC regime the interparticle distances are very large and as a result the electron-hole Cooper pairs can be assumed to be perfect bosons which can form a BEC. The critical temperature of the system can therefore be determined by imposing that not all the bosons can be put in excited states, i.e.

$$n = \frac{2}{AN2d} \sum_{\mathbf{k}} \frac{1}{e^{(\varepsilon_{\mathbf{k},1c} - \varepsilon_{\mathbf{k},2v} - \varepsilon_{0,1c} + \varepsilon_{0,2v})/(k_B T_c^{\text{BEC}})} - 1}. \quad (8.22)$$

The critical temperatures obtained from the above two expressions are shown in Fig. 8.7 as a function of the density. In the intermediate density region the critical temperature interpolates between these two limiting cases but it is not possible to determine the exact values in the current framework. However, it is known that the BCS formalism can give a good estimate of the critical temperature up to about halfway across the crossover regime, whereas the BEC formalism only gives reliable results in the deep BEC regime [270]. Therefore, a possible interpolation

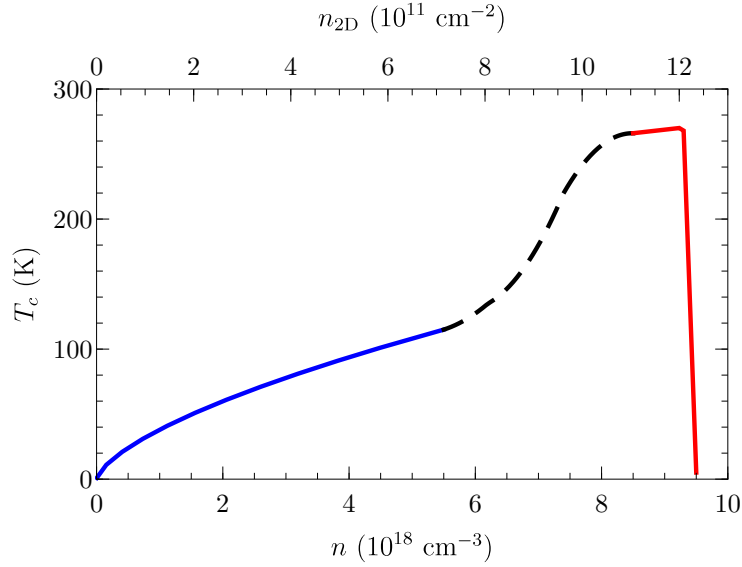


Figure 8.7: BEC (solid, blue) and BCS (solid, red) critical temperature calculated as a function of the 3D and effective 2D density. The dashed black curve is a possible interpolation of the critical temperature between the BEC and BCS expressions.

between the two limiting results is shown in Fig. 8.7 which starts from the BCS result in the crossover regime and which smoothly decreases with decreasing density to the BEC result well into the BEC regime. The final result has a maximum critical temperature of 270 K, i.e. close to room temperature, in the crossover regime.

In order to estimate whether the superfluid can reach this mean field critical temperature, or whether it is hindered by a BKT transition at lower temperatures, the phase coherence length should be calculated. As discussed at the end of section 8.3, this length scale determines whether the superfluid acts 2D or 3D. However, this is an extensive calculation which lies outside the scope of this thesis. Fortunately, the system has another fundamental length scale which can indirectly answer the question about the dimensionality: the pair correlation length, which is given by [271]

$$\xi_{P,i}^2 = \frac{\sum_{\mathbf{k}} \left(\frac{\partial}{\partial k_i} u_{\mathbf{k}} v_{\mathbf{k}} \right)^2}{\sum_{\mathbf{k}} (u_{\mathbf{k}} v_{\mathbf{k}})^2}. \quad (8.23)$$

This length scale gives an indication of the size of the electron-hole Cooper pair and corresponds to the effective exciton Bohr radius in the low-density limit. In the

considered density range, the pair correlation length in the z -direction is found to vary between 0.55 nm and 0.67 nm. However, it is known that in the BCS limit the phase coherence length coincides with the pair correlation length, whereas in the BEC limit the phase coherence length is much larger than the pair correlation length [272]. Therefore, given the above values for the pair correlation length, it can be inferred that the phase coherence length will (significantly) exceed the periodic distance $2d = 1.3$ nm in the relevant density range, i.e. in the crossover regime, and that the superfluid will thus act 3D. It can thus be concluded that the proposed superlattice of TMD heterostructures exhibits high-temperature superfluidity, with critical temperatures possibly as high as 270 K. Note that this is a significantly higher value than what can be obtained in a single TMD heterostructure. In these systems the superfluid is 2D and as a result the critical temperature is determined by the BKT transition, which does not exceed 20 K in the density range considered here. However, due to the reduced dielectric screening, the onset density is much higher and as a result the BKT temperature is found to reach values up to 120 K. This result is part of a paper which has been submitted to Physical Review Letters.

8.5 Conclusion

In this chapter the possibility of an interlayer exciton superfluid in a superlattice of TMD heterostructures was investigated. The appropriate unscreened interaction potential was derived and an expression interpolating between the 2D and 3D limits was obtained. Polarization effects were included by means of the RPA and this potential was then used to solve the superfluid gap equation. By estimating the perpendicular phase coherence length and comparing it to the interlayer distance it was found that the superfluid in this system acts 3D. As a result, it is not hindered by a BKT transition and the calculated mean field critical temperatures which can reach up to 270 K, i.e. approaching room temperature, are applicable.

CHAPTER 9

Conclusion and outlook

9.1 Summary

Excitons have been extensively studied for almost a century, as briefly summarized in chapter 1. More recently, this research expanded to trions and biexcitons and it was found that the features of these three excitonic complexes become more pronounced when they are spatially confined. Therefore, in this thesis the properties of excitons, trions, and biexcitons are studied in a number of two-dimensional (2D) semiconductors, with the main focus lying on monolayer transition metal dichalcogenides (TMDs).

In chapter 2 the single-particle properties of electrons and holes in monolayer TMDs were first reviewed. It was explained how an effective 2D Dirac Hamiltonian, describing the highest valence band and lowest conduction band around the K and K' points, can be derived from tight-binding models. The Bloch basis functions on which this Hamiltonian is constructed are based on the d_0 and $d_{2\tau}$ atomic orbitals of the transition metal atom. It was also shown how to take into account the effect of spin-orbit coupling which is very strong in the highest valence band of monolayer TMDs. Next, the eigenvalues and eigenstates of the Hamiltonian were calculated and the latter were used to show that monolayer TMDs exhibit circular dichroism, i.e. charge carriers in the K (K') valley can be excited by means of left (right) circularly polarized light. The eigenvalues and eigenstates also allow to calculate the Berry curvature and the associated intrinsic orbital magnetic moment.

It was demonstrated that the latter leads to a type of valley Zeeman effect and as such helps to explain the Landau level spectrum of monolayer TMDs in the presence of a perpendicular magnetic field. The presence of an in-plane magnetic field was shown to allow for optical transitions between energy bands associated with opposite spins. Next, the interparticle interaction potential in monolayer TMDs was derived from Gauss's law and it was demonstrated that the 2D confinement of the charge carriers leads to a particular interaction potential known as the Keldysh potential. In the last section, this potential was used in a variational calculation of the different many-body phases of electrons in different monolayer TMDs. It was found that there are four phases with a step-wise reduction in spin/valley order with increasing electron density: a completely spin and valley polarized phase, a phase with spin-valley locking, a phase with spin polarization in only one of the valleys, and a phase with no spin or valley polarization. These phases were demonstrated to persist in the presence of a perpendicular magnetic field and in the specific case of MoS₂ an additional phase of complete valley polarization and little to no spin polarization was found to appear for magnetic fields larger than 7 T. Finally, it was found that the phase diagram of holes in monolayer TMDs is less rich as a result of the strong spin-orbit coupling in the valence band.

In chapter 3 the properties of excitons in monolayer TMDs were studied. First, a four-band exciton Hamiltonian was constructed based on the two-band electron and hole single-particle Hamiltonians derived in chapter 2. It was shown that the corresponding eigenvalue equation, which in position representation corresponds to a set of differential equations, can be solved numerically using the finite element method (FEM) by transforming to center of mass and relative coordinates and by separating the radial part from the angular part by exploiting the eigenstates of the exciton angular momentum operator which commutes with the exciton Hamiltonian. For excitons with non-zero center of mass momentum this approach is not feasible but nevertheless the exciton eigenvalue equation can still be solved by decoupling the set of equations to a single equation and solving it self-consistently. The exciton ground state binding energy was calculated for different monolayer TMDs and different substrates and very large values of more than 500 meV were obtained. The results were compared with those of a single-band model based on an effective mass approximation of the low-energy bands and it was found that multi-band effects reduce the exciton binding energy. Furthermore, good agreement was found with other theoretical studies while less satisfactory agreement was found with experimental results, for which substrate surface roughness and defect-bound excitons were proposed as possible explanations. Next, higher excited exciton states were studied leading to three important results: (1) For states

with the same principal quantum number those with higher (absolute value of) orbital angular momentum have lower energy. (2) The intervalley exciton ground state has angular momentum $j = -1$ which can be attributed to the pseudospin of the constituent electron and hole. (3) Intravalley excitons with angular momenta $\pm j$ are degenerate while for intervalley excitons (τ, j) and $(-\tau, -j)$ excitons are degenerate, suggesting that this may be related to the coupling between the orbital angular momentum of the exciton and the intrinsic angular momentum of the exciton, which is related to the Berry curvature. Furthermore, the exciton wave functions were calculated, including the non-dominant components which possess different orbital angular momentum characteristics and which lower the exciton binding energy. These wave functions were then used to calculate the average interparticle distance for different exciton states, different monolayer TMDs, and different substrates, as well as the excitonic absorbance spectrum.

In chapter 4 the properties of trions and biexcitons in monolayer TMDs were studied. It was shown that the FEM is not suitable for solving the eigenvalue equations of the trion and biexciton Hamiltonians. Therefore the stochastic variational method (SVM) based on correlated Gaussian basis functions was introduced and used to calculate the trion and biexciton binding energies for different monolayer TMDs and different substrates and very large values were found, i.e. up to 30 meV and up to 20 meV for trions and biexcitons, respectively. Good agreement was obtained with other theoretical studies and reasonably good agreement was found with experimental results for trions. For biexcitons there are very large differences with experimental results but it was explained that this may be the consequence of misinterpretation of the experimental results. Furthermore, the trion wave function was calculated for the ground state and for the second excited state, showing that for the former the three particles form a symmetric system whereas the latter can be viewed as an exciton with an additional particle circling around it.

In chapter 5 the presence of a uniform magnetic field was considered and its effect on excitonic complexes in monolayer TMDs was investigated. First, a four-band exciton Hamiltonian was constructed for the case of a perpendicular magnetic field, which allowed to obtain the exciton Landau level spectrum. It was found that the exciton Landau levels correspond qualitatively to the Landau levels of a 2D charged Schrödinger particle and that the magnetic field partially breaks the degeneracy between states with opposite relative angular momentum $\pm j_r$, i.e. the lowest $|j_r|$ Landau levels of the state with negative relative angular momentum are non-degenerate with the Landau levels of the state with opposite relative angular momentum. Next, it was shown that dark excitons in a tilted magnetic field, which brighten as a result of the in-plane component, exhibit an exciton valley Zeeman

effect, as a result of the perpendicular component, which is more than twice as strong as that of bright excitons. As a result of the sign of the spin-orbit coupling in the conduction band, this strong effect is only present for *A* excitons in tungsten-based TMDs. In the last section, the SVM was used to study the ground state properties of excitons, trions, and biexcitons in a perpendicular magnetic field and it was shown that the binding energy of all three excitonic complexes increases as a function of the magnetic field strength. Furthermore, the diamagnetic shift of trions and biexcitons was found to be almost an order of magnitude larger than that of excitons and the diamagnetic shift of all three excitonic complexes was shown to increase as a function of the substrate dielectric constant.

In chapter 6 attention was turned towards materials with anisotropic band structures, i.e. monolayer black phosphorus (bP) and TiS_3 . A slightly modified form of the SVM, to take into account the anisotropy, was used to calculate the binding energy of excitons, trions, and biexcitons, which yielded good agreement with other theoretical studies when available. It was found that the binding energies of excitonic complexes in TiS_3 are generally smaller than those of their counterparts in bP. In TiS_3 , negative trions are more tightly bound than positive trions, whereas in bP their binding energies are equal because of the (approximately) equal electron and hole band masses. Next, the correlation functions and average interparticle distances of the different excitonic complexes in these two materials were calculated, which showed that excitonic complexes in bP are strongly anisotropic whereas in TiS_3 they are almost isotropic, which is a consequence of the anisotropy of the constituent electrons and holes being equal in bP and opposite in TiS_3 . Finally, the effect of uniaxial tensile and compressive strain in different directions on the properties of excitons in bP was studied and it was found that applying tensile strain increases the exciton binding energy and restores the isotropy in the excitonic complexes, whereas compressive strain decreases the exciton binding energy and increases the anisotropy even further.

In chapter 7 interlayer excitons in TMD heterostructures were studied. The appropriate electron-hole interaction potential, taking into account the effect of the dielectric environment above, below, and between the two TMDs as well as polarization effects both in the transition metal layer and in the chalcogen layers of the TMDs, was first derived and used in a four-band model. The exciton binding energy and average interparticle distance were calculated for all combinations of TMDs, which led to the conclusion that the chalcogen atoms mostly influence the binding energy whereas the transition metal atoms mostly influence the interparticle distance. Next, the effect of different dielectric environments on the exciton binding energy was investigated and a remarkable dependence on the dielectric

constant of the barrier between the two TMDs was found, resulting from competing effects as a function of the in-plane and out-of-plane dielectric constants of the barrier. Furthermore, the polarization effects in the chalcogen layers, which in general reduce the exciton binding energy, can lead to an increase in binding energy in the presence of strong substrate effects by screening out the substrate. Finally, the excitonic absorbance spectrum was calculated and it was shown that the interlayer exciton peak depends linearly on a perpendicular electric field, in agreement with recent experimental results.

In chapter 8 the possible formation of an interlayer exciton superfluid in TMD heterostructures was investigated. A superlattice of these TMD heterostructures was considered in order to have a 3D superfluid and as such avoid the Berezinskiĭ-Kosterlitz-Thouless transition which limits the critical temperatures in 2D superfluids. First, the appropriate unscreened interaction potential was derived, taking into account the geometry of the system. Polarization effects were included by means of the random phase approximation (RPA). Using this screened RPA interaction potential, the superfluid gap equation was solved for different values of the chemical potential and very high critical temperatures of up to 270 K were obtained.

9.2 Situating the novelty of this thesis

This thesis provided an extensive study of excitons, trions, and biexcitons, which are few-body systems which can be found in semiconductors. In contrast to isolated atoms, for which the many-electron system can be reasonably well described by neglecting (Coulomb) correlations between the electrons (i.e. the Hartree-Fock method), interparticle correlations are extremely important in these systems. This was dramatically shown in this thesis, where it was found that neglecting angular correlations in trions leads to poor results, sometimes even predicting unstable trions. Accurately taking into account these correlations is a difficult task and was done here by means of the stochastic variational method, which is one of the most accurate methods available.

The attention was mainly focused on monolayer TMDs. The 2D nature of these systems leads to a peculiar interaction potential, which in turn causes the exciton levels to deviate from the 2D hydrogenic Rydberg series. Combined with the associated reduced dielectric screening this leads to exceptionally large binding energies for all three excitonic complexes, i.e. an order of magnitude larger than those in 3D semiconductors and in semiconductor quantum wells. These binding energies were calculated here for a range of TMDs and substrates and the results

were compared with theoretical and experimental results from the literature when available. Good agreement was found with other theoretical studies while less satisfactory agreement was found with experimental results, for which substrate surface roughness and misinterpretation of the PL spectra were suggested as possible explanations.

Another unique feature of monolayer TMDs, owing to their hexagonal lattice structure, is the fact that the low-energy charge carriers reside in the K and K' valleys at the corners of the hexagonal Brillouin zone, in contrast to most semiconductors where they are usually found at the Γ point. This allows for the possibility of both intra- and intervalley excitons, which in this thesis were shown to have different degeneracies and energy level orderings as a result of the Dirac nature of the charge carriers. Intervalley excitons can not be directly measured experimentally but they can affect the exciton dynamics in TMDs.

Previous studies of magnetic field effects on excitons in TMDs have mostly been limited to ground state properties. In this thesis it was shown how a perpendicular magnetic field leads to exciton Landau levels and partly breaks the degeneracy between states with opposite relative angular momentum. Furthermore, the exciton valley Zeeman effect, which is well-known in the literature for bright excitons, was here predicted to be more than twice as strong for dark excitons. This could in principle be measured experimentally by applying a tilted magnetic field. Little to no studies exist on the effect of a magnetic field on trions and biexcitons in TMDs. In this thesis it was shown how a perpendicular magnetic field leads to a stronger relative increase in binding energy for trions and biexcitons as compared to excitons and how their diamagnetic shifts can be tuned by means of a substrate.

The binding energies of excitonic complexes have also been calculated for two 2D semiconductors with anisotropic band structures, which included the first calculation of the biexciton binding energy in monolayer TiS_3 . Furthermore, it was shown here how the excitonic complexes in TiS_3 are actually almost isotropic and how the anisotropy of excitons in monolayer bP can be tuned by means of strain.

Different monolayer TMDs can be stacked to form TMD heterostructures in which interlayer excitons can form. An interlayer interaction potential was derived in this thesis which allows to describe layered substrates between the TMDs. This potential was then used to calculate the interlayer exciton binding energy for many different combinations of TMDs, many of which had not yet been reported in the literature, and to investigate how it can be tuned by the dielectric environment. Furthermore, it is possible for these interlayer excitons to form a superfluid, which in 2D systems is limited by the BKT transition. In order to circumvent this mechanism, a superlattice of TMD heterostructures was proposed in this thesis and high

critical temperatures approaching room temperature were predicted. This has potential for low-energy nanoelectronics, which is a challenging area for the present-day microelectronics industry, and is therefore actively pursued by for example the FLEET (Future Low-Energy Electronics Technologies) center of excellence in Australia.

9.3 Outlook

There are a number of possible ways to extend the work presented in this thesis. For example, it would be very interesting to implement the SVM method for the multi-band trion and biexciton Hamiltonians. This would allow to study the influence of multi-band effects, which are considerably more important for trions as compared to excitons as was shown in chapter 4, on the different properties of these excitonic complexes.

It is also worth investigating the effect of a perpendicular magnetic field on excitonic complexes in bP, possibly combined with an applied uniaxial strain, which provides a new way of realizing excitonic complexes with tunable anisotropy.

Furthermore, interlayer trions whose two equally charged particles are located in the same layer were recently predicted to be stable based on first-principles Bethe-Salpeter calculations [273], which followed a possible experimental observation of this new type of excitonic complex a year earlier [274]. It would be very interesting to try to reproduce these results using the SVM method, which would require implementing the interaction potential derived in chapter 7, and then to extend these calculations to interlayer biexcitons.

Finally, it is worth investigating interlayer excitonic superfluidity in TMD heterostructure superlattices with an indirect band gap, which would result in a superfluid with non-zero center of mass momentum. The symmetric orientation of the different conduction band minima with respect to the valence band maxima might result in a plethora of different superfluid phases.

APPENDIX A

Three-band tight-binding Hamiltonian for monolayer TMDs

In Ref. [60] a three-band tight-binding Hamiltonian involving only nearest neighbor d - d hoppings in the basis of Bloch functions based on the atomic orbital states $\{|d_{z^2}\rangle, |d_{x^2-y^2}\rangle, |d_{xy}\rangle\}$ was introduced which can be written as

$$H^{NN}(\mathbf{k}) = \begin{pmatrix} h_0 & h_1 & h_2 \\ h_1^* & h_{11} & h_{12} \\ h_2^* & h_{12}^* & h_{22} \end{pmatrix}, \quad (\text{A.1})$$

with

$$\begin{aligned} h_0 &= 2t_0(\cos 2\alpha + 2 \cos \alpha \cos \beta) + \epsilon_1, \\ h_1 &= -2\sqrt{3}t_2 \sin \alpha \sin \beta + 2it_1(\sin 2\alpha + \sin \alpha \cos \beta), \\ h_2 &= 2t_2(\cos 2\alpha - \cos \alpha \cos \beta) + 2\sqrt{3}it_1 \cos \alpha \sin \beta, \\ h_{11} &= 2t_{11} \cos 2\alpha + (t_{11} + 3t_{22}) \cos \alpha \cos \beta + \epsilon_2, \\ h_{22} &= 2t_{22} \cos 2\alpha + (3t_{11} + t_{22}) \cos \alpha \cos \beta + \epsilon_2, \\ h_{12} &= \sqrt{3}(t_{22} - t_{11}) \sin \alpha \sin \beta + 4it_{12} \sin \alpha (\cos \alpha - \cos \beta), \\ (\alpha, \beta) &= \left(\frac{1}{2}k_x a, \frac{\sqrt{3}}{2}k_y a \right). \end{aligned} \quad (\text{A.2})$$

This Hamiltonian, which for simplicity does not include spin-orbit coupling, contains eight parameters which are determined using the Slater-Koster method [275] by fitting its band structure to density functional theory calculations and are listed in Table A.1. Using these parameters, the resulting band structure is shown in Fig. A.1(a). This shows that it is in very good agreement with density functional theory calculations for the highest valence band, lowest conduction band, and a higher conduction band around the K and K' point but diverges from the density functional theory calculations when moving away from these points. This issue can be resolved by including up to third nearest neighbor hoppings. In that case the Hamiltonian is given by

$$H^{TNN}(\mathbf{k}) = \begin{pmatrix} g_0 & g_1 & g_2 \\ g_1^* & g_{11} & g_{12} \\ g_2^* & g_{12}^* & g_{22} \end{pmatrix}, \quad (\text{A.3})$$

with

$$\begin{aligned} g_0 &= h_0 + 2r_0(2 \cos 3\alpha \cos \beta + \cos 2\beta) + 2u_0(2 \cos 2\alpha \cos 2\beta + \cos 4\alpha), \\ g_1 &= h_1 + 2(r_1 + r_2) \sin 3\alpha \sin \beta - 2\sqrt{3}u_2 \sin 2\alpha \sin 2\beta \\ &\quad + 2i(r_1 - r_2) \sin 3\alpha \cos \beta + 2iu_1 \sin 2\alpha(2 \cos 2\alpha + \cos 2\beta), \\ g_2 &= h_2 - \frac{2}{\sqrt{3}}(r_1 + r_2)(\cos 3\alpha \cos \beta - \cos 2\beta) + 2u_2(\cos 4\alpha - \cos 2\alpha \cos 2\beta) \\ &\quad + \frac{2}{\sqrt{3}}i(r_1 - r_2) \sin \beta(\cos 3\alpha + 2 \cos \beta) + 2\sqrt{3}iu_1 \cos 2\alpha \sin 2\beta, \\ g_{11} &= h_{11} + 4r_{11} \cos 3\alpha \cos \beta + 2(r_{11} + \sqrt{3}r_{12}) \cos 2\beta \\ &\quad + (u_{11} + 3u_{22}) \cos 2\alpha \cos 2\beta + 2u_{11} \cos 4\alpha, \\ g_{22} &= h_{22} + 2r_{11}(2 \cos 3\alpha \cos \beta + \cos 2\beta) + \frac{2}{\sqrt{3}}r_{12}(4 \cos 3\alpha \cos \beta - \cos 2\beta) \\ &\quad + (3u_{11} + u_{22}) \cos 2\alpha \cos 2\beta + 2u_{22} \cos 4\alpha, \\ g_{12} &= h_{12} + 4r_{12} \sin 3\alpha \sin \beta + \sqrt{3}(u_{22} - u_{11}) \sin 2\alpha \sin 2\beta \\ &\quad + 4iu_{12} \sin 2\alpha(\cos 2\alpha - \cos 2\beta). \end{aligned} \quad (\text{A.4})$$

This Hamiltonian, which again does not include spin-orbit coupling, contains eleven additional parameters which are again determined using the Slater-Koster method by fitting its band structure to density functional theory calculations and are, together with the previous eight parameters, listed in Table A.2. Using these parameters, the resulting band structure is shown in Fig. A.1(b), which shows that it is in

very good agreement with the density functional theory calculations for the highest valence band, lowest conduction band, and a higher conduction band throughout the entire first Brillouin zone.

	ϵ_1	ϵ_2	t_0	t_1	t_2	t_{11}	t_{12}	t_{22}
MoS ₂	1.046	2.104	-0.184	0.401	0.507	0.218	0.338	0.057
MoSe ₂	0.919	2.065	-0.188	0.317	0.456	0.211	0.290	0.130
WS ₂	1.130	2.275	-0.206	0.567	0.536	0.286	0.384	-0.061
WSe ₂	0.943	2.197	-0.207	0.457	0.486	0.263	0.329	0.034

Table A.1: Three-band nearest neighbor tight-binding Hamiltonian parameters (eV), obtained using the Slater-Koster method by fitting to density functional theory calculations based on a generalized gradient approximation, for different monolayer TMDs. Table taken from Ref. [60].

	ϵ_1	ϵ_2	t_0	t_1	t_2	t_{11}	t_{12}	t_{22}
	r_0	r_1	r_2	r_{11}	r_{12}	u_0	u_1	u_2
	u_{11}	u_{12}	u_{22}					
MoS ₂	0.683	1.707	-0.146	-0.114	0.506	0.085	0.162	0.073
	0.060	-0.236	0.067	0.016	0.087	-0.038	0.046	0.001
	0.266	-0.176	-0.150					
MoSe ₂	0.684	1.546	-0.146	-0.130	0.432	0.144	0.117	0.075
	0.039	-0.209	0.069	0.052	0.060	-0.042	0.036	0.008
	0.272	-0.172	-0.150					
WS ₂	0.717	1.916	-0.152	-0.097	0.590	0.047	0.178	0.016
	0.069	-0.261	0.107	-0.003	0.109	-0.054	0.045	0.002
	0.325	-0.206	-0.163					
WSe ₂	0.728	1.655	-0.146	-0.124	0.507	0.117	0.127	0.015
	0.036	-0.234	0.107	0.044	0.075	-0.061	0.032	0.007
	0.329	-0.202	-0.164					

Table A.2: Three-band third nearest neighbor tight-binding Hamiltonian parameters (eV), obtained using the Slater-Koster method by fitting to density functional theory calculations based on a generalized gradient approximation, for different monolayer TMDs. Table taken from Ref. [60].

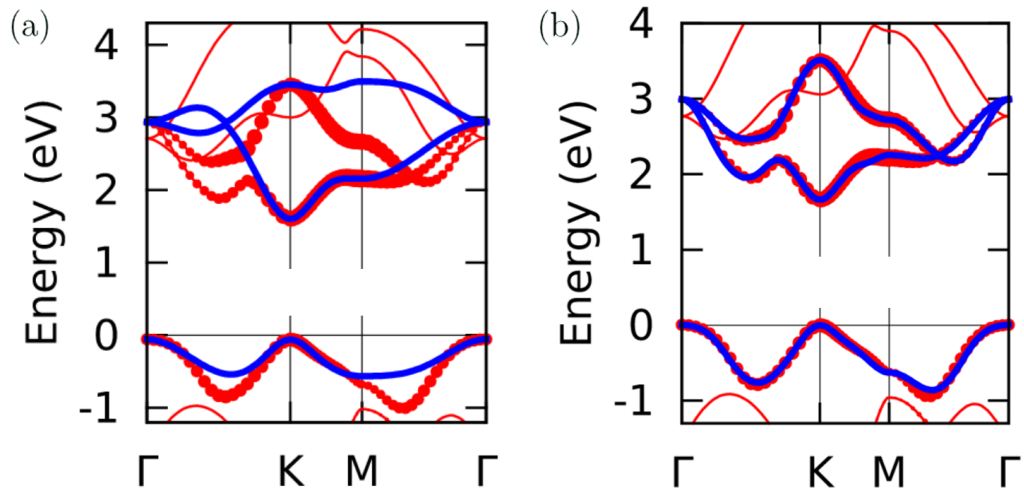


Figure A.1: Nearest neighbor (a) and third nearest neighbor (b) tight-binding band structures (blue) compared with density functional theory calculations based on a generalized gradient approximation (red) for MoS_2 . The size of the dots indicates the contribution from the atomic orbital states $\{|d_{z^2}\rangle, |d_{x^2-y^2}\rangle, |d_{xy}\rangle\}$ to the three bands which are compared with the tight-binding results. Figure taken from Ref. [60].

APPENDIX B

Derivation of the spin-orbit coupling

B.1 Relativistic quantum mechanical approach

The Dirac equation is, in the presence of a scalar potential, given by

$$i\hbar \frac{\partial \psi}{\partial t} = (c\boldsymbol{\alpha} \cdot \mathbf{p} + \beta m_0 c^2 + V) \psi, \quad (\text{B.1})$$

with c the speed of light, $V = -e\phi$ the scalar potential associated with the electrostatic potential ϕ , and with

$$\boldsymbol{\alpha} = \begin{pmatrix} 0 & \boldsymbol{\sigma} \\ \boldsymbol{\sigma} & 0 \end{pmatrix}, \quad \beta = \begin{pmatrix} I_2 & 0 \\ 0 & -I_2 \end{pmatrix}. \quad (\text{B.2})$$

For a stationary state

$$\psi = e^{-\frac{i}{\hbar}(m_0 c^2 + E)t} \begin{pmatrix} \varphi \\ \chi \end{pmatrix}, \quad (\text{B.3})$$

with φ and χ both time-independent two-component spinors and where the energy is defined relative to the rest energy to allow to easily take the non-relativistic limit, the Dirac equation becomes

$$c \begin{pmatrix} \boldsymbol{\sigma} \cdot \mathbf{p} \chi \\ \boldsymbol{\sigma} \cdot \mathbf{p} \varphi \end{pmatrix} - 2m_0 c^2 \begin{pmatrix} 0 \\ \chi \end{pmatrix} + V \begin{pmatrix} \varphi \\ \chi \end{pmatrix} = E \begin{pmatrix} \varphi \\ \chi \end{pmatrix}. \quad (\text{B.4})$$

From the second equation it follows that

$$\chi = \frac{c}{E - V + 2m_0c^2} \boldsymbol{\sigma} \cdot \mathbf{p} \varphi \approx \frac{1}{2m_0c} \left(\boldsymbol{\sigma} \cdot \mathbf{p} - \frac{E - V}{2m_0c^2} \boldsymbol{\sigma} \cdot \mathbf{p} \right) \varphi, \quad (\text{B.5})$$

which shows that in the non-relativistic limit the component χ is much smaller than the component φ . Inserting this expression into the first equation of Eq. (B.4) introduces a term

$$H_1 = \frac{1}{4m_0^2c^2} (\boldsymbol{\sigma} \cdot \mathbf{p}) V (\boldsymbol{\sigma} \cdot \mathbf{p}) \quad (\text{B.6})$$

to the effective Hamiltonian for the dominant spinor component φ . Using the identity

$$(\boldsymbol{\sigma} \cdot \mathbf{a})(\boldsymbol{\sigma} \cdot \mathbf{b}) = \mathbf{a} \cdot \mathbf{b} I_2 + i \boldsymbol{\sigma} \cdot (\mathbf{a} \times \mathbf{b}), \quad (\text{B.7})$$

this term can be rewritten as

$$H_1 = \frac{1}{4m_0^2c^2} \left((V \mathbf{p}^2 I_2 - i \hbar (\nabla V) \cdot \mathbf{p} I_2 + \hbar \boldsymbol{\sigma} \cdot (\nabla V \times \mathbf{p})) \right). \quad (\text{B.8})$$

Using

$$\nabla V = \frac{1}{r} \frac{dV(r)}{dr} \mathbf{r}, \quad (\text{B.9})$$

which is valid for a central potential, the last term in Eq. (B.8) becomes

$$H_{so} = \frac{1}{2m_0^2c^2} \frac{1}{r} \frac{dV(r)}{dr} \mathbf{L} \cdot \mathbf{S}, \quad (\text{B.10})$$

with $\mathbf{L} = \mathbf{r} \times \mathbf{p}$ and $\mathbf{S} = (\hbar/2)\boldsymbol{\sigma}$. This is the spin-orbit coupling term.

B.2 Classical approach

It is possible to find the same result as obtained above by following a more intuitive classical approach. Consider the motion of an electron around a nucleus. The electron has a magnetic moment $\boldsymbol{\mu}$ associated with its intrinsic spin \mathbf{S} which is given by

$$\boldsymbol{\mu} = -g_s \frac{e}{2m_0} \mathbf{S}, \quad (\text{B.11})$$

with $g_s = 2$ the spin g-factor which follows from relativistic quantum mechanics. In the presence of a magnetic field this magnetic moment has an energy contribution

$$H_{so} = -\boldsymbol{\mu} \cdot \mathbf{B}. \quad (\text{B.12})$$

In the rest frame of the nucleus the electron feels an electric field \mathbf{E} but no magnetic field. In the rest frame of the electron, however, the nucleus is moving and as such the electron feels a magnetic field

$$\mathbf{B} = -\frac{\mathbf{v} \times \mathbf{E}}{c^2}, \quad (\text{B.13})$$

with \mathbf{v} the velocity of the electron, which follows from a Lorentz transformation in which the non-relativistic limit $v \ll c$ was assumed. Assuming that the potential of the nucleus $V(r)$ is central, the corresponding electric field is given by

$$\mathbf{E} = -\nabla\phi = \frac{1}{er} \frac{dV}{dr} \mathbf{r}, \quad (\text{B.14})$$

with $\phi = -V/e$ the electrostatic potential. Putting everything together and using $\mathbf{p} = m_0\mathbf{v}$ and $\mathbf{L} = \mathbf{r} \times \mathbf{p}$ then leads to

$$H_{so} = \frac{1}{m_0^2 c^2} \frac{1}{r} \frac{dV(r)}{dr} \mathbf{L} \cdot \mathbf{S}. \quad (\text{B.15})$$

Notice that this expression differs by a factor 2 from the expression derived from the Dirac equation. The reason behind this discrepancy is the fact that the electron rest frame is not inertial: it accelerates as the electron orbits around the nucleus. This can be resolved by performing the Lorentz transformation from the electron rest frame to the rest frame of the electron at an infinitesimal time dt later together with a rotation to account for the new position of the electron. Adding this effect, which is known as Thomas precession [276], leads to the missing factor 2 in the denominator of the above expression. It should be noted that the expression for the spin-orbit coupling can also be derived in the rest frame of the nucleus, which is inertial. In this case there is no magnetic field, but the moving magnetic dipole of the electron acquires an electric dipole which in turn couples with the electric field of the nucleus to give the same result. However, this derivation is more extensive and is therefore not given here.

APPENDIX C

Matrix elements between correlated Gaussian basis functions

Kinetic energy

The kinetic energy of an N -particle complex can be written as

$$T = T_x + T_y = \frac{\vec{p}_x^T \Lambda \vec{p}_x}{2} + \frac{\vec{p}_y^T \Lambda \vec{p}_y}{2}, \quad (\text{C.1})$$

where \vec{p}_x and \vec{p}_y are N -dimensional vectors containing, respectively, the x - and y -components of the momenta of the different particles and with Λ a diagonal matrix containing the inverse effective masses of the particles. However, the derivation below holds for any symmetric matrix Λ . Applying the first term to the x -dependent part of a correlated Gaussian basis function (4.11) leads to

$$\begin{aligned} T_x \varphi(\vec{x}) &= -\frac{\hbar^2}{2} \sum_{i,j} \Lambda_{ij} \frac{\partial}{\partial x_i} \frac{\partial}{\partial x_j} e^{-\frac{1}{2} \sum_{k,l} A_{kl} x_k x_l} \\ &= \frac{\hbar^2}{2} \sum_{i,j} \Lambda_{ij} \frac{\partial}{\partial x_i} \left(A_{jl} x_l e^{-\frac{1}{2} \sum_{k,l} A_{kl} x_k x_l} \right) \\ &= \frac{\hbar^2}{2} \sum_{i,j} \Lambda_{ij} \left(A_{ij} - \sum_{k,l} A_{jl} x_l A_{ik} x_k \right) e^{-(\vec{x}^T A \vec{x})/2}, \end{aligned} \quad (\text{C.2})$$

where the fact that A is a symmetric matrix, i.e. $A_{ij} = A_{ji}$, was used. The second term in the above expression can be integrated by introducing a source term $\vec{J}^T \cdot \vec{x}$ to the basis functions:

$$\begin{aligned}
\int d\vec{x} x_k x_l e^{-(\vec{x}^T A \vec{x})/2} &= \int d\vec{x} \frac{d}{dJ_k} \frac{d}{dJ_l} e^{-(\vec{x}^T A \vec{x})/2 + \vec{J}^T \cdot \vec{x}} \Big|_{\vec{J}=0} \\
&= \frac{d}{dJ_k} \frac{d}{dJ_l} \prod_{i=1}^N \int dt_i e^{-\lambda_i t_i^2/2 + O_i t_i} \Big|_{\vec{J}=0} = \left(\frac{(2\pi)^N}{\det(A)} \right)^{\frac{1}{2}} \frac{d}{dJ_k} \frac{d}{dJ_l} e^{\frac{1}{2} \sum_i O_i^2 / \lambda_i} \Big|_{\vec{J}=0} \\
&= \left(\frac{(2\pi)^N}{\det(A)} \right)^{\frac{1}{2}} \frac{d}{dJ_k} \frac{d}{dJ_l} e^{\frac{1}{2} \sum_{i,j} A_{ij}^{-1} J_i J_j} \Big|_{\vec{J}=0} = \left(\frac{(2\pi)^N}{\det(A)} \right)^{\frac{1}{2}} A_{kl}^{-1},
\end{aligned} \tag{C.3}$$

where the matrix A with eigenvalues λ_i is diagonalized using the unitary transformation U and with $\vec{t} = U^T \vec{x}$ and $\vec{O} = U^T \vec{J}$, in analogy to the calculation in Eq. (4.14). Putting everything together, the matrix element of the kinetic energy between two correlated Gaussian basis functions with parameter matrices A and A' is given by

$$\begin{aligned}
\langle T \rangle &= \hbar^2 S_0^2 \left(\sum_{i,j} A_{ij} \Lambda_{ji} - \sum_{i,j,k,l} A_{ik} (A + A')_{kl}^{-1} A_{lj} \Lambda_{ji} \right) \\
&= \hbar^2 S_0^2 \text{tr} (A(I_N - (A + A')^{-1} A) \Lambda) \\
&= \hbar^2 S_0^2 \text{tr} (A(A + A')^{-1} A' \Lambda),
\end{aligned} \tag{C.4}$$

with S_0 the 1D overlap between the basis functions which is calculated in Eq. (4.14).

Delta function

The matrix element of the Dirac delta function in Eq. (4.15) between two correlated Gaussian basis functions can be calculated by rewriting it as an inverse Fourier transformation:

$$\begin{aligned}
\langle \delta(\vec{w}^T \vec{r} - \mathbf{r}_0) \rangle &= \frac{1}{(2\pi)^2} \int d\mathbf{k} e^{i\mathbf{k} \cdot \mathbf{r}_0} \int d\vec{x} e^{-(\vec{x}^T (A+A') \vec{x})/2 + ik_x \vec{w}^T \vec{x}} \\
&\quad \times \int d\vec{y} e^{-(\vec{y}^T (A+A') \vec{y})/2 + ik_y \vec{w}^T \vec{y}},
\end{aligned} \tag{C.5}$$

with \vec{w} with an N -dimensional vector containing the real constants w_k and with \vec{r} an N -dimensional vector whose components are the 2D position vectors of the

different particles. The exponent in the second integral can be rewritten as

$$\begin{aligned}
& -\frac{1}{2} (\vec{x}^T (A + A') \vec{x}) + ik_x \vec{w}^T \vec{x} = -\frac{1}{2} (\vec{x}^T - ik_x \vec{w}^T (A + A')^{-1}) (A + A') \\
& \times (\vec{x} - (A + A')^{-1} ik_x \vec{w}) + \frac{1}{2} ik_x \vec{w}^T (A + A')^{-1} ik_x \vec{w},
\end{aligned} \tag{C.6}$$

and the exponent in the third integral can be rewritten analogously. Integrating the first term in the above expression again leads to a factor S_0 since the coordinates \vec{x} are simply shifted. As such, the matrix element (C.5) reduces to

$$\begin{aligned}
\langle \delta (\vec{w}^T \vec{r} - r_0) \rangle &= \frac{S_0^2}{(2\pi)^2} \int d\mathbf{k} e^{-(\vec{w}^T (A + A')^{-1} \vec{w} k^2)/2 + i\mathbf{k} \cdot \mathbf{r}_0} \\
&= \frac{S_0^2}{2\pi \vec{w}^T (A + A')^{-1} \vec{w}} e^{-r_0^2 / (2\vec{w}^T (A + A')^{-1} \vec{w})}.
\end{aligned} \tag{C.7}$$

Keldysh potential

Using the above result and Eq. (4.15), it follows that the matrix element of the two-particle interaction potential between two correlated Gaussian basis functions is given by

$$\langle V(|\mathbf{r}_i - \mathbf{r}_j|) \rangle = \frac{S_0^2 c}{\pi} \int d\mathbf{r} V(\mathbf{r}) e^{-c r^2}, \tag{C.8}$$

with $c = 1/(2\vec{w}^T (A + A')^{-1} \vec{w})$ and $w_k = \delta_{ik} - \delta_{jk}$. This can be rewritten using Parseval's theorem, which states that

$$\int d\mathbf{r} f(\mathbf{r}) g(\mathbf{r}) = \frac{1}{(2\pi)^2} \int d\mathbf{k} \mathcal{F}[f](\mathbf{k}) \mathcal{F}[g](\mathbf{k}). \tag{C.9}$$

It follows from Eqs. (2.39) and (2.40) that the Fourier transform of the Keldysh potential is given by

$$\mathcal{F}[V](\mathbf{k}) = v_0 \frac{2\pi}{k + r_0 k^2}, \quad \text{with} \quad v_0 = \frac{e^2}{4\pi \kappa \epsilon_0}. \tag{C.10}$$

Furthermore, the Fourier transform of the Gaussian in Eq. (C.8) is given by

$$\mathcal{F}[e^{-c r^2}](\mathbf{k}) = \int d\mathbf{r} e^{-c r^2} e^{-i\mathbf{k} \cdot \mathbf{r}} = 2\pi \int dr r J_0(kr) e^{-c r^2} = \frac{\pi e^{-k^2/(4c)}}{c}. \tag{C.11}$$

As a result, the matrix element of the two-particle Keldysh potential between two correlated Gaussian basis functions reduces to

$$\langle V(|\mathbf{r}_i - \mathbf{r}_j|) \rangle = v_0 S_0^2 \int_0^\infty dk \frac{e^{-k^2/(4c)}}{1 + r_0 k} = \frac{v_0 S_0^2}{2r_0} \left(2\sqrt{\pi} F(\gamma) - e^{-\gamma^2} \text{Ei}(\gamma^2) \right), \quad (\text{C.12})$$

with $\gamma = 1/(2\sqrt{cr_0})$, F the Dawson function, and Ei the exponential integral.

Permutation operator

When the excitonic complex contains indistinguishable particles, the correlated Gaussian basis functions (4.11) are antisymmetrized accordingly. This means that the basis functions can contain terms in which the particles have been permuted, i.e. $\vec{\mathbf{r}} \rightarrow T_P \vec{\mathbf{r}}$ with T_P the permutation matrix. A matrix element involving a permuted term with parameter matrix A is equivalent to the matrix element involving the non-permuted term with parameter matrix $T_P^T A T_P$.

APPENDIX D

Kinetic energy of single vortices and vortex-antivortex pairs

The second-quantized form of the kinetic energy contribution to the Hamiltonian of a many-body system is in terms of field operators given by

$$\hat{H}_{kin} = -\frac{\hbar^2}{2m} \int d^2r \hat{\psi}^\dagger(\mathbf{r}) \nabla^2 \hat{\psi}(\mathbf{r}). \quad (\text{D.1})$$

For a macroscopically occupied ground state it is possible to assume $\hat{\psi}(\mathbf{r}) \approx \Psi(\mathbf{r})\hat{1}$ with

$$\Psi(\mathbf{r}) = \sqrt{n_s} e^{i\varphi(\mathbf{r})} \quad (\text{D.2})$$

the ground state wave function with n_s the uniform superfluid density and φ the phase. As such the kinetic energy can be written as

$$E_{kin} = \frac{n_s \hbar^2}{2m} \int d^2r |\nabla \varphi(\mathbf{r})|^2. \quad (\text{D.3})$$

Constructing the Heisenberg equation for the field operator $\hat{\psi}(\mathbf{r})$, again making the substitution $\hat{\psi}(\mathbf{r}) \approx \Psi(\mathbf{r})\hat{1}$, and deriving a continuity equation from the resulting equation allows to identify a velocity given by

$$\mathbf{v} = \frac{\hbar}{m} \nabla \varphi. \quad (\text{D.4})$$

This allows to find the circulation around a single (anti)vortex to be

$$\Gamma = \oint_C \mathbf{v} \cdot d\mathbf{l} = \frac{\hbar}{m} \oint_C \nabla \varphi \cdot d\mathbf{l} = \pm 2\pi \frac{\hbar}{m}, \quad (\text{D.5})$$

since the phase of the system changes by 2π (-2π) when moving around a vortex (antivortex). Furthermore, from the cylindrical symmetry of the (anti)vortex it follows that $\mathbf{v}(\mathbf{r}) = v(r)\mathbf{e}_\theta$, which combined with the above expression leads to

$$v(r) = \pm \frac{\hbar}{mr}. \quad (\text{D.6})$$

Inserting this in Eq. (D.3) then gives the kinetic energy of a single (anti)vortex:

$$E_{kin} = \frac{\pi n_s \hbar^2}{m} \ln \left(\frac{R}{\xi} \right), \quad (\text{D.7})$$

with R the radius of the system and where the density was assumed to be zero inside the (anti)vortex core of radius ξ .

For a bound vortex-antivortex pair separated by a distance d the contribution to the total velocity stemming from the vortex will approximately cancel with that from the antivortex for $r > d/2$. As such the kinetic energy of the pair becomes

$$E_{kin} = \frac{\pi n_s \hbar^2}{m} \ln \left(\frac{d}{2\xi} \right). \quad (\text{D.8})$$

This is an approximate result, however the crucial point is that it does not depend on R .

APPENDIX E

Derivation of the superfluid gap equation

The question that needs to be answered is whether there exists a state which has lower energy with respect to the interacting superlattice Hamiltonian (8.13) than the normal ground state in which all single-particle states surrounded by the Fermi surface are occupied for both electrons and holes. Therefore a variational state of the form

$$|\Phi\rangle = \prod_{\mathbf{k}} \left(u_{\mathbf{k}} + v_{\mathbf{k}} \hat{a}_{-\mathbf{k}}^\dagger \hat{b}_{\mathbf{k}}^\dagger \right) |\emptyset\rangle, \quad (\text{E.1})$$

with $|\emptyset\rangle$ the vacuum state of completely filled valence bands and empty conduction bands and with $u_{\mathbf{k}}$ and $v_{\mathbf{k}}$ the variational parameters which are chosen to be real and to obey $u_{\mathbf{k}} = u_{-\mathbf{k}}$ and $v_{\mathbf{k}} = v_{-\mathbf{k}}$, is used to search for the true ground state. The band indices of the operators have been dropped for notational simplicity. For this state to be normalized the variational parameters need to fulfill the relation

$$u_{\mathbf{k}}^2 + v_{\mathbf{k}}^2 = 1, \quad \forall \mathbf{k}. \quad (\text{E.2})$$

When $u_{\mathbf{k}} = \Theta(\mathbf{k} \notin \mathcal{V})$ and $v_{\mathbf{k}} = \Theta(\mathbf{k} \in \mathcal{V})$, with \mathcal{V} the volume in reciprocal space surrounded by the Fermi surface, the variational state reduces to the normal ground state. When both $u_{\mathbf{k}}$ and $v_{\mathbf{k}}$ are non-zero for the same \mathbf{k} , however, the variational state contains a superposition of an empty state and an electron-hole state, i.e. it does not have a fixed number of particles.

Furthermore, it is convenient to perform the so-called Bogoliubov transformation to the new set of operators

$$\hat{\alpha}_{\mathbf{k}} = u_{\mathbf{k}}\hat{a}_{-\mathbf{k}} - v_{\mathbf{k}}\hat{b}_{\mathbf{k}}^{\dagger}, \quad \hat{\beta}_{\mathbf{k}} = v_{\mathbf{k}}\hat{a}_{-\mathbf{k}}^{\dagger} + u_{\mathbf{k}}\hat{b}_{\mathbf{k}}, \quad (\text{E.3})$$

which have the very useful property that the variational state (E.1) is their ground state, i.e.

$$\hat{\alpha}_{\mathbf{k}}|\Phi\rangle = \hat{\beta}_{\mathbf{k}}|\Phi\rangle = 0. \quad (\text{E.4})$$

It follows from the fermionic anticommutation relations of the electron and hole operators $\hat{a}_{\mathbf{k}}$ and $\hat{b}_{\mathbf{k}}$ that the above operators adhere to the same set of rules, i.e.

$$\begin{aligned} \{\hat{\alpha}_{\mathbf{k}'}, \hat{\alpha}_{\mathbf{k}}\} &= \{\hat{\alpha}_{\mathbf{k}'}^{\dagger}, \hat{\alpha}_{\mathbf{k}}^{\dagger}\} = \{\hat{\beta}_{\mathbf{k}'}, \hat{\beta}_{\mathbf{k}}\} = \{\hat{\beta}_{\mathbf{k}'}^{\dagger}, \hat{\beta}_{\mathbf{k}}^{\dagger}\} = 0, \\ \{\hat{\alpha}_{\mathbf{k}'}, \hat{\beta}_{\mathbf{k}}\} &= \{\hat{\alpha}_{\mathbf{k}'}^{\dagger}, \hat{\beta}_{\mathbf{k}}\} = \{\hat{\alpha}_{\mathbf{k}'}, \hat{\beta}_{\mathbf{k}}^{\dagger}\} = \{\hat{\alpha}_{\mathbf{k}'}^{\dagger}, \hat{\beta}_{\mathbf{k}}^{\dagger}\} = 0, \\ \{\hat{\alpha}_{\mathbf{k}'}, \hat{\alpha}_{\mathbf{k}}^{\dagger}\} &= \{\hat{\beta}_{\mathbf{k}'}, \hat{\beta}_{\mathbf{k}}^{\dagger}\} = \delta_{\mathbf{k},\mathbf{k}'}. \end{aligned} \quad (\text{E.5})$$

Using these new operators, the expectation value of the Hamiltonian (8.13) with respect to the variational state (E.1) can be calculated and minimized, with the chemical potentials μ_e and μ_h taking into account the boundary condition of a fixed number of electrons and holes. The expectation value of the electron kinetic energy becomes

$$\begin{aligned} E_0^e &= \sum_{\mathbf{k}} \xi_{\mathbf{k}}^e \langle \Phi | \hat{a}_{\mathbf{k}}^{\dagger} \hat{a}_{\mathbf{k}} | \Phi \rangle = \sum_{\mathbf{k}} \xi_{\mathbf{k}}^e \langle \Phi | \left(u_{\mathbf{k}} \hat{\alpha}_{-\mathbf{k}}^{\dagger} + v_{\mathbf{k}} \hat{\beta}_{-\mathbf{k}} \right) \left(u_{\mathbf{k}} \hat{\alpha}_{-\mathbf{k}} + v_{\mathbf{k}} \hat{\beta}_{-\mathbf{k}}^{\dagger} \right) | \Phi \rangle \\ &= \sum_{\mathbf{k}} \xi_{\mathbf{k}}^e \langle \Phi | v_{\mathbf{k}}^2 \hat{\beta}_{-\mathbf{k}} \hat{\beta}_{-\mathbf{k}}^{\dagger} | \Phi \rangle = \sum_{\mathbf{k}} \xi_{\mathbf{k}}^e v_{\mathbf{k}}^2, \end{aligned} \quad (\text{E.6})$$

with $\xi_{\mathbf{k}}^e = \varepsilon_{\mathbf{k},1c} - \mu_e$. A completely analogous calculation for the hole kinetic energy gives $E_0^h = \sum_{\mathbf{k}} \xi_{\mathbf{k}}^h v_{\mathbf{k}}^2$ with $\xi_{\mathbf{k}}^h = -\varepsilon_{\mathbf{k},2v} - \mu_h$.

The expectation value of the electron-hole interaction term is given by

$$\begin{aligned} I_{eh} &= \sum_{\mathbf{k},\mathbf{k}'} V_{\mathbf{k},\mathbf{k}'} \langle \Phi | \hat{a}_{-\mathbf{k}'}^{\dagger} \hat{b}_{\mathbf{k}'}^{\dagger} \hat{b}_{\mathbf{k}} \hat{a}_{-\mathbf{k}} | \Phi \rangle = \sum_{\mathbf{k},\mathbf{k}'} V_{\mathbf{k},\mathbf{k}'} \langle \Phi | \left(u_{\mathbf{k}'} \hat{\alpha}_{\mathbf{k}'}^{\dagger} + v_{\mathbf{k}'} \hat{\beta}_{\mathbf{k}'} \right) \\ &\quad \times \left(u_{\mathbf{k}'} \hat{\beta}_{\mathbf{k}'}^{\dagger} - v_{\mathbf{k}'} \hat{\alpha}_{\mathbf{k}'} \right) \left(u_{\mathbf{k}} \hat{\beta}_{\mathbf{k}} - v_{\mathbf{k}} \hat{\alpha}_{\mathbf{k}}^{\dagger} \right) \left(u_{\mathbf{k}} \hat{\alpha}_{\mathbf{k}} + v_{\mathbf{k}} \hat{\beta}_{\mathbf{k}}^{\dagger} \right) | \Phi \rangle \\ &= \sum_{\mathbf{k},\mathbf{k}'} V_{\mathbf{k},\mathbf{k}'} \left(v_{\mathbf{k}'} u_{\mathbf{k}'} u_{\mathbf{k}} v_{\mathbf{k}} \langle \Phi | \hat{\beta}_{\mathbf{k}'} \hat{\beta}_{\mathbf{k}'}^{\dagger} \hat{\beta}_{\mathbf{k}} \hat{\beta}_{\mathbf{k}}^{\dagger} | \Phi \rangle + v_{\mathbf{k}'}^2 v_{\mathbf{k}}^2 \langle \Phi | \hat{\beta}_{\mathbf{k}'} \hat{\alpha}_{\mathbf{k}'} \hat{\alpha}_{\mathbf{k}}^{\dagger} \hat{\beta}_{\mathbf{k}}^{\dagger} | \Phi \rangle \right) \\ &= \sum_{\mathbf{k},\mathbf{k}'} V_{\mathbf{k},\mathbf{k}'} v_{\mathbf{k}'} u_{\mathbf{k}'} u_{\mathbf{k}} v_{\mathbf{k}} + \sum_{\mathbf{k}} V_{\mathbf{k},\mathbf{k}} v_{\mathbf{k}}^4, \end{aligned} \quad (\text{E.7})$$

with $V_{\mathbf{k},\mathbf{k}'}$ shorthand notation for the screened interaction potential (8.16). Note that the first term in the above result vanishes in the normal state limit, while it lowers the total energy for a state for which $u_{\mathbf{k}}$ and $v_{\mathbf{k}}$ are non-zero simultaneously. This term will drive the system towards the superfluid state, i.e. states for which $u_{\mathbf{k}}v_{\mathbf{k}} \neq 0$ represent electron-hole Cooper pairs. The second term on the other hand is also non-zero in the normal state and acts as a correction term $-V_{\mathbf{k},\mathbf{k}}v_{\mathbf{k}}^2$ on the kinetic energy. The expectation value of the electron-electron interaction term is given by

$$\begin{aligned} I_{ee} &= \sum_{\mathbf{k},\mathbf{k}'} V_{\mathbf{k},\mathbf{k}'}^{ee} \langle \Phi | \hat{a}_{-\mathbf{k}'}^\dagger \hat{a}_{\mathbf{k}'}^\dagger \hat{a}_{\mathbf{k}} \hat{a}_{-\mathbf{k}} | \Phi \rangle = \sum_{\mathbf{k},\mathbf{k}'} V_{\mathbf{k},\mathbf{k}'}^{ee} \langle \Phi | \left(u_{\mathbf{k}'} \hat{a}_{\mathbf{k}'}^\dagger + v_{\mathbf{k}'} \hat{\beta}_{\mathbf{k}'} \right) \\ &\quad \times \left(u_{\mathbf{k}'} \hat{\alpha}_{-\mathbf{k}'}^\dagger + v_{\mathbf{k}'} \hat{\beta}_{-\mathbf{k}'} \right) \left(u_{\mathbf{k}} \hat{\alpha}_{-\mathbf{k}} + v_{\mathbf{k}} \hat{\beta}_{-\mathbf{k}}^\dagger \right) \left(u_{\mathbf{k}} \hat{\alpha}_{\mathbf{k}} + v_{\mathbf{k}} \hat{\beta}_{\mathbf{k}}^\dagger \right) | \Phi \rangle \quad (\text{E.8}) \\ &= \sum_{\mathbf{k},\mathbf{k}'} V_{\mathbf{k},\mathbf{k}'}^{ee} v_{\mathbf{k}'}^2 v_{\mathbf{k}}^2 \langle \Phi | \hat{\beta}_{\mathbf{k}'} \hat{\beta}_{-\mathbf{k}'} \hat{\beta}_{-\mathbf{k}}^\dagger \hat{\beta}_{\mathbf{k}}^\dagger | \Phi \rangle = \sum_{\mathbf{k}} V_{\mathbf{k},\mathbf{k}}^{ee} v_{\mathbf{k}}^4. \end{aligned}$$

A completely analogous calculation shows that $I_{hh} = I_{ee}$. The electron-electron and hole-hole interaction terms need to be multiplied with an additional factor 1/2 to avoid double counting and have opposite sign compared to the electron-hole interaction term. Therefore, the kinetic energy corrections due to the three interaction terms cancel each other since for small momentum exchange the interaction potentials between particles with opposite charge and between particles with the same charge are equal.

Putting everything together, the expectation value of the Hamiltonian is given by

$$\langle \hat{H} \rangle = \sum_{\mathbf{k}} (\xi_{\mathbf{k}}^e + \xi_{\mathbf{k}}^h) v_{\mathbf{k}}^2 - \sum_{\mathbf{k},\mathbf{k}'} V_{\mathbf{k},\mathbf{k}'} v_{\mathbf{k}'} u_{\mathbf{k}'} u_{\mathbf{k}} v_{\mathbf{k}}. \quad (\text{E.9})$$

Minimizing this expression with respect to $v_{\mathbf{k}}$ and taking into account that

$$\frac{\partial u_{\mathbf{k}}}{\partial v_{\mathbf{k}}} = -\frac{v_{\mathbf{k}}}{u_{\mathbf{k}}} \quad (\text{E.10})$$

leads to the equation

$$2 (\xi_{\mathbf{k}}^e + \xi_{\mathbf{k}}^h) v_{\mathbf{k}} - \sum_{\mathbf{k}'} 2V_{\mathbf{k},\mathbf{k}'} v_{\mathbf{k}'} u_{\mathbf{k}'} \left(-\frac{v_{\mathbf{k}}}{u_{\mathbf{k}}} \right) v_{\mathbf{k}} - \sum_{\mathbf{k}'} 2V_{\mathbf{k},\mathbf{k}'} v_{\mathbf{k}'} u_{\mathbf{k}'} u_{\mathbf{k}} = 0. \quad (\text{E.11})$$

Multiplying with $u_{\mathbf{k}}$ and introducing a help function

$$\Delta_{\mathbf{k}} = \sum_{\mathbf{k}'} V_{\mathbf{k},\mathbf{k}'} u_{\mathbf{k}'} v_{\mathbf{k}'} \quad (\text{E.12})$$

reduces this to

$$(\xi_{\mathbf{k}}^e + \xi_{\mathbf{k}}^h) u_{\mathbf{k}} v_{\mathbf{k}} + \Delta_{\mathbf{k}} (v_{\mathbf{k}}^2 - u_{\mathbf{k}}^2) = 0. \quad (\text{E.13})$$

Writing $u_{\mathbf{k}} = \cos(\theta_{\mathbf{k}}/2)$ and $v_{\mathbf{k}} = \sin(\theta_{\mathbf{k}}/2)$ to account for the normalization condition allows to obtain

$$u_{\mathbf{k}}^2 = \frac{1}{2} \left(1 + \frac{\xi_{\mathbf{k}}}{E_{\mathbf{k}}} \right), \quad v_{\mathbf{k}}^2 = \frac{1}{2} \left(1 - \frac{\xi_{\mathbf{k}}}{E_{\mathbf{k}}} \right), \quad E_{\mathbf{k}} = \sqrt{\xi_{\mathbf{k}}^2 + \Delta_{\mathbf{k}}^2}, \quad \xi_{\mathbf{k}} = \frac{\xi_{\mathbf{k}}^e + \xi_{\mathbf{k}}^h}{2}, \quad (\text{E.14})$$

and as such the help function is found to obey the self-consistent equation

$$\Delta_{\mathbf{k}} = \sum_{\mathbf{k}'} V_{\mathbf{k},\mathbf{k}'} \frac{\Delta_{\mathbf{k}'}}{2E_{\mathbf{k}'}}. \quad (\text{E.15})$$

Although it is already clear that $\Delta_{\mathbf{k}}$ is directly related to the superfluid state, it is at this point not yet known what exactly is its physical significance. However, it is easy to show that $u_{\mathbf{k}} v_{\mathbf{k}} = \langle \Phi | \hat{a}_{-\mathbf{k}}^\dagger \hat{b}_{\mathbf{k}}^\dagger | \Phi \rangle$, which implies that $\Delta_{\mathbf{k}}$ is related to the pair correlation function of the electron-hole Cooper pair. Furthermore, it is insightful to break up one such electron-hole Cooper pair, i.e. set $u_{\mathbf{k}} v_{\mathbf{k}} = 0$ for one particular value of \mathbf{k} . As such, the interaction energy in the expectation value (E.9) is increased by an amount of $2\Delta_{\mathbf{k}} u_{\mathbf{k}} v_{\mathbf{k}}$. On the other hand, the kinetic energy is changed from the first term in (E.9) for the value of \mathbf{k} to either $\xi_{\mathbf{k}}^e$ or $\xi_{\mathbf{k}}^h$. When for example the hole (electron) is removed, the energy difference between the broken pair state (BP) and the superfluid ground state (GS) is given by

$$E_{\text{BP}} - E_{\text{GS}} = \xi_{\mathbf{k}}^{e(h)} - (\xi_{\mathbf{k}}^e + \xi_{\mathbf{k}}^h) v_{\mathbf{k}}^2 + 2\Delta_{\mathbf{k}} u_{\mathbf{k}} v_{\mathbf{k}} = \frac{\xi_{\mathbf{k}}^{e(h)} - \xi_{\mathbf{k}}^{h(e)}}{2} + \sqrt{\xi_{\mathbf{k}}^2 + \Delta_{\mathbf{k}}^2}, \quad (\text{E.16})$$

which at the Fermi surface reduces to $\Delta_{\mathbf{k}_F}$. This shows that the function $\Delta_{\mathbf{k}}$ is related to the energy required to break up an electron-hole pair. It is also interesting to note that

$$\begin{aligned} \hat{\alpha}_{\mathbf{k}}^\dagger | \Phi \rangle &= \left(u_{\mathbf{k}} \hat{a}_{-\mathbf{k}}^\dagger - v_{\mathbf{k}} \hat{b}_{\mathbf{k}} \right) \left(u_{\mathbf{k}} + v_{\mathbf{k}} \hat{a}_{-\mathbf{k}}^\dagger \hat{b}_{\mathbf{k}}^\dagger \right) | \emptyset \rangle \\ &= \left(u_{\mathbf{k}}^2 \hat{a}_{-\mathbf{k}}^\dagger + v_{\mathbf{k}}^2 \hat{a}_{-\mathbf{k}}^\dagger \hat{b}_{\mathbf{k}} \hat{b}_{\mathbf{k}}^\dagger \right) | \emptyset \rangle = \hat{a}_{-\mathbf{k}}^\dagger | \emptyset \rangle, \end{aligned} \quad (\text{E.17})$$

where the variational state was limited to a single electron-hole Cooper pair for notational simplicity. An analogous calculation leads to $\hat{\beta}_{\mathbf{k}}^\dagger | \Phi \rangle = \hat{b}_{\mathbf{k}}^\dagger | \emptyset \rangle$. This shows that the operator $\hat{\alpha}_{\mathbf{k}}^\dagger$ ($\hat{\beta}_{\mathbf{k}}^\dagger$) breaks up an electron-hole Cooper pair and only retains the electron (hole), i.e. it creates an excitation with energy $E_{\mathbf{k}} + \xi_{\mathbf{k}}^\delta$ ($E_{\mathbf{k}} - \xi_{\mathbf{k}}^\delta$), with $\xi_{\mathbf{k}}^\delta = (\xi_{\mathbf{k}}^e - \xi_{\mathbf{k}}^h)/2$. Since these operators satisfy the fermionic anticommutation

relations (E.5), the excitations which they create can be treated as non-interacting fermions which, at non-zero temperature and thermal equilibrium, obey the Fermi-Dirac distribution:

$$\langle \hat{\alpha}_{\mathbf{k}}^\dagger \hat{\alpha}_{\mathbf{k}} \rangle = \frac{1}{e^{(E_{\mathbf{k}} + \xi_{\mathbf{k}}^\delta)/(k_B T)} + 1}, \quad \langle \hat{\beta}_{\mathbf{k}'}^\dagger \hat{\beta}_{\mathbf{k}'} \rangle = \frac{1}{e^{(E_{\mathbf{k}'} - \xi_{\mathbf{k}'}^\delta)/(k_B T)} + 1}. \quad (\text{E.18})$$

By using these expressions to calculate the expectation values of the kinetic energy and interaction terms, using Wick decomposition for the latter, and minimizing the result, an expression for the temperature-dependent gap equation can be found. The details will not be given here but the result is given by

$$\Delta_{\mathbf{k}}(T) = \sum_{\mathbf{k}'} V_{\mathbf{k}, \mathbf{k}'} \frac{\Delta_{\mathbf{k}'}(T)}{2E_{\mathbf{k}'}} \frac{\sinh\left(\frac{E_{\mathbf{k}'}}{k_B T}\right)}{\cosh\left(\frac{E_{\mathbf{k}'}}{k_B T}\right) + \cosh\left(\frac{\xi_{\mathbf{k}'}^\delta}{k_B T}\right)}. \quad (\text{E.19})$$

Finally, the zero-temperature electron and hole densities are given by

$$n_e = \frac{2}{AN2d} \sum_{\mathbf{k}} \langle \Phi | \hat{a}_{\mathbf{k}}^\dagger \hat{a}_{\mathbf{k}} | \Phi \rangle = \frac{2}{AN2d} \sum_{\mathbf{k}} v_{\mathbf{k}}^2 = n_h, \quad (\text{E.20})$$

with N the number of TMD heterostructures of surface area A and interlayer distance d , which follows from an analogous calculation as that shown in Eq. (E.6). The factor 2 in the numerator is due to the spin/valley-degeneracy in the system. Furthermore, since $u_{\mathbf{k}}v_{\mathbf{k}}$ represents the distribution of electron-hole Cooper pairs, it follows that the condensate density is found by adding an additional factor $u_{\mathbf{k}}^2$ in the above definition. However, it is more insightful to immediately calculate the condensate fraction, which is the ratio of the condensate density to the total density and is therefore given by

$$c = \frac{\sum_{\mathbf{k}} (u_{\mathbf{k}}v_{\mathbf{k}})^2}{\sum_{\mathbf{k}} (v_{\mathbf{k}})^2}. \quad (\text{E.21})$$

Bibliography

- [1] J. Frenkel, *On the transformation of light into heat in solids*, Physical Review **37**, 17 (1931).
- [2] G. H. Wannier, *The structure of electronic excitation levels in insulating crystals*, Physical Review **52**, 191 (1937).
- [3] R. J. Elliott, *Intensity of optical absorption by excitons*, Physical Review **108**, 1384 (1957).
- [4] G. G. Macfarlane, T. P. McLean, J. E. Quarrington, and V. Roberts, *Fine structure in the absorption-edge spectrum of ge*, Physical Review **108**, 1377 (1957).
- [5] G. G. Macfarlane, T. P. McLean, J. E. Quarrington, and V. Roberts, *Fine structure in the absorption-edge spectrum of si*, Physical Review **111**, 1245 (1958).
- [6] D. G. Thomas and J. J. Hopfield, *Exciton spectrum of cadmium sulfide*, Physical Review **116**, 573 (1959).
- [7] D. G. Thomas, *The exciton spectrum of zinc oxide*, Journal of Physics and Chemistry of Solids **15**, 86 (1960).
- [8] M. D. Sturge, *Optical absorption of gallium arsenide between 0.6 and 2.75 eV*, Physical Review **127**, 768 (1962).

- [9] M. Rohlfing and S. G. Louie, *Electron-hole excitations in semiconductors and insulators*, Physical Review Letters **81**, 2312 (1998).
- [10] H. Tang, F. Lévy, H. Berger, and P. E. Schmid, *Urbach tail of anatase TiO₂*, Physical Review B **52**, 7771 (1995).
- [11] R. Asahi, Y. Taga, W. Mannstadt, and A. J. Freeman, *Electronic and optical properties of anatase TiO₂*, Physical Review B **61**, 7459 (2000).
- [12] X. L. Yang, S. H. Guo, F. T. Chan, K. W. Wong, and W. Y. Ching, *Analytic solution of a two-dimensional hydrogen atom. I. Nonrelativistic theory*, Physical Review A **43**, 1186 (1991).
- [13] R. C. Miller, D. A. Kleinman, W. T. Tsang, and A. C. Gossard, *Observation of the excited level of excitons in GaAs quantum wells*, Physical Review B **24**, 1134 (1981).
- [14] J. C. Maan, G. Belle, A. Fasolino, M. Altarelli, and K. Ploog, *Magneto-optical determination of exciton binding energy in GaAs-Ga_{1-x}Al_xAs quantum wells*, Physical Review B **30**, 2253(R) (1984).
- [15] L. C. Andreani and A. Pasquarello, *Accurate theory of excitons in GaAs-Ga_{1-x}Al_xAs quantum wells*, Physical Review B **42**, 8928 (1990).
- [16] S. Schmitt-Rink, D. S. Chemla, and D. A. B. Miller, *Linear and nonlinear optical properties of semiconductor quantum wells*, Advances in Physics **38**, 89 (1989).
- [17] R. E. Peierls, *Quelques propriétés typiques des corps solides*, Annales de l'institut Henri Poincaré **5**, 177 (1935).
- [18] L. D. Landau, *Zur theorie der phasenumwandlungen II*, Physikalische Zeitschrift der Sowjetunion **11**, 26 (1937).
- [19] N. D. Mermin and H. Wagner, *Absence of ferromagnetism or antiferromagnetism in one- or two-dimensional isotropic Heisenberg models*, Physical Review Letters **17**, 1133 (1966).
- [20] P. C. Hohenberg, *Existence of long-range order in one and two dimensions*, Physical Review **158**, 383 (1967).
- [21] N. D. Mermin, *Crystalline order in two dimensions*, Physical Review **176**, 250 (1968).

- [22] J. A. Venables, G. D. T. Spiller, and M. Handbucken, *Nucleation and growth of thin films*, Reports on Progress in Physics **47**, 399 (1984).
- [23] K. S. Novoselov, A. K. Geim, S. V. Morozov, D. Jian, Y. Zhang, S. V. Dubonos, I. V. Grigorieva, and A. A. Firsov, *Electric field effect in atomically thin carbon films*, Science **306**, 666 (2004).
- [24] K. S. Novoselov, D. Jian, F. Schedin, T. J. Booth, V. V. Khotkevich, S. V. Morozov, and A. K. Geim, *Two-dimensional atomic crystals*, Proceedings of the National Academy of Sciences of the United States of America **102**, 10451 (2005).
- [25] A. K. Geim and K. S. Novoselov, *The rise of graphene*, Nature Materials **6**, 183 (2007).
- [26] A. K. Geim, *Graphene prehistory*, Physica Scripta **2012**, 014003 (2012).
- [27] J. C. Meyer, A. K. Geim, M. I. Katsnelson, K. S. Novoselov, T. J. Booth, and S. Roth, *The structure of suspended graphene sheets*, Nature **446**, 60 (2007).
- [28] M. I. Katsnelson, *Graphene: Carbon in two dimensions*, Materials Today **10**, 20 (2007).
- [29] S. Morozov, K. S. Novoselov, M. Katsnelson, F. Schedin, D. Elias, J. Jaszczak, and A. K. Geim, *Giant intrinsic carrier mobilities in graphene and its bilayer*, Physical Review Letters **100**, 016602 (2008).
- [30] A. A. Balandin, S. Ghosh, W. Bao, I. Calizo, D. Teweldebrhan, F. Miao, and C. N. Lau, *Superior thermal conductivity of single-layer graphene*, Nano Letters **8**, 902 (2008).
- [31] R. Prasher, *Graphene spreads the heat*, Science **328**, 185 (2010).
- [32] J. Moser, A. Barreiro, and A. Bachtold, *Current-induced cleaning of graphene*, Applied Physics Letters **91**, 163513 (2007).
- [33] C. Lee, X. Wei, J. W. Kysar, and J. Hone, *Measurement of the elastic properties and intrinsic strength of monolayer graphene*, Science **321**, 385 (2008).
- [34] K. F. Mak, C. Lee, J. Hone, J. Shan, and T. F. Heinz, *Atomically thin MoS₂: A new direct-gap semiconductor*, Physical Review Letters **105**, 136805 (2010).

- [35] C. R. Dean, A. F. Young, I. Meric, C. Lee, L. Wang, S. Sorgenfrei, K. Watanabe, T. Taniguchi, P. Kim, K. L. Shepard, and J. Hone, *Boron nitride substrates for high-quality graphene electronics*, *Nature Nanotechnology* **5**, 722 (2010).
- [36] A. Kara, H. Enriquez, A. P. Seitsonen, L. L. Y. Voon, S. Vizzini, B. Aufray, and H. Oughaddou, *A review on silicene - New candidate for electronics*, *Surface Science Reports* **67**, 1 (2012).
- [37] F. Xia, H. Wang, and Y. Jia, *Rediscovering black phosphorus as an anisotropic layered material for optoelectronics and electronics*, *Nature Communications* **5**, 4458 (2014).
- [38] A. Castellanos-Gomez, *Black phosphorus: Narrow gap, wide applications*, *Journal of Physical Chemistry Letters* **6**, 4280 (2015).
- [39] A. K. Geim and I. V. Grigorieva, *Van der Waals heterostructures*, *Nature* **499**, 419 (2013).
- [40] S. Bertolazzi, J. Brivio, and A. Kis, *Stretching and breaking of ultrathin MoS₂*, *ACS Nano* **8**, 9703 (2011).
- [41] C. Ataca, H. Şahin, and S. Ciraci, *Stable, single-layer MX₂ transition-metal oxides and dichalcogenides in a honeycomb-like structure*, *Journal of Physical Chemistry* **116**, 8983 (2012).
- [42] B. Radisavljevic, A. Radenovic, J. Brivio, V. Giacometti, and A. Kis, *Single-layer MoS₂ transistors*, *Nature Nanotechnology* **6**, 147 (2011).
- [43] Y. Yoon, K. Ganapathi, and S. Salahuddin, *How good can monolayer MoS₂ transistors be*, *Nano Letters* **11**, 3768 (2011).
- [44] Z. Yin, H. Li, H. Li, L. Jiang, Y. Shi, Y. Sun, G. Lu, Q. Zhang, X. Chen, and H. Zhang, *Single-layer MoS₂ phototransistors*, *ACS Nano* **6**, 74 (2012).
- [45] O. Lopez-Sanchez, D. Lembke, M. Kayci, A. Radenovic, and A. Kis, *Ultra-sensitive photodetectors based on monolayer MoS₂*, *Nature Nanotechnology* **8**, 497 (2013).
- [46] H. S. Lee, S.-W. Min, Y.-G. Chang, M. K. Park, T. Nam, H. Kim, J. H. Kim, S. Ryu, and S. Im, *MoS₂ nanosheet phototransistors with thickness-modulated optical energy gap*, *Nano Letters* **12**, 3695 (2012).

- [47] J. S. Ross, P. Klement, A. M. Jones, N. J. Ghimire, J. Yan, D. G. Mandrus, T. Taniguchi, K. Watanabe, K. Kitamura, W. Yao, D. H. Cobden, and X. Xu, *Electrically tunable excitonic light-emitting diodes based on monolayer WSe₂ p-n junctions*, Nature Nanotechnology **9**, 268 (2014).
- [48] B. W. H. Baugher, H. O. H. Churchill, Y. Yang, and P. Jarillo-Herrero, *Optoelectronic devices based on electrically tunable p-n diodes in a monolayer dichalcogenide*, Nature Nanotechnology **9**, 262 (2014).
- [49] A. Pospischil, M. M. Furchi, and T. Mueller, *Solar-energy conversion and light emission in an atomic monolayer p-n diode*, Nature Nanotechnology **9**, 257 (2014).
- [50] K. Wang, J. Wang, J. Fan, M. Lotya, A. O'Neill, D. Fox, Y. Feng, X. Zhang, B. Jiang, Q. Zhao, H. Zhang, J. N. Coleman, L. Zhang, and W. J. Blau, *Ultrafast saturable absorption of two-dimensional MoS₂ nanosheets*, ACS Nano **7**, 9260 (2013).
- [51] H. Zhang, S. B. Lu, J. Zheng, J. Du, S. C. Wen, D. Y. Tang, and K. P. Log, *Molybdenum disulfide (MoS₂) as a broadband saturable absorber for ultrafast photonics*, Optics Express **22**, 7249 (2014).
- [52] A. Castellanos-Gomez, N. Agrait, and G. Rubio-Bollinger, *Optical identification of atomically thin dichalcogenide crystals*, Applied Physics Letters **96**, 213116 (2010).
- [53] S. Wu, S. Buckley, J. R. Schaibley, L. Feng, J. Yan, D. G. Mandrus, F. Hatami, W. Yao, J. Vučković, A. Majumdar, and X. Xu, *Monolayer semiconductor nanocavity lasers with ultralow thresholds*, Nature **520**, 69 (2015).
- [54] Y. Ye, Z. J. Wong, X. Lu, X. Ni, H. Zhu, X. Chen, Y. Wang, and X. Zhang, *Monolayer excitonic laser*, Nature Photonics **9**, 733 (2015).
- [55] A. Laturia, M. L. Van de Put, and W. G. Vandenberghe, *Dielectric properties of hexagonal boron nitride and transition metal dichalcogenides: From monolayer to bulk*, Nature Partner Journals 2D Materials and Applications **2**, 6 (2018).
- [56] D. Xiao, G.-B. Liu, W. Feng, X. Xu, and W. Yao, *Coupled spin and valley physics in monolayers of MoS₂ and other group-VI dichalcogenides*, Physical Review Letters **108**, 196802 (2012).

- [57] Q. H. Wang, K. Kalantar-Zadeh, A. Kis, J. N. Coleman, and M. S. Strano, *Electronics and optoelectronics of two-dimensional transition metal dichalcogenides*, *Nature Nanotechnology* **7**, 699 (2012).
- [58] A. Splendiani, L. Sun, Y. Zhang, T. Li, J. Kim, C.-Y. Chim, G. Galli, and F. Wang, *Emerging photoluminescence in monolayer MoS₂*, *Nano Letters* **10**, 1271 (2010).
- [59] E. Cappelluti, R. Roldán, J. A. Silva-Guillén, P. Ordejón, and F. Guinea, *Tight-binding model and direct-gap/indirect-gap transition in single-layer and multilayer MoS₂*, *Physical Review B* **88**, 075409 (2013).
- [60] G.-B. Liu, W.-Y. Shan, Y. Yao, W. Yao, and D. Xiao, *Three-band tight-binding model for monolayers of group-VIB transition metal dichalcogenides*, *Physical Review B* **88**, 085433 (2013).
- [61] H. Rostami, A. G. Moghaddam, and R. Asgari, *Effective lattice Hamiltonian for monolayer MoS₂: Tailoring electronic structure with perpendicular electric and magnetic fields*, *Physical Review B* **88**, 085440 (2013).
- [62] P.-L. Löwdin, *A note on the quantum-mechanical perturbation theory*, *The Journal of Chemical Physics* **19**, 1396 (1951).
- [63] K. Kośmider, J. W. González, and J. Fernández-Rossier, *Large spin splitting in the conduction band of transition metal dichalcogenide monolayers*, *Physical Review B* **88**, 245436 (2013).
- [64] Z. Y. Zhu, Y. C. Cheng, and U. Schwingenschlögl, *Giant spin-orbit-induced splitting in two-dimensional transition-metal dichalcogenide semiconductors*, *Physical Review B* **84**, 153402 (2011).
- [65] T. Cao, G. Wang, W. Han, H. Ye, C. Zhu, J. Shi, Q. Niu, P. Tan, E. Wang, B. Liu, and J. Feng, *Valley-selective circular dichroism of monolayer molybdenum disulphide*, *Nature Communications* **3**, 887 (2012).
- [66] H. Zeng, J. Dai, W. Yao, D. Xiao, and X. Cui, *Valley polarization in MoS₂ monolayers by optical pumping*, *Nature Nanotechnology* **7**, 490 (2012).
- [67] K. F. Mak, K. He, J. Shan, and T. F. Heinz, *Control of valley polarization in monolayer MoS₂ by optical helicity*, *Nature Nanotechnology* **7**, 494 (2012).

- [68] J. Xiao, Z. Ye, Y. Wang, H. Zhu, Y. Wang, and X. Zhang, *Nonlinear optical selection rule based on valley-exciton locking in monolayer WS₂*, *Light: Science & Applications* **4**, e366 (2015).
- [69] W. Yao, D. Xiao, and Q. Niu, *Valley-dependent optoelectronics from inversion symmetry breaking*, *Physical Review B* **77**, 235406 (2008).
- [70] G.-B. Liu, D. Xiao, Y. Yao, X. Xu, and W. Yao, *Electronic structures and theoretical modelling of two-dimensional group-VIB transition metal dichalcogenides*, *Chemical Society Reviews* **44**, 2643 (2015).
- [71] M. V. Berry, *Quantal phase factors accompanying adiabatic changes*, *Proceedings of the Royal Society A* **392**, 45 (1984).
- [72] D. Xiao, M.-C. Chang, Q. Niu, *Berry phase effects on electronic properties*, *Reviews of Modern Physics* **82**, 1959 (2010).
- [73] M.-C. Chang and Q. Niu, *Berry phase, hyperorbits, and the Hofstadter spectrum: Semiclassical dynamics in magnetic Bloch bands*, *Physical Review B* **53**, 7010 (1996).
- [74] D. Xiao, W. Yao, and Q. Niu, *Valley-contrasting physics in graphene: Magnetic moment and topological transport*, *Physical Review Letters* **99**, 236809 (2007).
- [75] T. Cai, S. A. Yang, X. Li, F. Zhang, J. Shi, W. Yao, and Q. Niu, *Magnetic control of the valley degree of freedom of massive Dirac fermions with application to transition metal dichalcogenides*, *Physical Review B* **88**, 115140 (2013).
- [76] M. R. Molas, C. Faugeras, A. O. Slobodeniuk, K. Nogajewski, M. Bartos, D. M. Basko, and M. Potemski, *Brightening of dark excitons in monolayers of semiconducting transition metal dichalcogenides*, *2D Materials* **4**, 021003 (2017).
- [77] M. Trushin, M. O. Goerbig, and W. Belzig, *Optical absorption by Dirac excitons in single-layer transition-metal dichalcogenides*, *Physical Review B* **94**, 041301(R) (2016).
- [78] P. Cudazzo, I. V. Tokatly, and A. Rubio, *Dielectric screening in two-dimensional insulators: Implications for excitonic and impurity states in graphene*, *Physical Review B* **84**, 085406 (2011).

- [79] A. V. Chaplik and M. V. Éntin, *Charged impurities in very thin layers*, Soviet Physics Journal of Experimental and Theoretical Physics **34**, 1335 (1971) (Zhurnal Èksperimental'noi i Teoreticheskoi Fiziki **61**, 2496 (1972)).
- [80] L. V. Keldysh, *Coulomb interaction in thin semiconductor and semimetal films*, Journal of Experimental and Theoretical Physics Letters **29**, 658 (1979) (Pis'ma v Zhurnal Èksperimental'noi i Teoreticheskoi Fiziki **29**, 716 (1979)).
- [81] T. C. Berkelbach, M. S. Hybertsen, and D. R. Reichman, *Theory of neutral and charged excitons in monolayer transition metal dichalcogenides*, Physical Review B **88**, 045318 (2013).
- [82] F. Bloch, *Bemerkung zur elektronentheorie des ferromagnetismus und der elektrischen leitfähigkeit*, Zeitschrift für Physik **57**, 545 (1929).
- [83] F. Iwamoto and K. Sawada, *Stability of the plane wave Hartree-Fock ground state*, Physical Review **126**, 887 (1962).
- [84] S. Misawa, *Ferromagnetism of an electron gas*, Physical Review **140**, A1645 (1965).
- [85] D. Ceperley, *Ground state of the fermion one-component plasma: A Monte Carlo study in two and three dimensions*, Physical Review B **18**, 3126 (1978).
- [86] D. M. Ceperley and B. J. Alder, *Ground state of the electron gas by a stochastic method*, Physical Review Letters **45**, 566 (1980).
- [87] C. Attaccalite, S. Moroni, P. Gori-Giorgi, and G. B. Bachelet, *Correlation energy and spin polarization in the 2D electron gas*, Physical Review Letters **88**, 256601 (2002).
- [88] C. C. Grimes, *Electrons in surface states on liquid helium*, Surface Science **73**, 379 (1978).
- [89] V. Shikin, *Theory of localized electron states on the liquid helium surface*, Surface Science **73**, 396 (1978).
- [90] F. M. Peeters and P. M. Platzman, *Electrons on films of helium: A quantum mechanical two-dimensional fermion system*, Physical Review Letters **50**, 2021 (1983).

- [91] E. Y. Andrei, C. C. Grimes, and G. Adams, *Electrons on helium - The "polaron" transition*, *Surface Science* **142**, 104 (1982).
- [92] K. S. Novoselov, A. K. Geim, S. V. Morozov, D. Jiang, M. I. Katsnelson, I. V. Grigorieva, S. V. Dubonos, and A. A. Firsov, *Two-dimensional gas of massless Dirac fermions in graphene*, *Nature* **438**, 197 (2005).
- [93] N. M. R. Peres, F. Guinea, and A. H. Castro Neto, *Coulomb interactions and ferromagnetism in pure and doped graphene*, *Physical Review B* **72**, 174406 (2005).
- [94] J. Nilsson, A. H. Castro Neto, N. M. R. Peres, and F. Guinea, *Electron-electron interactions and the phase diagram of a graphene bilayer*, *Physical Review B* **73**, 214418 (2006).
- [95] J. Luxa, O. Jankovský, D. Sedmidubský, R. Medlín, M. Maryško, M. Pumera, and Z. Sofer, *Origin of exotic ferromagnetic behavior in exfoliated layered transition metal dichalcogenides MoS₂ and WS₂*, *Nanoscale* **8**, 1960 (2016).
- [96] X.-L. Fan, Y.-R. An, and W.-J. Guo, *Ferromagnetism in transition metal-doped MoS₂ monolayer*, *Nanoscale Research Letters* **11**, 154 (2016).
- [97] P. Kumar, R. Skomski, and R. Pushpa, *Magnetically ordered transition-metal-intercalated WSe₂*, *ACS Omega* **2**, 7985 (2017).
- [98] D. Zhong, K. L. Seyler, X. Linpeng, R. Cheng, N. Sivadas, B. Huang, E. Schmidgall, T. Taniguchi, K. Watanabe, M. A. McGuire, W. Yao, D. Xiao, K.-M. C. Fu, X. Xu, *Van der Waals engineering of ferromagnetic semiconductor heterostructures for spin and valleytronics*, *Science Advances* **3**, e1603113 (2017).
- [99] J. Du, C. Xia, W. Xiong, T. Wang, Y. Jia, and J. Li, *Two-dimensional transition-metal dichalcogenides-based ferromagnetic van der Waals heterostructures*, *Nanoscale* **9**, 17585 (2017).
- [100] Y. Zhou, C. Yang, X. Xiang, and X. Zu, *Remarkable magnetism and ferromagnetic coupling in semi-sulfuretted transition-metal dichalcogenides*, *Physical Chemistry Chemical Physics* **15**, 14202 (2013).

- [101] J. He and S. Li, *Two-dimensional Janus transition-metal dichalcogenides with intrinsic ferromagnetism and half-metallicity*, Computational Materials Science **152**, 151 (2018).
- [102] M. Van der Donck and F. M. Peeters, *Rich many-body phase diagram of electrons and holes in doped monolayer transition metal dichalcogenides*, Physical Review B **98**, 115432 (2018).
- [103] J. E. H. Braz, B. Amorim, and E. V. Castro, *Valley-polarized magnetic state in hole-doped monolayers of transition-metal dichalcogenides*, Physical Review B **98**, 161406(R) (2018).
- [104] D. K. Mukherjee, A. Kundu, and H. A. Fertig, *Spin response and collective modes in simple metal dichalcogenides*, Physical Review B **98**, 184413 (2018).
- [105] D. Miserev, J. Klinovaja, and D. Loss, *Exchange intervalley scattering and magnetic phase diagram of transition metal dichalcogenide monolayers*, Physical Review B **100**, 014428 (2019).
- [106] J. T. Ye, Y. J. Zhang, R. Akashi, M. S. Bahramy, R. Arita, and Y. Iwasa, *Superconducting dome in a gate-tuned band insulator*, Science **338**, 1193 (2012).
- [107] M. Zarenia, D. Neilson, B. Partoens, and F. M. Peeters, *Wigner crystallization in transition metal dichalcogenides: A new approach to correlation energy*, Physical Review B **95**, 115438 (2017).
- [108] J. G. Roch, G. Froehlicher, N. Leisgang, P. Makk, K. Watanabe, T. Taniguchi, and R. J. Warburton, *Spin-polarized electrons in monolayer MoS₂*, Nature Nanotechnology **14**, 432 (2019).
- [109] O. L. Berman, R. Y. Kezerashvili, and K. Ziegler, *Superfluidity of dipole excitons in the presence of band gaps in two-layer graphene*, Physical Review B **85**, 035418 (2012).
- [110] O. L. Berman, R. Y. Kezerashvili, and K. Ziegler, *Coupling of two Dirac particles*, Physical Review A **87**, 042513 (2013).
- [111] O. L. Berman and R. Y. Kezerashvili, *High-temperature superfluidity of the two-component Bose gas in a transition metal dichalcogenide bilayer*, Physical Review B **93**, 245410 (2016).

- [112] C. Zhang, H. Wang, W. Chan, C. Manolatu, and F. Rana, *Absorption of light by excitons and trions in monolayers of metal dichalcogenide MoS₂: Experiments and theory*, Physical Review B **89**, 205436 (2014).
- [113] H. Wang, C. Zhang, and F. Rana, *Ultrafast dynamics of defect-assisted electron-hole recombination in monolayer MoS₂*, Nano Letters **15**, 339 (2014).
- [114] E. A. A. Pogna, M. Marsili, D. De Fazio, S. D. Conte, C. Manzoni, D. Sangalli, D. Yoon, A. Lombardo, A. C. Ferrari, A. Marini, G. Cerullo, and D. Prezzi, *Photo-induced bandgap renormalization governs the ultrafast response of single-layer MoS₂*, ACS Nano, **10**, 1182 (2015).
- [115] M. Van der Donck, M. Zarenia, and F. M. Peeters, *Excitons and trions in monolayer transition metal dichalcogenides: A comparative study between the multiband and the quadratic single-band model*, Physical Review B **96**, 035131 (2017).
- [116] M. Z. Mayers, T. C. Berkelbach, M. S. Hybertsen, and D. R. Reichman, *Binding energies and spatial structures of small carrier complexes in monolayer transition-metal dichalcogenides via diffusion Monte Carlo*, Physical Review B **92**, 161404(R) (2015).
- [117] I. Kylänpää and H.-P. Komsa, *Binding energies of exciton complexes in transition metal dichalcogenide monolayers and effect of dielectric environment*, Physical Review B **92**, 205418 (2015).
- [118] D. W. Kidd, D. K. Zhang, and K. Varga, *Binding energies and structures of two-dimensional excitonic complexes in transition metal dichalcogenides*, Physical Review B **93**, 125423 (2016).
- [119] D. Y. Qiu, T. Cao, and S. G. Louie, *Nonanalyticity, valley quantum phases, and lightlike exciton dispersion in monolayer transition metal dichalcogenides: Theory and first-principles calculations*, Physical Review Letters **115**, 176801 (2015).
- [120] F. Wu, F. Qu, and A. H. MacDonald, *Exciton band structure of monolayer MoS₂*, Physical Review B **91**, 075310 (2015).
- [121] C. Robert, M. A. Semina, F. Cadiz, M. Manca, E. Courtade, T. Taniguchi, K. Watanabe, H. Cai, S. Tongay, B. Lassagne, P. Renucci, T. Amand, X.

- Marie, M. M. Glazov, and B. Urbaszek, *Optical spectroscopy of excited exciton states in MoS₂ monolayers in van der Waals heterostructures*, *Physical Review Materials* **2**, 011001(R) (2018).
- [122] A. R. Klots, A. K. M. Newaz, B. Wang, D. Prasai, H. Krzyzanowska, J. Lin, D. Caudel, N. J. Ghimire, J. Yan, B. L. Ivanov, K. A. Velizhanin, A. Burger, D. G. Mandrus, N. H. Tolk, S. T. Pantelides, and K. I. Bolotin, *Probing excitonic states in suspended two-dimensional semiconductors by photocurrent spectroscopy*, *Scientific Reports* **4**, 6608 (2014).
- [123] H. J. Liu, L. Jiao, L. Xie, F. Yang, J. L. Chen, W. K. Ho, C. L. Gao, J. F. Jia, X. D. Cui, and M. H. Xie, *Molecular-beam epitaxy of monolayer and bilayer WSe₂: a scanning tunneling microscopy/spectroscopy study and deduction of exciton binding energy*, *2D Materials* **2**, 034004 (2015).
- [124] M. M. Ugeda, A. J. Bradley, S.-F. Shi, F. H. da Jornada, Y. Zhang, D. Y. Qiu, W. Ruan, S.-K. Mo, Z. Hussain, Z.-X. Shen, F. Wang, S. G. Louie, and M. F. Crommie, *Giant bandgap renormalization and excitonic effects in a monolayer transition metal dichalcogenide semiconductor*, *Nature Materials* **13**, 1091 (2014).
- [125] Y. Wang, S. Zhang, D. Huang, J. Cheng, Y. Li, and S. Wu, *Screening effect of graphite and bilayer graphene on excitons in MoSe₂ monolayer*, *2D Materials* **4**, 015021 (2017).
- [126] A. Chernikov, T. C. Berkelbach, H. M. Hill, A. Rigosi, Y. Li, O. B. Aslan, D. R. Reichman, M. S. Hybertsen, and T. F. Heinz, *Exciton binding energy and nonhydrogenic Rydberg series in monolayer WS₂*, *Physical Review Letters* **113**, 076802 (2014).
- [127] G. Plechinger, P. Nagler, A. Arora, A. G. del Águila, M. V. Ballottin, T. Frank, P. Steinleitner, M. Gmitra, J. Fabian, P. C. M. Christianen, R. Bratschitsch, C. Schüller, and T. Korn, *Excitonic valley effects in monolayer WS₂ under high magnetic fields*, *Nano Letters* **16**, 7899 (2016).
- [128] B. Zhu, X. Chen, and X. Cui, *Exciton binding energy of monolayer WS₂*, *Scientific Reports* **5**, 9218 (2015).
- [129] A. V. Stier, K. M. McCreary, B. T. Jonker, J. Kono, and S. A. Crooker, *Exciton diamagnetic shifts and valley Zeeman effects in monolayer WS₂ and MoS₂ to 65 Tesla*, *Nature Communications* **7**, 10643 (2016).

- [130] Z. Ye, T. Cao, K. O'Brien, H. Zhu, X. Yin, Y. Wang, S. G. Louie, and X. Zhang, *Probing excitonic dark states in single-layer tungsten disulphide*, Nature **513**, 214 (2014).
- [131] K. He, N. Kumar, L. Zhao, Z. Wang, K. F. Mak, H. Zhao, and J. Shan *Tightly bound excitons in monolayer WSe₂*, Physical Review Letters **113**, 026803 (2014).
- [132] A. V. Stier, N. P. Wilson, G. Clark, X. Xu, and S. A. Crooker, *Probing the influence of dielectric environment on excitons in monolayer WSe₂: Insight from high magnetic fields*, Nano Letters **16**, 7054 (2016).
- [133] J. Huang, T. B. Hoang, and M. H. Mikkelsen, *Probing the origin of excitonic states in monolayer WSe₂*, Scientific Reports **6**, 22414 (2016).
- [134] G. Wang, X. Marie, I. Gerber, T. Amand, D. Lagarde, L. Bouet, M. Vidal, A. Balocchi, and B. Urbaszek, *Giant enhancement of the optical second-harmonic emission of WSe₂ monolayers by laser excitation at exciton resonances*, Physical Review Letters **114**, 097403 (2015).
- [135] S. Brem, M. Selig, G. Berghäuser, and E. Malic, *Exciton relaxation cascade in two-dimensional transition metal dichalcogenides*, Scientific Reports **8**, 8238 (2018).
- [136] M. Van der Donck and F. M. Peeters, *Spectrum of exciton states in monolayer transition metal dichalcogenides: Angular momentum and Landau levels*, Physical Review B **99**, 115439 (2019).
- [137] A. Srivastava and A. Imamoğlu, *Signatures of bloch-band geometry on excitons: Nonhydrogenic spectra in transition-metal dichalcogenides*, Physical Review Letters **115**, 166802 (2015).
- [138] M. Kira and S. W. Koch, *Many-body correlations and excitonic effects in semiconductor spectroscopy*, Progress in Quantum Electronics **30**, 155 (2006).
- [139] G. Berghäuser and E. Malic, *Analytical approach to excitonic properties of MoS₂*, Physical Review B **89**, 125309 (2014).
- [140] H. Haug and S. W. Koch, *Quantum theory of the optical and electronic properties of semiconductors*, (World Scientific Publishing, Singapore, 2004).

- [141] K. F. Mak, K. He, C. Lee, G. H. Lee, J. Hone, T. F. Heinz, and J. Shan, *Tightly bound trions in monolayer MoS₂*, *Nature Materials* **12**, 207 (2013).
- [142] S. Tongay, J. Suh, C. Ataca, W. Fan, A. Luce, J. S. Kang, J. Liu, C. Ko, R. Raghunathanan, J. Zhou, F. Ogletree, J. Li, J. C. Grossman, and J. Wu, *Defects activated photoluminescence in two-dimensional semiconductors: interplay between bound, charged, and free excitons*, *Scientific Reports* **3**, 2657 (2013).
- [143] J. A. Wheeler, *Polyelectrons*, *Annals of The New York Academy of Sciences* **48**, 219 (1946).
- [144] M. A. Lampert, *Mobile and immobile effective-mass-particle complexes in nonmetallic solids*, *Physical Review Letters* **1**, 450 (1958).
- [145] G. Munschy and B. Stébé, *Existence and binding energy of the excitonic ion*, *Physica Status Solidi B* **64**, 213 (1974).
- [146] C. Riva, F. M. Peeters, and K. Varga, *Excitons and charged excitons in semiconductor quantum wells*, *Physical Review B* **61**, 13873 (2000).
- [147] C. Riva, F. M. Peeters, and K. Varga, *Magnetic field dependence of the energy of negatively charged excitons in semiconductor quantum wells*, *Physical Review B* **63**, 115302 (2001).
- [148] A. V. Filinov, C. Riva, F. M. Peeters, Y. E. Lozovik, and M. Bonitz, *Influence of well-width fluctuations on the binding energy of excitons, charged excitons, and biexcitons in GaAs-based quantum wells*, *Physical Review B* **70**, 035323 (2004).
- [149] K. Kheng, R. T. Cox, M. Y. d'Aubigné, F. Bassani, K. Saminadayar, and S. Tatarenko, *Observation of negatively charged excitons X^- in semiconductor quantum wells*, *Physical Review Letters* **71**, 1752 (1993).
- [150] A. J. Shields, M. Pepper, M. Y. Simmons, and D. A. Ritchie, *Spin-triplet negatively charged excitons in GaAs quantum wells*, *Physical Review B* **52**, 7851 (1995).
- [151] G. Finkelstein, H. Shtrikman, and I. Bar-Joseph, *Negatively and positively charged excitons in GaAs/Al_xGa_{1-x}As quantum wells*, *Physical Review B* **53**, R1709(R) (1996).

- [152] M. Hayne, C. L. Jones, R. Bogaerts, C. Riva, A. Usher, F. M. Peeters, F. Herlach, V. V. Moshchalkov, and M. Henini, *Photoluminescence of negatively charged excitons in high magnetic fields*, Physical Review B **59**, 2927 (1999).
- [153] V. Bellani, F. Rossella, F. Dionigi, M. Goiran, S. George, G. Biasiol, and L. Sorba, *Trion confinement and exciton shrinkage in the 2DEG at high magnetic fields*, Solid State Communications **152**, 1123 (2012).
- [154] W. F. Brinkman, T. M. Rice, and B. Bell, *The excitonic molecule*, Physical Review B **8**, 1570 (1973).
- [155] D. A. Kleinman, *Binding energy of biexcitons and bound excitons in quantum wells*, Physical Review B **28**, 871 (1983).
- [156] O. Mayrock, H.-J. Wünsche, F. Henneberger, C. Riva, V. A. Schweigert, and F. M. Peeters, *Weak localization of biexcitons in quantum wells*, Physical Review B **60**, 5582 (1999).
- [157] P. L. Gourley and J. P. Wolfe, *Thermodynamics of excitonic molecules in silicon*, Physical Review B **20**, 3319 (1979).
- [158] R. C. Miller, D. A. Kleinman, A. C. Gossard, and O. Munteanu, *Biexcitons in GaAs quantum wells*, Physical Review B **25**, 6545 (1982).
- [159] F. Kreller, M. Lowisch, J. Puls, and F. Henneberger, *Role of biexcitons in the stimulated emission of wide-gap II-VI quantum wells*, Physical Review Letters **75**, 2420 (1995).
- [160] V. I. Kukulin and V. M. Krasnopol'sky, *A stochastic variational method for few-body systems*, Journal of Physics G: Nuclear Physics **3**, 795 (1976).
- [161] Y. Suzuki and K. Varga, *Stochastic variational approach to quantum mechanical few-body problems*, (Springer-Verlag, Berlin, 1998).
- [162] J. Mitroy, S. Bubin, W. Horiuchi, Y. Suzuki, L. Adamowicz, W. Cencek, K. Szalewicz, J. Komasa, D. Blume, and K. Varga, *Theory and application of explicitly correlated Gaussians*, Reviews of Modern Physics **85**, 693 (2013).
- [163] K. Varga, *Solution of few-body problems with the stochastic variational method II: Two-dimensional systems*, Computer Physics Communications **179**, 591 (2008).

- [164] M. Van der Donck, M. Zarenia, and F. M. Peeters, *Excitons, trions, and biexcitons in transition-metal dichalcogenides: Magnetic-field dependence*, Physical Review B **97**, 195408 (2018).
- [165] M. Szyniszewski, E. Mostaani, N. D. Drummond, and V. I. Fal'ko, *Binding energies of trions and biexcitons in two-dimensional semiconductors from diffusion quantum Monte Carlo calculations*, Physical Review B **95**, 081301(R) (2017).
- [166] J. S. Ross, S. Wu, H. Yu, N. J. Ghimire, A. M. Jones, G. Aivazian, J. Yan, D. G. Mandrus, D. Xiao, W. Yao, and X. Xu, *Electrical control of neutral and charged excitons in a monolayer semiconductor*, Nature Communications **4**, 1474 (2013).
- [167] G. Plechinger, P. Nagler, J. Kraus, N. Paradiso, C. Strunk, C. Schüller, and T. Korn, *Identification of excitons, trions and biexcitons in single-layer WS₂*, Physica Status Solidi **9**, 457 (2015).
- [168] J. Jadcak, J. Kutrowska-Girzycka, P. Kapuscinski, J. Debus, D. Kudlacik, D. Schmidt, Y. S. Huang, M. Bayer, and L. Bryja, *Observation of three-particle complexes in WS₂ monolayers*, arXiv:1612.04122 (2016).
- [169] A. A. Mitioglu, P. Plochocka, J. N. Jadcak, W. Escoffier, G. L. J. A. Rikken, L. Kulyuk, and D. K. Maude, *Optical manipulation of the exciton charge state in single-layer tungsten disulfide*, Physical Review B **88**, 245403 (2013).
- [170] K. Wei, Y. Liu, H. Yang, X. Cheng, and T. Jian, *Large range modification of exciton species in monolayer WS₂*, Applied Optics **55**, 6251 (2016).
- [171] A. M. Jones, H. Yu, N. J. Ghimire, S. Wu, G. Aivazian, J. S. Ross, B. Zhao, J. Yan, D. G. Mandrus, D. Xiao, W. Yao, and X. Xu, *Optical generation of excitonic valley coherence in monolayer WSe₂*, Nature Nanotechnology **8**, 634 (2013).
- [172] E. Courtade, M. Semina, M. Manca, M. M. Glazov, C. Robert, F. Cadiz, G. Wang, T. Taniguchi, K. Watanabe, M. Pierre, W. Escoffier, E. L. Ivchenko, P. Renucci, X. Marie, T. Amand, and B. Urbaszek, *Charged excitons in monolayer WSe₂: Experiment and theory*, Physical Review B **96**, 085302 (2017).

- [173] C. Mai, A. Barrette, Y. Yu, Y. G. Semenov, K. W. Kim, L. Cao, and K. Gundogdu, *Many-body effects in valleytronics: Direct measurement of valley lifetimes in single-layer MoS₂*, *Nano Letters* **14**, 202 (2014).
- [174] E. J. Sie, A. J. Frenzel, Y.-H. Lee, J. Kong, and N. Gedik, *Intervalley biexcitons and many-body effects in monolayer MoS₂*, *Physical Review B* **92**, 125417 (2015).
- [175] K. Hao, J. F. Specht, P. Nagler, L. Xu, K. Tran, A. Singh, C. K. Dass, C. Schüller, T. Korn, M. Richter, A. Knorr, X. Li, and G. Moody, *Neutral and charged inter-valley biexcitons in monolayer MoSe₂*, *Nature Communications* **8**, 15552 (2017).
- [176] R. K. Chowdhury, S. Nandy, S. Bhattacharya, M. Karmakar, S. N. B. Bhaktha, P. K. Datta, A. Taraphder, and S. K. Ray, *Ultrafast time-resolved investigations of excitons and biexcitons at room temperature in layered WS₂*, *2D Materials* **6**, 015011 (2019).
- [177] Y. You, X.-X. Zhang, T. C. Berkelbach, M. S. Hybertsen, D. R. Reichman, and T. F. Heinz, *Observation of biexcitons in monolayer WSe₂*, *Nature Physics* **11**, 477 (2015).
- [178] A. Streinhoff, M. Florian, A. Singh, K. Tran, M. Kolarczik, S. Helmrich, A. W. Achtstein, U. Woggon, N. Owschimikow, F. Jahnke, and X. Li, *Biexciton fine structure in monolayer transition metal dichalcogenides*, *Nature Physics* **14**, 1199 (2018).
- [179] D. V. Tuan, B. Scharf, I. Žutić, and H. Dery, *Marrying excitons and plasmons in monolayer transition-metal dichalcogenides*, *Physical Review X* **7**, 041040 (2017).
- [180] N. Miura, *Physics of semiconductors in high magnetic fields*, (Oxford University Press, New York, 2008).
- [181] Y. Li, J. Ludwig, T. Low, A. Chernikov, X. Cui, G. Arefe, Y. D. Kim, A. M. van der Zande, A. Rigosi, H. M. Hill, S. H. Kim, J. Hone, Z. Li, D. Smirnov, and T. F. Heinz, *Valley splitting and polarization by the Zeeman effect in monolayer MoSe₂*, *Physical Review Letters* **113**, 266804 (2014).
- [182] D. MacNeill, C. Heikes, K. F. Mak, Z. Anderson, A. Kormányos, V. Zólyomi, J. Park, and D. C. Ralph, *Breaking of valley degeneracy by magnetic field in monolayer MoSe₂*, *Physical Review Letters* **114**, 037401 (2015).

- [183] G. Aivazian, Z. Gong, A. M. Jones, R.-L. Chu, J. Yan, D. G. Mandrus, C. Zhang, D. Cobden, W. Yao, and X. Xu, *Magnetic control of valley pseudospin in monolayer WSe₂*, Nature Physics **11**, 148 (2015).
- [184] A. Srivastava, M. Sidler, A. V. Allain, D. S. Lembke, A. Kis, and A. Imamoglu, *Valley Zeeman effect in elementary optical excitations of monolayer WSe₂*, Nature Physics **11**, 141 (2015).
- [185] G. Wang, L. Bouet, M. M. Glazov, T. Amand, E. L. Ivchenko, E. Palleau, X. Marie, and B. Urbaszek, *Magneto-optics in transition metal diselenide monolayers*, 2D Materials **2**, 034002 (2015).
- [186] A. Kormányos, G. Burkard, M. Gmitra, J. Fabian, V. Zolyomi, N. D. Drummond, and V. Fal'ko, *$k \cdot p$ theory for two-dimensional transition metal dichalcogenide semiconductors*, 2D Materials **2**, 022001 (2015).
- [187] J. P. Echeverry, B. Urbaszek, T. Amand, X. Marie, and I. C. Gerber, *Splitting between bright and dark excitons in transition metal dichalcogenide monolayers*, Physical Review B **93**, 121107(R) (2016).
- [188] M. Van der Donck, M. Zarenia, and F. M. Peeters, *Strong valley Zeeman effect of dark excitons in monolayer transition metal dichalcogenides in a tilted magnetic field*, Physical Review B **97**, 081109(R) (2018).
- [189] G. Wang, L. Bouet, D. Lagarde, M. Vidal, A. Balocchi, T. Amand, X. Marie, and B. Urbaszek, *Valley dynamics probed through charged and neutral exciton emission in monolayer WSe₂*, Physical Review B **90**, 075413 (2014).
- [190] S. N. Walck and T. L. Reinecke, *Exciton diamagnetic shift in semiconductor nanostructures*, Physical Review B **57**, 9088 (1997).
- [191] G. Qin, Q.-B. Yan, Z. Qin, S.-Y. Yue, M. Hu, and G. Su, *Anisotropic intrinsic lattice thermal conductivity of phosphorene from first principles*, Physical Chemistry Chemical Physics **17**, 4854 (2015).
- [192] M. Li, J. Dai, and X. C. Zeng, *Tuning the electronic properties of transition-metal trichalcogenides via tensile strain*, Nanoscale **7**, 15385 (2015).
- [193] A. N. Rudenko and M. I. Katsnelson, *Quasiparticle band structure and tight-binding model for single- and bilayer black phosphorus*, Physical Review B **89**, 201408(R) (2014).

- [194] D. Çakır, H. Sahin, and F. M. Peeters, *Tuning of the electronic and optical properties of single-layer black phosphorus by strain*, Physical Review B **90**, 205421 (2014).
- [195] Y. Du, H. Liu, Y. Deng, and P. D. Ye, *Device perspective for black phosphorus field-effect transistors: Contact resistance, ambipolar behavior, and scaling*, ACS Nano **8**, 10035 (2014).
- [196] N. Youngblood, C. Chen, S. L. Koester, and M. Li, *Waveguide-integrated black phosphorus photodetector with high responsivity and low dark current*, Nature Photonics **9**, 247 (2015).
- [197] M. Engel, M. Steiner, and P. Avouris, *Black phosphorus photodetector for multispectral, high-resolution imaging*, Nano Letters **14**, 6414 (2014).
- [198] J. Dai, M. Li, and X. C. Zeng, *Group IVB transition metal trichalcogenides: a new class of 2D layered materials beyond graphene*, WIREs Computational Molecular Science **6**, 211 (2016).
- [199] J. A. Silva-Guillén, E. Canadell, P. Ordejón, F. Guinea, and R. Roldán, *Anisotropic features in the electronic structure of the two-dimensional transition metal trichalcogenide TiS_3 : electron doping and plasmons*, 2D Materials **4**, 025085 (2017).
- [200] J. O. Island, M. Buscema, M. Barawi, J. M. Clamagirand, J. R. Ares, C. Sánchez, I. J. Ferrer, G. A. Steele, H. S. J. van der Zant, and A. Castellanos-Gomez, *Ultrahigh photoresponse of few-layer TiS_3 nanoribbon transistors*, Advanced Optical Materials **2**, 641 (2014).
- [201] J. O. Island, M. Barawi, R. Biele, A. Almazán, J. M. Clamagirand, J. R. Ares, C. Sánchez, H. S. J. van der Zant, J. V. Álvarez, R. D'Agosta, I. J. Ferrer, and A. Castellanos-Gomez, *TiS_3 transistors with tailored morphology and electrical properties*, Advanced Materials **27**, 2595 (2015).
- [202] Y. Aierken, D. Çakır, and F. M. Peeters, *Strain enhancement of acoustic phonon limited mobility in monolayer TS_3* , Physical Chemistry Chemical Physics **18**, 14434 (2016).
- [203] J. Qiao, X. Kong, Z.-X. Hu, F. Yang, and W. Ji, *High-mobility transport anisotropy and linear dichroism in few-layer black phosphorus*, Nature Communications **5**, 4475 (2014).

- [204] J. A. Silva-Guillén, E. Canadell, F. Guinea, and R. Roldán, *Strain tuning of the anisotropy in the optoelectronic properties of TiS_3* , ACS Photonics **5**, 3231 (2018).
- [205] J. O. Island, R. Biele, M. Barawi, J. M. Clamagirand, J. R. Ares, C. Sánchez, H. S. J. van der Zant, I. J. Ferrer, R. D'Agosta, and A. Castellanos-Gomez, *Titanium trisulfide (TiS_3): a 2D semiconductor with quasi-1D optical and electronic properties*, Scientific Reports **6**, 22214 (2016).
- [206] K. Khaliji, A. Fallahi, and T. Low, *Tunable polarization rotation using black phosphorous monolayers*, 41st International Conference on Infrared, Millimeter, and Terahertz waves, (Copenhagen, Denmark, 2016).
- [207] M. Van der Donck and F. M. Peeters, *Excitonic complexes in anisotropic atomically thin two-dimensional materials: Black phosphorus and TiS_3* , Physical Review B **98**, 235401 (2018).
- [208] A. Castellanos-Gomez, L. Vicarelli, E. Prada, J. O. Island, K. L. Narasimha-Acharya, S. I. Blanter, D. J. Groenendijk, M. Buscema, G. A. Steele, J. V. Alvarez, H. W. Zandbergen, J. J. Palacios, and H. S. J. van der Zant, *Isolation and characterization of few-layer black phosphorus*, 2D Materials **1**, 025001 (2014).
- [209] E. Torun, H. Sahin, A. Chaves, L. Wirtz, and F. M. Peeters, *Ab initio and semiempirical modeling of excitons and trions in monolayer TiS_3* , Physical Review B **98**, 075419 (2018).
- [210] A. Chaves, M. Z. Mayers, F. M. Peeters, and D. R. Reichman, *Theoretical investigation of electron-hole complexes in anisotropic two-dimensional materials*, Physical Review B **93**, 115314 (2016).
- [211] A. S. Rodin, A. Carvalho, and A. H. Castro Neto, *Excitons in anisotropic two-dimensional semiconducting crystals*, Physical Review B **90**, 075429 (2014).
- [212] V. Tran, R. Soklaski, Y. Liang, and L. Yang, *Layer-controlled band gap and anisotropic excitons in few-layer black phosphorus*, Physical Review B **89**, 235319 (2014).
- [213] Z. Jiang, Y. Li, S. Zhang, and W. Duan, *Realizing an intrinsic excitonic insulator by decoupling exciton binding energy from the minimum band gap*, Physical Review B **98**, 081408(R) (2018).

- [214] X. Wang, A. M. Jones, K. L. Seyler, V. Tran, Y. Jia, H. Zhao, H. Wang, L. Yang, X. Xu, and F. Xia, *Highly anisotropic and robust excitons in monolayer black phosphorus*, Nature Nanotechnology **10**, 517 (2015).
- [215] J. Yang, R. Xu, J. Pei, Y. W. Myint, F. Wang, Z. Wang, S. Zhang, Z. Yu, and Y. Lu, *Optical tuning of exciton and trion emissions in monolayer phosphorene*, Light: Science & Applications **4**, e312 (2015).
- [216] C.-H. Lee, G.-H. Lee, A. M. Van Der Zande, W. Chen, Y. Li, M. Han, X. Cui, G. Arefe, C. Nuckolls, T. F. Heinz, J. Guo, J. Hone, and P. Kim, *Atomically thin p-n junctions with van der Waals heterointerfaces*, Nature Nanotechnology **9**, 676 (2014).
- [217] P. Rivera, J. R. Schaibley, A. M. Jones, J. S. Ross, S. Wu, G. Aivazian, P. Klement, K. Seyler, G. Clark, N. J. Ghimire, J. Yan, D. G. Mandrus, W. Yao, and X. Xu, *Observation of long-lived interlayer excitons in monolayer MoSe₂-WSe₂ heterostructures*, Nature Communications **6**, 6242 (2015).
- [218] H. Heo, J. H. Sung, S. Cha, B.-G. Jang, J.-Y. Kim, G. Jin, D. Lee, J.-H. Ahn, M.-J. Lee, J. H. Shim, H. Choi, and M.-H. Jo, *Interlayer orientation-dependent light absorption and emission in monolayer semiconductor stacks*, Nature Communications **6**, 7372 (2015).
- [219] A. T. Hanbicki, H.-J. Chuang, M. R. Rosenberger, C. S. Hellberg, S. V. Sivaram, K. M. McCreary, I. I. Mazin, and B. T. Jonker, *Double indirect interlayer exciton in a MoSe₂/WSe₂ van der Waals heterostructure*, ACS Nano **12** 4719 (2018).
- [220] M. Palummo, M. Bernardi, and J. C. Grossman, *Exciton radiative lifetimes in two-dimensional transition metal dichalcogenides*, Nano Letters **15**, 2794 (2015).
- [221] J. Kang, S. Tongay, J. Zhou, J. Li, and J. Wu, *Band offsets and heterostructures of two-dimensional semiconductors*, Applied Physics Letters **102**, 012111 (2013).
- [222] K. Kósmider and J. Fernández-Rossier, *Electronic properties of the MoS₂-WS₂ heterojunction*, Physical Review B **87**, 075451 (2013).
- [223] H. Terrones, F. Lopez-Urias, and M. Terrones, *Novel hetero-layered materials with tunable direct band gaps by sandwiching different metal disulfides and diselenides*, Scientific Reports **3**, 1549 (2013).

- [224] C. Gong, H. Zhang, W. Wang, L. Colombo, R. M. Wallace, and K. Cho, *Band alignment of two-dimensional transition metal dichalcogenides: Application in tunnel field effect transistors*, Applied Physics Letters **103**, 053513 (2013).
- [225] M.-H. Chiu, C. Zhang, H.-W. Shiu, C.-P. Chuu, C.-H. Chen, C.-Y. S. Chang, C.-H. Chen, M.-Y. Chou, C.-K. Shih, and L.-J. Li, *Determination of band alignment in the single-layer $\text{MoS}_2/\text{WSe}_2$ heterojunction*, Nature Communications **6**, 7666 (2015).
- [226] M. Van der Donck and F. M. Peeters, *Interlayer excitons in transition metal dichalcogenide heterostructures*, Physical Review B **98**, 115104 (2018).
- [227] Z. Gong, G.-B. Liu, H. Yu, D. Xiao, X. Cui, X. Xu, and W. Yao, *Magneto-electric effects and valley-controlled spin quantum gates in transition metal dichalcogenide bilayers*, Nature Communications **4**, 2053 (2013).
- [228] Y. Wang, Z. Wang, W. Yao, G.-B. Liu, and H. Yu, *Interlayer coupling in commensurate and incommensurate bilayer structures of transition-metal dichalcogenides*, Physical Review B **95**, 115429 (2017).
- [229] D. V. Tuan, M. Yang, and H. Dery, *Coulomb interaction in monolayer transition-metal dichalcogenides*, Physical Review B **98**, 125308 (2018).
- [230] L. S. R. Cavalcante, A. Chaves, B. Van Duppen, F. M. Peeters, and D. R. Reichman, *Electrostatics of electron-hole interactions in van der Waals heterostructures*, Physical Review B **97**, 125427 (2018).
- [231] E. Torun, H. P. C. Miranda, A. Molina-Sánchez, and L. Wirtz, *Interlayer and intralayer excitons in MoS_2/WS_2 and $\text{MoSe}_2/\text{WSe}_2$ heterobilayers*, Physical Review B **97**, 245427 (2018).
- [232] S. Ovesen, S. Brem, C. Linderålv, M. Kuisma, P. Erhart, M. Selig, and E. Malic, *Interlayer exciton dynamics in van der Waals heterostructures*, Communications Physics **2**, 23 (2019).
- [233] J. He, K. Hummer, and C. Franchini, *Stacking effects on the electronic and optical properties of bilayer transition metal dichalcogenides MoS_2 , MoSe_2 , WS_2 , and WSe_2* , Physical Review B **89**, 075409 (2014).

- [234] K. Xu, Y. Xu, H. Zhang, B. Peng, H. Shao, G. Ni, J. Li, M. Yao, H. Lu, H. Zhu, C. M. Soukoulis, *The role of Anderson's rule in determining electronic, optical and transport properties of transition metal dichalcogenide heterostructures*, *Physical Chemistry Chemical Physics* **20**, 30351 (2018).
- [235] L. A. Jauregui, A. Y. Joe, K. Pistunova, D. S. Wild, A. A. High, Y. Zhou, G. Scuri, K. De Greve, A. Sushko, C.-H. Yu, T. Taniguchi, K. Watanabe, D. J. Needleman, M. D. Lukin, H. Park, and P. Kim, *Electrical control of interlayer exciton dynamics in atomically thin heterostructures*, arXiv:1812.08691 (2018).
- [236] H. Kamerlingh Onnes, *Further experiments with liquid helium*, *Koninklijke Nederlandsche Akademie van Wetenschappen Proceedings* **13**, 1093 (1911).
- [237] P. Kapitza, *Viscosity of liquid helium below the λ -point*, *Nature* **141**, 74 (1938).
- [238] J. F. Allen and A. D. Misener, *Flow phenomena in liquid helium II*, *Nature* **142**, 643 (1938).
- [239] F. London, *The λ -phenomenon of liquid helium and the Bose-Einstein degeneracy*, *Nature* **141**, 643 (1938).
- [240] S. N. Bose, *Plancks gesetz und lichtquantenhypothese*, *Zeitschrift für Physik* **26**, 178 (1924).
- [241] A. Einstein, *Quantentheorie des einatomigen idealen gases*, *Sitzungsberichte der Preussischen Akademie der Wissenschaften* **1**, 3 (1925).
- [242] D. D. Osheroff, R. C. Richardson, and D. M. Lee, *Evidence for a new phase of solid He^3* , *Physical Review Letters* **28**, 885 (1972).
- [243] D. D. Osheroff, W. J. Gully, R. C. Richardson, and D. M. Lee, *New magnetic phenomena in liquid He^3 below 3 mK*, *Physical Review Letters* **29**, 920 (1972).
- [244] A. J. Leggett, *Interpretation of recent results on He^3 below 3 mK: A new liquid phase?*, *Physical Review Letters* **29**, 1227 (1972).
- [245] H. Fröhlich, *Theory of the superconducting state. I. The ground state at the absolute zero of temperature*, *Physical Review* **79**, 845 (1950).

- [246] L. N. Cooper, *Bound electron pairs in a degenerate Fermi gas*, Physical Review **104**, 1189 (1956).
- [247] J. Bardeen, L. N. Cooper, and J. R. Schrieffer, *Theory of superconductivity*, Physical Review **108**, 1175 (1957).
- [248] J. M. Blatt, K. W. Böer, and W. Brandt, *Bose-Einstein condensation of excitons*, Physical Review **126**, 1691 (1962).
- [249] Y. E. Lozovik and V. I. Yudson, *Feasibility of superfluidity of paired spatially separated electrons and holes; a new superconductivity mechanism*, Journal of Experimental and Theoretical Physics Letters **22**, 274 (1975) (Pis'ma v Zhurnal Èksperimental'noi i Teoreticheskoi Fiziki **22**, 576 (1975)).
- [250] T. Fukuzawa, E. E. Mendez, and J. M. Hong, *Phase transition of an exciton system in GaAs coupled quantum wells*, Physical Review Letters **64**, 3066 (1990).
- [251] I. B. Spielman, J. P. Eisenstein, L. N. Pfeiffer, and K. W. West, *Resonantly enhanced tunneling in a double layer quantum hall ferromagnet*, Physical Review Letters **84**, 5808 (2000).
- [252] A. A. High, J. R. Leonard, M. Remeika, L. V. Butov, M. Hanson, and A. C. Gossard, *Condensation of excitons in a trap*, Nano Letters **12**, 2605 (2012).
- [253] Y. E. Lozovik and A. A. Sokolik, *Electron-hole pair condensation in a graphene bilayer*, Journal of Experimental and Theoretical Physics Letters **87**, 55 (2008) (Pis'ma v Zhurnal Èksperimental'noi i Teoreticheskoi Fiziki **87**, 61 (2008)).
- [254] C.-H. Zhang and Y. N. Joglekar, *Excitonic condensation of massless fermions in graphene bilayers*, Physical Review B **77**, 233405 (2008).
- [255] H. Min, R. Bistritzer, J.-J. Su, and A. H. MacDonald, *Room-temperature superfluidity in graphene bilayers*, Physical Review B **78**, 121401(R) (2008).
- [256] A. Perali, D. Neilson, and A. R. Hamilton, *High-temperature superfluidity in double-bilayer graphene*, Physical Review Letters **110**, 146803 (2013).
- [257] G. W. Burg, N. Prasad, K. Kim, T. Taniguchi, K. Watanabe, A. H. MacDonald, L. F. Register, and E. Tutuc, *Strongly enhanced tunneling at total charge neutrality in double-bilayer graphene-WSe₂ heterostructures*, Physical Review Letters **120**, 177702 (2018).

- [258] M. Zarenia, A. Perali, D. Neilson, and F. M. Peeters, *Enhancement of electron-hole superfluidity in double few-layer graphene*, Scientific Reports **4**, 7319 (2014).
- [259] M. M. Fogler, L. V. Butov, and K. S. Novoselov, *High-temperature superfluidity with indirect excitons in van der Waals heterostructures*, Nature Communications **5**, 4555 (2014).
- [260] V. L. Berezinskiĭ, *Destruction of long-range order in one-dimensional and two-dimensional systems possessing a continuous symmetry group. II. Quantum systems*, Soviet Physics Journal of Experimental and Theoretical Physics **34**, 610 (1972) (Zhurnal Èksperimental'noi i Teoreticheskoi Fiziki **61**, 1144 (1972)).
- [261] J. M. Kosterlitz and D. J. Thouless, *Ordering, metastability and phase transitions in two-dimensional systems*, Journal of Physics C: Solid State Physics **6**, 1181 (1973).
- [262] A. L. Fetter, *Electrodynamics of a layered electron gas. II. Periodic array*, Annals of Physics **88**, 1 (1974).
- [263] V. N. Kotov, B. Uchoa, V. M. Pereira, F. Guinea, and A. H. Castro Neto, *Electron-electron interactions in graphene: Current status and perspectives*, Reviews of Modern Physics **84**, 1067 (2012).
- [264] I. Sodemann, D. A. Pesin, and A. H. MacDonald, *Interaction-enhanced coherence between two-dimensional Dirac layers*, Physical Review B **85**, 195136 (2012).
- [265] Y. E. Lozovik, S. L. Ogarkov, and A. A. Sokolik, *Condensation of electron-hole pairs in a two-layer graphene system: Correlation effects*, Physical Review B **86**, 045429 (2012).
- [266] M. Franz, *Importance of fluctuations*, Nature Physics **3**, 686 (2007).
- [267] A. Perali, P. Pieri, G. C. Strinati, and C. Castellani, *Pseudogap and spectral function from superconducting fluctuations to the bosonic limit*, Physical Review B **66**, 024510 (2002).
- [268] P. Nozières and S. Schmitt-Rink, *Bose condensation in an attractive fermion gas: From weak to strong coupling superconductivity*, Journal of Low Temperature Physics **59**, 195 (1985).

- [269] C. A. R. Sá de Melo, M. Randeria, and J. R. Engelbrecht, *Crossover from BCS to Bose superconductivity: Transition temperature and time-dependent Ginzburg-Landau theory*, Physical Review Letters **71**, 3202 (1993).
- [270] E. Burovski, E. Kozik, N. Prokof'ev, B. Svistunov, and M. Troyer, *Critical temperature curve in BEC-BCS crossover*, Physical Review Letters **101**, 090406 (2008).
- [271] F. Pistolesi and G. C. Strinati, *Evolution from BCS superconductivity to Bose condensation: Role of the parameter $k_F\xi$* , Physical Review B **49**, 6356 (1994).
- [272] F. Pistolesi and G. C. Strinati, *Evolution from BCS superconductivity to Bose condensation: Calculation of the zero-temperature phase coherence length*, Physical Review B **53**, 15168 (1996).
- [273] T. Deilmann and K. S. Thygesen, *Interlayer trions in the MoS_2/WS_2 van der Waals heterostructure*, Nano Letters **18**, 1460 (2018).
- [274] S. Mouri, W. Zhang, D. Kozawa, Y. Miyauchi, G. Eda, and K. Matsuda, *Thermal dissociation of inter-layer excitons in $\text{MoS}_2/\text{MoSe}_2$ hetero-bilayers*, Nanoscale **9**, 6674 (2017).
- [275] J. C. Slater and G. F. Koster, *Simplified LCAO method for the periodic potential problem*, Physical Review **94**, 1498 (1954).
- [276] L. H. Thomas, *The motion of the spinning electron*, Nature **117**, 514 (1926).

Curriculum Vitae

Personal Data

NAME: Matthias Van der Donck
PLACE AND DATE OF BIRTH: Brasschaat, Belgium | July 20, 1992
ADDRESS: Elisabethlaan 170/1, 2600 Berchem, Belgium
PHONE: +32 478 547444
EMAIL: matthias.vanderdonck@uantwerpen.be

Education

- 2015 - 2019 **FWO Aspirant - PhD student**
University of Antwerp
Thesis: Excitonic complexes in transition metal dichalcogenides and related materials
Supervisor: Prof. Dr. F. M. PEETERS
- 2013 - 2015 **Master of Science in Physics**
Summa cum laude (92%), University of Antwerp
Thesis: Enormous pseudomagnetic fields in bilayer graphene
Supervisor: Prof. Dr. F. M. PEETERS
- 2010 - 2013 **Bachelor of Science in Physics**
Magna cum laude (83%), University of Antwerp
Thesis (theoretical): Berry phase in single layer and bilayer graphene
Supervisor: Prof. Dr. B. PARTOENS
Thesis (experimental): Study of the underlying event using Monte Carlo simulations
Supervisor: Prof. Dr. P. VAN MECHELEN

Publications

1. **M. Van der Donck**, F. M. Peeters, and B. Van Duppen, *Transport properties of bilayer graphene in a strong in-plane magnetic field*, Physical Review B **93**, 115423 (2016).

2. **M. Van der Donck**, F. M. Peeters, and B. Van Duppen, *Comment on “Creating in-plane pseudomagnetic fields in excess of 1000 T by misoriented stacking in a graphene bilayer”*, Physical Review B **93**, 247401 (2016).
3. **M. Van der Donck**, C. De Beule, B. Partoens, F. M. Peeters, and B. Van Duppen, *Piezoelectricity in asymmetrically strained bilayer graphene*, 2D Materials **3**, 035015 (2016).
4. **M. Van der Donck**, M. Zarenia, and F. M. Peeters, *Excitons and trions in monolayer transition metal dichalcogenides: A comparative study between the multiband and the quadratic single-band model*, Physical Review B **96**, 035131 (2017).
5. **M. Van der Donck**, M. Zarenia, and F. M. Peeters, *Strong valley Zeeman effect of dark excitons in monolayer transition metal dichalcogenides in a tilted magnetic field*, Physical Review B **97**, 081109(R) (2018).
6. W. Wang, B. Van Duppen, **M. Van der Donck**, and F. M. Peeters, *Magnetopolaron effect on shallow-impurity states in the presence of magnetic and intense terahertz laser fields in the Faraday configuration*, Physical Review B **97**, 064108 (2018).
7. **M. Van der Donck**, M. Zarenia, and F. M. Peeters, *Excitons, trions, and biexcitons in transition-metal dichalcogenides: Magnetic-field dependence*, Physical Review B **97**, 195408 (2018).
8. H. M. Abdullah, **M. Van der Donck**, H. Bahlouli, F. M. Peeters, and B. Van Duppen, *Graphene quantum blisters: A tunable system to confine charge carriers*, Applied Physics Letters **112**, 213101 (2018).
9. **M. Van der Donck** and F. M. Peeters, *Interlayer excitons in transition metal dichalcogenide heterostructures*, Physical Review B **98**, 115104 (2018).
10. **M. Van der Donck** and F. M. Peeters, *Rich many-body phase diagram of electrons and holes in doped monolayer transition metal dichalcogenides*, Physical Review B **98**, 115432 (2018).
11. **M. Van der Donck** and F. M. Peeters, *Excitonic complexes in anisotropic atomically thin two-dimensional materials: Black phosphorus and TiS_3* , Physical Review B **98**, 235401 (2018).

12. **M. Van der Donck** and F. M. Peeters, *Spectrum of exciton states in monolayer transition metal dichalcogenides: Angular momentum and Landau levels*, Physical Review B **99**, 115439 (2019).
13. **M. Van der Donck**, S. Conti, A. Perali, A. R. Hamilton, B. Partoens, F. M. Peeters, and D. Neilson, *High temperature 3D electron-hole superfluidity in a superlattice*, Nature Physics (submitted).
14. S. Conti, **M. Van der Donck**, A. Perali, F. M. Peeters, and D. Neilson, *Exploiting multicomponent effects in bilayer transition metal dichalcogenides for enhanced electron-hole superfluidity*, Physical Review Letters (submitted)
15. L. L. Li, **M. Van der Donck**, and F. M. Peeters, *Strain tunable plasmons and excitons in monolayer and bilayer phosphorene*, (manuscript in preparation).
16. J. Merckx, **M. Van der Donck**, B. Van Duppen, and F. M. Peeters, *Inhomogeneous magnetic field effects in kinked, rippled, and wrinkled graphene*, (manuscript in preparation)
17. T. Rey, R. Van Pottelberge, **M. Van der Donck**, F. M. Peeters, and B. Van Duppen, *Hydrogen-like confinement in anisotropic TMTs: Breaking of angular degeneracy*, (manuscript in preparation)

Conferences and Courses

- 2015 COMSOL Multiphysics Free Introduction Course, COMSOL, Antwerp
- 2015 Quantum mechanics without wave functions: from Wigner to signed particles, Antwerp
- 2017 Dirac physics: from graphene to topological phases, Antwerp
- 2017 Advance electromagnetism, Antwerp
- 2018 Leadership and Teamwork, Antwerp Doctoral School, Antwerp
- 2018 BPS General Scientific Meeting, Antwerp (poster)
- 2018 Graphene Week, San Sebastian (poster)

Teaching Experience

- 2015 - 2018 Introduction to Quantum Mechanics (Exercise sessions)
University of Antwerp, Bachelor in Physics

Computer Skills

OPERATING SYSTEMS: Linux, Windows
TEXT AND TYPESETTING EDITORS: Excel, Powerpoint, Word, L^AT_EX
PROGRAMMING LANGUAGES: Python, C/C++, Fortran, JavaScript
MATHEMATICAL SOFTWARE: MATLAB, Mathematica, COMSOL, Maple
OTHER LANGUAGES/SKILLS: SQL, HTML, CSS, Bash, Git
MACHINE LEARNING: Neural Networks, Linear Regression, Random Forests, Naive Bayes Classifier, Support Vector Machines, K-Nearest Neighbors, K-Means Clustering

Languages

DUTCH: Native
ENGLISH: Fluent
FRENCH: Intermediate

Personal Competences

Analytical Thinker, Independent Worker, Quick Learner, Creative, Accurate, Well-Organized

Interests and Activities

Football, Squash, Travelling, Playing Drums, Web Development